Dissertation

Submitted to the

Combined Faculty of Natural Sciences and Mathematics

Heidelberg University, Germany

for the degree of

Doctor of Natural Sciences (Dr. rer. nat.)

Presented by

M. Sc. Hao Zhang

Oral examination: September 24th, 2021

Styrylbenzene and Phenyleneethynylene Derivatives: Synthesis, Properties and Their Application in Fluorescent Sensor Field

Gutachter: Prof. Dr. Uwe H. F. Bunz

Prof. Dr. Milan Kivala

Acknowledgement

The completion of this thesis is attributed to the support and encouragement of many people. Many thanks go to:

- My supervisor, Prof. Dr. Uwe H. F. Bunz, for his constant guidance and valuable suggestions through the entire academic studies. His profound academic accomplishments, strong sense of responsibility and professional dedication always influence me and benefit me a lot.
- Prof. Dr. Milan Kivala for kindly accepting to be my second reviewer.
- Dr. Jan Freudenberg and Dr. Kai Seehafer for their expert and valuable advices and paper revision.
- My collaborators, Prof. Dr. Rasmus R. Schröder and Dr. Irene Wacker (Cryo Electron Microscopy, BioQuant, Universitatsklinikum Heidelberg) for their kind supports on the SEM characterization.
- Dr. Frank Rominger for his assistance with single crystal analysis.
- Frau Kerstin Windisch, Frau Kerstin Brödner, Frau Olena Tverskoy and Herr Holger Lambert for their friendly help and effective organization to provide a stable working environment for us.
- All employees of the OCI for their kind help in measurements, like MS analysis, NMR spectra and elemental analysis, and also administration departments.
- My intelligent colleagues, Dr. Soh Kushida, Dr. Maximilian Bojanowski, Dr. Benhua Wang, Dr. Wei Huang, Dr. Gaozhan Xie, Dr. Sebastian Intorp, Dr. Lukas Ahrens, Steffen Maier, Thomas Wiesner, Wansheng Zong, Daniel Ehjeij and Saskia Braun for their great support and fruitful discussions during my research.
- The whole working group members for the friendly cooperation and cozy atmosphere they creat.
- My dear friends, Eugen Kotlear, Lei Li, Chao Hu, and Xiaokun Huang who have walked alongside me during these years. I will never forget those days we studied and played together.
- The CSC (Chinese Scholarship Council) for their financial support of my Ph.D. research.
- My dear family for their love and great faith in me for many years. My beloved wife, Suyun Yang, thoughtful parents and considerate sisters, have always been there for me all the time. Thank you for having provided me with a loving environment and having given me unwavering support.

Abstract

Chemically tailorable styrylbenzene and phenyleneethynylene derivatives (SBs and PEs) are the subject of intense research, and are relevant in the fields of sensory materials and optoelectronic device engineering. To this end, the focus of this thesis is construction of SBs and PEs and investigating their optical properties and sensing applications.

In chapter 2, we focus on the styrylbenzene derivatives. On the basis of tristyrylbenzene (TSB), we take the advantage of aggregation-induced emission (AIE) into account, design two isomers and explore the regioisomerism effect on the optical properties (chapter 2.1). Then, using the 1,3,5-tristyrylbenzene as a star-shaped core, we extend the moleculer skeleton and design a series of tristyrylbenzene derivatives to investigate their photophysical properties and optical response to acid and metal ions. The transition metals such as Al^{3+}, Mn^{2+}, Fe^{3+}, Fe^{2+}, Cd^{2+}, Ag^{+} and Hg^{2+} can be well discriminated by these SBs (chapter 2.2).

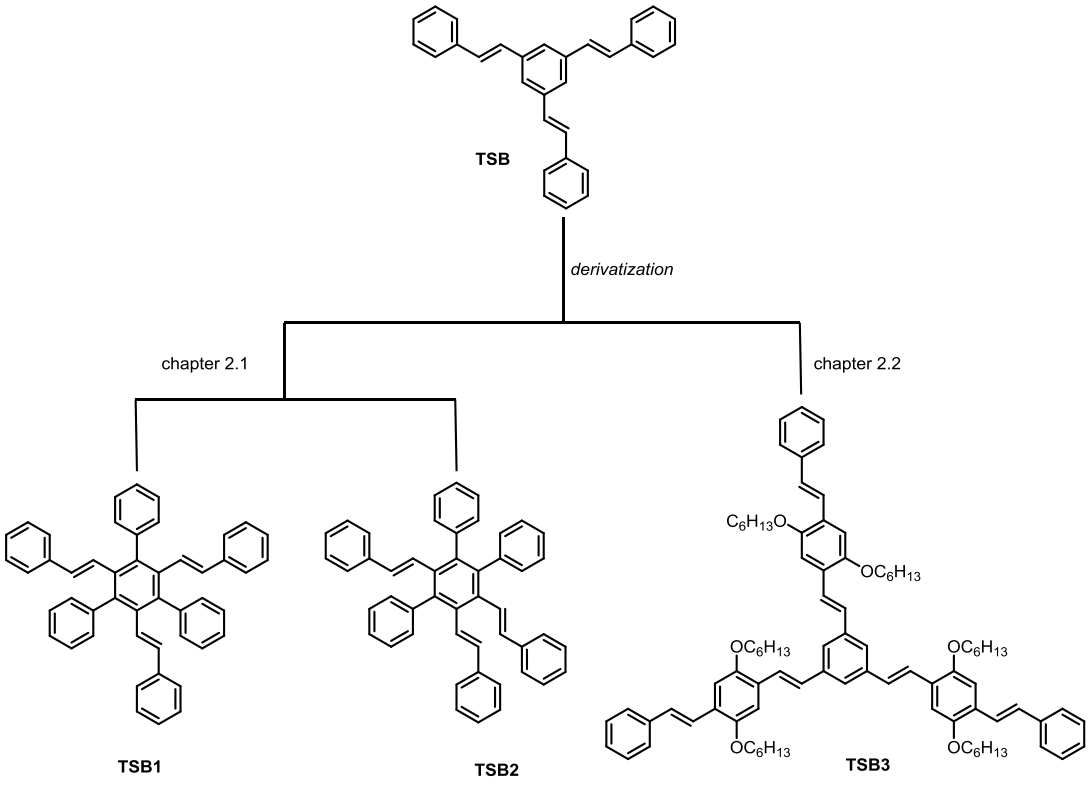

Scheme 1. Structure of representative SBs explored in this work.

Using ionic phenyleneethynylene derivatives as sensors for analytes with similar structure is interesting. In chapter 3, we focus on the phenyleneethynylene derivatives. We first construct a sensor array composed of three anionic poly(*p*-phenyleneethynylene)s (PPEs), and their electrostatic complexes with metal ions (Fe^{2+}, Cu^{2+}, Co^{2+}). This array discriminates PTH-amino acid residues degraded from an oligopeptide through Edman sequencing (chapter 3.1). Given that synthesis of guanidine-substituted PEs and their characterization remains a challenge, we design a series of PE-trimers bearing *N*-Boc-protected guanidine side groups, to address the deprotection defects under regular condition

(DCM/TFA). Meanwhile, their optical properties are discussed (chapter 3.2). On the basis of above research, we prepare the true guanidinium-PPE (chapter 3.3) and reveal that this material is a precious sensor for nitroaromatics. The guanidinium-PPE could detect picric acid with high selectivity and sensitivity in water.

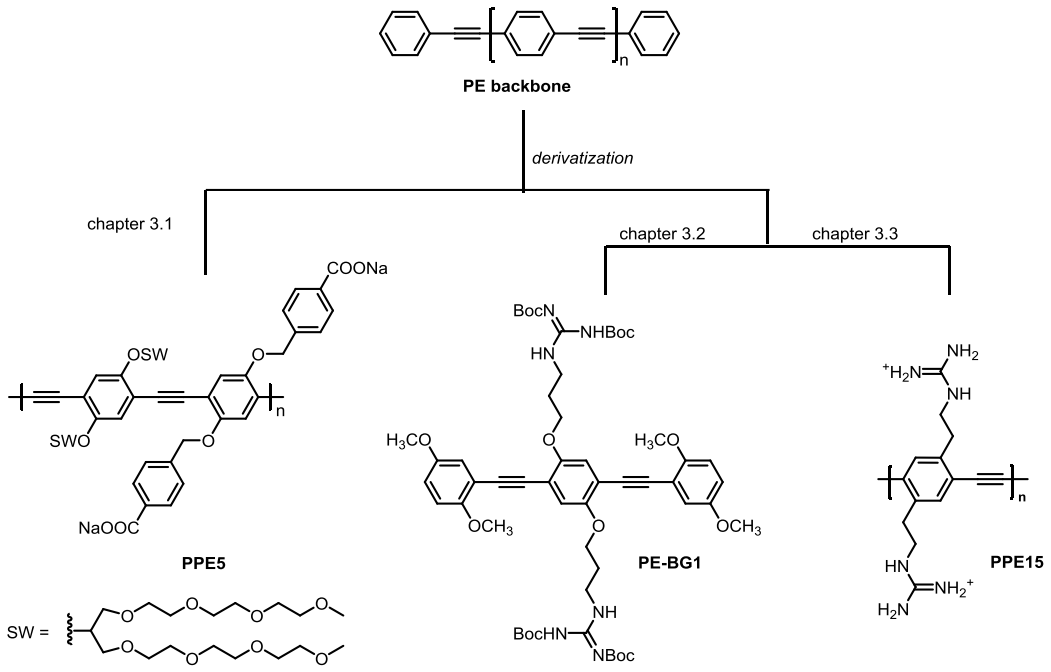

Scheme 2. Structure of representative PEs explored in this work.

All together, these results contribute to the development of research on hydrocarbon AIEgens and the application of SB/PE-based materials for luminescent chemosensors.

Zusammenfassung

Die chemisch anpassbaren Styrylbenzol- und Phenylenethinylen-Derivate (SBs und PEs) sind Gegenstand intensiver Forschung. Sie sind insbesondere in den Bereichen sensorische Materialien und optoelektronische Gerätetechnik relevant. Zu diesem Zweck liegt der Fokus dieser Arbeit auf der Konstruktion von SBs und PEs und der Untersuchung ihrer optischen Eigenschaften und Sensoranwendungen.

In Kapitel zwei konzentrieren wir uns auf die Styrylbenzol-Derivate. Anhand von Tristyrylbenzol (TSB) berücksichtigen wir den Vorteil der aggregationsinduzierten Emission (AIE), designen zwei Isomere und untersuchen den Einfluss der Regioisomerie auf die optischen Eigenschaften (Kapitel 2.1). Dann erweitern wir mit 1,3,5-Tristyrylbenzol als sternförmigen Kern das Molekülgerüst und entwerfen eine Reihe von Tristyrylbenzol-Derivaten, um ihre photophysikalischen Eigenschaften und ihre optische Reaktion auf Säure- und Metallionen zu untersuchen. Übergangsmetalle wie Al^{3+}, Mn^{2+}, Fe^{3+}, Fe^{2+}, Cd^{2+}, Ag^{+} und Hg^{2+} können durch diese SBs gut unterschieden werden (Kapitel 2.2).

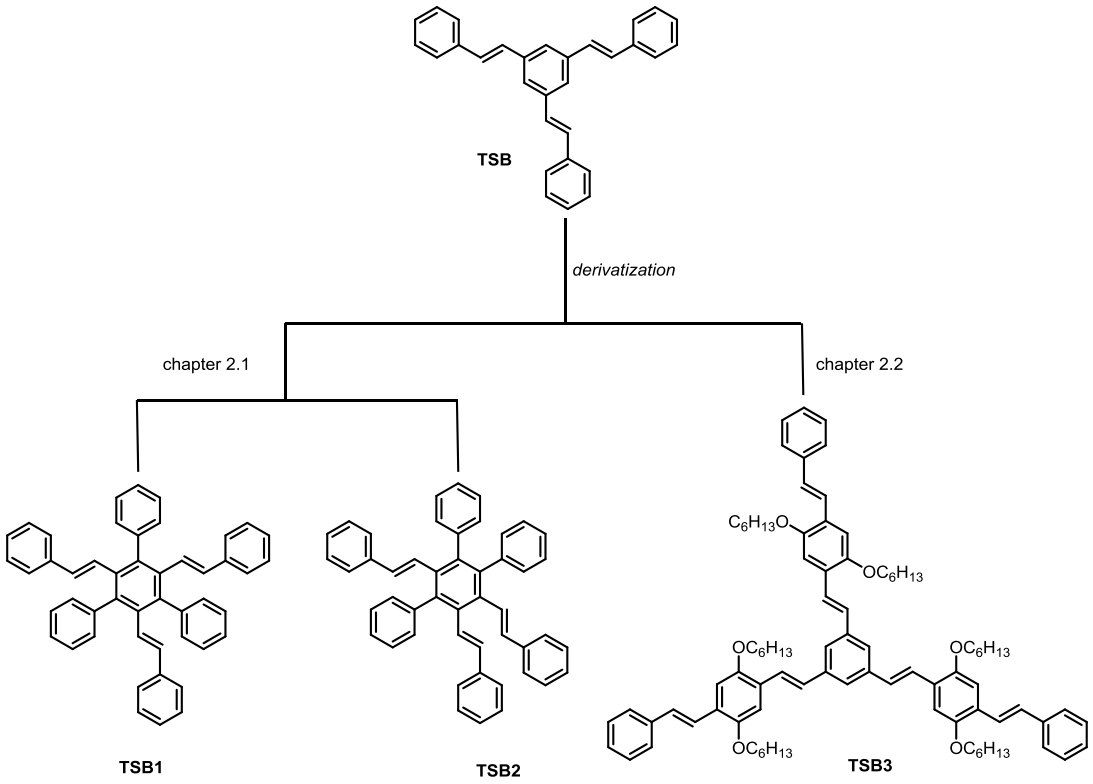

Schema 1. Struktur repräsentativer SBs, die in dieser Arbeit untersucht wurden.

Interessant ist die Verwendung von Phenylenethinylenderivaten vom Ionentyp als Sensoren für Analyten mit ähnlicher Struktur. In Kapitel drei konzentrieren wir uns auf die Phenylenethinylen-Derivate. Wir konstruieren zunächst eine Sensorenanordnung aus drei anionischen Poly(*p*-phenylenethinylenen) (PPEs) und ihren elektrostatischen Komplexen mit Metallionen (Fe^{2+}, Cu^{2+}, Co^{2+}). Diese Sensorenanordnung unterscheidet PTH-Aminosäurereste, die von einem Oligopeptid durch Edman-Sequenzierung abgebaut wurden (Kapitel 3.1). Da die Synthese von Guanidin-substituierten PEs

und deren Charakterisierung eine Herausforderung bleibt, entwickeln wir eine Reihe von PE-Trimeren mit *N*-Boc-geschützten Guanidin-Seitengruppen, um die Entschützungsprobleme unter normalen Bedingungen (DCM/TFA) zu beheben. Inzwischen werden ihre optischen Eigenschaften diskutiert (Kapitel 3.2). Auf der Grundlage der obigen Forschung bereiten wir das echte Guanidinium-PPE (Kapitel 3.3) vor und sagen, dass dieses Material ein wertvoller Sensor für Nitroaromaten ist. Guanidinium-PPE erkennt Pikrinsäure mit hoher Selektivität und Empfindlichkeit in Wasser.

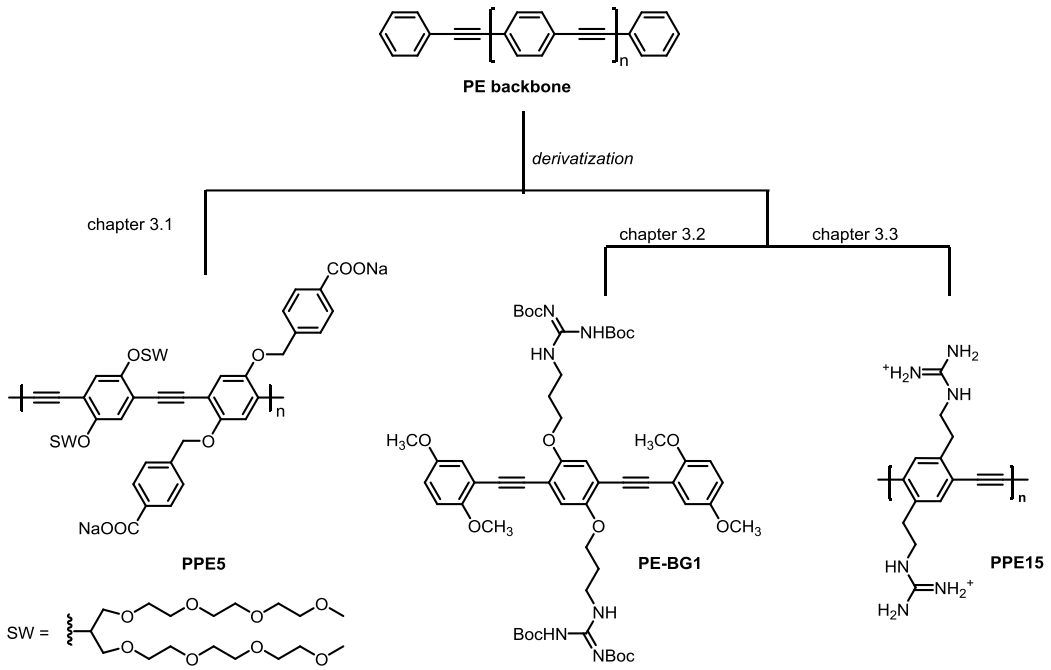

Schema 2. Struktur repräsentativer PEs, die in dieser Arbeit untersucht wurden.

Zusammengenommen tragen diese Ergebnisse zur Entwicklung der Forschung an Kohlenwasserstoff-AIEgens und zur Anwendung von SB/PE-basierten Materialien für lumineszierende Chemosensoren bei.

Publications

Hao Zhang, Frank Rominger, Uwe H. F. Bunz* and Jan Freudenberg*, Aggregation-Induced Emission of Triphenyl-Substituted Tristyrylbenzenes. *Chem. Eur. J*. **2019**, *25*, 11218-11222.

Hao Zhang, Eugen A. Kotlear, Soh Kushida, Steffen Maier, Frank Rominger, Jan Freudenberg and Uwe H. F. Bunz*. Linear and Star-Shaped Extended Di- and Tristyrylbenzenes: Synthesis, Characterization and Optical Response to Acid and Metal Ions. *Chem. Eur. J.* **2020**, *26*, 8137-8143.

Hao Zhang, Benhua Wang, Kai Seehafer and Uwe H. F. Bunz*. Sensor Array Based Determination of Edman Degradated Amino Acids Using Poly(*p*-phenyleneethynylene)s. *Chem. Eur. J.* **2020**, *26*, 7779-7782.

Benhua Wang, Jinsong Han, Hao Zhang, Markus Bender, Aike Biella, Kai Seehafer and Uwe H. F. Bunz*. Detecting Counterfeit Brandies. *Chem. Eur. J.* **2018**, *24*, 17361-17366.

Abbreviations

a.u.	arbitrary units
abs	absorption
em	emission
AIE	aggregation-induced emission
Ar	argon gas
Bu	butyl
ca.	circa
DCM	dichlormethane
MeOH	methanol
DFT	density functional theory
TDDFT	time-dependent density functional theory
DMF	dimethyl formamide
DMSO	dimethyl sulfoxide
Tol	toluene
Top	tris(o-tolyl)phosphine
DSB	distyrylbenzene
EA	ethyl acetate
eq	equivalents
ESI	electrospray ionization
et al.	*et alii*
EI	electron impact
FAB	fast atom bombardment
APCI	atmosphere pressure chemical ionization
MALDI	matrix-assisted laser desorption/ionization
FMO	frontier molecular orbitals
HOMO	highest occupied molecular orbitals
LUMO	lowest unoccupied molecular orbitals
g	gram
mg	milligram
GP	general procedure
δ	chemical shift
J	coupling constant
Hz	hertz
MHz	megahertz
m	multiplet

FTIR	fourier transform infrared spectroscopy
KO^{t}Bu	potassium tert-butoxide
L	liter
mL	milliliter
LDA	linear discriminant analysis
PCA	principal component analysis
HCA	hierarchical cluster analysis
M	molar
mmol	millimol
M.p	melting point
m/z	mass to charge ratio
n-BuLi	*n*-butyllithium
nm	nanometer
NMR	nuclear magnetic resonance
PE	petrolether
Ph	phenyl
ppm	parts per million
t-BuLi	*tert*-butyllithium
t	triplet
T	temperature
^{t}Bu	*tert*-Butyl
TEA	triethylamine
TMS	trimethylsilyl
THF	tetrahydrofuran
TPE	tetraphenylethene
UPLC-MS	ultra performance liquid chromatography-mass spectrometry
UV	ultraviolet
VIS	visible
λ	wavelength
ν	wavenumber
τ	lifetime
Φ	fluorescence quantum yield
FRET	fluorescence resonance energy transfer
GC-MS	gas chromatography-mass spectrometry
HPLC	high-performance liquid chromatography
HR-MS	high resolution mass spectra
ICT	intermolecular charge transfer
IDA	indicator displacement assay

MANOVA	multivariate analysis of variance
MS	mass spectrometry
NIR	near-infrared spectroscopy
NMR	nuclear magnetic resonance
PET	photo-induced electron transfer
PPE	poly(*para*-phenyleneethynylene)
PPV	poly(*para*-phenylenevinylene)
SW	swallowtail (oligoethyleneglycol side-chains)
TLC	thin layer chromatography
UV-Vis	ultraviolet-visible spectrophotometry
XRD	X-ray diffraction
calcd.	calculated
FL	fluorescence

Table of Contents

Chapter 1. Introduction

1.1 π-Conjugated Molecules and Polymers

Functional π-conjugated organic small molecules and polymers, which feature delocalized electrons along their π-conjugated backbones (sp or sp^2 hybridized), have been extensively studied and applied in material science.[1] Studies on optoelectronic devices together with luminescent sensing, include organic light-emitting diodes (OLEDs),[2] solar cells,[3] nonlinear optical (NLO) materials,[4] chemical sensors and biological imaging.[5]

π-Conjugated molecules and polymers have various structural skeletons.[6] Typical motifs include biphenylenes, poly(*para*-phenylenes) (PPPs), *E*/*Z*-stibenes, poly(*para*-phenylenevinylenes) (PPVs), diphenylacetylenes and poly(*para*-phenyleneethynylenes) (PPEs) (Figure 1). Styrylbenzene and phenyleneethynylene derivatives (SBs and PEs) are easy to synthesize, conveniently functionalized and properties facily adjusted. These make them a useful class of conjugated materials. In this thesis, we focus on describing the synthesis, optical properties and sensing applications of SBs and PEs.

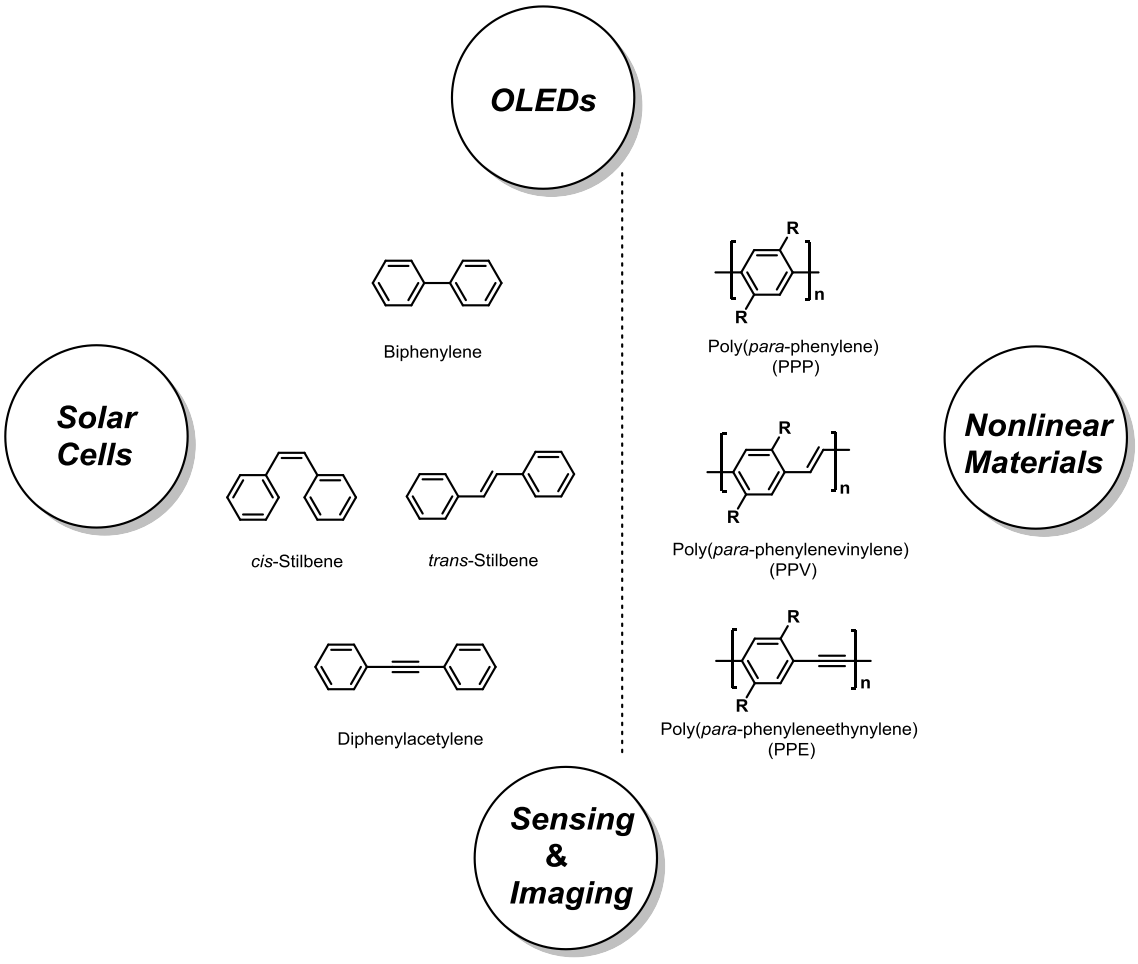

Figure 1. Typical π-conjugated molecules, macromolecules and their applications.[2-5]

1.1.1 Synthesis and Properties of SBs

1.1.1.1 Synthesis

Styrylbenzene derivatives (SBs), or stilbenes, are structurally composed of two phenyl units connected by vinylene group. Stilbene itself has two isomers: *cis* and *trans* (Figure 1). The carbon–carbon double bond formation is an important reaction in organic chemistry. Multiple approaches[7] for the synthesis of styrylbenzene derivatives address their regio- and stereochemical demands, including metal-involved and metal-free routes (Scheme 3).

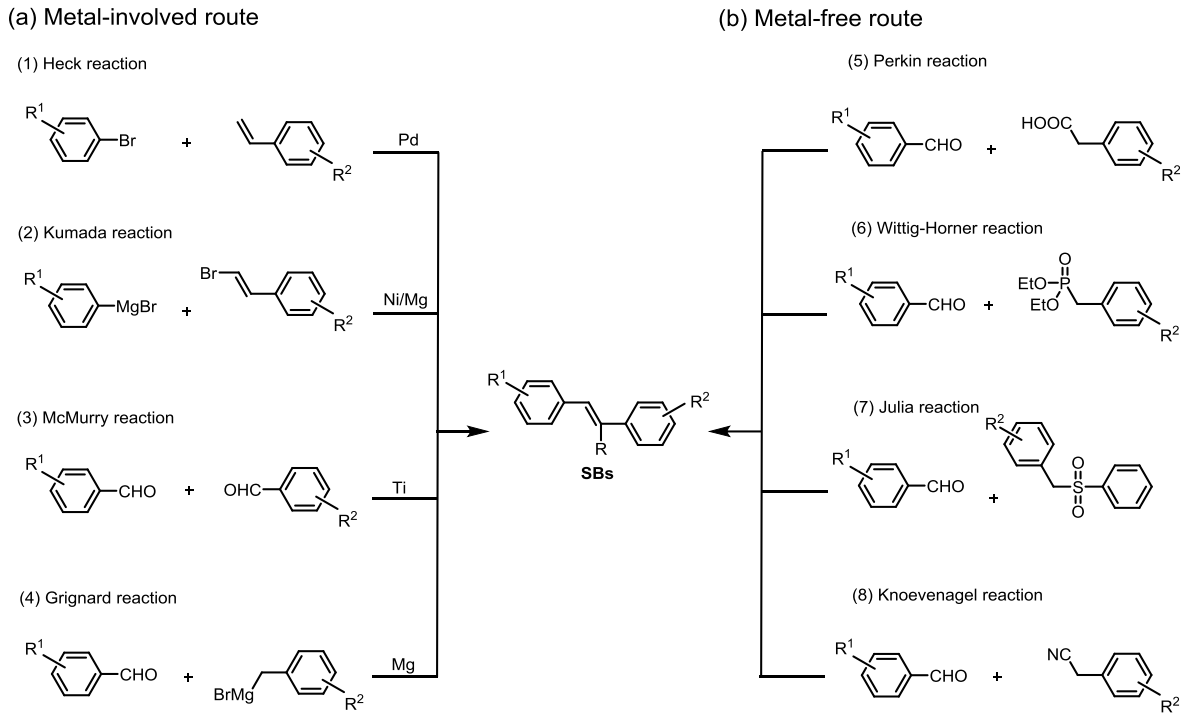

Scheme 3. Summary of methods for preparation of SBs, including (a) transition-metal-catalyzed[7a-f] and (b) transition-metal-free routes.[7g-k]

Metal-involved routes, include Heck couplings, Kumada, Mcmurry and Grignard reactions. The Kumada coupling is useful to generate carbon–carbon bonds by the reaction of a Grignard reagent and an organic halide.[7a] The McMurry reaction builds up C=C double bonds from ketones, and has been widely used to prepare tetraphenylethylene (TPE) and its derivatives.[7b, c] However, the products of the McMurry reactions are usually stereo-random. In the Grignard reaction, alkyl, allyl, vinyl, or aryl magnesium halides (Grignard reagents) add to a carbonyl group such as aldehydes or ketones; olefins are formed after dehydration.[7d] The Heck reaction is defined as the C=C coupling reaction of an aryl halide or a vinyl halide with an activated olefin under the catalysis of palladium in the presence of a base. This coupling reaction is stereoselective with a propensity for *trans* coupling and is applied industrially in the production of naproxen and the sunscreen component octyl methoxycinnamate.[7e, f]

The above metal reagents are expensive and generate toxic waste.[8] From economic and environmental viewpoints, the metal-free systems, including Perkin reaction, Wittig-Horner reaction, Julia reaction and Knoevenagel reaction, are powerful methods for preparing styrylbenzene derivatives.

The Perkin reaction uses aromatic aldehydes and anhydrides to make α- and β-unsaturated carboxylic acids. After condensation, decarboxylation is performed.[7g] The Knoevenagel reaction is carried out by condensation of a carbonyl compound with an active methylene compound using weak bases as catalysts. Aromatic aldehydes, ketones and aliphatic aldehydes react, expanding the scope of application. The Knoevenagel reaction is one of the most common methods for preparing α, β-unsaturated compounds, but it is limited to stabilized nucleophiles.[7h, i] The Julia olefination is based on a two-step reductive elimination process of β-acyloxy aryl sulfones.[7j] Both the Perkin reaction and Julia reaction require several steps, complicated conditions and overcoming over-reduction issues, which limit their applications. The Horner reaction is a modification of the Wittig reaction. Its reaction conditions are mild and the by-products are water-soluble. The product is *trans* configured.[7k] Thus, the most useful strategies to install an ethylenic bridge rely on Wittig-Horner reaction.

Even though there are numerous methods to prepare stilbenes, the one-pot protocol Heck coupling and Wittig-Horner reaction are extensively employed since they are convenient in operation, good functional group tolerance and high stereoselectivity. During this thesis, these strategies were successfully used in a high yielding and stereoselective synthesis of various styryl-containing products.

1.1.1.2 Properties

Tuning and switching of the luminescence of organic compounds is attractive for developing optoelectronic devices. Since structure determines property, understanding the structure–property relationship guides the rational design of SB-based luminogens through molecular engineering. In the following part, the photocyclization, aggregation-induced emission, two-photo absorption properties and stimuli-responsive behaviors of SB-based luminogens are discussed.

(a) Photocyclization[9]

Around 50 years ago, Mallory discovered the oxidative photocyclization reaction of stilbenes, as shown in Scheme 4. The *cis/trans*-isomerization of stilbene occurs rapidly under irradiation of ultraviolet light. The *cis*-isomer **2** undergos further cyclization reaction, producing the intermediate dihydrophenanthrene **3**, which is irreversibly transformed to phenanthrene **4** in the presence of oxidants such as iodine or oxygen. This reaction has become a useful tool in synthetic organic chemistry and been applied to many hexatriene systems.

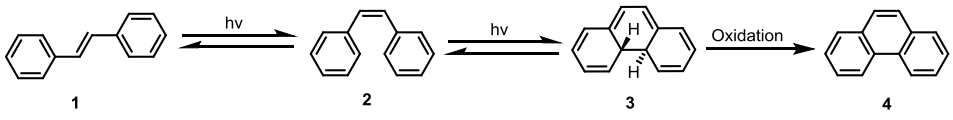

Scheme 4. Photocyclization of stilbenes.[9]

However, for the SB-based luminescent materials, the photostability is important and this undesired photoreactivity to phenanthrene should be suppressed. To this end, Muszkat et al. designed stable *cis*-stilbene **5** by substitution of the reactive *ortho*-positions with electron-negative fluorine atom.[10] Using similar strategy, Freudenberg and Bunz reported a fluorine-substituted tetraaryldistyrylbenzene derivative **7**. Although the photocyclization was efficiently suppressed, *cis/trans*-isomerization was detected for this AIE emitter **7**.[11]

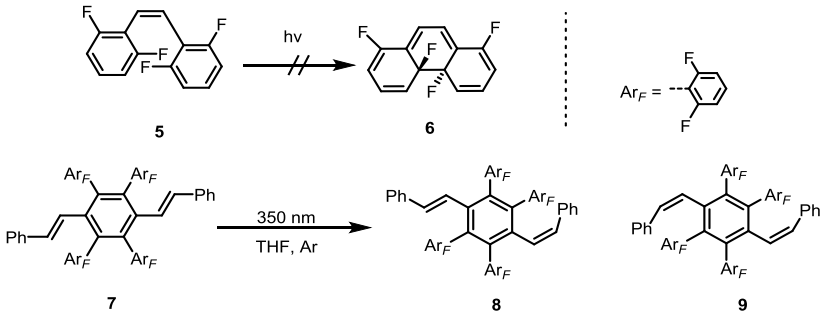

Scheme 5. Suppression of photocyclizations.[10-11]

(b) Aggregation-induced emission[12]

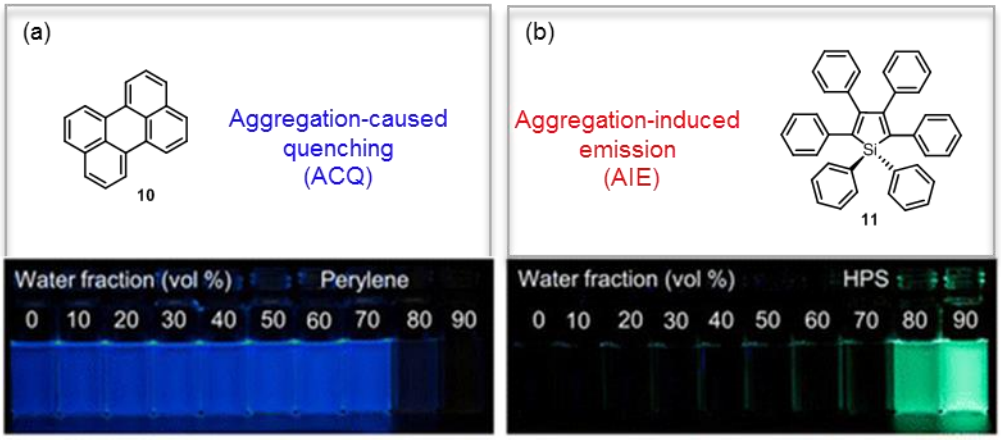

Figure 2. Fluorescence photographs of solutions or suspensions of (a) perylene **10** (20 μM) and (b) hexaphenylsilole (HPS **11**, 20 μM) in THF/water mixtures with different fractions of water, respectively. Reproduced with permission from ref.[13] © 2015 American Chemical Society.

The solid state or aggregate state of organic molecules has been widely used in optoelectronics or biomedical research.[14] However, when luminophores aggregate, they are usually weakly luminescent or luminescence is totally quenched (aggregation-caused quenching effect, ACQ). This results from the intense intermolecular π–π stacking interactions between adjacent aromatic rings, also known as the result of H-aggregate.[13] Perylene **10** is a typical example illustrating the ACQ effect (Figure 2a).

The ACQ effect is harmful to practical applications. Chemical approaches like attaching branched and non-planar molecular architectures, physical approaches like controlling the J-aggregate formation and engineering approaches have been utilized to mitigate ACQ.[15] Aggregation-induced emission (AIE) is

the opposite of the ACQ, which was coined by Tang and co-workers in 2001.[16] A luminogen such as **11**, hexaphenylsilole (HPS), exhibiting AIE is termed AIEgen.

From a structural point of view, **10** adopts a planar structure, while **11** adopts a twisted structure and has freely rotatable phenyl groups. The rotation of phenyl rings in solution dissipates the excited-state energy and the nonradiative decay dominates the excited-state relaxation, suggesting molecular motion responsible for the emission quenching. In aggregate state, however, the intramolecular rotations are restricted due to the high steric hindrance and the non-radiative decay channels are blocked, which makes **11** emissive. Based on the experimental and theoretical works[17], restriction of intramolecular motion (RIM), including restriction of intramolecular rotation (RIR) and restriction of intramolecular vibration (RIV), was considered as the working mechanism for AIE effect and become generally applicable to most AIE systems.[18]

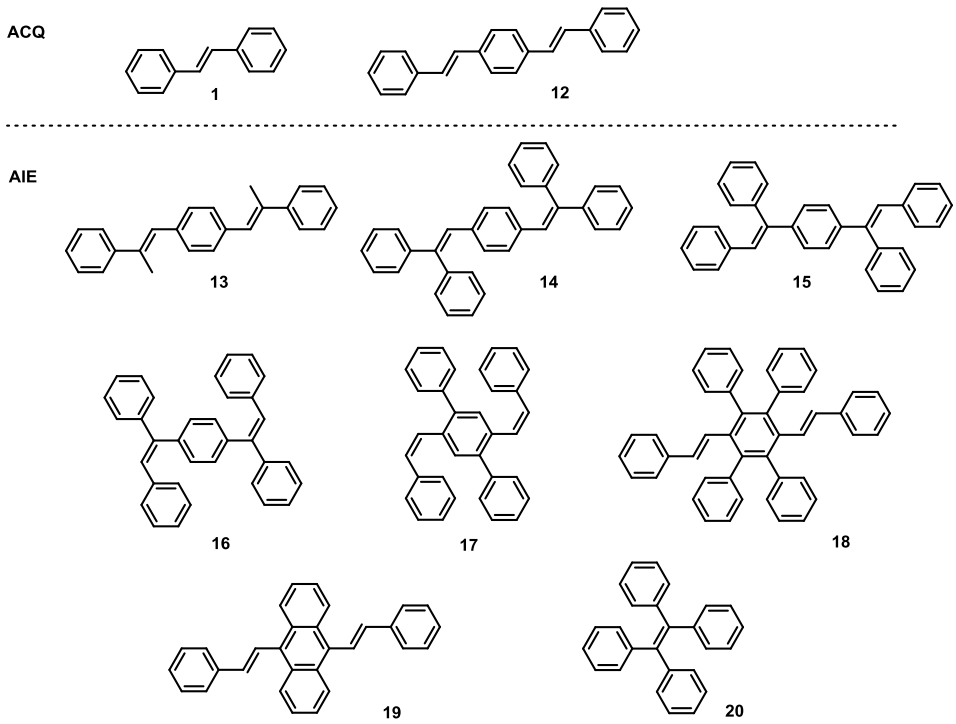

Figure 3. Examples of hydrocarbon AIEgens derived from SB.[19]

Based on SB, various hydrocarbon,[19] cyano-substitued[20] and triphenylamine-containing AIEgens[21] have been developed. Some examples of hydrocarbon SB-AIEgens are listed in Figure 3. The ACQ luminophore distyrylbenzene (DSB) can be endowed with AIE properties by introducing bulky groups to α/β-position of the vinylic bonds, or to the central phenyl ring of DSB.[19] Due to the formation of twisted geometry, compounds **13-19** are AIE-active.

It was found that compound **16**, as the *Z* isomer of **15**, also shows AIE activity. In general, a *Z* isomer usually shows weaker luminescence due to its poorer electronic conjugation. However, in the solid state, the structure of the *Z*-isomer is significantly deviated from planarity owing to torsion conformation,

which could suppress the fluorescence quenching and even enhance the fluorescence emission in the solid state.[22] Similarly, compound **17** with a *Z*-structure is also AIE-active.[23]

TPE **20** is an AIEgen. Meanwhile, it is also a stilbene derivative. It could undergo *Z/E* isomerization and photocyclization upon excitation. In this case, the RIR mechanism remains controversial. Tang and co-workers have disclosed that TPE and its derivatives underwent C=C bond elongation, quasi C=C bond twisting, phenyl torsion and photocyclization are the sequentially dominant processes upon photoexcitation in solution. The suppression of non-radiative relaxation channel in the aggregated state is responsible for the emission enhancement.[24]

(c) Two-photon absorption (TPA)[25]

TPA, as one of the nonlinear optical phenomena, involves electronic excitation of a molecule induced by a pair of photons of the same or different energy. The magnitude of the TPA cross-section is important for applications such as optical switching and photodynamic therapy.[26] Generally, a large TPA cross section can be achieved by increasing donor-acceptor strength, extending the conjugated length, expanding the molecular dimensionality and changing the character of the conjugated bridge.[27] For example, Fu and co-workers successfully designed a turn-on TPA dye based on SBs in 2019.[28] Upon addition of *β*-CD, Ald-DSB **22** with greater "push–pull" strength exhibits much larger TPA value (2421 GM) compared with that of Ace-DSB **21** (93 GM), similar to that of unmodified distyrylbenzene.

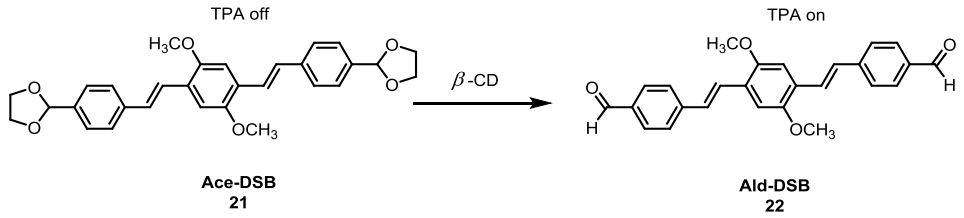

Figure 4. The conversion of Ace-DSB **21** to compound Ald-DSB **22**.[28]

(d) Stimuli-responsive behaviors[29]

Stimuli-responsive organic molecules are sensitive to external stimuli (heating, pressure, grinding, light, pH, etc), with change of their physical-chemical properties such as shape, color, and luminescence. Especially, the solid-state emission of molecules is strongly affected by the intramolecular conformation and packing modes. For instance, molecules with large and bulky groups can adopt a twisted structure, which has two advantages: (1) forming J-aggregate or the X-aggregate and leading to a higher emission efficiency than the H-aggregate; (2) inducing the formation of crystal polymorphs, which differ slightly in the stabilization energy and easily show phase transition upon applying external stimuli. Molecules with heteroatoms (N, O, S or F) always experience weak supramolecular interactions, such as C–H/N(O) hydrogen bond or van der Waals forces, which can restrict intramolecular motions, thus enhancing the emission.[30] Moreover, heteroatoms endow the molecules with donor-acceptor (D-A) structure, making their luminescent properties sensitive to the external environment.[31] Compound **23**, reported by Zhang and Wang et al., is an electron donor−acceptor system.[32] This orange-red emissive SB derivative

exhibits piezochromic fluorescence by grinding, with emission color changing between orange-red and yellow. The stilbene-aromatic-amine framework in **23** has a torsion angle of about 16.1°, playing an effective role in the stacking process and further impacting the properties in various states.

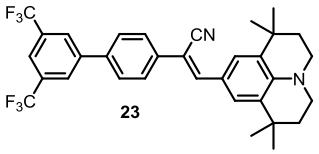

Figure 5. Molecular structure of **23**.

1.1.2 Synthesis and Properties of PEs

1.1.2.1 Synthesis

Phenyleneethynylene derivatives (PEs), are composed of a diphenylacetylene parent structure, two phenyls connected by an ethynylene group. There are several methods to construct phenyleneethynylenes, including alkyne metathesis,[33] fluoride-induced addition-elimination coupling[34] and Sonogashira coupling[35] (Scheme 6).

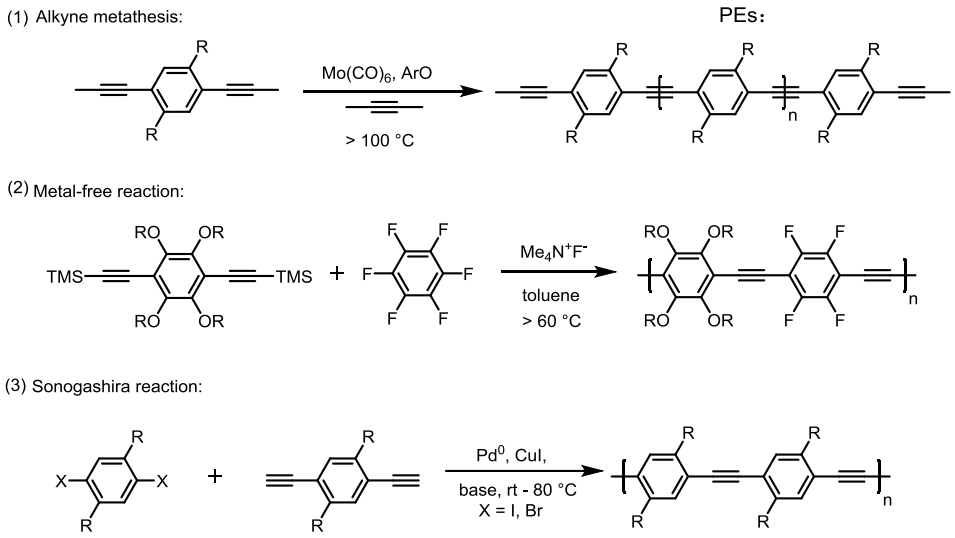

Scheme 6. (1) Alkyne metathesis,[33] (2) fluoride-induced addition-elimination coupling[34] and (3) Sonogashira coupling[35] for preparation of PEs.

Although alkyne metathesis and fluoride-induced addition-elimination coupling could produce desired PEs, they do not tolerate functional groups during the synthesis. The palladium catalyzed Sonogashira coupling performed under mild reaction conditions could address these tolerance defects.[35] The general catalytic cycle of Sonogashira coupling includes three elementary steps: oxidative addition, transmetalation, and reductive elimination.[36] It is employed in synthesis of PEs in this thesis.

1.1.2.2 Properties

In addition to the facile synthesis and modification, phenyleneethynylene derivatives also display stable photoluminescence and high quantum yields probably due to their rigid structure. The optical properties are changed by their conformation (planar or twisted form), molecular packing (aggregated or scattered state), and the surrounding environment (solvent, temperature, humidity, pH values and other factors). The delocalized backbones and tunable optical properties suggest promising applications, such as sensing, fluorescent imaging and disease therapy.[37]

Assembling the receptor pendants through the polymer backbone is an excellent approach to amplify the fluorescent signals. As shown in Figure 6, in a small molecule sensor, the binding site is attached to a single fluorophore and interaction with an analyte can only partly quench the fluorescence. While in the case of polymer sensor, a complete fluorescence quenching effect could be observed because one single interaction can quench multiple fluorophores via the migration of electrons along the polymer chain and thus the signal is amplified. This is called "molecular wire effect", which was first described by Swager and coworkers.[38]

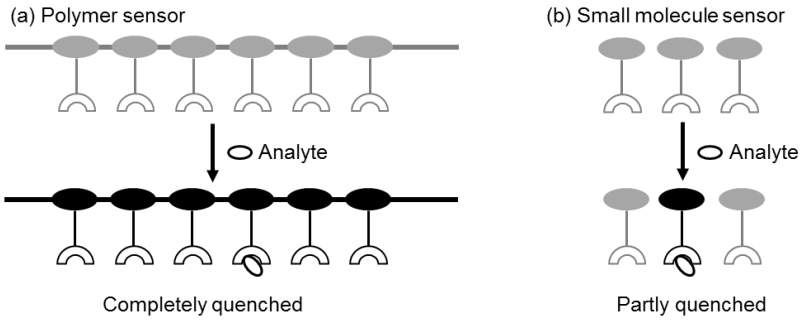

Figure 6. Schematic illustration of the "molecular wire effect" expressed by conjugated polymers. Adapted with permission from ref. [39] © 2009, Elsevier.

1.2 Fluorescent Sensors

Fluorescent sensors are indispensable tools for visualizing ions and neutral analytes at the molecular level. They can provide a simple, fast, selective, accurate, and cost-efficient real-time monitoring.[40] As it is defined, a fluorescent sensor is a self-contained analytical device that provides information about the composition of its environment with a detectable change in the luminescence signal, such as a change in the magnitude of emission intensity (for example, turn on or off mode) or the wavelength of the emission maximum (color change mode).[41] Following is the discussion related to the different detection mechanisms and sensor design strategies.

1.2.1 Detection Mechanisms

1.2.1.1 Detection Based on Conventional Mechanisms

There are several conventional mechanisms responsible for the fluorescence signal changes of chemical sensors, including photoinduced electron transfer (PET), intramolecular charge transfer (ICT), Förster resonance energy transfer (FRET) and excimer formation (Figure 7).

(a) Photo-induced Electron Transfer (PET)[42]

The optical sensor usually has two essential parts: a receptor and a transducer. The receptor (or ionophore) bearing a non-bonding electron pair can be used to bind the analyte and a transducer (or fluorophore) expresses the associated binding event. In PET process (Figure 7a), an electron is transferred from the HOMO of the ionophore to the HOMO of the photo-excited fluorophore. The excited electron of LUMO can no longer relax to the HOMO and radiative decay process is restricted, leading to the quenched fluorescence (PET on). On binding of the guest analyte, the electron transfer (PET process) is restricted, making the fluorophore show emission (PET off).

(b) Intramolecular Charge Transfer (ICT)[43]

The ICT-based sensor is the combination of electron donating and electron accepting groups within a conjugated π systems. In the ICT process (Figure 7b), a redistribution of electrons from an electron donating group (often an amino group) to an electron accepting group occurs upon light excitation, thus creating a dipole moment. When the guest analyte binds to the donor part, this dipole moment is reduced and blue shifted emission is expected. Conversely, when the guest analyte binds to the acceptor part, the dipole moment is enhanced and the emission should be red-shifted.

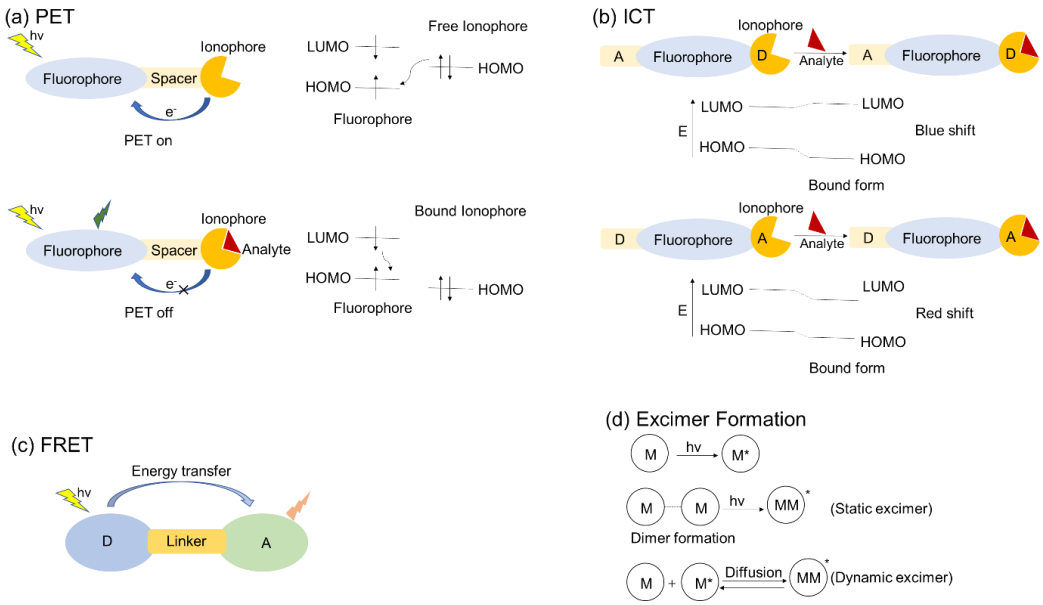

Figure 7. Illustration of typical examples of photophysical processes. (a) Photo-induced electron transfer; (b) Intramolecular charge transfer; (c) Förster resonance energy transfer; (d) Excimer formation. Figure 7a-c adapted with permission from ref.[44] © 2016 the Royal Society of Chemistry and Figure 7d adapted with permission from ref.[45] © 2021 the Royal Society of Chemistry.

(c) Förster Resonance Energy Transfer (FRET)[46]

FRET is a non-radiative energy transfer process, which occurs between donor (or emitter) and acceptor (or absorber molecule). For an effective FRET process (Figure 7c), it is highly dependent on two indispensable factors: a considerable spectral overlap between the emission profile of the donor and absorption profile of the acceptor and a close enough distance between donor–acceptor pair (up to 10 nm). FRET is always used to build ratiometric fluorescent systems to quantitatively detect the analytes.

(d) Excimer Formation[47]

Excimers include static excimers and dynamic excimers (Figure 7d). Static excimer is formed when the dimer in the ground state is photoexcited. Conventional dynamic excimer is formed when a fluorophore in the excited state interacts with the same fluorophore in the ground state by π-π stacking. Excimer emission typically shows a red-shifted broad fluorescence band compared with that of the monomer and a dual emission from the monomer and excimer is often observed simultaneously. The stacking of excimers can be modulated by guest analyte binding, enabling the system to be used as ratiometric sensors by monitoring the monomer to excimer fluorescence intensity ratio.

1.2.1.2 Dectection Based on Noncovalent or Covalent Interactions

In addition, with regard to the fluorescence signal changes of chemical sensors, the following factors need to be considered: (1) experimental parameters like solvent, temperature and concentration of components and (2) the association between the analyte and sensors. The association between the analyte and sensors can occur either via covalent or noncovalent interactions (Figure 8).

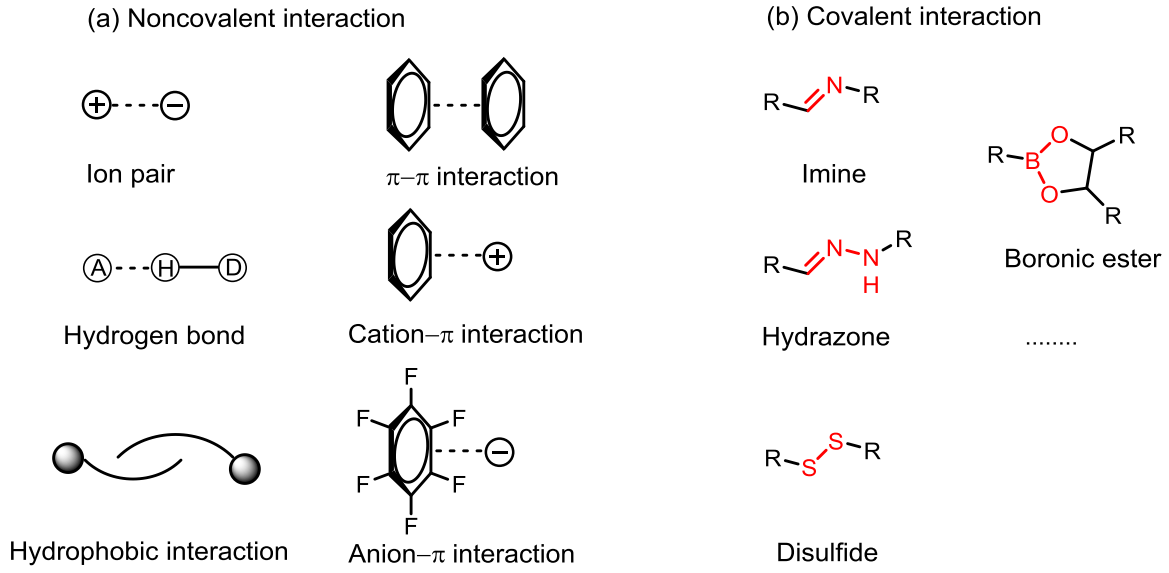

Figure 8. Illustration of typical examples of noncovalent or covalent interactions.[48]

Covalent bonds determine the primary structure of a molecule (position of atoms), while the non-covalent interactions, such as hydrophobic interactions, electrostatic interactions, hydrogen bonding,

ion-π interactions, and π–π stacking interactions, etc. control or organize the conformation, aggregation, tertiary and quaternary structure of the molecule.[49] Numerous efficient sensors based on noncovalent interactions have been developed. For example, the hydrogen bonding between a donor (D) and acceptor (A) in the moiety D–H···A is well studied and established.[50] Chemosensors containing thiourea/urea, amide/sulfonamide, imidazoline/imidazole, indole, pyrrole, Schiff base, and other groups as binding units can be used to selectively recognition of fluorides on the basis of hydrogen-bond and π–π interactions.[51].

Chemosensors based on convalent interactions (or reaction-based sensors) have been extensively evaluated for many years. Analytes can form covalent bonds with receptors, which trigger highly selective reactions and induce changes in optical (emission or absorption) properties. Common covalent interactions consist of imine formation and exchange,[52] disulfide exchange,[53] olefin metathesis,[54] and F-promoted bond cleavage[51], etc. Although many covalent interaction-based sensors depend on irreversible reactions, they are being promoted as target-specific sensors and under active study because their selectivities are often higher than those of conventional sensors.[55]

1.2.1.3 Other Mechanisms

In addition to the above stated examples, a few other interesting mechanisms have also been emerged. For instance, aggregation-induced emission (AIE)[12, 56] and C=N isomerization[57], inner filter effect (IFE)[58] and excited-state intramolecular proton transfer (ESIPT)[59], etc. With the rapid development of supramolecular chemistry, one can gain a deep understanding of these photophysical phenomena and detection mechanisms, which provide guidelines to construct new systems for recognizing analytes. In next part (**1.3**), a few typical examples were selected for detailed discussions.

1.2.2 Sensor Design Strategies

As shown in Figure 9, the three main sensor design strategies adopted for molecular sensing studies are: (a) direct-binding assay (DBA); (b) indicator-displacement assay (IDA); (c) sensor array (chemical tongue).[60] In a direct sensing approach, a signalling unit is covalently and permanently connected to a recognition unit and binding of the guest analyte to the recognition unit can lead to change. For example, boronic acids covalently bind to diols, thus, in sugar sensing, the recognition unit often contains a boronic acid moiety and fluorophore is chosen as signalling unit.[61]

Since the signalling unit and the recognition unit are covalently linked in DBAs, the selectivity of the sensing system is difficult to tune. Another strategy for the design of chemosensors is a displacement approach (IDA), in which the indicator and receptor are separate molecules, weakly bound together by non-covalent interactions to form a supramolecular sensor. Upon addition of guest analyte, the indicator is then displaced by the analyte, leading to a optical signal change. Early examples of IDAs were reported by the pioneers Inouye, Shinkai, and Anslyn.[62] Although properties of an IDA sensing system can be tuned more easily due to the the non-covalent linkage, it is not always able to sense similar

analytes effectively.

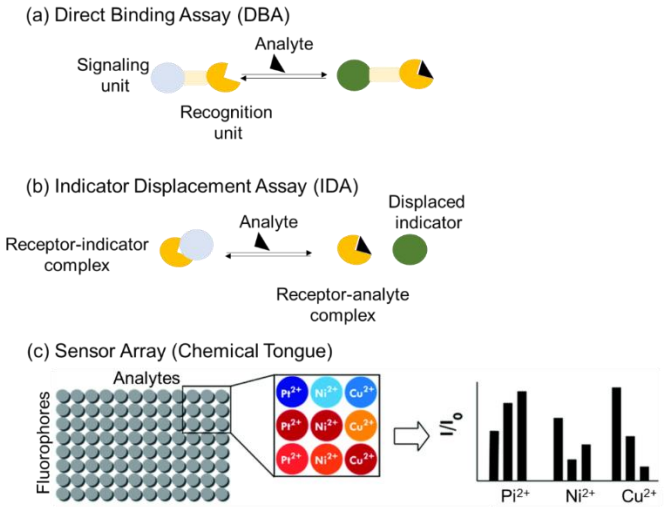

Figure 9. Illustration of typical design strategies for molecular sesning. Figure 9a,b adapted with permission from ref.[48] © 2015, American Chemical Society and Figure 9c adapted with permission from ref.[63] © 2017 the Royal Society of Chemistry.

Unlike the lock-and-key method, in which a single response is specific towards a given analyte, sensor arrays are composed of a number of sensor or receptor elements that react with multiple types of analytes.[48, 64] Various signals are produced and following subsequent statistical analysis (e.g. linear discriminant analysis [LDA] or principal components analysis [PCA]), patterns or components can be isolated that can be used to unambiguously identify the specific analytes.[65] Optical sensor arrays, are also named optoelectronic chemical tongues or noses and this fundamental concepts and their use were demonstrated by Anslyn, Suslick, Rotello and Bunz et al.[66] Owing to good sensitivity and a versatile, easy to read output, an array could be designed to identify a single analyte, distinguish between complex mixtures, to determine the concentration of a specific analyte in a complex solution.

1.3 Sensing Applications Based on SBs and PEs

Due to the ease in preparation, convenience in properties adjustment, SBs and PEs have become popular in sensing applications. In the following section, SBs or PEs serving as sensors for a broad range of analytes, such as ions, small molecules, macromolecules and complex mixtures are presented.

1.3.1 Sensing of Ions

The detection of biologically relevant or highly toxic ions, both cations and anions, is important in the biological and chemical science.[67] For cation detection, using electrostatic interaction or coordination between the cationic analytes and the sensor are two common strategies. SB-based cation sensors have been developed by incorporating a binding unit comprising of multiple carboxylate groups, crown ethers moieties, calixarene or other lewis-base group to the fluorophores and they can efficiently detect cations, such as H^+, K^+, Ag^+, Hg^{2+}, Cu^{2+}, Zn^{2+}, Pb^{2+}, and Fe^{3+}.[68]

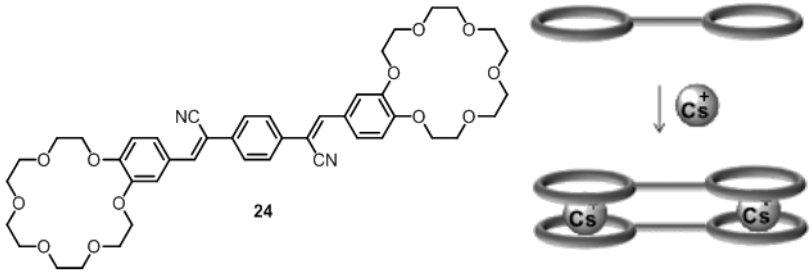

Figure 10. Structure of **24** and its sandwich complex with Cs^+ ions. Reproduced with permission from ref.[69] © 2016 Elsevier.

For instance, Xia and co-workers[69] developed a fluorescent sensor (**24**, Figure 10) for Cs^+ based on dicyano-substituted distyrylbenzenes with crown-6 rings appended. The Cs^+ ions electrostatically coordinated with **24** in a 1:1 stoichiometry and generated a sandwich structure. The competitive selectivity experiment showed that **24** exhibited a selective fluorescent enhancement upon addition of Cs^+ in the presence of other alkali metal ions, like K^+ or Na^+.

Bunz and co-workers have also made some efforts on the cation sensing using SB/PE-based sensors. They are pioneers in developing cross-conjugated cruciform fluorophores with pyridine or alkylamino units as cation sensors. Presence of nitrogen atoms with lone electron pairs allows cruciforms to act as effective complexing agents or as bases that can be protonated. Several representative examples **25-28** are shown in Figure 11.[70] Upon addition of increasing equivalents of Zn^{2+} ions to **25** in chloroform, a rare two-stage fluorescence response was observed: the emission color changes from orange to blue and then to green. The initial blue shift results from the first coordination at the anilines and the second bathochromic shift is caused by the coordination at the pyridyl nitrogens.

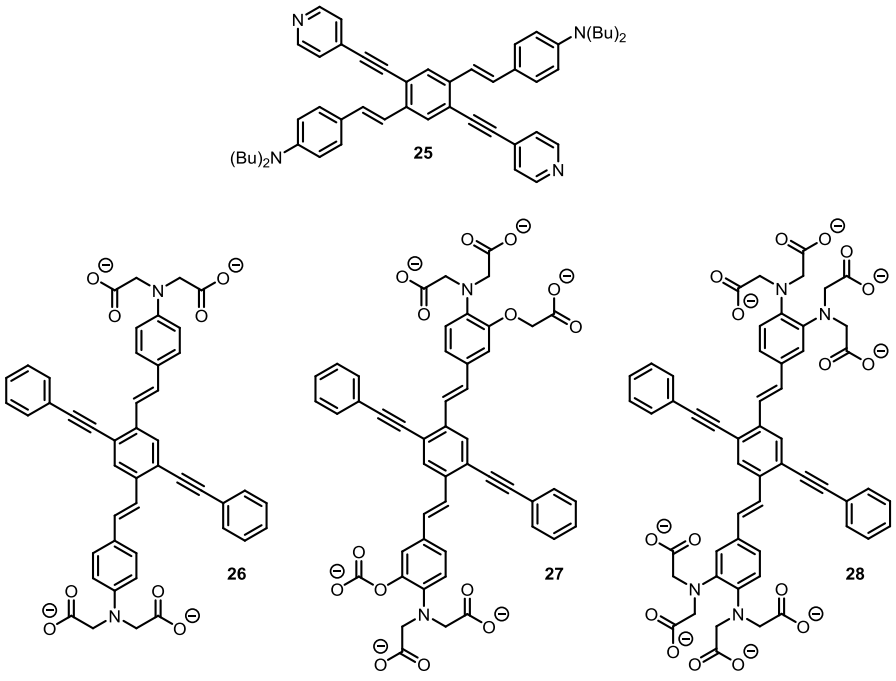

Figure 11. Structure of **25-28**.

Since most cations in nature are present in aqueous environments, the water solubility of sensors is important. To this end, Bunz et al. used carboxylate units as charged appendages to generate three water-soluble XFs **26-28,** which result in an attractive zinc-specific response and effective detection. Similarly, the attachment of carboxylate groups renders the poly(*p*-phenyleneethynylene)s (**PPE1-3**, Figure 12) water-soluble and their emission is quenched by H^+, Hg^{2+} and Pb^{2+}. Log K_{SV} values of up to 4.8 for mercury ions is achieved by **PPE2**.[71]

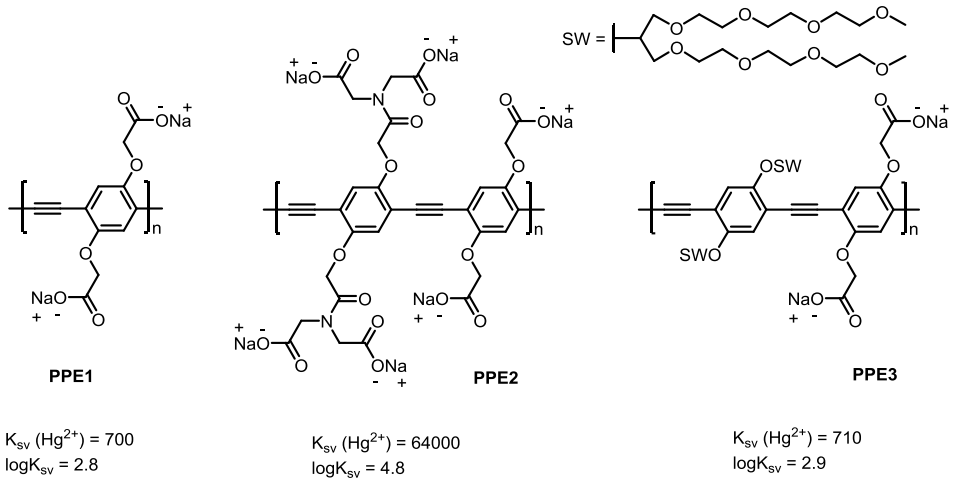

Figure 12. Structure of **PPE1-3** and their binding constants towards metal ions.[71]

Fluoride (F^-) is one of the most important ions, necessary in small quantities for mineralizing tissues but in large quantities potentially leading to harmful fluorosis. Hence, the sensitive and accurate detection of the presence of fluoride ions is important.[72] Recently, Liu et al. has developed a new chemodosimeter **29** for fluoride ions based on F^- triggered dual Si–O bond cleavage of distyrylbenzenes derivatives.[73] The addition of fluoride ions can lead to the apparent color change of **29**, from blue to faint yellow. Moreover, the sensor has higher selectivity for fluoride over other common anions and the limit of detection could be as low as 89.8 nM (Figure 13).

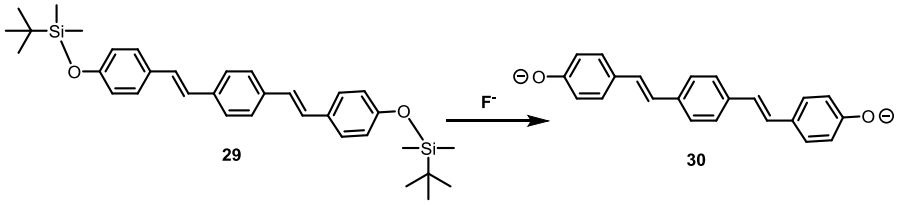

Figure 13. Structure of **29** and its transformation upon addition of F^-.[73]

1.3.2 Sensing of Small Molecules

The detection of small molecules, such as carbon-dioxide, hydrogen sulfide thiols, explosives, amines, hydrogen peroxide, thiol and nerve agents etc. is of importance, considering their effects on human health and the environment.[74] Attachment of hydrophilic units such as hydroxyl, amino, ammonium, glycol and sulfonate groups to fluorophores can render them water soluble. For example, a series of

aldehyde-substituted and water-soluble distyrylbenzenes react with amines to give imines or aminals with dramatically changed fluorescence,[75] which could achieve the detection and recognition of amines in water.

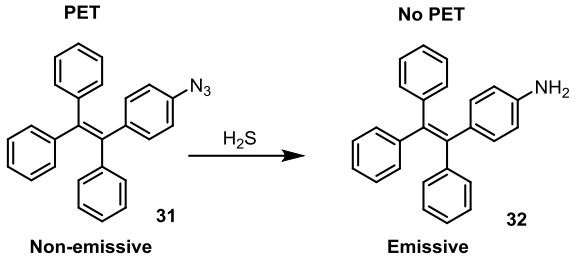

Figure 14. Schematic illustration of detection of hydrogen sulfide by the SBs with an azido group.[76]

By taking advantage of AIE and the chemical reactivity of azido group to H_2S (Figure 14), Tang and coworkers developed a novel tetraphenylethene-based fluorescent H_2S probe **31**.[76] **31** was non-luminescent in solution due to the PET effect caused by the azido group. Upon incubation with NaHS, a commonly-used source of H_2S, a remarkably increased fluorescence was observed because the reduction of **31** could generate the amino-substituted **32**, thus eliminating the PET effect and restoring the AIE of the TPE moiety. Moreover, this approach allows direct indication of H_2S concentration in blood and unknown samples possible.

1.3.3 Sensing of Macromolecules

Fluorescent SBs/PEs have also been widely used to detect a variety of macromolecules such as proteins and DNA.[77] For example, our group has used water-soluble, aldehyde-appended distyrylbenzene (DSB) derivatives to construct a sensor array, which could detect and identify even within a family of proteins.[78] The turn-on fluorescence signals arose from a combination of imine/N,S-aminal formation and hydrophobic interactions between the DSBs and the proteins.

More recently, Tian and coworkers have designed a label-free platform for single nucleotide polymorphism (SNP) detection by using AIE-active molecule **33**[77] and water-soluble carbon nanotubes. **33** could aggregate on wild DNA (P1-T1) or mutated-DNA (P1-SM1) through the intercalation, electrostatic interactions and hydrophobic interactions, thus generating strong fluorescence in the solution. The fluorescence changes upon the addition of carbon nanotubes. Because the intercalation interactions between **33** and P1-SM1 are weaker than those between **33** and P1-T1, some molecules **33** can be pulled out from P1-SM1 by the carbon nanotubes through the strong electrostatic interaction, resulting in the partial fluorescent quenching in the solution. Therefore, this approach allows the detection of SNP in the random DNA sequence (Figure 15).

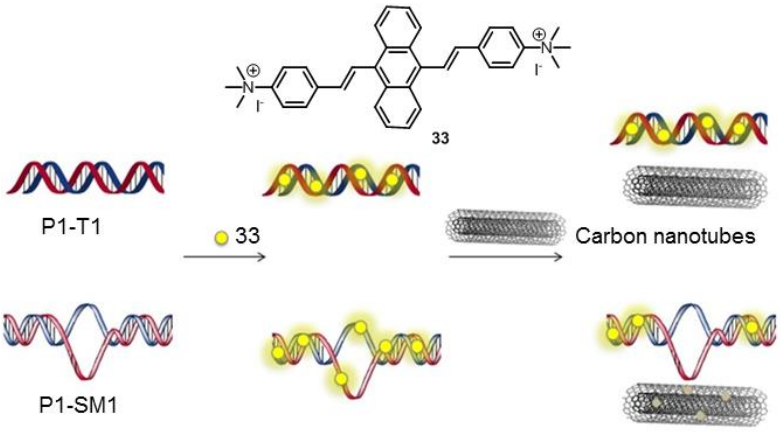

Figure 15. Structure of **33**; sensing mechanism for SNP analysis using **33** and carbon nanotubes. P1, T1, and SM1 represent the single-strand DNA sequence. Adapted with permission from ref.[77] © 2017 Elsevier.

1.3.4 Sensing of Complex Mixtures

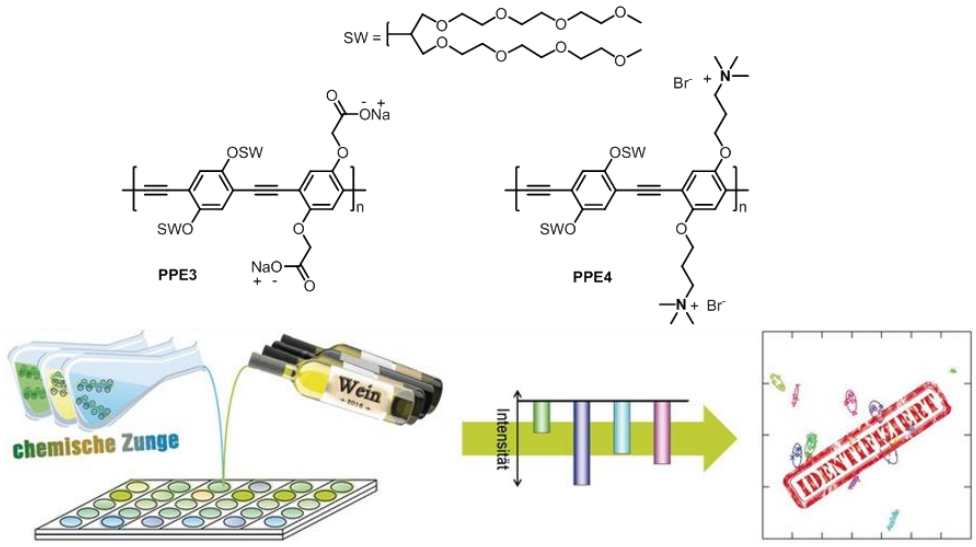

Figure 16. Structure of **PPE3-4**; representation of the PE-based sensor array for the discrimination of white wine. Reproduced with permission from ref.[79] © 2016 Wiley-VCH Verlag GmbH & Co. KGaA.

Quality control and quality assurance of complex analytes, like wine, food and beverages are challenging due to the similarity and complexity of their compositions. Array-based sensing approaches offer an alternative to detect multiple components in a complex mixture. This method detects the presence of unknown and unexpected analytes in a given sample which is not possible in specific sensing. Since this concept was proposed and popularized by Suslick et al.[80] and Anslyn et al.[81], different arrays have been developed to detect of a wide range of analytes like bacteria[82] and disease cells,[83] etc. Bunz and coworkers have also made progresses in developing minimalist sensor arrays with charged PPEs, which successfully discern mixtures like different teas[84]and wine[85] etc. In one of such examples (Figure 16), they used an anionic **PPE3** and a cationic **PPE4** and their electrostatic complex to build a simple sensor array, which differentiates 13 kinds of different white wines.[79]

1.4 Objective

Prior studies have demonstrated SBs and PEs as superior fluorescent molecules possess various unique properties, such as good water solubility and stability when substituted with hydrophilic groups, the advantages of low cost, easy preparation and tunable fluorescence. All these features are important for applications in fluorescence sensing. SB/PE-based sensors can supply a feasible and superior platform to maintain stability, rapidity, selectivity and sensitivity for detecting analytes.

In the current work, the aim is to design and synthesize novel chemosensors on the basis of SBs or PEs, and provide guidance for the further design and potential applications of related fluorescent materials.

Chapter 2. Styrylbenzene Derivatives: Synthesis, Properties and Sensing Applications

2.1 Aggregation-Induced Emission of Triphenyl-Substituted Tristyrylbenzenes

In this part, we show the synthesis, properties and X-ray single crystal structures of two regioisomeric triphenyltristyrylbenzenes (**TSB1** and **TSB2**). Both C_{3v} and C_s derivatives display classic aggregation-induced emission (AIE) behavior. Regioisomerism has an impact on the solid-state intermolecular interactions, the photophysical characteristics and photostability in solution.

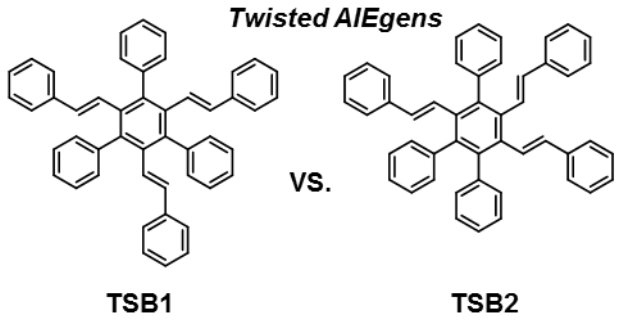

Figure 17. Schematic representation of aggregation-induced emission of triphenyl-substituted tristyrylbenzenes. Adapted with permission from ref.[86] © 2019 Wiley-VCH Verlag GmbH & Co. KGaA.

2.1.1 Tristyrylbenzene (TSB) and Its Derivatives

Star-shaped molecules are attracting attention because of their highly branched architecture, ready availability through iterative synthesis and interesting photophysical properties.[87] 1,3,5-Tristyrylbenzene (TSB) possesses a C_3 symmetry, three *meta*-branched rigid arms, and long-lived excited singlet state, which makes it an excellent building core for the construction of star-shaped molecules.[88] The introduction of different groups, both at peripheral positions and at the core, is an excellent approach for the appropriate tuning of properties.[88b] Although the electronic influence of substituents on the three phenylenevinylene chromophores was hindered by cross-conjugation of the arms, the substituents can control the intermolecular interactions, which adjust the molecular stacking. For example, when alkoxy chains were attached at the peripheral position of TSB, the produced derivative could form liquid crystalline (LC) phases.[89] Many star-shaped structured molecules containing TSB as a core (TSBs) have been designed, synthesized and used as organic light-emitting diodes,[90]organic two-photon materials[91] and sensors.[92]

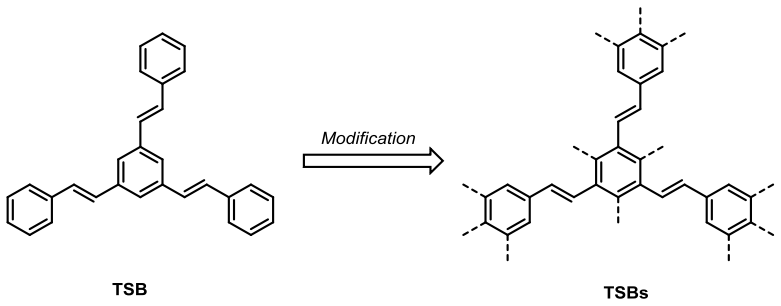

Scheme 7. Tristyrylbenzene and its modification.

As mentioned above, since its first report by Tang et al. in 2001, new types of AIE luminophores have been explored and used in various areas including OLEDs, biological imaging and theranostics.[93]

However, studies on AIE-active TSB derivatives have rarely been reported.[94] We have recently introduced AIE properties to distyrylbenzenes through tetraphenylation and variation of functional substituents on the styrene arms.[95] Further decrease of steric hindrance at the core retained AIE properties of a tetrastyryldiphenylbenzene derivative.[96] On the other hand, constitutional isomers display different properties, enabling the study of configuration-property relationships. Herein, symmetric **TSB1** was bulit by introduction of phenyl to the 1,3,5-tristyrylbenzene core and its constitutional isomer **TSB2** was employed for the comparative and systematic study (Scheme 8, symmetric **TSB1** and asymmetric **TSB2**).

In this contribution, the regioisomeric effects on the optical and structural characteristics of triphenylated, core-substituted tristyrylbenzenes were investigated and we clarify the relationship between the molecular structure and resulting properties, and also discuss the effect of regioisomerism on photostability.

2.1.2 Synthesis

The synthesis of **TSB1** and **TSB2** is depicted in Scheme 8 and 9. Symmetric **TSB1** was obtained in a yield of 93% as a colorless solid, which was synthesized in five steps from mesitylene **34** after iodination and Suzuki-coupling, followed by Wohl-Ziegler bromination,[97] Arbuzow and final Horner reaction.

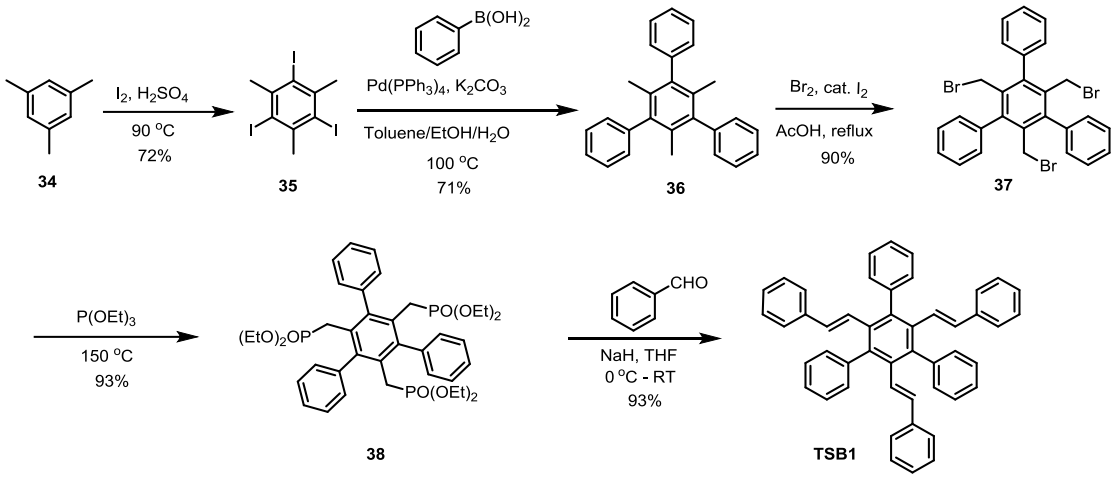

Scheme 8. Synthesis of compound **TSB1**.

Similarly, asymmetric **TSB2** was synthesized in four steps, starting from propynylbenzene **39**, which was initially cyclotrimerized furnishing asymmetric quaterphenyl **40**, accompanied by its difficult to separate regioisomeric side product. Compound **TSB2** was isolated in a yield of 67% as a yellow solid after chromatographic purification. Both **TSB1** and **TSB2** were found to be soluble in toluene, CH_2Cl_2, DMF, etc., but insoluble in water and methanol.

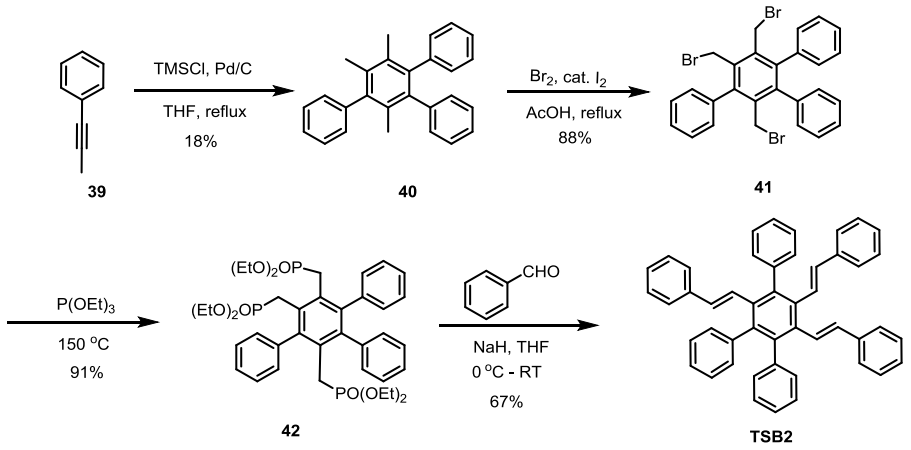

Scheme 9. Synthesis of compound **TSB2**.

2.1.3 Photophysical Property

The normalized absorption and emission spectra of **TSB1** and **TSB2** in dilute THF and in the solid state (Film) are displayed in Figure 18, while Table 1 summarizes the photophysical data. The UV-vis spectra of **TSB1** and **TSB2** are very similar with peak maxima at around 307 nm and 309 nm, respectively, corresponding to the main electronic transition of the styryl arms. Both **TSB1** and **TSB2** show spectroscopic features similar to that of *trans*-stilbene,[98] suggesting the decreased interactions of between the three styryl arms. Compared with their absorption in solution, both **TSB1** and **TSB2** show broadened and red-shifted absorption spectra in films (**TSB1**: 350 nm, **TSB2**: 319 nm), with **TSB1** displaying a larger shift (43 nm). The regioisomerism of the styryl arms has a considerable influence on the photoluminescence of the triphenyl substituted tristyrylbenzenes, both in solution and in thin films.

The emission maximum (λ_{em}) in solution of **TSB1** appears at 421 nm, redshifted by 32 nm compared to non-phenylated 1,3,5-tristyrylbenzene (λ_{em} = 389 nm).[90b] **TSB2** emits at an even longer wavelength compared to **TSB1**, as it possesses higher conjugation. The styryl units of **TSB1** are meta-conjugated, whereas those of **TSB2** interact electronically on the same plane via the benzene core. In contrast, the fluorescence of **TSB2** is also red-shifted with respect to that of *p*-DSB (λ_{em} = 410 nm),[99] with a large Stokes' shift of 9941 cm^{-1} (Table 1).

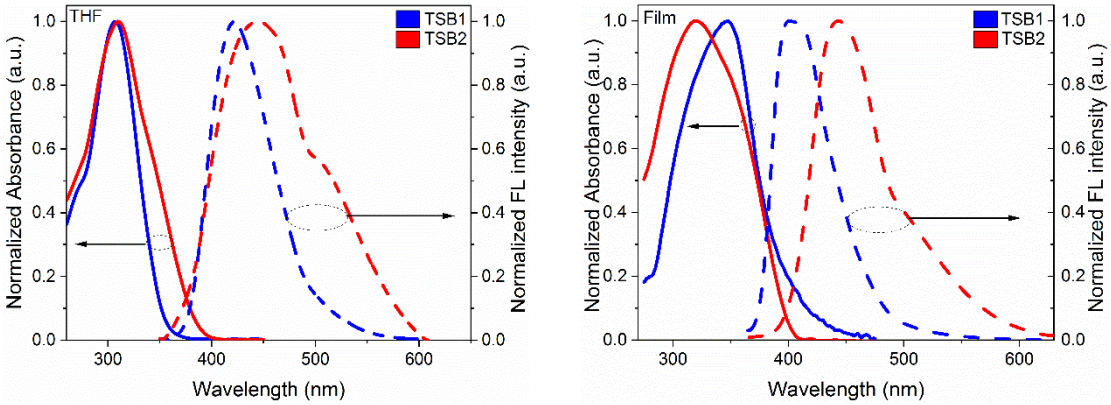

Figure 18. Normalized absorption (solid lines) and emission (dashed lines) spectra of **TSB1** and **TSB2** in THF (left) and solid state (film, right). Adapted with permission from ref.[86] © 2019 Wiley-VCH Verlag GmbH & Co. KGaA.

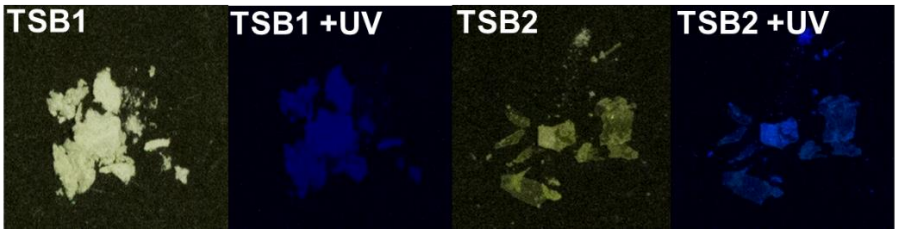

Figure 19. Appearance of **TSB1** and **TSB2** under normal light and 365 nm UV light. Adapted with permission from ref.[86] © 2019 Wiley-VCH Verlag GmbH & Co. KGaA.

Both the fluorescence quantum yields (Φ_F) of **TSB1** and **TSB2** (<1%) are lower than *trans*-stilbene[98] and they are virtually non-luminescent when dissolved in good solvents like THF. In thin films spuncast from THF, quantum yields of blue-emitting **TSB1** and **TSB2** slightly increased to Φ_F = 2.8% and 4.7%, indicating that aggregation has turned on their emission. For **TSB1**, emission is broadened and slightly blue-shifted by 19 nm compared to its fluorescence in THF. Figure 19 shows a photograph of the solid state of **TSB1** and **TSB2** under normal light and 365 nm UV light. It was found that both the colorless **TSB1** and yellowish **TSB2** emit in the blue region upon excitation.

Table 1. Photophysical properties of compounds **TSB1** and **TSB2**.[a]

		$\lambda_{max,\ abs}$ (nm)	$\lambda_{max,\ em}$ (nm)	$\Delta\upsilon_{st}$[b] (cm^{-1})	ε ($M^{-1}\cdot cm^{-1}$)	Φ_F
TSB1	THF	307	421	8820	5.8×10^4	<1%
	Film[a]	350	402	3696	-	2.8%
TSB2	THF	309	446	9941	4.4×10^4	<1%
	Film[a]	319	444	8825	-	4.7%

[a] Film prepared by spin-coating on glass substrate from corresponding THF solution (5.0 mg/mL, 1000 rpm) on glass substrates. [b] $\Delta\upsilon_{st} = 1/\lambda_{abs}-1/\lambda_{em}$.

To examine whether **TSB1** and **TSB2** are AIE-active, the effect of solvent viscosity on the emission characteristics was studied (Figure 20). With increasing viscosity of the solution controlled through the relative volume fraction of ethylene glycol f_g (up to 90%), the fluorescence intensity of **TSB1** increases with the volume fraction of ethylene glycol up to 11-fold. In a similar experiment **TSB2** experiences an 20-fold increase of emission intensity. A significant blue shift of the emission in **TSB2** was observed, indicating a highly twisted conformation formed during viscosity increase.[100] The emission enhancement from f_g = 0 to 90% in the case of **TSB1** (11-fold) is a little weaker compared to **TSB2,** which suggested **TSB2** possesses enhanced AIE effect from solution to aggregates.

This increased intensity trend was also reproduced when one compared the emission enhancement of **TSB1** and **TSB2** in THF/H_2O from f_w = 0 to f_w = 99 % (**TSB1**, almost 3-fold; **TSB2**, almost 6-fold, Figure 21 and 22, f_w denoting the volume fraction of water). We attribute the difference in fluorescence enhancement to the nature of the aggregates formed. Apart from the enhancement in emission intensity, **TSB1** reveals in aqueous mixtures an emission shift from 421 nm to 401 nm, similar to its thin film emission (Figure 21).

However, in asymmetric **TSB2**, the maximum emission wavelength almost remains unchanged at a water fraction of 99%. The reason for the distinct fluorescent behavior of **TSB1** and **TSB2** may be tentatively ascribed to their molecular structures. **TSB1** is *meta*-conjugated and has a more non-planar geometry in aggregate state in comparison with in solution, leading to the apparent blue shift.[101] As for **TSB2**, there may have not been much change in conformation between the aggregate state and solution.

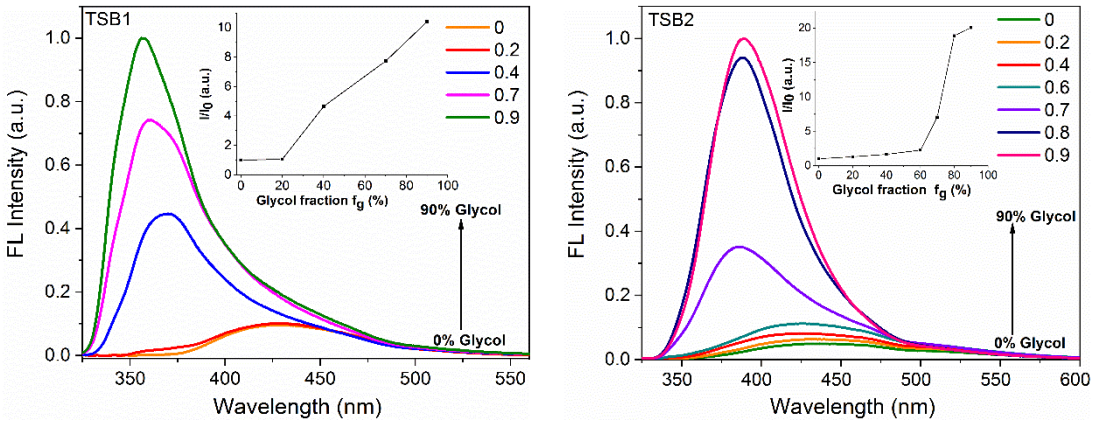

Figure 20. Variation of the fluorescence intensity of **TSB1** and **TSB2** with a gradually increasing viscosity in a THF/ethylene glycol gradient (from 0 to 90%, v/v). Inset: Fluorescence intensity I versus glycol fraction f_g. Adapted with permission from ref.[86] © 2019 Wiley-VCH Verlag GmbH & Co. KGaA.

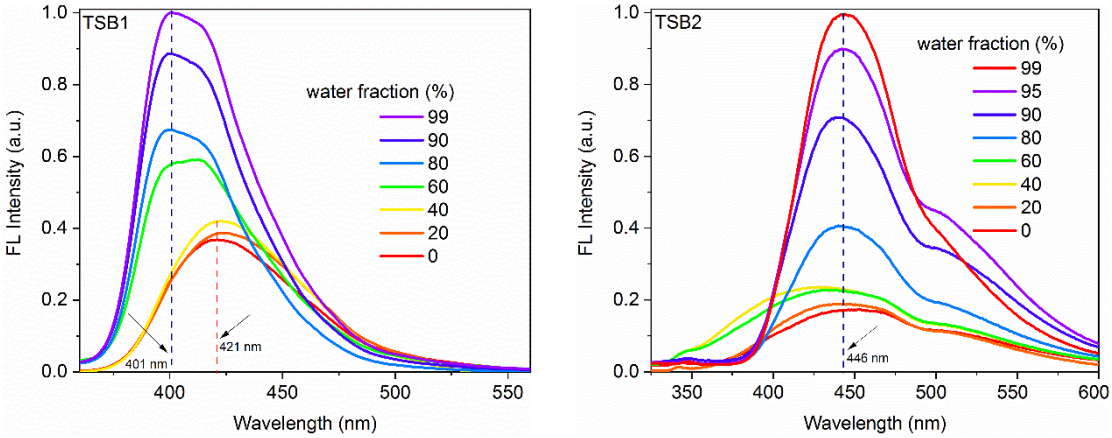

Figure 21. FL spectra of **TSB1** and **TSB2** in the THF/water mixtures. Adapted with permission from ref.[86] © 2019 Wiley-VCH Verlag GmbH & Co. KGaA.

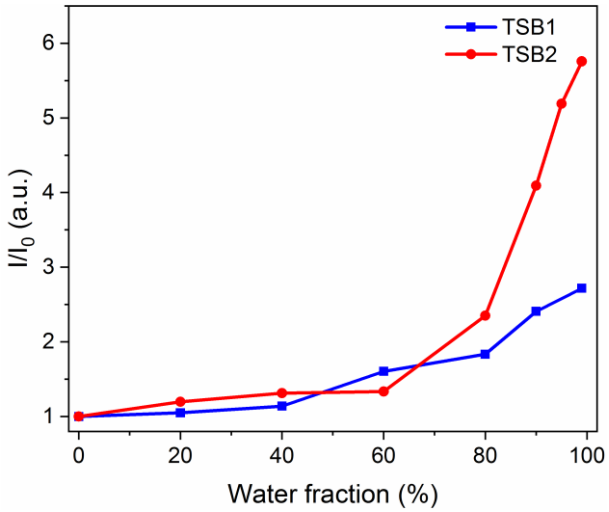

Figure 22. Plots of fluorescence intensity I against water fraction for **TSB1** and **TSB2** in THF/water mixtures. Adapted with permission from ref.[86] © 2019 Wiley-VCH Verlag GmbH & Co. KGaA.

With the assistance of Dr. Irene Wacker (group member of Prof. Rasmus Schröder, University of Heidelberg), we performed the SEM analysis to investigate the difference in the strength of the AIE-effect. Herein, we appreciate her help. The results showed that **TSB2** forms spherical nanoparticles with the diameter up to 500 nm from THF/water but exhibits homogeneous structures from THF/glycol (Figure 23). In contrast, different sizes of rod-like nanoaggregates from THF/water or THF/glycol, depending on the mode of preparation, are observed for **TSB1**, suggesting that morphology influences AIE effect strongly.

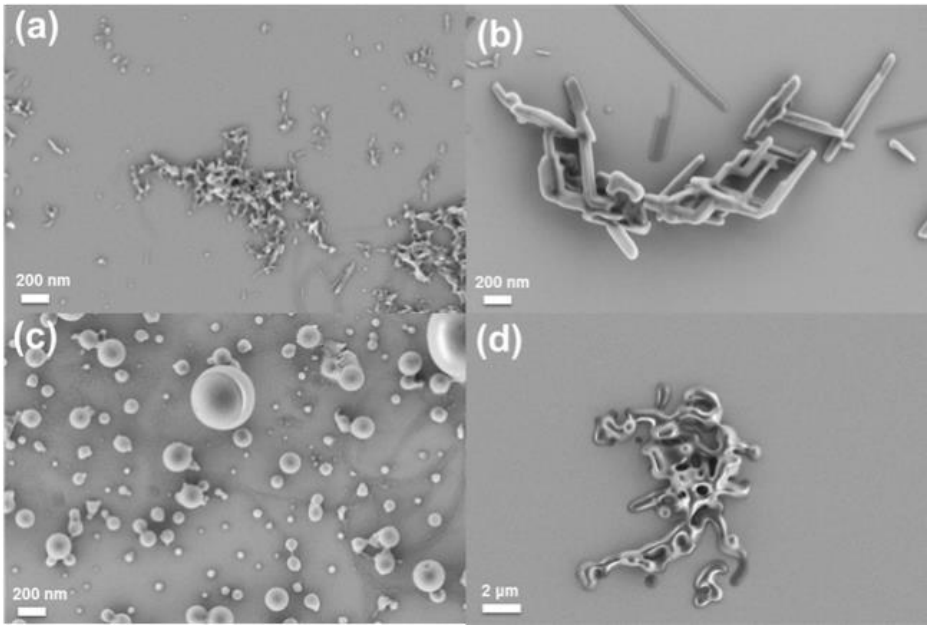

Figure 23. SEM images of (a) **TSB1** from THF/water (10:90); (b) **TSB1** from THF/ethylene glycol (10:90); (c) **TSB2** from THF/water (10:90); (d) **TSB2** from THF/ethylene glycol (10:90). Reproduced with permission from ref.[86] © 2019 Wiley-VCH Verlag GmbH & Co. KGaA.

2.1.4 X-ray Single Crystal Analyses

Suitable single crystals for X-ray crystal structure analyses were obtained by slow diffusion of methanol into a solution of **TSB1** or **TSB2** in dichloromethane at room temperature (Figure 24). The torsion between the six benzene rings on the periphery and the central benzene core is a distinct feature for **TSB1** and **TSB2**. For **TSB1**, the torsion angles between the peripheral phenyl rings and the benzene core range from 58°-69° and the torsion angles between the phenyl rings on vinylic linkers and the benzene core range from 21°-43° (Table 2). Compound **TSB1** crystallizes with two independent molecules in the unit cell, which together form two independent one-dimensional inclined stacks. Although its twisted geometry helps in reducing the face-to-face π-π stacking, one can observe strong edge-to-face (C-H···π) interactions (the distance between H atoms and benzene centroid). The interactions of C_{72}-H_{72}···π (2.82 Å) and C_{76}-H_{76}···π (2.74 Å) lead to two head-to-tail molecules with distances of 4.45 Å and 4.31 Å (between central phenyls), respectively. They are interlinked through C_{56}-H_{56}···π (2.77 Å) and C_{52}-H_{52}···π (2.70 Å) to form stacks.

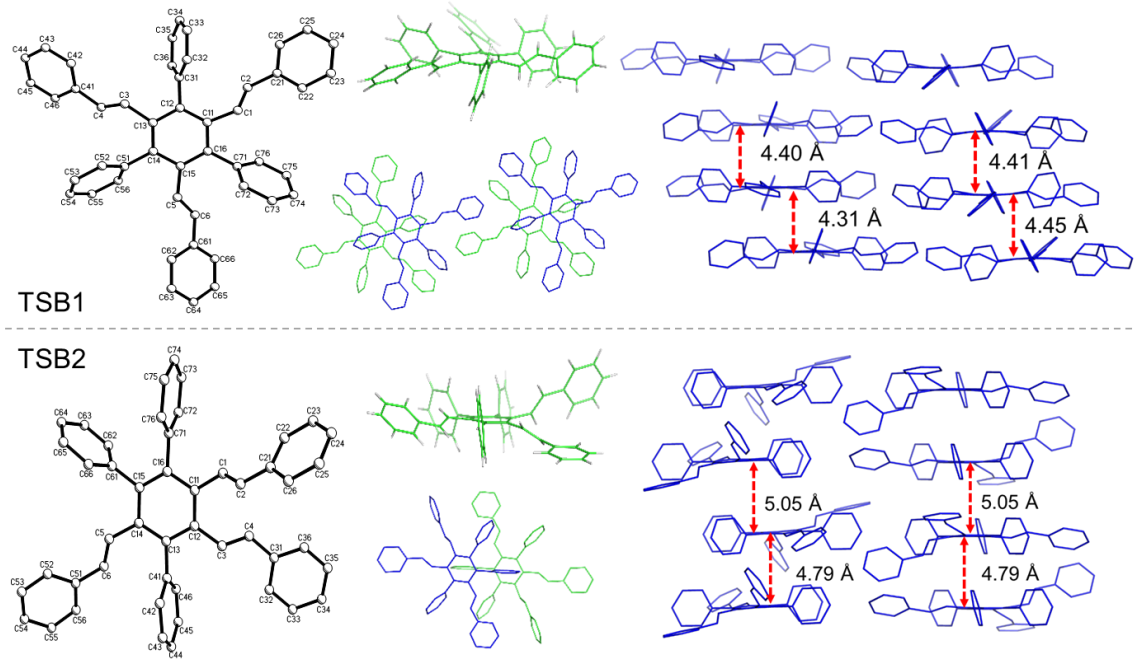

Figure 24. Solid-state structures (left), side view and visualization of overlap (middle) and packing (right) for **TSB1** and **TSB2**. Adapted with permission from ref.[86] © 2019 Wiley-VCH Verlag GmbH & Co. KGaA.

Table 2. Crystallographic properties of compounds **TSB1** and **TSB2.**

compound	crystal shape	crystal system	space group	Z	Torsion core-Ar1[b]	Torsion core-Ar2[c]
TSB1[a]	brick	triclinic	$P\bar{1}$	4	58°, 67°, 69°; 62°, 64°,70°	21°, 22°, 43°; 37°, 38°,40°
TSB2	needle	monoclinic	$P2_1/c$	4	77°, 81°, 82°	9°,31°, 59°

[a] Two independent crystallographic molecules. [b] Torsion of the outer phenyl substituents vs the central benzene ring. [c] Torsion of the outer phenyl in styryl arm vs the central benzene ring.

However, unlike **TSB1**, **TSB2** crystallizes with one molecule per unit cell. The molecules form stacks, with a distance of 4.79 Å and 5.05 Å (between central phenyls), in which two adjacent molecules are related to each other by a crystallographic inversion center. When hydrophobic molecules **TSB1** and **TSB2** form aggregates, the intramolecular rotations of phenyls are restricted by the aboved C-H···π interaction, which prevent the non-radiative pathway, thus the emission was enhanced.

On the other hand, the stronger intermolecular interactions (Figure 25) and shorter interplanar distances (Figure 24) in **TSB1** induce rigid contacts with adjacent molecules compared to the relatively loose intermolecular contacts in **TSB2**. The reinforced intermolecular interactions owing to alternate arrangements of phenyl and styryl units on **TSB1** were verified by comparing the melting points of two molecules. There is a significant difference in melting points between **TSB1** and **TSB2** (264 °C and 186 °C), indicating the stronger packing of **TSB1**.

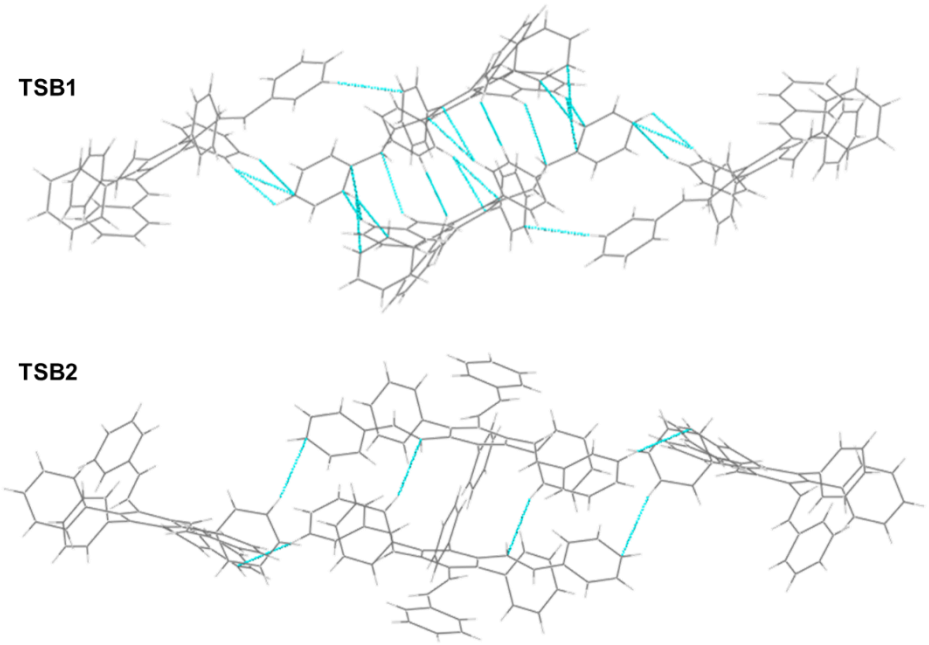

Figure 25. Schematic intermolecular interactions in the crystal of compound **TSB1** (range: 2.375 Å–2.889 Å) and **TSB2** (range: 2.701 Å–2.881 Å). Adapted with permission from ref.[86] © 2019 Wiley-VCH Verlag GmbH & Co. KGaA.

2.1.5 DFT Calculations

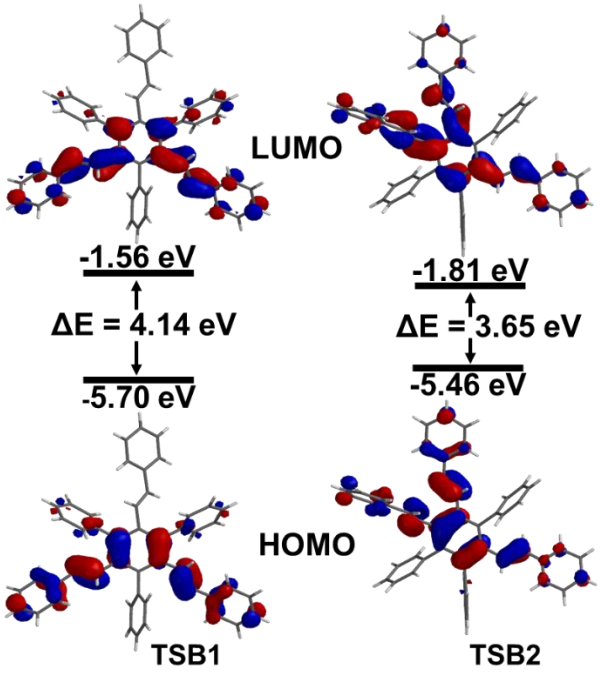

Figure 26. Frontier molecular orbital levels of compounds **TSB1** and **TSB2** (DFT, B3LYP/6-311++G**). Adapted with permission from ref.[86] © 2019 Wiley-VCH Verlag GmbH & Co. KGaA.

DFT calculations were carried out at the hybrid B3LYP level by employing the split valence 6-311++G** basis set (Spartan,[102] Figure 26). The results reveal that for **TSB1**, orbital coefficients of HOMO and LUMO are mainly located on the benzene core conjugated with two styryl units, which

leads to poor electronic communication and a short conjugation length. However, in th case of **TSB2**, its HOMO and LUMO are dominated by the orbitals from the benzene core conjugated with three styryl units. In addition, by investigating the possible quasi-degenerate molecular energy levels and the corresponding spatial orbital distributions, it was found **TSB1** displays doubly-degenerate HOMOs and the HOMO of **TSB2** is not degenerate.The calculated bandgap of **TSB1** is 4.14 eV and it is wider than that of **TSB2** (3.65 eV), which agrees well with the red shifts in absorption and emission of **TSB2** relative to that of **TSB1**.

2.1.6 Photostability

Photostability was assessed by exposing the two regioisomeric compounds to UV light in a photoreactor; their photoproducts were obtained by column chromatography as an inseparable mixture. Upon irradiation (λ_{ex} = 300 nm) for 1.5 hours, both **TSB1** and **TSB2** transform into the cyclization products (**TSB1a** and **TSB2a**) after triple cyclization of three distyryl units and subsequent [1,5]-hydrogen shifts.[103]. Scheme 10 shows the possible constitutional isomers and partial stereoisomers of **TSB1a** and either one of the isomers forms or both, but **TSB1a-2** was more favorable (see below).

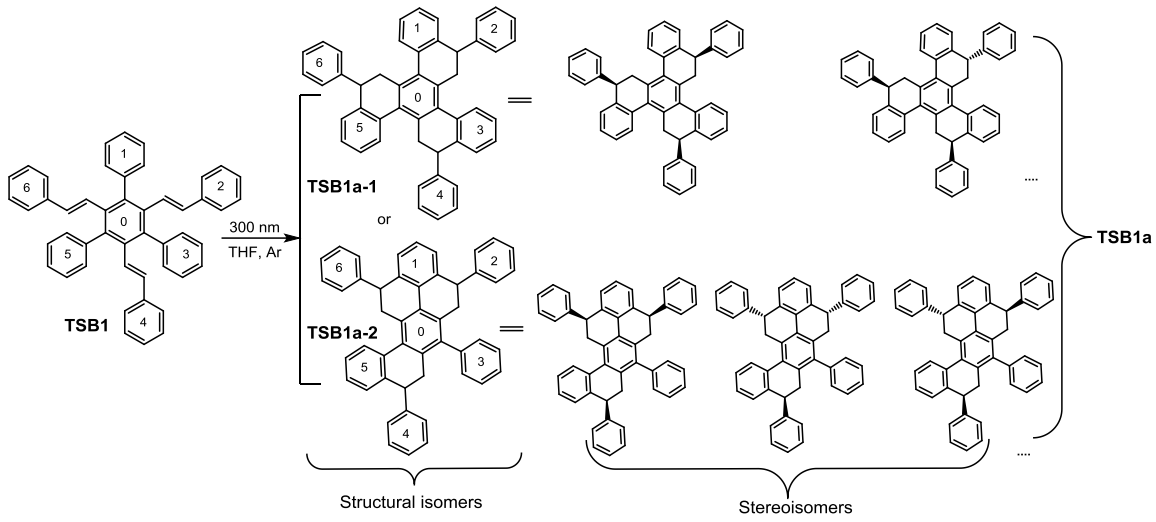

Scheme 10. Photocyclization of **TSB1**. Adapted with permission from ref.[86] © 2019 Wiley-VCH Verlag GmbH & Co. KGaA.

After a number of failed attempts to obtain the suitable crystal for analysis, ^{1}H NMR spectra, IR spectra and MS spectra were used to identify the isomers of **TSB1a** and **TSB2a**. The IR spectra before and after irradiation (Figure 27) reveal the disappearance of the bending vibration of the trans olefin (970 cm^{-1}) as well as the generation of aliphatic C-H stretching vibrations attributed to methylene group (-CH_2-) and methine group (-CH-) at 2920 cm^{-1}. HRMS confirms the sole formation of isomers without any decomposition or loss of hydrogen after irradiation (see Experimental Section). A comparison of the proton NMR spectra before and after irradiation is depicted in Figure 28. The olefinic doublets at about 5.7 and 6.4 ppm disappeared, while resonances of the methylene group (-CH_2-) and methenyl group (-

CH-) appear at 2.9-3.6 ppm and 4.1 ppm, respectively. Upon closer examination of the integral of signals belong to methylene group (-CH_2-) at δ = 2.9 and 3.6 ppm, the ratio between them was found to be 2:1, which suggested the formation of asymmetric photoproduct **TSB1a-2** was favorable. However, due to their small differences in structure and polarity, the separation of the individual isomers of **TSB1a** by preparative methods remained problematic, rendering the assignment of photoproducts challenging.

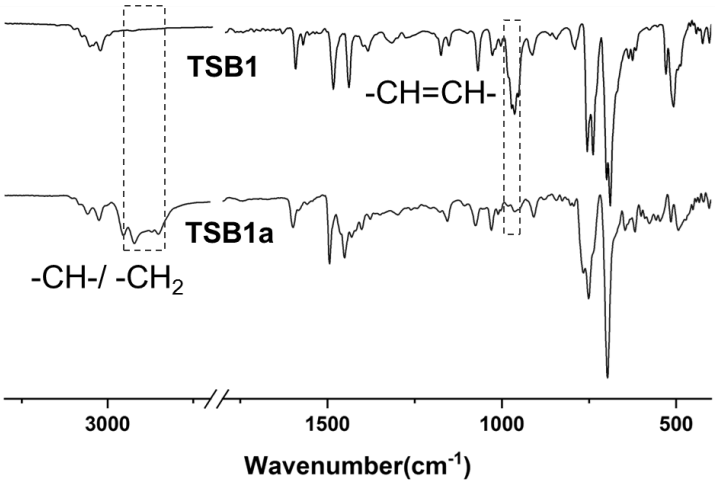

Figure 27. IR spectroscopy of **TSB1** and **TSB1a**. Adapted with permission from ref.[86] © 2019 Wiley-VCH Verlag GmbH & Co. KGaA.

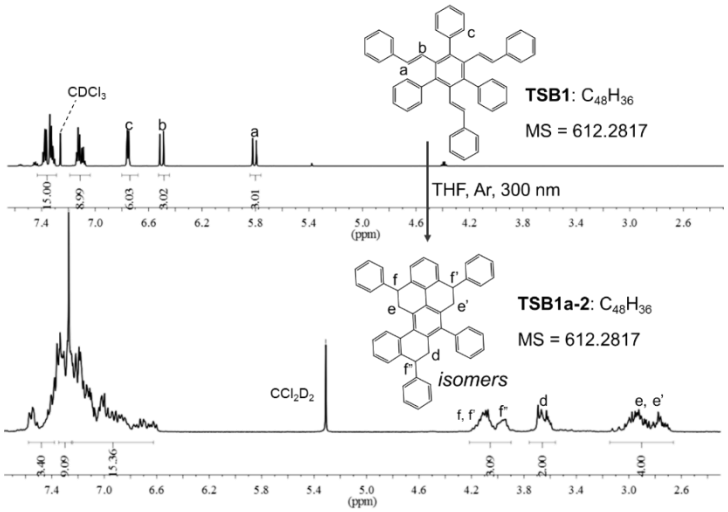

Figure 28. ^{1}H NMR spectra of **TSB1** and **TSB1a-2**. Adapted with permission from ref.[86] © 2019 Wiley-VCH Verlag GmbH & Co. KGaA.

As to **TSB2**, its photoproduct **TSB2a** was obtained in a similar way (Scheme 11). However, due to their structural differences (**TSB2a-1** or **TSB2a-2**), the photoproduct could not be assigned from NMR, MS and IR spectrum, that is, both are possible photoproducts. Either one of the isomers forms or both. The normalized absorption and emission spectra of photoproduct **TSB1a** and **TSB2a** in dilute THF were shown in Figure 29.

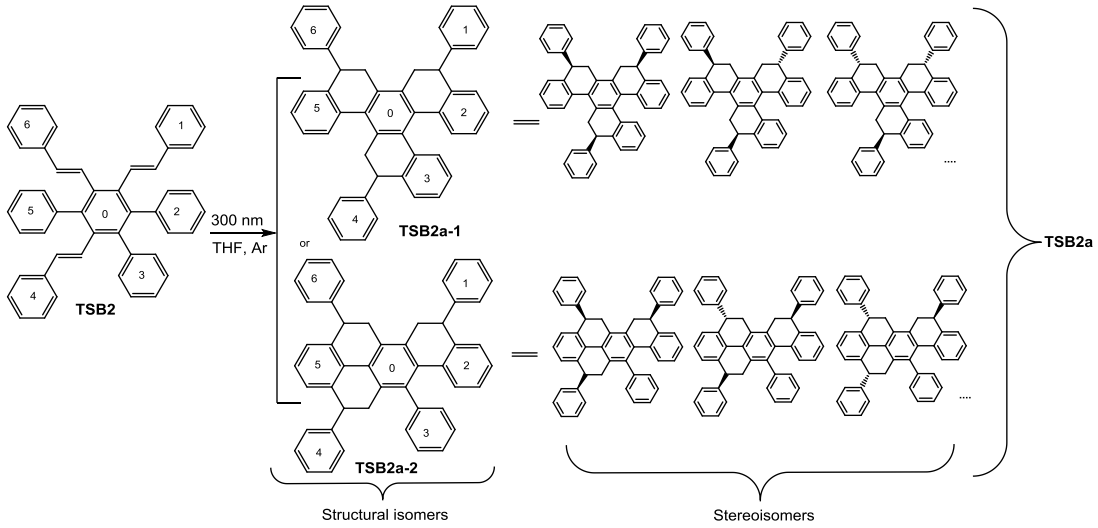

Scheme 11. Photocyclization of **TSB2**. Adapted with permission from ref.[86] © 2019 Wiley-VCH Verlag GmbH & Co. KGaA.

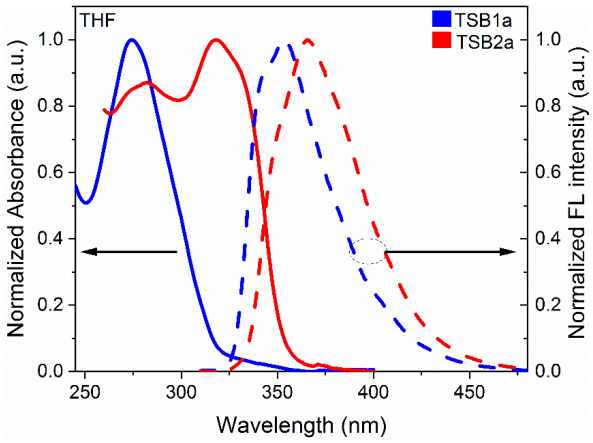

Figure 29. Normalized absorption (solid lines) and emission (dashed lines) spectra of **TSB1a** (blue) and **TSB2a** (red) in THF solution. Adapted with permission from ref.[86] © 2019 Wiley-VCH Verlag GmbH & Co. KGaA.

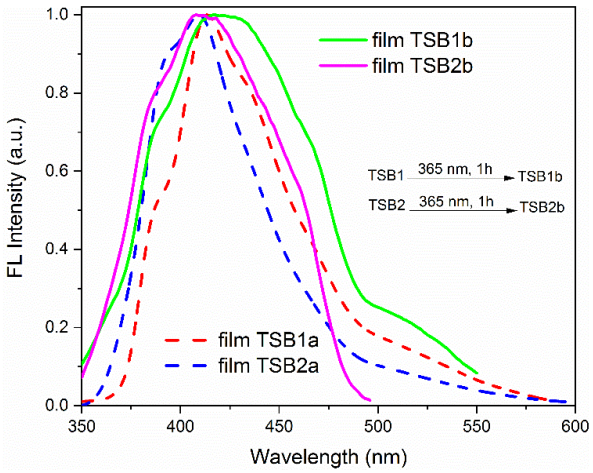

Figure 30. Fluorescence emission spectra of **TSB1a,b** and **TSB2a,b** in solid state. Adapted with permission from ref.[86] © 2019 Wiley-VCH Verlag GmbH & Co. KGaA.

To verify the stability of **TSB1** and **TSB2** in solid state, their films were irradiated for 1 hour using hand-held UV light (365 nm) and photoproduct **TSB1b** and **TSB2b** were obatined. As shown in Figure 30, it was found that the emission peak of **TSB1b** (417 nm) and **TSB2b** (414 nm) shifted compared with that of **TSB1** (402 nm) and **TSB2** (444 nm) in film. In addition, the emission peaks of film **TSB1a** and **TSB1b** are almost overlapped and similar phenomenon was also observed in **TSB2a** and **TSB2b**, which suggest this cyclization also occurs in thin films. For both **TSB1** and **TSB2**, the photocyclization reaction occurs both in solution and solid states like thin film.

2.1.7 Conclusion

In summary, the molecular design, synthesis, and properties of two novel regioisomeric triphenyl substituted tristyrylbenzenes **TSB1** and **TSB2** have been presented. In comparison with the meta-conjugated **TSB1**, **TSB2** with two styryl arms in the para position showed a red-shifted emission in its solution and solid state due to its higher conjugation. We have found that both **TSB1** and **TSB2**, similar to the tetraphenyl tristyrylbenzenes, display AIE characteristics, and **TSB2** has the enhanced AIE effects. Because of their twisted structures, **TSB1** and **TSB2** experienced little π-π stacking interaction in their solid state. The optical properties in the solution and solid-state optical properties are a consequence of their molecular structure. Upon UV irradiation in solution, both **TSB1** and **TSB2** underwent a photocyclizations. Our results not only provide information on the effect of regioisomerism, but also insights into the design of tristyrylbenzene-based AIE materials.

2.2 Linear and Star-Shaped Extended Di- and Tristyrylbenzenes: Synthesis, Characterization and Optical Response to Acid and Metal Ions

In this part, we prepared two linear 1,4-distyrylbenzenes derivatives (**DSB1-2**) and five star-shaped 1,3,5-tristyrylbenzene derivatives (**TSB3-7**) and they were spectroscopically characterized. The photophysical properties, optical response to acid and metal ions were investigated and discussed. Upon backbone extension of linear distyrylbenzenes or the introduction of the electron-donating dibutylanilines to star-shaped tristyrylbenzenes, the electronic spectra are red-shifted. Incorporation of electron-deficient pyridyl units does not significantly affect the optical properties. The fluorescence response to acids and metal ions was tuned by variation of the number of pyridine rings and substitution pattern. The novel arenes are attractive to discriminate metal ions such as Al^{3+}, Mn^{2+}, Fe^{3+}, Fe^{2+}, Cd^{2+}, Ag^{+} and Hg^{2+}.

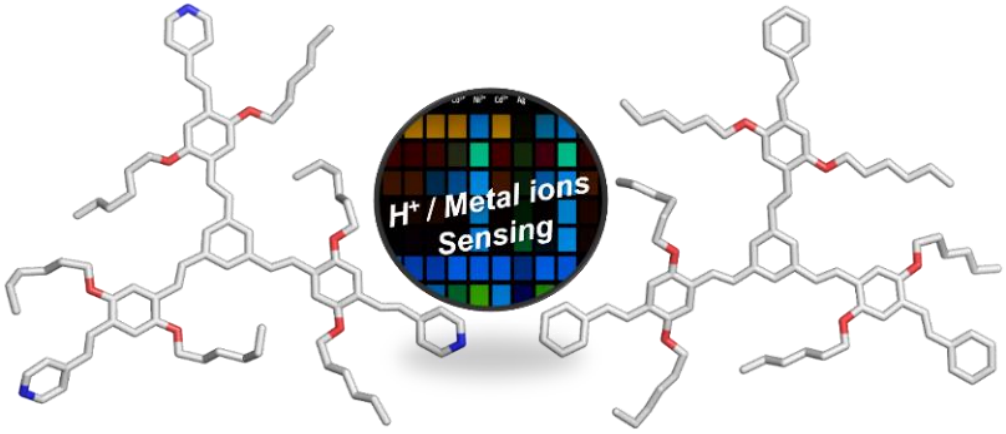

Figure 31. Schematic representation of linear and star-shaped extended di- and tristyrylbenzenes: synthesis, characterization and optical response to acid and metal ions. Reproduced with permission from ref.[104] © 2020 Wiley-VCH Verlag GmbH & Co. KGaA.

2.2.1 Linear, X-shaped and Star-Shaped Chromophores

Functional π-conjugated chromophores with linear,[105] X-shaped,[106] or star-shaped geometry[88b, 107] are attractive as sensors in analytical chemistry, biology, biomedicine, and materials science.[108] Previous study in our lab indicates that subtle manipulation of the substituents in X-shaped conjugated fluorophores (cruciforms) leads to disjunct frontier molecular orbitals and tunable optical properties.[70a, 75, 106, 109] If pyridines or dialkylanilines are incorporated, they become acidochromic because of the electronic lone pairs at nitrogen. Meanwhile, both size and symmetry of the conjugated system were found to affect the properties and performance in applications.[6, 110]

2.2.2 TSB Derivatives in Sensing Application

The appropriate functionalization of the fluorescent TSBs can give rise to new and interesting sensing applications.[92b, 111] For example, García-Martínez et al. synthesized two 1,3,5-tristyrylbenzenes decorated with polyamine and poly(amidoamine) chains at the periphery. The two molecules showed linear dependence of the fluorescence lifetime in different pH ranges, which is valuble for fluorescence lifetime sensors and imaging microscopy.[92b] More recently, Sánchez-Ruiz et al. reported three turn-off fluoride sensors **43-45**, which are based on TSB with a *tert*-butyldimethylsilyl (TBDMS) group at the periphery. These sensors displayed good selectivity over a variety of other anions and high sensitivity over fluoride in the lower μM range when dissolved in DMSO.[111] C_3 symmetric TSB **46** was synthesized by linking three tris(*N*-salicylideneaniline) units to the TSB core.[94] **46** underwent efficient excited-state intramolecular proton transfer (ESIPT) in solution because of the presence of C=N···H−O hydrogen-bond. In addition, **46** exhibited strong AIE characteristics in DMSO/water mixtures and could serve as a turn-on sensor for Zn^{2+} ions.

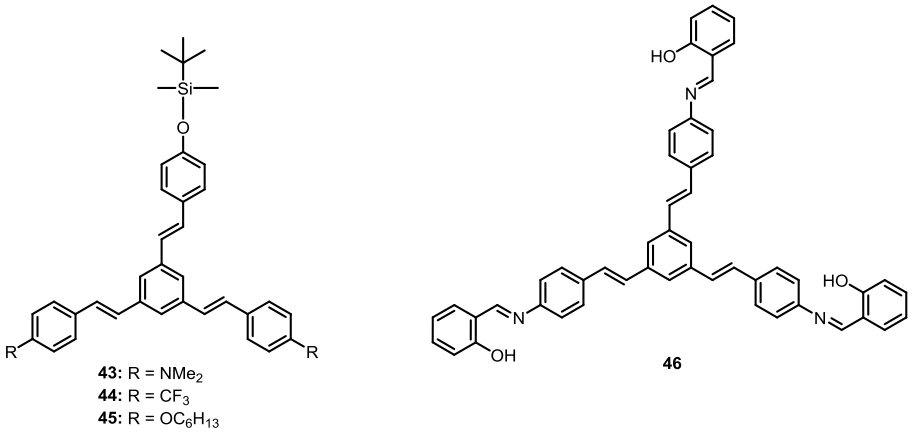

Figure 32. The structure of TSBs used for sensors.[94, 111]

The current work describes two linear 1,4-distyryl (**DSB1-2**) and five star-shaped tristyrylbenzene derivatives (**TSB3-7**) as well as their photophysical characterization, and acid/metal ion response studies. We dissect the influence of symmetry on their optical properties and metal-sensing abilities.

2.2.3 Synthesis

The chemical structures and synthetic strategy adopted for these SBs are outlined in Scheme 12 and 13. **DSB1** is a distyrylbenzene substituted with two pyridyls. **DSB2** was designed as an analogue of **DSB1** with a longer effective conjugation length, a so-called extended distryrylbenzene.[112] **TSB3** is a star-shaped and C_3-symmetric π-system with three identical arms, which was reported by Maier *et al.*[113] Based on this known skeleton (**TSB3**), **TSB4-7** are formally obtained either by changing the number of pyridine rings or the introduction of electron-rich dibutylaniline groups, respectively.

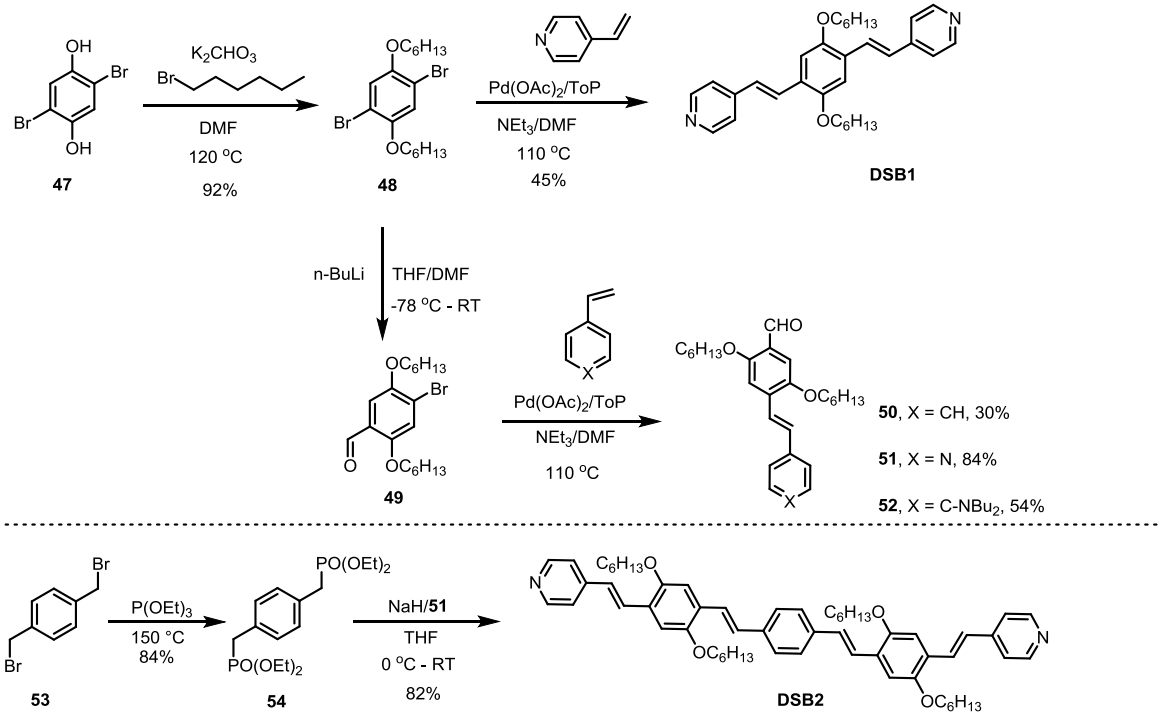

Scheme 12. Synthetic route to linear 1,4-distyrylbenzenes (**DSB1,2**).

Compound **48** was obtained by **47** reacting with 1-bromohexane (K_2CO_3, anhydrous DMF). As reference systems, Heck reaction of **48** and 4-vinylpyridine gave the distyrylbenzene **DSB1** (45%). **48** was transformed by a Bouveault reaction to the monoaldehyde **49**. Heck coupling between **49** and three arylethylenes produced **50-52**. **53** was subjected to an Arbuzow reaction with triethyl phosphite **54**, followed by a Horner reaction with monoaldehyde **51** to furnish **DSB2** in good yields (82%) after purification via column chromatography on silica gel.

50-52 were subjected to Horner reactions with triphosphonate **60** in the presence of sodium hydride to generate **TSB3** (77%), **TSB6** (33%) and **TSB7** (68%). **TSB4** and **TSB5** were synthesized via two one-pot procedures starting from **55** with aldehydes **51** and **50,** respectively. For **TSB4**, the first Horner reaction of **55** with monoaldehyde **51** (molar ratio: 1:1.1) gave **56**, which in situ was subjected to a second Wittig-Horner reaction with monoaldehyde **50** (yield: 28% over two steps). Similarly, **TSB5** was isolated by a two-step routine with a yield of 44% by changing the stoichiometry of **55** and **51** (1:2.2). Note that potassium *tert*-butoxide as a base did not work in our cases.[114] **TSB7** is a yellow oil, while **DSB1,2** and **TSB3-6** are yellow or orange solids. They are well soluble in common organic solvents.

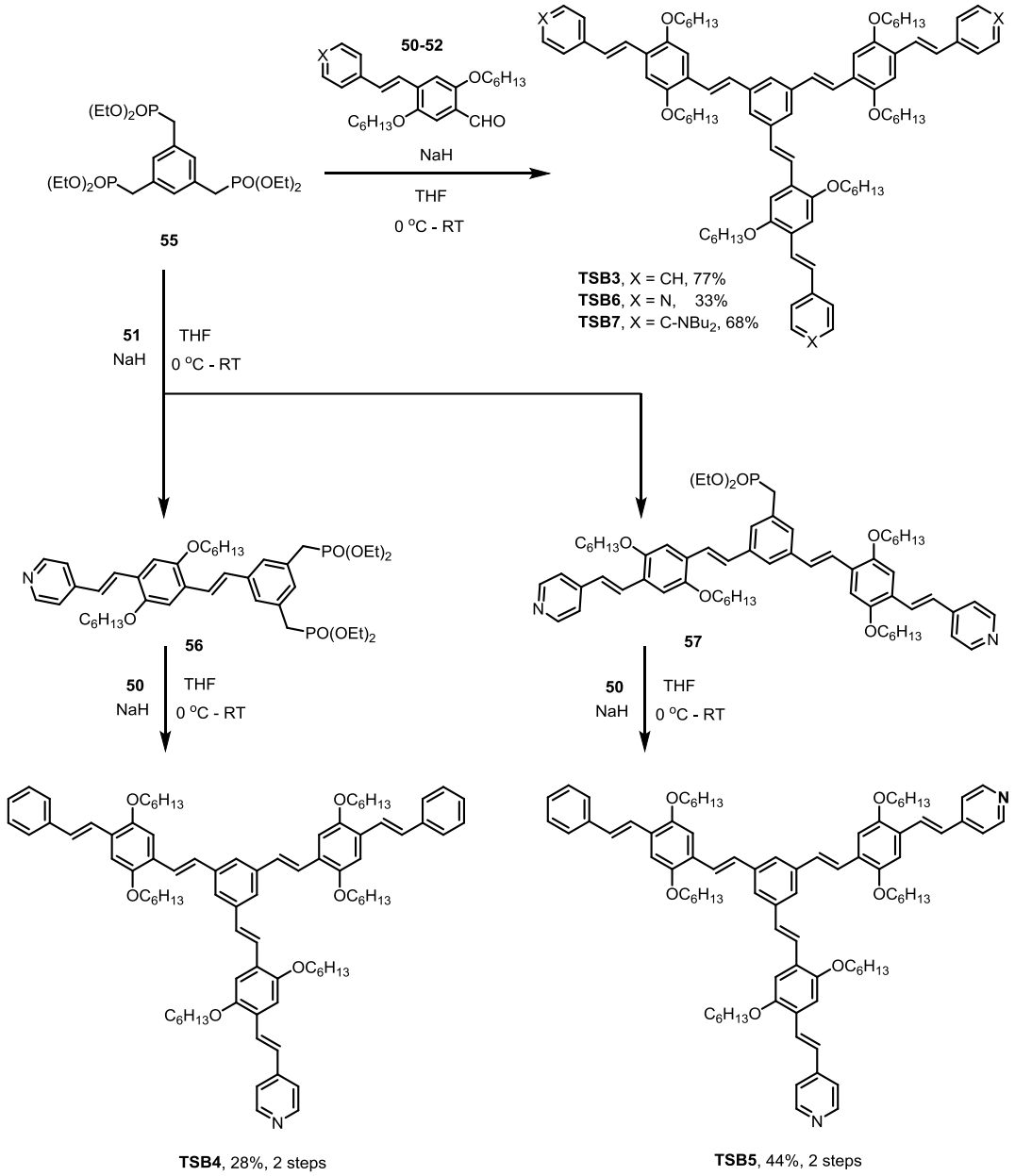

Scheme 13. Synthetic route to star-shaped 1,3,5-tristyrylbenzene derivatives (**TSB3-7**).

2.2.4 X-ray Analyses and Liquid Crystalline Behaviors

We obtained single crystals for **TSB3** (by overlaying DCM with MeOH), **DSB2** and **TSB6** (from DCM/n-hexane) suitable for X-ray analysis. Figure 33 depicts the structures. All of derivatives are planar to a certain extent and their vinylic linkers display *E*-configuration. However, the packing patterns of **DSB2**, **TSB3** and **TSB6** differ significantly. **DSB2** packs in parallel layer stacks with a distance of 2.811 Å and 3.568 Å, respectively. Some displacement can be observed between layers. In **TSB3**, there is a parallel stacking that leads to a 2-dimensional wall-like arrangement with differing orientation of the molecular planes in adjacent parallel walls. In **TSB6**, a pattern of parallel planes was observed, with extending in three directions.

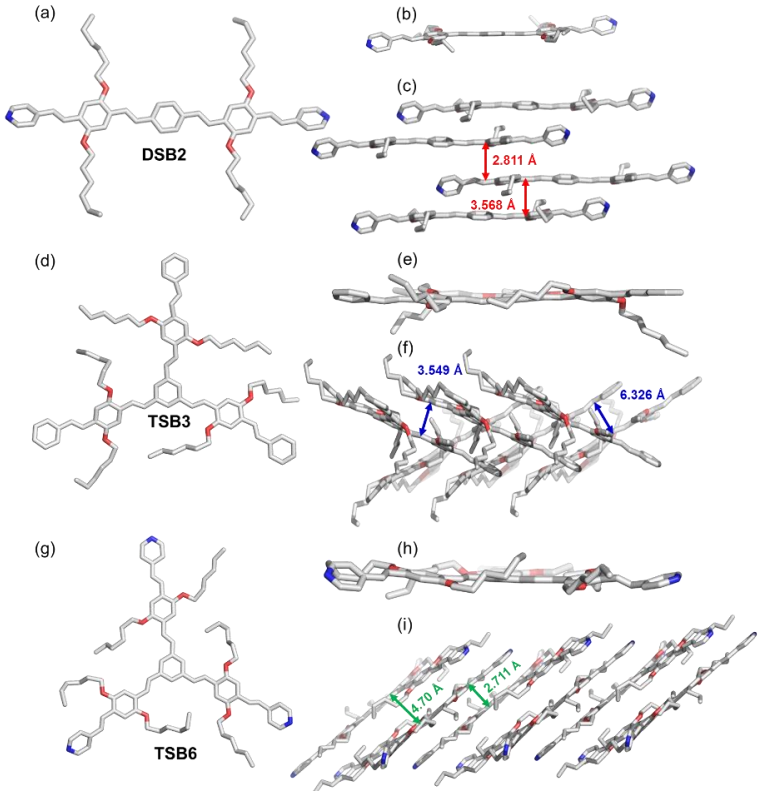

Figure 33. Solid-state structures (a, d, g), side view (b, e, h) and visualization of packing (c, f, i) for **DSB2**, **TSB3** and **TSB6**. Adapted with permission from ref.[104] © 2020 Wiley-VCH Verlag GmbH & Co. KGaA.

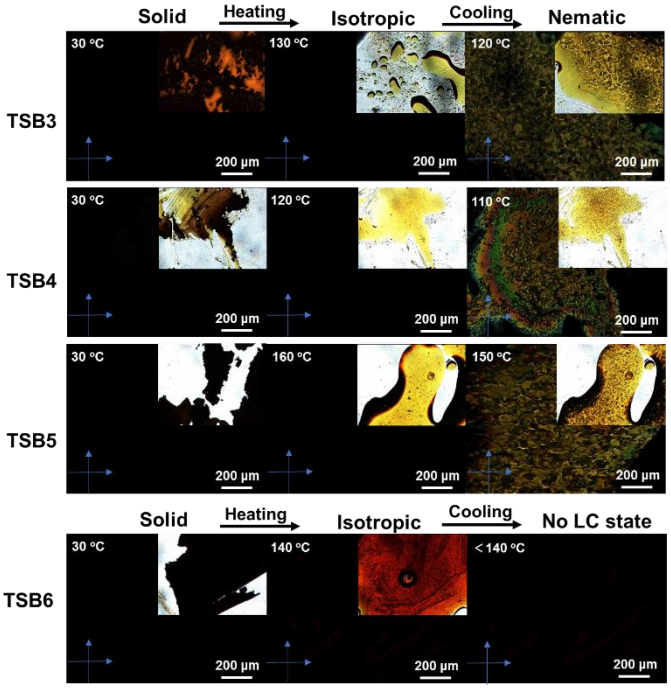

Figure 34. Polarization micrographs under crossed polarizers at given temperatures while heating and cooling samples of **TSB3-6**. Insets: Optical micrographs from the corresponding samples. Adapted with permission from ref.[104] © 2020 Wiley-VCH Verlag GmbH & Co. KGaA.

The molecular design implicated the possibility of liquid crystalline (LC) phases. The phase transitions for star-shaped SBs were investigated with a polarized optical microscope (POM). As shown in Figure

34, nematic liquid crystalline phases form, from isotropic ones during cooling scans observed for **TSB3-5**, which is similar to Maier's star-shaped compounds.[113] In the case of oily **TSB7**, no liquid crystalline behaviour was observed.

2.2.5 Photophysical Properties

The normalized absorption and emission spectra of these SBs in dilute THF are shown in Figure 35, while Table 3 summarizes the photophysical data. Because of the *meta*-conjugation, absorption spectra of star-shaped series **TSB3-6** are essentially superimposable to that of **DSB1**, with a maximum absorption centered at around 400 nm and a shoulder peak located at higher energies (326-348 nm). However, in the case of **DSB2** and **TSB7**, the weakening of the absorption peak in the higher energy region is apparent and the maximum absorption peak shifts bathochromically (**DSB2**: 432 nm; **TSB7**: 427 nm) relative to that of the other SBs, attributed to the extension of conjugation or the introduction of electron-rich dibutylaniline groups.

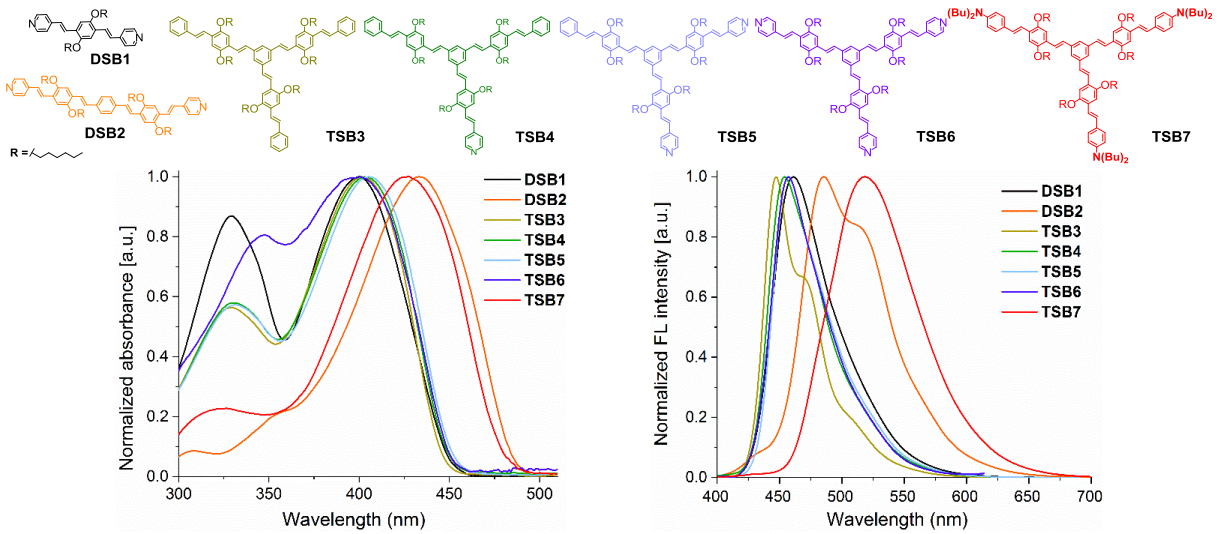

Figure 35. Normalized UV-Vis absorption (left) and emission (right) spectra of SBs in THF. Adapted with permission from ref.[104] © 2020 Wiley-VCH Verlag GmbH & Co. KGaA.

Table 3. Photophysical data (in THF) and calculated energy gaps for SBs.

Compounds	λ_{abs} [nm][a]	$\lambda_{max,em}$ [nm]	QY[b]	τ_f [ns]	λ_{st} [nm]/$\Delta\upsilon_{st}$ [cm^{-1}][c]	calcd. energy gap [eV, nm]
DSB1	329 (2.37), 400 (2.88)	461	0.64	2.00	61, 3308	3.06, 405
DSB2	432 (7.31)	485	0.68	1.10	53, 2529	2.56, 484
TSB3	329 (6.17), 401 (11.0)	447	0.82	1.39	46, 2566	2.97, 417
TSB4	330 (5.68), 403 (9.89)	454	0.73	1.51	51, 2787	2.86, 433
TSB5	331 (7.13), 405 (12.4)	456	0.72	1.52	51, 2761	2.87, 432
TSB6	348 (2.29), 401 (2.86)	457	0.79	1.67	56, 3118	2.96, 418
TSB7	326 (1.91), 427 (8.64)	519	0.61	1.41	92, 4151	2.82, 440

[a] Measured in THF and extinction coefficients ($\varepsilon_{max} \times 10^4\ M^{-1}\cdot cm^{-1}$) are shown in parentheses. [b] QY = quantum yield. [c] $\Delta\upsilon_{st} = 1/\lambda_{abs}-1/\lambda_{em}$.

In THF, the emission maxima trend follows the order **TSB7** > **DSB2** > **DSB1** > **TSB6** > **TSB5** > **TSB4** > **TSB3**. Compared with **DSB1**, **DSB2** exhibits a red-shifted green emission with a vibronic structure, resulting from its longer conjugation length. Asymmetric **TSB4** and **TSB5** show similar emission maxima in comparison to symmetric **TSB6**, while their maxima are redshifted by ca. 10 nm compared to symmetric hydrocarbon **TSB3**, indicating that the incorporation of electron-withdrawing pyridyl units has a negligible effect on the tristyrylbenzene derivatives. However, when the strong electron-donating dibutylaniline groups were introduced, the fluorescence maximum of **TSB7** bathochromically shifted to 519 nm with a Stokes shift of 4151 cm^{-1}. This is caused by its higher dipole moment in its excited state stabilized in more polar solvents.[115] **DSB1** and **TSB3-6** show blue emission in THF with quantum yields (Φ_f) varying from 0.64 to 0.82, while **DSB2** and **TSB7** exhibit green fluorescence with a quantum yield of 0.68 and 0.61, respectively. The lower quantum yield of dibutylamine-containing **TSB7** might be attributed to the free intramolecular rotation or the existence of photoelectron transfer facilitated by the flexible dibutylamine groups.[116]

2.2.6 Theoretic Calculations

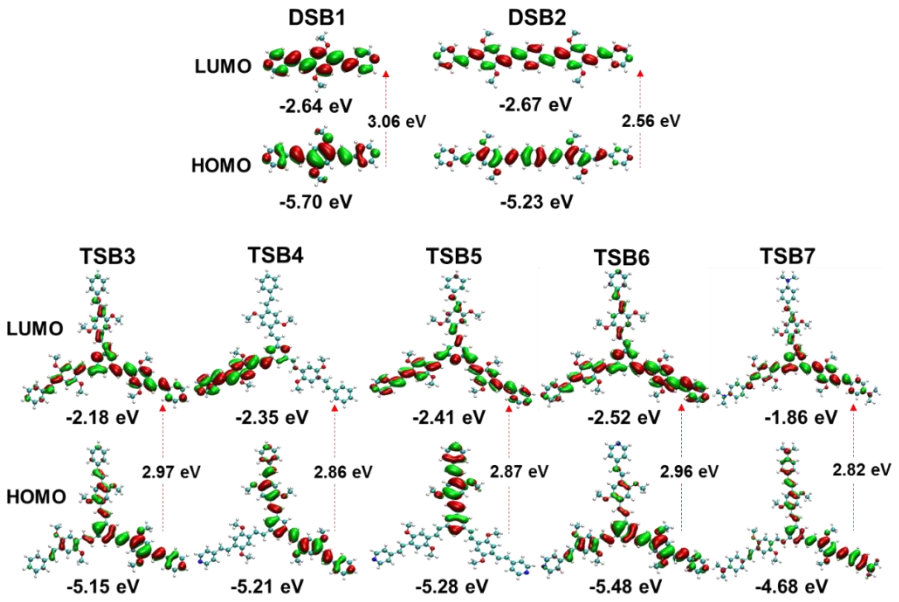

Figure 36. Frontier molecular orbital levels of SBs (DFT, B3LYP/6-311++G**).[117] Aliphatic chain approximated by a methyl group. Adapted with permission from ref.[104] © 2020 Wiley-VCH Verlag GmbH & Co. KGaA.

Density functional theory (DFT) calculations (B3LYP/6-31++G**)[118] was performed, which could give further insight into optoelectronics (Figure 36). The study of energy level structures indicates that **TSB3** and **TSB6-7** display triply quasi-degenerate HOMOs due to their symmetrical conformation. The calculated HOMO−LUMO energy gaps for **DSB1-2** and **TSB3-7** are in the range from 2.56 to 3.06 eV. The lower gaps of **TSB7** or **DSB2** clearly indicate their larger delocalization, which result in a distinct bathochromic shift in the electronic absorption spectrum. These results, as well as the trend of absorption maxima calculated by TDDFT methods (Figure 37) are consistent with the experiment.

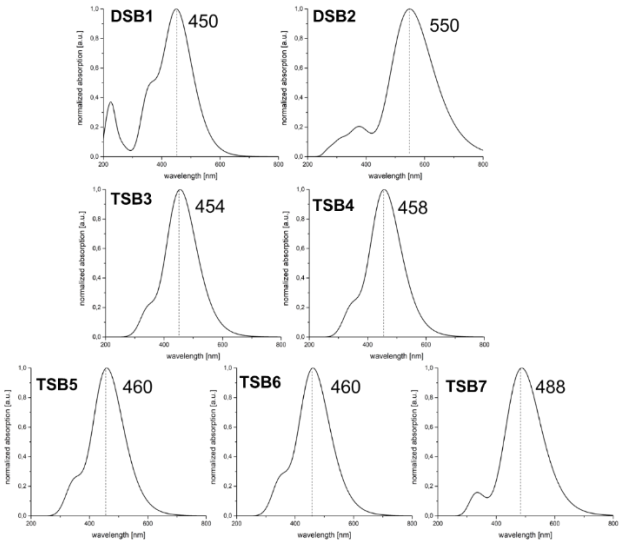

Figure 37. UV-Vis spectra calculated from the optimized geometries of the ground states using TDDFT B3LYP/def2svp.[117] Adapted with permission from ref.[104] © 2020 Wiley-VCH Verlag GmbH & Co. KGaA.

2.2.7 Fluorochromicity

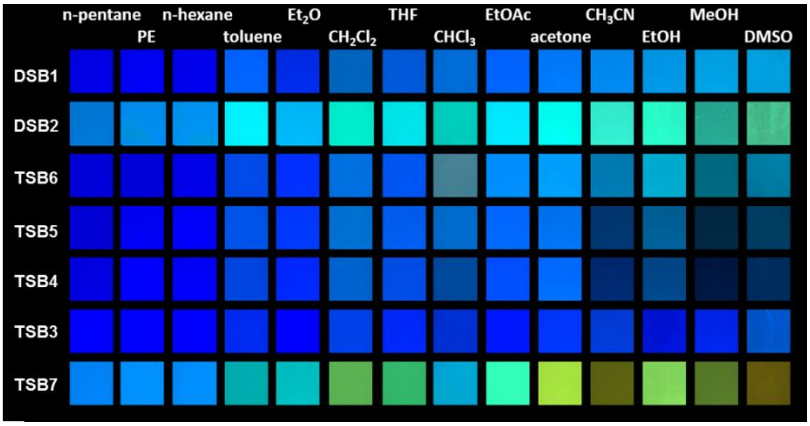

Figure 38. Photograph of SBs (c = 2 μg/mL) in different solvents under a hand-held black light with illumination at 365 nm. Adapted with permission from ref.[104] © 2020 Wiley-VCH Verlag GmbH & Co. KGaA.

The emission behaviors of SBs in solvents with different polarity are shown in Figure 38. The emission colors of **DSB1** and **TSB3-6** displayed negligible changes. However, for **DSB2** and **TSB7**, with increasing solvent polarity, red-shifted emission to varying degrees were observed in solvents of medium polarity (DCM and THF) and polar solvents (acetonitrile and DMF), suggesting positive fluorochromicity.[115] The emission color of **TSB7** ranges from light blue (PE, toluene) to green (EtOAc) and to yellow (DMSO).The effect of solvents on the emission features was evaluated by the Lippert–Mataga plot.[119]

$$\Delta\nu = \Delta\nu_{abs} - \Delta\nu_{em} = \frac{2(\mu_e - \mu_g)^2 \Delta f}{hca^3} + \text{constant} \quad (1)$$

$$\Delta f = \frac{\varepsilon - 1}{2\epsilon + 1} - \frac{n^2 - 1}{2n^2 + 1} \quad (2)$$

In eq 1, Δν is the Stokes shift; $\Delta\nu_{abs}$ and $\Delta\nu_{em}$ represent the wavenumbers of absorption and emission peaks; h is Planck's constant; c is the speed of light and a corresponds to the Onsager cavity radius; μ_e and μ_g are the excited and ground state dipole moments. In eq 2, Δf is the orientational polarizability of solvent; ε is the dielectric constant; n is refractive index of the solvent. The photophsical data of SBs in selected solvents was shown in Experimental Section. The relationship of the Stokes shift (Δν) and the orientational polarizability (Δf) of the solvents was plotted in Figure 39, and the corresponding slopes of Lippert-Mataga plot for SBs were summarized in Table 10 (Experimental Section).

It was found that all the SBs displayed linear dependence of Δν on Δf together with different slopes. **DSB2** and **TSB7** showed a much larger slope. The slope of the fitting line for **TSB7** is highest, up to 9673 cm^{-1}, comparable to that of the X-shaped distyrylbenzenes,[120] further indicating its larger dipole moment changes between the ground and excited states (μ_e-μ_g), leading to the pronounced solvent sensitivity.[121] **TSB7** is able to serve as a promising fluorescence polarity indicator.

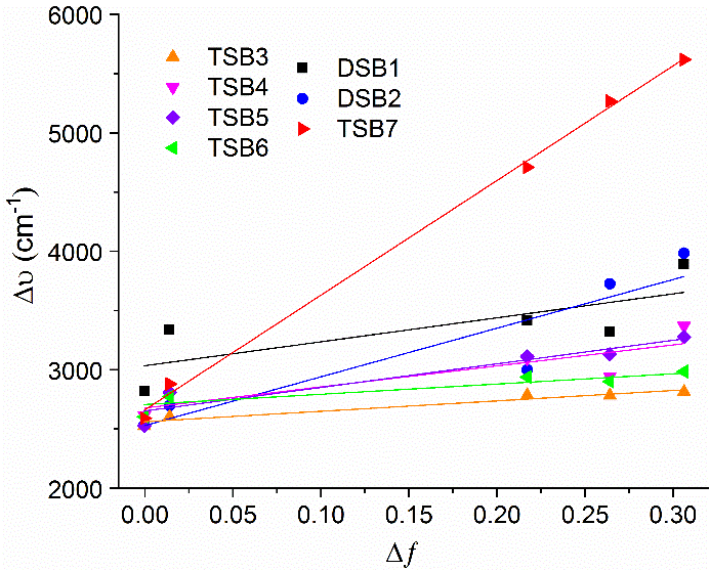

Figure 39. Stokes shifts (Δυ) of as a function of solvent polarity parameter (Δf). Adapted with permission from ref.[104] © 2020 Wiley-VCH Verlag GmbH & Co. KGaA.

2.2.8 Optical Response to Protons

As pyridines or dibutylanilines are basic, all SBs (except **TSB3**) display a significant change of their absorption and emission spectra when protonated by trifluoroacetic acid (TFA) in THF (Figure 40). All of the SBs with pyridine units experience a red-shift, accompanied with a loss of fluorescence intensity. This is easily explained as upon protonation the donor−acceptor character of these SBs dramatically increases and therefore internal charge transfer is favored. However, the addition of TFA to **TSB7** leads to strongly blue emissive species, in which the dibutylamino groups are protonated and the HOMO is stabilized by protonation, resulting in an increased HOMO-LUMO gap.[70b] Due to three pyridine rings as interaction sites, **TSB6** is more sensitive to protonation in comparison with **TSB4** and **TSB5**. The increasing of TFA content induces a color change detected by naked eyes.

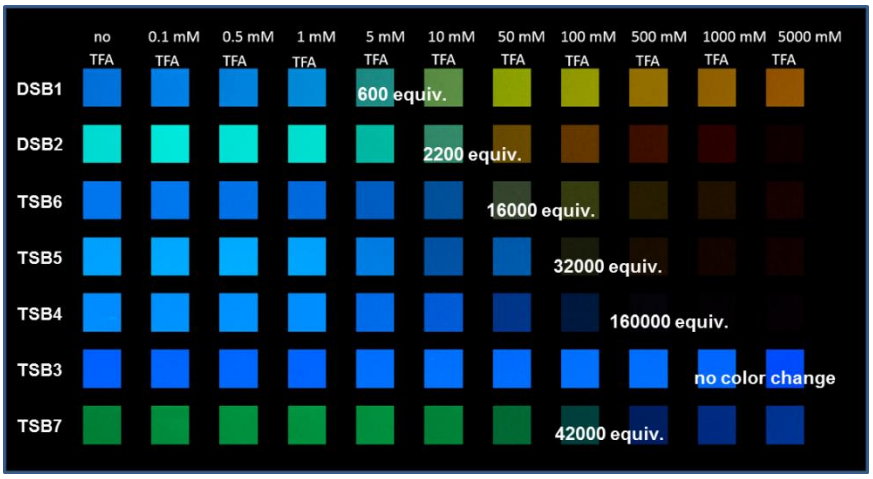

Figure 40. Photograph of SBs in THF (c = 4 µg/mL) with increasing content of TFA under a hand-held black light with illumination at 365 nm (inset data: the number of equivalents of TFA). Adapted with permission from ref.[104] © 2020 Wiley-VCH Verlag GmbH & Co. KGaA.

Figure 41 shows the normalized UV-Vis absorption and emission spectra for the TFA titrations of **TSB6** and **TSB7** in THF. **TSB6** shows a red-shifted absorption (30 nm) and a 100 nm red shift and distinct attenuation of its emission, when -log [TFA] of approx. 1.30 is reached (c = 50 mM). With excess acid (c = 500 mM, -log [TFA] < 1.0), the original absorption band of **TSB7** at around 427 nm diminished and a new distinct band formed at 338 nm. Meanwhile, a blue shift in emission of $\Delta\lambda$ = -69 nm was observed. Understanding this inherent relationship between the chemical structures and acid sensitivity would be helpful to design pH probes.

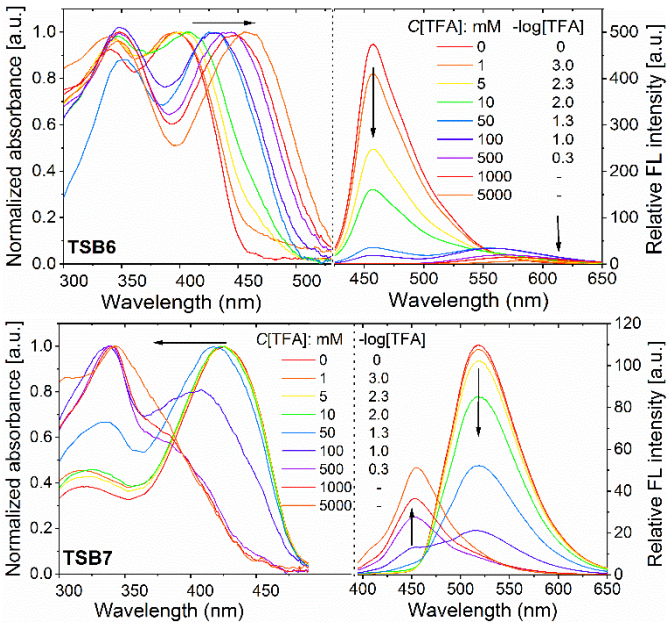

Figure 41. Normalized UV-Vis absorption (left) and emission (right) spectra for the titrations of **TSB6** (top) and **TSB7** (down) in THF with different concentration of TFA (**TSB6** and **TSB7**: 2.5 µM). Adapted with permission from ref.[104] © 2020 Wiley-VCH Verlag GmbH & Co. KGaA.

2.2.9 Optical Response to Metal Ions

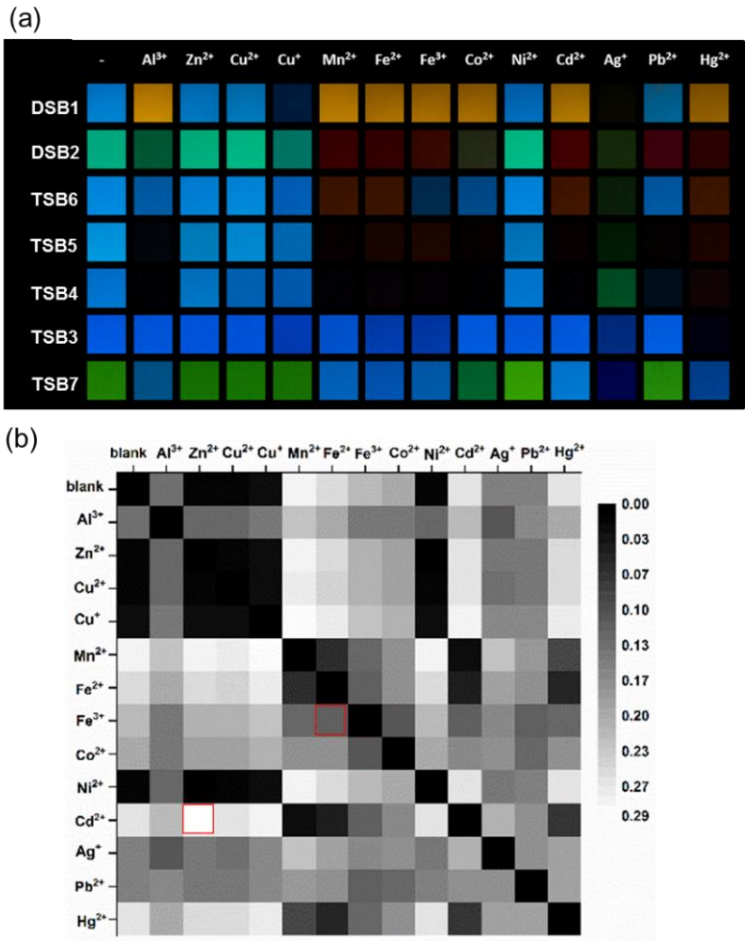

Figure 42. (a) Exposure of all the SBs (10 μM) to different metal cations in DCM. Photographs were taken under a hand-held black light (365 nm) with a digital camera; (b) Autocorrelation plot (RAW rg values) of all the SBs in DCM after exposure to metal ions. Adapted with permission from ref.[104] © 2020 Wiley-VCH Verlag GmbH & Co. KGaA.

In DCM, all the SBs were exposed to an excess of 13 cation salts, including Al^{3+}, Zn^{2+}, Cu^{2+}, Cu^{+}, Mn^{2+}, Fe^{2+}, Fe^{3+}, Co^{2+}, Ni^{2+}, Cd^{2+}, Ag^{+}, Pb^{2+} and Hg^{2+} (added as perchlorates, and CuI). Figure 42a summarizes the emission color changes resulting from these additions. For **TSB3**, only Hg^{2+} quenches its luminescence. Except for Zn^{2+}, Cu^{2+}, Ni^{2+}, the addition of the remaining ten metal ions leads to either quenching or a red shift in emission of SBs with pyridine units (**DSB1-2**and **TSB4-6**). In the case of **TSB7**, Al^{3+}, Mn^{2+}, Fe^{3+}, Fe^{2+}, Cd^{2+}, Ag^{+}, and Hg^{2+} induce a blue shift in emission, as expected for a coordination at the aniline nitrogen. Al^{3+}, Mn^{2+}, Cd^{2+} and Co^{2+} are quenchers for **TSB4** and **TSB5**, but they less impact photoluminescence of **TSB6**. Al^{3+}, Mn^{2+}, Fe^{3+}, Fe^{2+}, Cd^{2+}, Ag^{+} and Hg^{2+} can be easily distinguished from each other through the responses of the SBs by the naked eye. It is challenging to discriminate Cd^{2+} from Zn^{2+}.[122] SBs with pyridine or dibutylaniline groups display fluorescence response in the presence of Cd^{2+} but no response when reacted with Zn^{2+} (the red square). The color change observed in **TSB6** upon exposure to Fe^{2+} but not Fe^{3+} makes **TSB6** useful for the differentiation

of iron species in different oxidative states (the red square). These findings indicate that linear and star-shaped styrylbenzene derivatives are differential sensors for transition metal ions.

$$\sigma_{m,n}(r,g) = \sqrt{\frac{\sum_{SBs1}^{SBs7}(r_n - r_m)^2 + (g_n - g_m)^2}{3*7}} \qquad (3)$$

We performed statistical evaluation of differences in emission colors after exposure to metal ions. The autocorrelation plot of their response was shown in Figure 42b. The brightness independent color coordinates rg of the RAW data of the photographs were determined and treated with MANOVA statistics (eq. 3).[123] The color depth of square in matrix defines the ease of discrimination between two metal ions. The lighter the color, the easier discrimination. Because of their weak coordination, Zn^{2+}, Cu^{2+} and Ni^{+} are hard to discern, leading to similar dark color responses. However, all of the other investigated metal ions are clearly distinguished.

2.2.10 Conclusion

In summary, we have prepared linear 1,4-distyryl and star-shaped 1,3,5-tristyrylbenzene derivatives (**DSB1-2**and **TSB3-7**). These compounds are strongly fluorescent in dilute solutions, like THF. **TSB7** is able to work as polarity sensor owing to its response to different solvents. Upon protonation, all of the pyridine-containing **DSB1-2** and **TSB3-6** compounds show an obvious red shift, and the fluorophore with dibutylaniline groups **TSB7** displays a dramatic blue shift in emission. Ten metal ions such as Al^{3+}, Mn^{2+}, Fe^{3+}, Fe^{2+}, Cd^{2+}, Ag^{+} and Hg^{2+} were well discriminated by our SB-based sensor array.

Chapter 3. Phenyleneethynylene Derivatives: Synthesis, Properties and Sensing Applications

3.1 Sensor Array Based Determination of Edman Degradated Amino Acids Using Poly(*para*-phenyleneethynylene)s

In this section, an optical cross-reactive sensor array based on poly(*p*-phenyleneethynylenes) (PPEs) to facilitate the determination of Edman degradated amino acids was developed. We report a sensor array composed of three anionic PPEs (Figure 48), and their corresponding electrostatic complexes with metal ions (Fe^{2+}, Cu^{2+}, Co^{2+}). Distinct FL response patterns as "fingerprints" of this chemical tongue toward each of the standard phenylthiohydantoin (PTH) amino acids were recorded, analyzed, and converted into canonical scores by linear discrimination analysis (LDA), which permitted clear differentiation between PTH-amino acids. Importantly, this array was readily utilized for determination of PTH-amino acid residues degraded from an oligopeptide by means of Edman sequencing. The nine-element sensor array composed of three anionic PPEs and the corresponding electrostatic complex formed with metal cations can be easily used to identify and determine PTH amino acids. This method is a supplement to the chromatographic method which rely on the retain time and MS for determination. Our array has the advantage of simplicity.

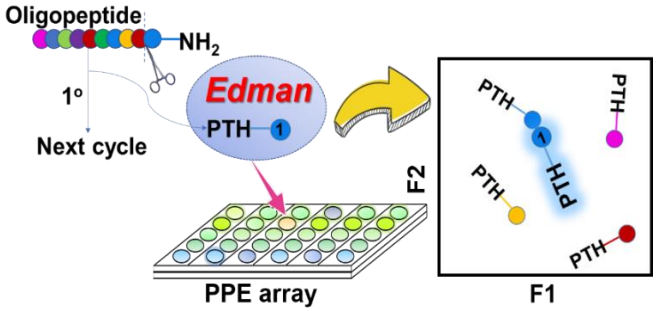

Figure 43. Schematic representation of sensor array based determination of Edman degradated amino acids using poly(*p*-phenyleneethynylene)s. Reproduced with permission from ref.[124] © 2020 Wiley-VCH Verlag GmbH & Co. KGaA.

3.1.1 Phenylthiohydantoin (PTH) Amino Acids and Their Detection

PTH-amino acids could be furnished from the twenty natural amino acids in the presence of organic base and phenyl isothiocyanate (PITC).[125] Taking PTH-S as an example, we can synthesize it by using Ser as amino acid. The route is described in Scheme 14. The structure of 20 PTH-amino acids are shown in Figure 44. They possess diverse structural characteristics.[126]

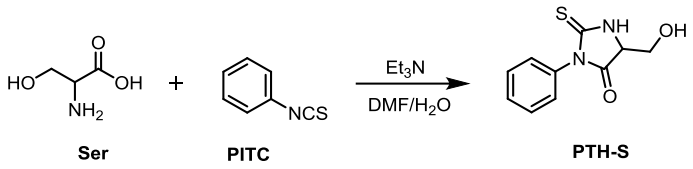

Scheme 14. The synthesis route to PTH-S.[125]

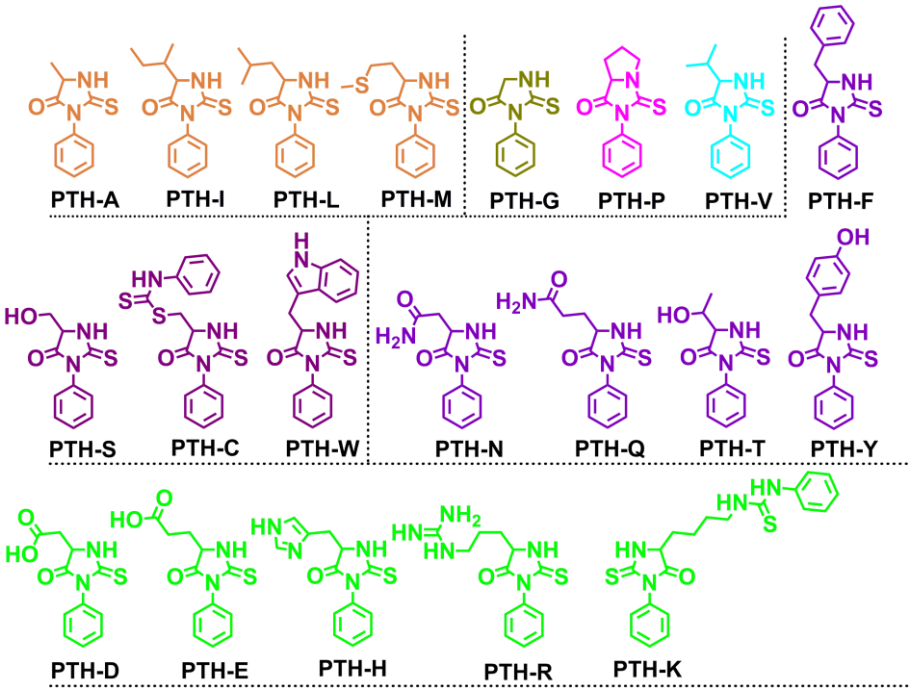

Figure 44. Structures of the investigated standard PTH-amino acids. Reproduced with permission from ref.[124] © 2020 Wiley-VCH Verlag GmbH & Co. KGaA.

Their detection and differentiation is attractive in oligopeptide or protein sequencing.[127] PTH-amino acids have been previously identified by chromatographic techniques[128] including paper chromatography, thin-layer chromatography, gas liquid chromatography, mass spectroscopy and, recently, high-performance liquid chromatography (HPLC). The identification of PTH-amino acids based on chromatographic technique depends on two factors: resolution of one PTH-amino acid from another, and coincidence of elution position of the unknown PTH-amino acid with that of a known standard.[129] This method is straightforward and helpful, but high cost instrumentation is required.[130] Compared with chromatographic technique, fluorescence-based sensing and detection have become more and more popular due to the advantages of high sensitivity, fast response, good selectivity and low

cost in instrumentation. The objectives of this study are to use a sensor array to identify PTH-amino acids standards or the prodcuts from *N*-terminal Edman degradation.

3.1.2 Array-Based Sensing and Statistical Methods

PTH-amino acids could provide excellent sensing targets for sensor arrays. Array-based sensing methods[48, 64, 131] based on organic fluorophores, nanoparticles or quantum dots[132] provide flexible options to identify different analytes or mixed samples; they show operational simplicity and usually have high sensitivity.

There are many statistical analysis methods available to process the response data. Three common methods used in sensor array are hierarchical cluster analysis (HCA), principal component analysis (PCA) and linear discriminant analysis (LDA).[80] HCA can cluster data points based on the Euclidean distance between the experimental data. It provides a straightforward tree diagram where the nearest neighbor data points are paired into a single cluster, and then paired with other nearest clusters until all points and clusters are connected to each other (Figure 45). However, it is not easy to identify unknown samples and perform accurate analysis.[133]

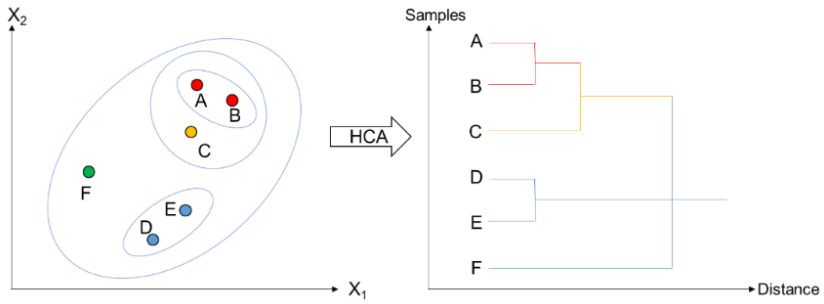

Figure 45. Graphical illustration of HCA. The data points are shown in a two-dimensional measurement space defined by the variables X_1 and X_2. Adapted with permission from ref.[133] © 2017 the Royal Society of Chemistry.

By decomposing the data into eigenvectors and eigenvalues, PCA reduces the dimensionality of a data set to two or three principal components (PCs), which contribute the most to the differentiation. The extracted and formed PCs are able to represent the data patterns and reflect the original variable information. Loading values represent the contribution of each sensor element to each PC axis. Thus, PCA is more suitable for evaluation of sensor elements.[134]

LDA is a type of linear combination, a mathematical process that applies functions to separately analyze multiple classes of items.[83] The items are projected onto a straight line so that the projection points of similar items are as close as possible and the projection points of dissimilar items are as far as possible. Simply speaking, the projection minimizes the intra-class variance and maximizes the inter-class variance (Figure 46). LDA can be used for dimensionality reduction, but also for classification. LDA has been widely employed for pattern-based identification in sensor array and predicting unknown samples by comparing the distance between categories.

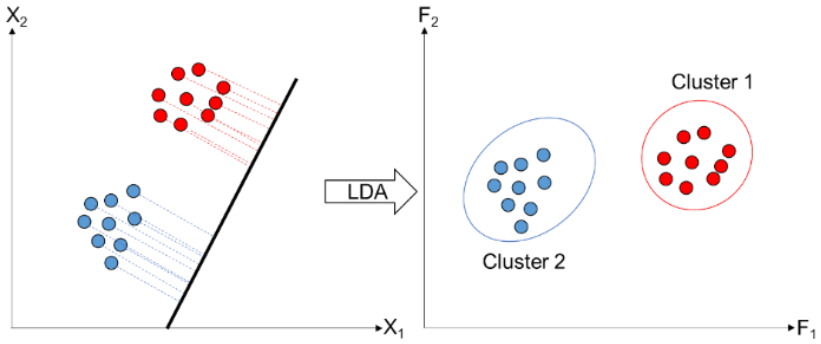

Figure 46. Graphical illustration of LDA. The data points are shown in a two-dimensional measurement space defined by the variables X_1 and X_2.

3.1.3 Array Construction

Our group is interested in water-soluble conjugated poly(p-phenyleneethynylene)s (PPEs), which can serve as responsive elements for small sensor arrays to discriminate wines,[79, 85, 135] explosives,[136] bacteria,[137] teas[84] and other analytes.[138] To the best of knowledge, there is no report about identification of PTH-amino acids based on sensor array. Here, we studied PPE alone and used transition metal cations as adjuvants to distinguish 20 different PTH-amino acids – the product of the Edman degradation of proteins/peptides. (Figure 47).

Figure 47. Schematic representation of the sensor array using PPEs. (a) An array involving PPEs and metal cations was constructed to identify PTH-amino acid standards. (b) *N*-terminal Edman degradation. (c) Determination of the amino acids from Edman degradation using an array. Reproduced with permission from ref.[124] © 2020 Wiley-VCH Verlag GmbH & Co. KGaA.

Our methodology consists of two steps. In the first step, we bulid a sensor array to study PTH-amino acid standards and optimize the discrimination (Figure 47a). The second step is degrading an oligopeptide by *N*-terminal Edman sequencing chemistry and identifying the Edman degradated amino acids on the basis of our established array (Figure 47b, c).

In the beginning, we selected seven PPEs including negatively charged **PPE3,5,6**; positively charged **PPE4,7** and neutral **PPE8,9** as potential sensing elements (Figure 48). **P2**, **P5** and **P6** (2 μM) were treated with 12 randomly chosen PTH-amino acids (1 mg/mL) in four different solvents, including DMSO, DMSO/MeOH (1:1), DMSO/acetone (1:1), DMSO/H_2O (1:1). We found the PPE with negative charges **PPE5** showed the most obvious response to PTH-amino acids in DMSO/H_2O (1:1), followed by neutral **PPE9** and positively charged **PPE4** (Figure 49). After this cursory evaluation, we tried to employ the negatively charged (**PPE3,5,6**) and neutral polymers **(PPE8,9)** in DMSO/H_2O (1:1) for the discrimination experiments. However, most of the amino acids are tightly bound in the LDA graph.

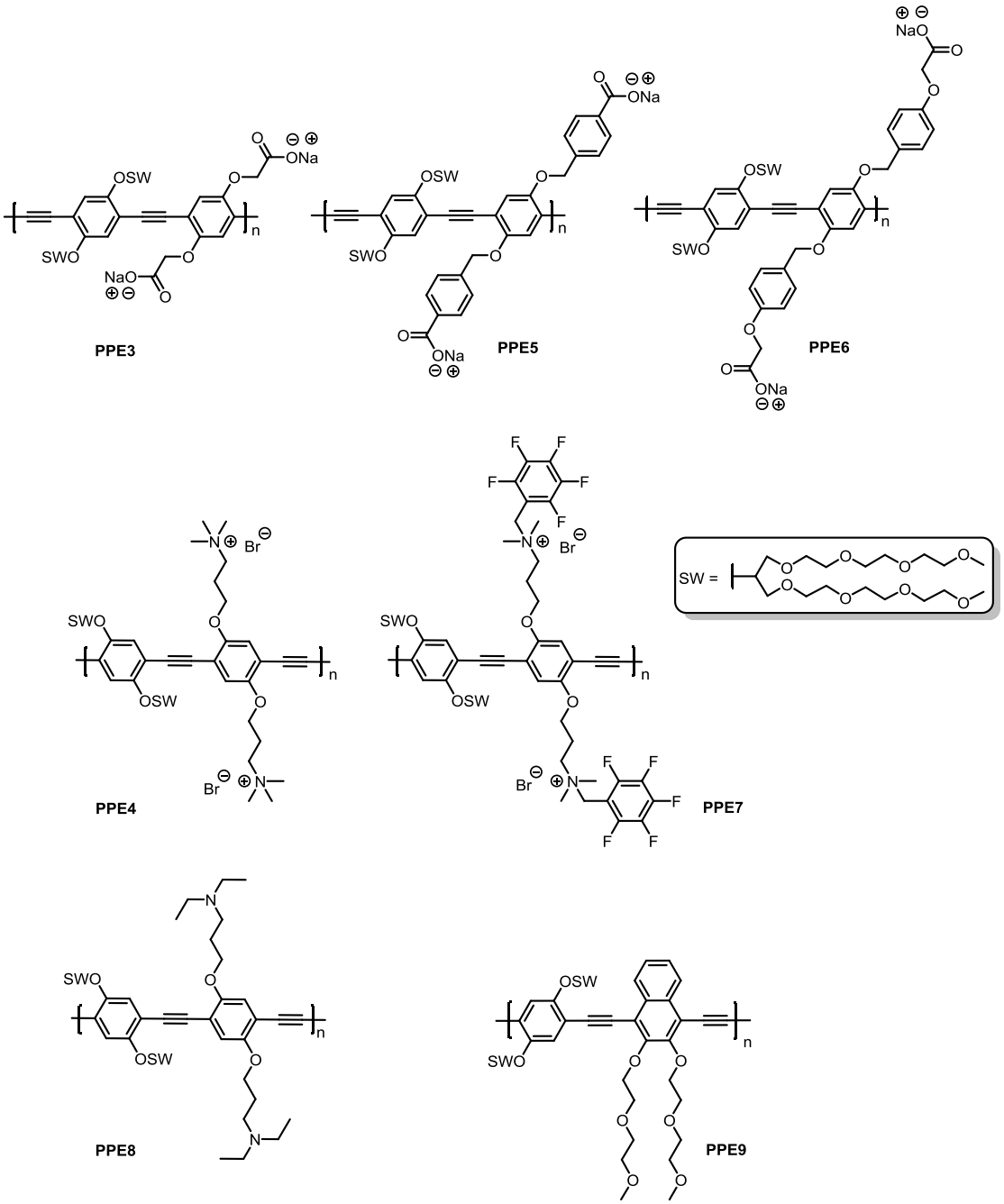

Figure 48. Chemical structures of the investigated poly(*p*-phenyleneethynylene)s.

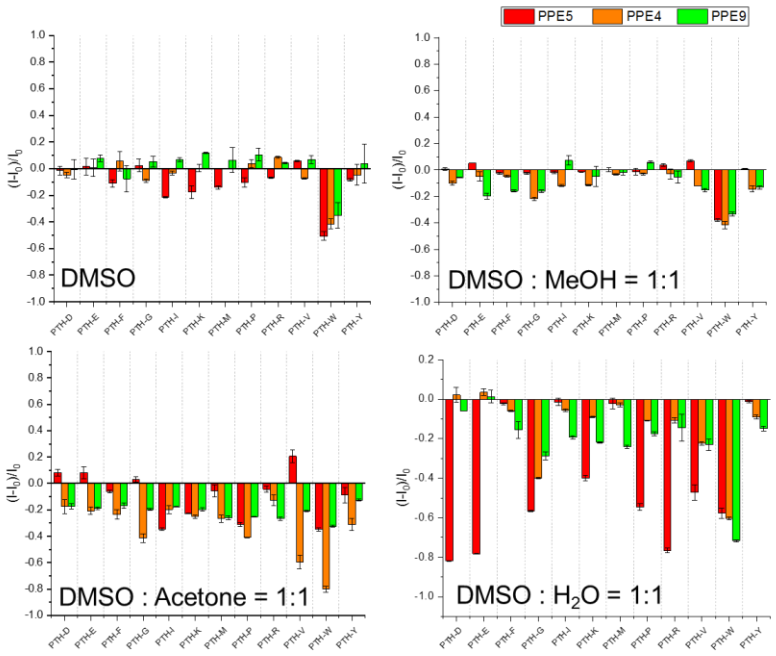

Figure 49. Fluorescence response generated by **PPE4**, **PPE5** and **PPE9** (2 μM) with 12 randomly chosen PTH-amino acids (1 mg/mL) in four different solvents, including DMSO, DMSO/MeOH (1:1), DMSO/acetone (1:1), DMSO/H_2O (1:1). Adapted with permission from ref.[124] © 2020 Wiley-VCH Verlag GmbH & Co. KGaA.

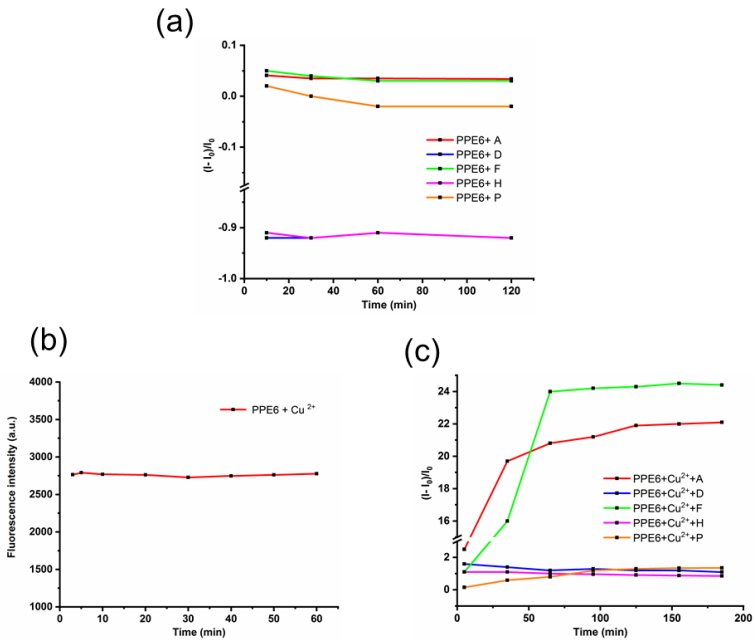

Figure 50. Interaction time study of among **PPE6** (2 μM), PTH-amino acids (1 mg/mL) and Cu^{2+} (10 μM). 'PTH' was omitted for clarity. Adapted with permission from ref.[124] © 2020 Wiley-VCH Verlag GmbH & Co. KGaA.

To construct a useful fluorescent sensor array, we studied the fluoresence response of negatively charged **PPE3, 5, 6** towards PTH-amino acids in the presence of metal cations (Fe^{2+}, Cu^{2+}, Co^{2+}). **PPE3, 5, 6** were mixed with metal cations first and after addtion of analytes, different levels of quenching as well as fluorescence turn-on were observed. In this study, we choosed about 10 μM Fe^{2+}, 10 μM Cu^{2+} and 1 mM Co^{2+} as adjuvants to obtain diverse response. As shown in Figure 50, the interaction of **PPE6** with

PTH-amino acid or metal ions was nearly completed within 20 min at ambient temperature, while the **PPE6**-Cu^{2+} complex showed slower response, achieving a plateau within 2 h. Therefore, the sample with incubation 2 h at ambient temperature was finally chosen for further sensing experiments.

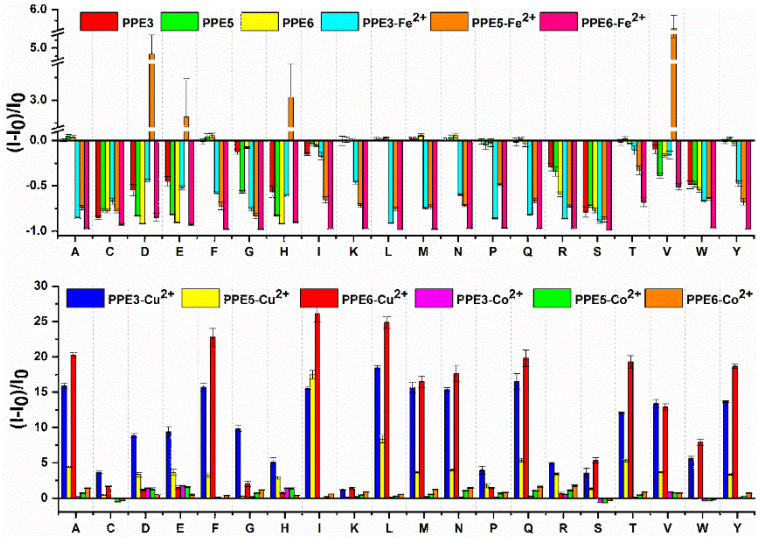

Figure 51. Fluorescence response pattern ($(I - I_0)/I_0$) obtained by **PPE3, 5, 6** (2 μM) and their metal-complexes (Fe^{2+}, Cu^{2+}: 10 μM; Co^{2+}: 1 mM) treated with PTH-amino acids (1 mg/mL) in DMSO/H_2O (1:1) after incubation for 2 h at room temperature. Each value is the average of five independent measurements and each error bar shows the standard error of these measurements. 'PTH' was omitted for clarity. Adapted with permission from ref.[124] © 2020 Wiley-VCH Verlag GmbH & Co. KGaA.

The response patterns of the twelve elements sensor array was shown in Figure 51. Three negatively charged fluorescent **PPE3, 5, 6** themselves or their complexes with metal cations have diverse binding interaction for a specific analyte, thus generating unique FL response for discrimination. Five measurements were performed with 20 analytes to provide a training matrix of 12 sensing elements × 20 PTH-amino acids × 5 replicates. With this twelve-element tongue in hand, we processed the resulting training data through PCA first and then LDA.

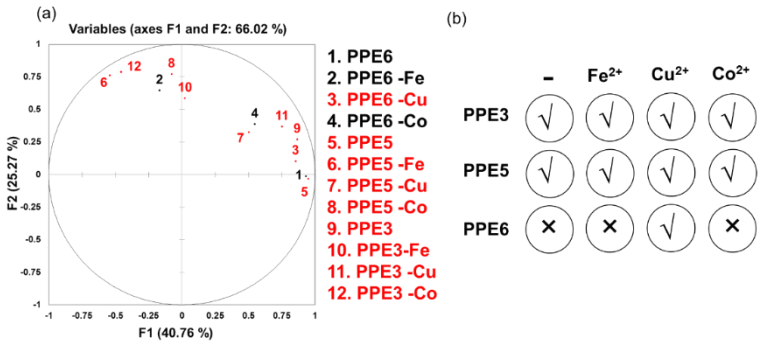

Figure 52. Loading plot of the principal component analysis, identifying the contribution of each element to an axis. The finally selected nine elements are labeled in red (a); systematic screening of the successful array elements for sensing (b). Adapted with permission from ref.[124] © 2020 Wiley-VCH Verlag GmbH & Co. KGaA.

We performed a screening process employing principal component analysis (PCA) to find the final nine elements that contribute most to the discrimination and then an optimized nine-element tongue was obtained. The chosen elements were marked in red, as shown in Figure 52.

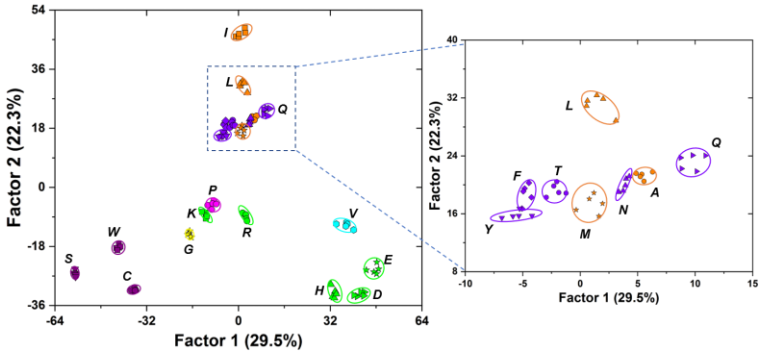

Figure 53. 2-D canonical score plot for the first two factors of fluorescence response patterns obtained by a nine-element sensor array with 95% confidence ellipses. 'PTH' was omitted for clarity. Reproduced with permission from ref.[124] © 2020 Wiley-VCH Verlag GmbH & Co. KGaA.

The linear discriminant analysis (LDA) plot of all of the investigated PTH-amino acids based on the nine elements was shown in Figure 53. The jackknifed classification matrix with cross validation reveals 100% accuracy. In addition, the PTH-amino acid with identical molecular weight and similar structure, PTH-I and PTH-L (248 Da), can be separated easily. Clearly, the 20 PTH-amino acids were-separated into twenty clusters with excellent spatial resolution, demonstrating that the simple nine-element sensory array was adequate to accurately identify all of PTH-amino acids. A well-clustered three-dimensional plot visualized from these unique patterns is shown in Figure 54.

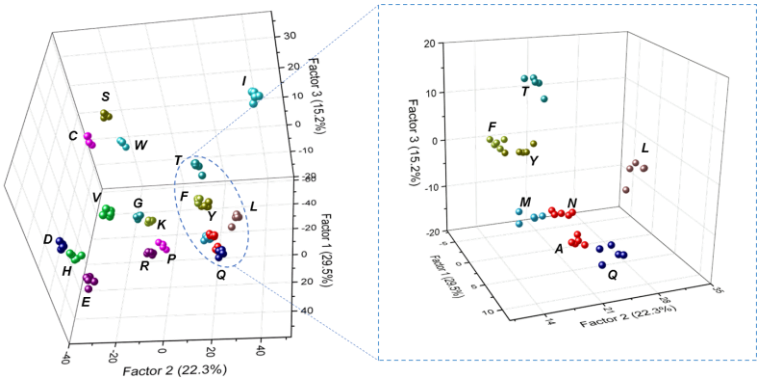

Figure 54. 3D canonical score plot for the first three factors of fluorescence response patterns obtained by a nine-element sensor array. Each point represents the response pattern for a single PTH-amino acid in the array. 'PTH' was omitted for clarity.

To further prove the efficiency of the optimized sensing system, we tested 60 samples of PTH-amino acids controlled at the same concentration (1 mg/mL) but with unknown identity, which were randomly chosen from the 20 kinds of amino acids mentioned above. The new cases were classified into different groups, generated from the training matrix, based on the shortest Mahalanobis distance to the respective group.[139] 53 of 60 unknown PTH-amino acids were identified, which represented an accuracy of 88%. These results indicated that this as-prepared sensor array is effective in discriminating the PTH-amino acids.

In view of the discrimination mechanism, the construction of the sensor array in our first step is based on the two ways of interaction, as demonstrated in Figure 55. One mechanism is based on a direct interaction, between the negatively charged **PPE3,5,6** and the PTH-amino acids. The direct interaction could result in minor changes or decrease of fluorescence intensity, due to the π–π stacking or the hydrophobic interactions between the PPEs and quenchers.[138, 140] The other is based on a competitive interaction among the polymers, the analytes and metal cations. It has been reported that metal ions are not only excellent fluorescence quenchers, but also display strong affinity over a wide range of biomolecules with chelating groups like -C=O and -NH.[141] The addition of Fe^{2+}, Cu^{2+} or Co^{2+} results in a decrease in fluorescence intensity of **PPE3,5,6** (Experimental Section), probably because of the formation of electrostatic complexes or coordination of metal ions to the branched oligoethylene glycol moieties on PPEs.[142] Upon the addition of PTH-amino acids, metal ions could interact with them, which will release PPEs and reduce the amounts of free analytes in solution, thus forming a competitive interaction among metal ions, PPEs and PTH-amino acids.[143] As expected, fluorescence turn-on was observed. PTH-amino acids were also able to bind the PPE-metal complexe to form ternary complexes, leading to additional quenching (Experimental Section). Disruption of the metal-PPE complexes can greatly enhance the discrimination ability of sensor array.

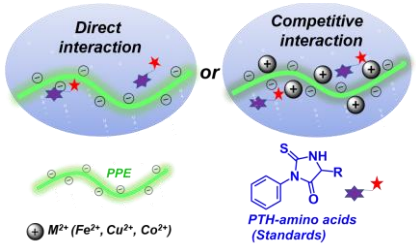

Figure 55. Schematic illustration of two ways of interaction in constructing a sensor array. Reproduced with permission from ref.[124] © 2020 Wiley-VCH Verlag GmbH & Co. KGaA.

3.1.4 Edman Degradation and Residue Identification

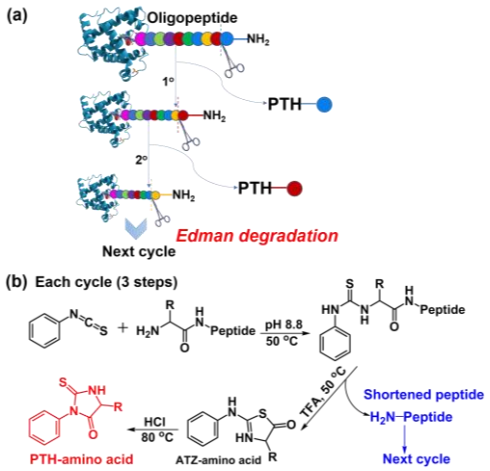

Figure 56. (a) *N*-terminal Edman sequencing chemistry and (b) detailed procedure for each cycle. Reproduced with permission from ref.[124] © 2020 Wiley-VCH Verlag GmbH & Co. KGaA.

Edman sequencing chemistry is a standard method for peptide sequencing,[127] which could be divided into three steps, as illustrated in Figure 56. The detailed procedure was shown in experimental section. It is a cyclic procedure where the *N*-terminal amino acid is cleaved off and identified and so forth. The final PTH-amino acids were generated by three continuous reaction steps of coupling, cleavage and transformation during Edman degradation (Figure 56b).

To explore the potential application of our established sensor array, Edman degradation was evaluated on a short model peptide, NH_2-Met-Ala-Ser-OH (Figure 57a). Due to the limit of manual degradation, we performed two cycles of degradation using the three-stage modified Edman procedure, with a yield of 80% and 62%, respectively. We compared the array response to each degradation residues (1 mg/mL) with the classification data from the optimized nine-element sensor array. It was found that the two residues were identified according to their placement in 2D-LDA plot in Figure 57b. The residue from the first cycle **C1** ends up in the PTH-M zone, while residue **C2** from cycle 2º was close to PTH-A, as expected from the oligopeptide structure, which indicated the potential applicability of this sensor array for discrimination of Edman degradated amino acids.

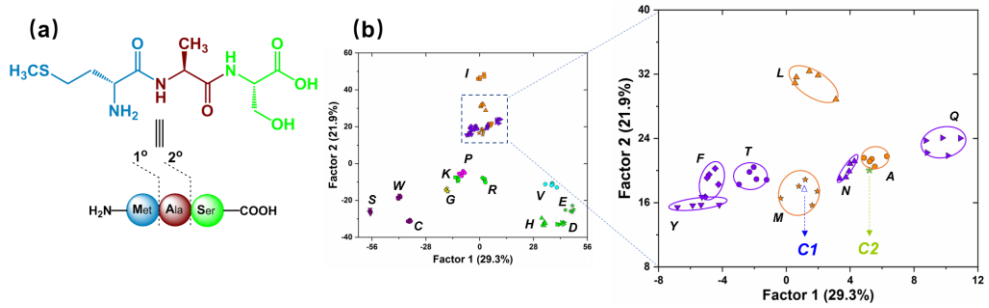

Figure 57. (a) The oligopeptide used for degradation. (b) Degradation residues (**C1** and **C2**, the average of three measurements) were clustered with the established reference PTH-amino acids via LDA. 'PTH' was omitted for clarity. Reproduced with permission from ref.[124] © 2020 Wiley-VCH Verlag GmbH & Co. KGaA.

GC-MS analyses were also conducted to understand the chemical composition of the degradation residues according to their retention times (Figure 58) and molecule weights and corresponding identification results were listed in Table 4. Although specialized GC-MS approach could also identify the degradation residues correctly, its high cost and inflexibility for use make it much more inconvenient in comparison with the sensor array. Our methodology based on the sensor array could provide an complementary way to determinate the Edman degradated amino acids.

Table 4. Degradation residues identification by GC-MS analysis.

Cycle	Degradation residue	Yield	Retention time (min)	m/z	Identified by GC-MS	Amino acid
1º	C1	80%	15.03	266	PTH-M	Met
2º	C2	62%	12.50	206	PTH-A	Ala

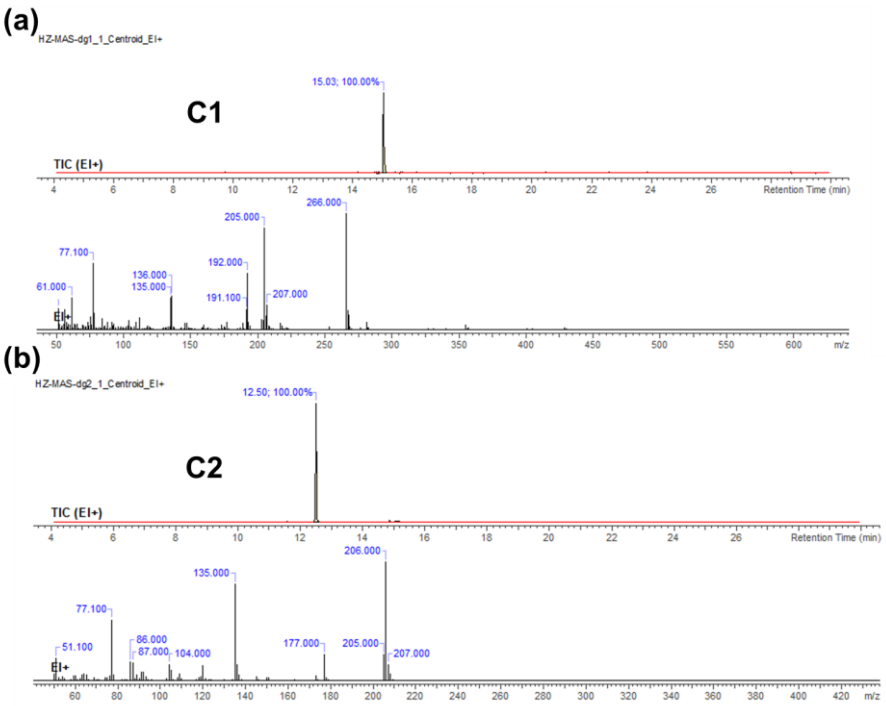

Figure 58. GC-MS spectrum of degradation residues generated from the two cycles. Reproduced with permission from ref.[124] © 2020 Wiley-VCH Verlag GmbH & Co. KGaA.

3.1.5 Conclusion

In conclusion, we have developed a simple nine-element sensor array by three anionic PPEs, together with the corresponding metal-complexes for the identification of twenty different PTH-amino acids and successfully applied this proposed array to determination of Edman degradated amino acids. With the benefit from the simple nine sensing elements and instrumentation, this effective and precise sensor array may provide a potential and powerful tool to determinate the primary structure of oligopeptide and proteins after Edman degradation.

3.2 Guanidine-Substituted Phenyleneethynylene Trimers: Synthesis and Photophysical Properties

In this part, a family of phenyleneethynylene (PE) trimers bearing *N*-Boc-protected guanidine side groups were designed based on a step-by-step molecule tailoring strategy and synthesized by the post-functionalization from the corresponding deprotected amine trimers. The Boc deprotection behaviour of guanidine trimers under regular condition (DCM/TFA) was investigated and compared. It was found that the removal of the Boc group is critically dependant upon the chemical nature of the linker. We unveil a general design principle toward guanidinylated PEs. This study demonstrates how to control the structure to yield the desired PE guanidium salts and thus serves as a guideline for further rationally design of guanidine-based PEs with increased length.

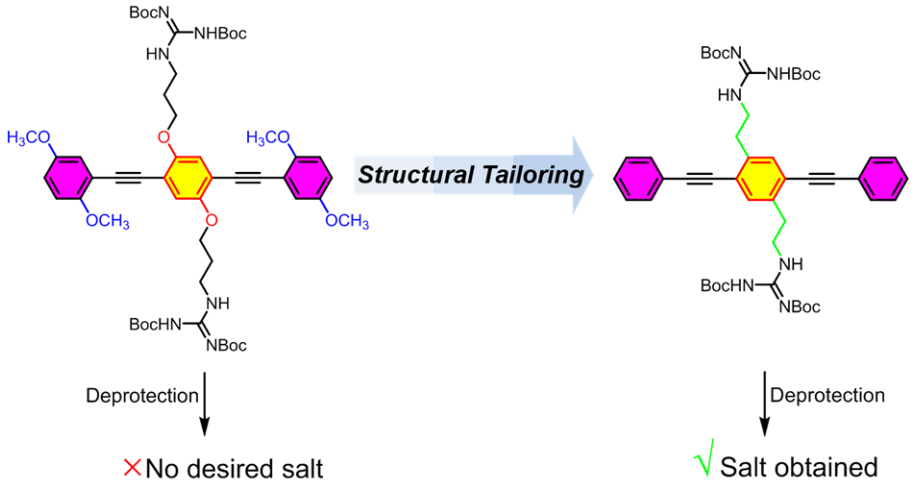

Figure 59. Schematic representation of guanidine-substituted phenyleneethynylene trimers: synthesis and photophysical properties.

3.2.1 Guanidine Derivatives

Guanidine is classified as a strong organobase with pKa value of conjugated acid being around 13. Its strong basicity results from the construction of highly effective conjugation system after protonation. As shown in Scheme 15, it is resonance through three canonical forms, also called Y aromaticity.[144] The change of substituent on nitrogen atoms can affect the basicity. Attaching electron-donating groups such as alkyls or heteroalkyls leads to an increase in basicity.[145] While if electron-withdrawing groups such as NO_2, CN, acyl or sulfonyl are introduced, the pKa values decrease.

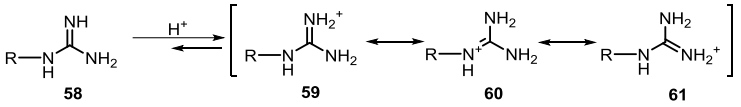

Scheme 15. Conjugation of guanidinium ions.[144]

Owing to the nucleophilicity,[146] the guanidine core was always protected. The *tert*-butyloxycarbonyl (Boc) group is a preferential amino protecting group in organic synthesis since its removal is easy, clean and practical when exposed in excess of organic acids such as TFA.[147] The guanidine derivatives are an important class of *N*-containing compounds, which could be utilized as building blocks for the construction of natural products, pharmaceuticals, agrochemicals, sensors and catalysts.[148] Due to its unique structure and hydrophilicity,[149] the guanidinium ion can bind anions in aqueous solution such as carboxylates, phosphates, sulfates and nitrates. This is achieved by strong non-covalent interactions, such as hydrogen bonding and charge pairing. For example, Shinkai and coworkers reported an AIE-based guanidinium bioprobe **62** in 2012.[150] This probe **62** realized selective detection of ATP through the cooperative self-assembly. It showed sensitive, nonlinear fluorescence response and high signal-to-background ratio.

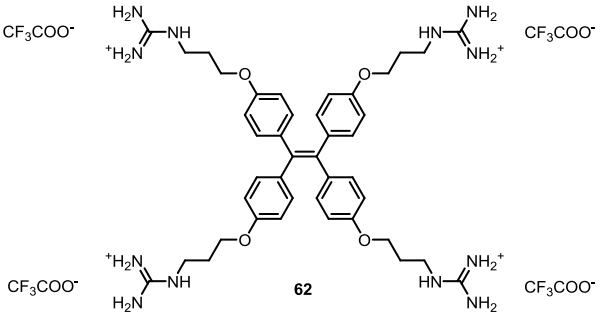

Figure 60. Structure of guanidinium-tethered tetraphenylethene (TPE) for ATP detection.[150]

3.2.2 Phenyleneethynylene Derivatives with Guanidinium Side Groups

Conjugated poly(*para*-phenyleneethynylene)s (PPEs) are sensitive to minor conformational or environmental changes due to the aromatic π-electrons delocalized in rigid hydrophobic backbones.[151] Previously, we successfully used ionic PPEs as sensing elements to construct sensor arrays to discriminate a series of analytes.[79, 85, 124, 135, 137] In view of the importance of guanidine and continuation

of our effort with ion-type PPEs, we decided to employ guanidine as terminal recognition group to construct novel conjugated PE-based sensors.

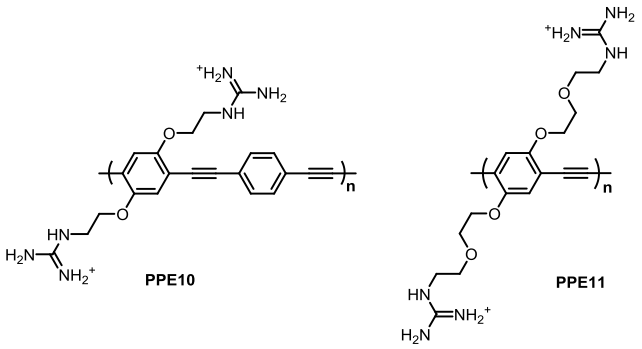

Figure 61. The structure of reported guanidinium-type PPE in literature.[166]

Currently, several kinds of PEs with guanidinium side groups have been reported (Figure 61).[166] The common construction procedure includes the synthesis of *N*-Boc-protected guanidine PEs and subsequent removal of the Boc group by TFA. However, a close look at the published analytical data is inconclusive with respect to the formation of guanidine-substituted PPEs. Two issues remain in the synthesis and unfortunately, they are often ignored. One is the Sonogashira-coupling of Boc-protected monomers into PPEs in the presence of DIPA or other secondary amines. While aminolysis of the Boc group results in an urea, especially under heating condition.[152] On the other hand, for most published examples proton NMR spectra were either not reported, or spectra were displayed with signals in the aromatic area, broadened to the extent that,[153] often rendering them unuseful as to decide if free guanidine-units are present. Thus, the deprotection of *N*-Boc-protected guanidine PEs and characterization of guanidium salts remain a challenge. Overcoming these issues requires a judicious design strategy of molecular structures, along with consideration of two indispensable factors in deprotection: the complete disappearance of Boc signal and the formation of clear aromatic area in NMR spectra.

Since small molecules are composed of defined structures and easy to characterize, we hypothesized that a stepwise modification of PE structure may address this problem elegantly and make it easy to obtain desired guanidium salts effectively. Herein, we use phenyleneethynylene trimers as test bed to find linkers that connect the guanidine to the aromatic core and that do not interfere with the deprotection protocol.

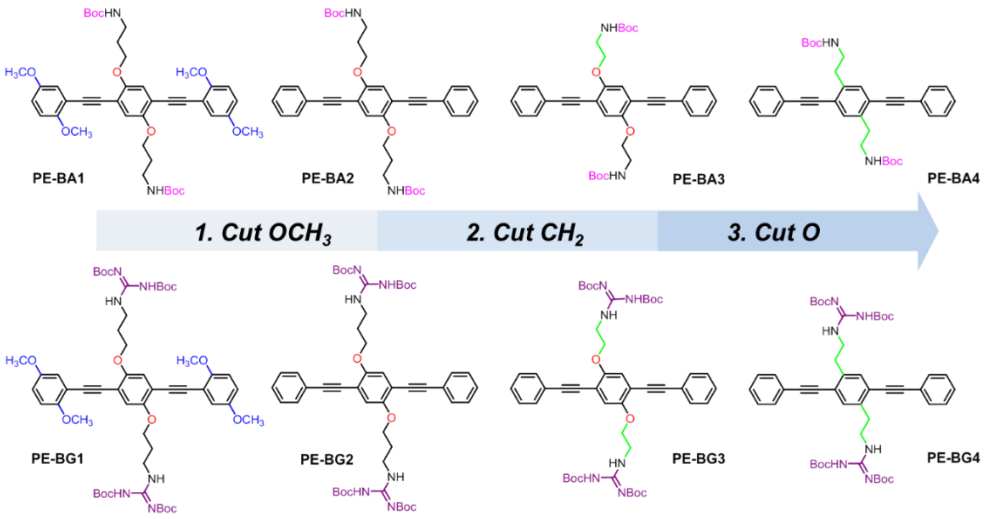

Figure 62. Structures of the *N*-Boc-protected amines (top) and guanidines (bottom) PEs explored in this study and the step-by-step structural tailoring strategy to address the deprotection defects. (1) Cutting off the OCH_3 group in backbone; (2) Shortening the side chain by removing the CH_2 group; (3) Cutting off the O atom in the side chain.

As shown in Figure 62, these PEs consist of identical backbone with three phenyl rings, in which different substituents and side chains were attached. This strategy would involve the modification of the backbone by removing OCH_3 group, and then the simplification of the side chains by removing the CH_2 group or the O atom.

3.2.3 Synthesis of Phenyleneethynylene Trimers

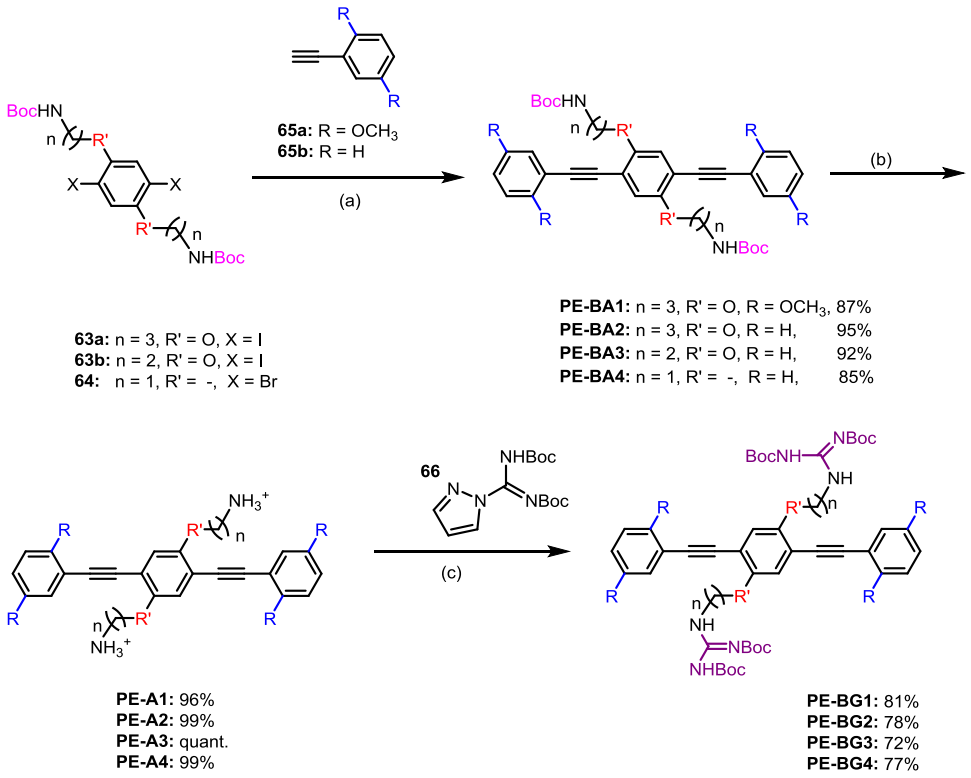

Scheme 16. Synthesis of *N*-Boc-protected amine/guanidine **PE-BA1-4** and **PE-BG1-4**. (a) $Pd(PPh_3)_2Cl_2$, CuI, THF/DIPA (3:2, v/v), 60 °C; (b) DCM/TFA (1:1, v/v), RT; (c) Et_3N, DCM, RT.

Scheme 16 displays the straightforward synthesis of the protected precursors **PE-BG1-4**. The synthesis for all PEs with *N*-Boc-protected guanidine group (**PE-BAs** and **PE-BGs**) is based on the same strategy. The coupling of **63a**,**b** or **64** with **65a**,**b** was performed under standard Sonogashira condition and gave **PE-BA1-4** in high isolated yields (85%-95%). Deprotection with TFA smoothly furnishes the ammonium salts **PE-A1-4**, which were rapidly transformed into *N*-Boc-protected **PE-BG1-4** using an activated and protected guanidine derivative. The subsequent hydrolysis of **PE-BGs** gave the guanidium salts (vide infra). It is worth to mention that no tedious column chromatography was needed for the ammonium/guanidinium salts purification.

3.2.4 Optical Properties of *N*-Boc-protected PEs

The optical and emissive properties of **PE-BA** and **PE-BG** are almost indistinguishable and only dependent upon the substituent pattern of the bisphenylethynylbenzene (Table 5and Figure 63). Due to the good molecular conjugation, **PE-BA1** exhibits longer-wavelength absorption and emission peaks at 378 and 413 nm, respectively, followed by **PE-BA2**, **PE-BA3** and **PE-BA4**. Well-resolved emissions were observed for **PE-BA1** and **PE-BA4**. The attachment of the protected guanidine group does not influence the optical properties. **PE-BAs** and **PE-BGs** show a strong blue emission in DCM and the quantum yields are very high, ranging from 75% to 89%, probably due to the stiff backbone and a low tendency of self-aggregation. The lifetimes of PE series **1-3** (1.28-1.35 ns) are much longer than that of PE series **4** (0.72-0.81 ns).

Table 5. Photophysical properties (in DCM) of all *N*-Boc-protected PEs.

Compounds	λ_{max} [nm][a]	λ_{em} [nm]	$\Delta\upsilon_{st}$ [cm^{-1}][b]	QY[%][c]	τ_f [ns]
PE-BA1	378	413	224	86±1	1.34
PE-BA2	363	399	249	87±1	1.35
PE-BA3	358	397	274	87±2	1.28
PE-BA4	327	355, 374	241	75±3	0.81
PE-BG1	375	410	228	76±3	1.27
PE-BG2	360	399	272	89±1	1.35
PE-BG3	361	395	238	87±1	1.28
PE-BG4	328	355, 374	232	79±2	0.72
PE-BU1	375	410	228	70±2	1.33
PE-BU2	363	400	255	83±1	1.38

[a] Absorption maximum at the longest wavelength. [b] Stokes shift. [c] Fluorescence quantum yield.

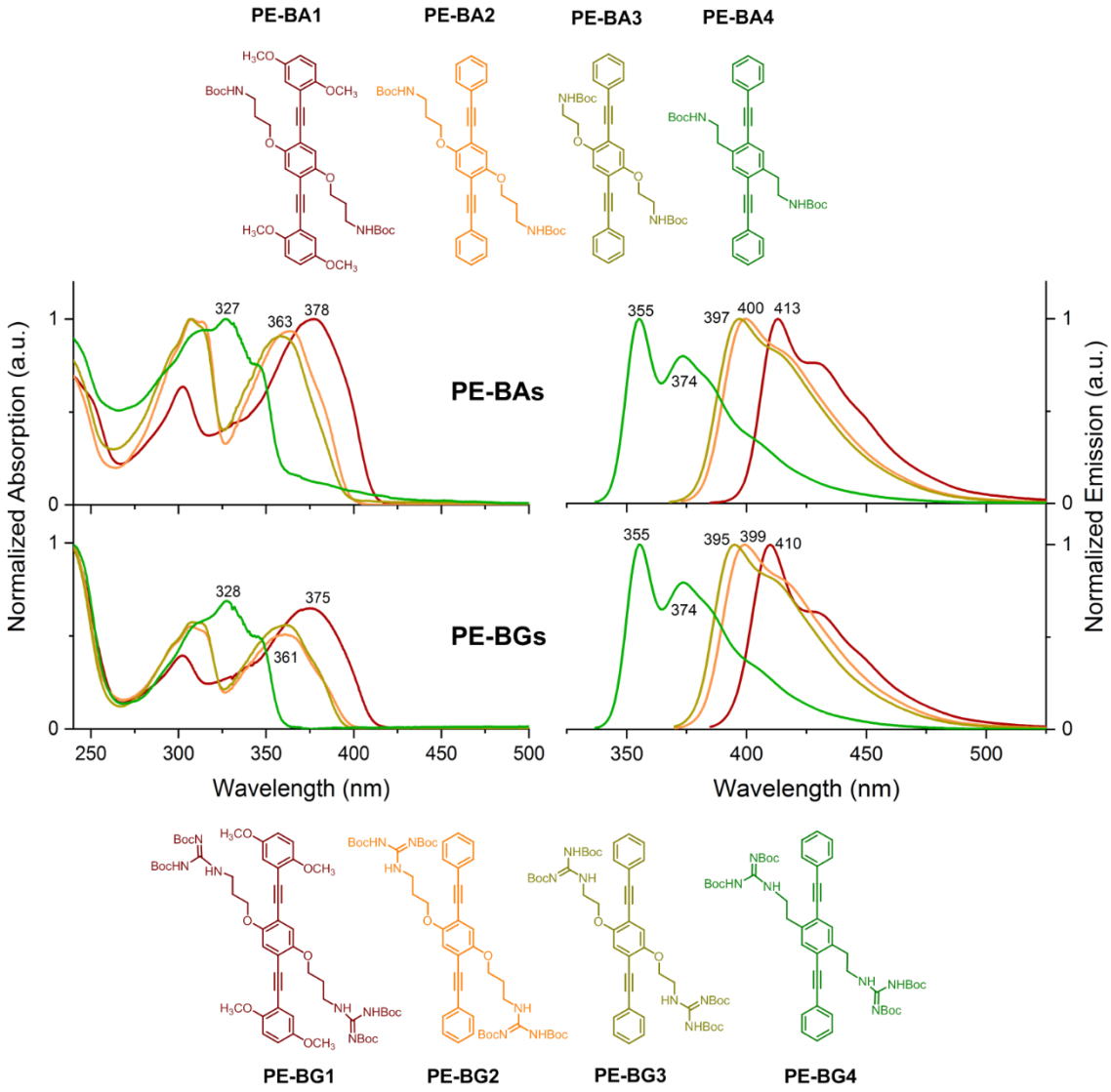

Figure 63. UV-Vis absorption (left) and emission spectra (right) of all *N*-Boc-protected PEs measured in DCM.

3.2.5 Synthesis and Optical Spectra of *Mono*-Boc-protected Amidinoureas

Similarly, **63a** was deprotected with TFA, yielding the salt **67**, which was used to furnish the Boc-protected guanidine monomer **68**. Initially, we attempted the synthesis of *bis*-Boc-protected guanidines **PE-BG1-2** by Sonogashira cross-coupling reaction of **68** and **65a,b** (Scheme 17). Unfortunately, the presence of DIPA leads to an aminolysis of the Boc groups during the coupling and finally mono-Boc-protected **PE-BU1-2** were isolated.

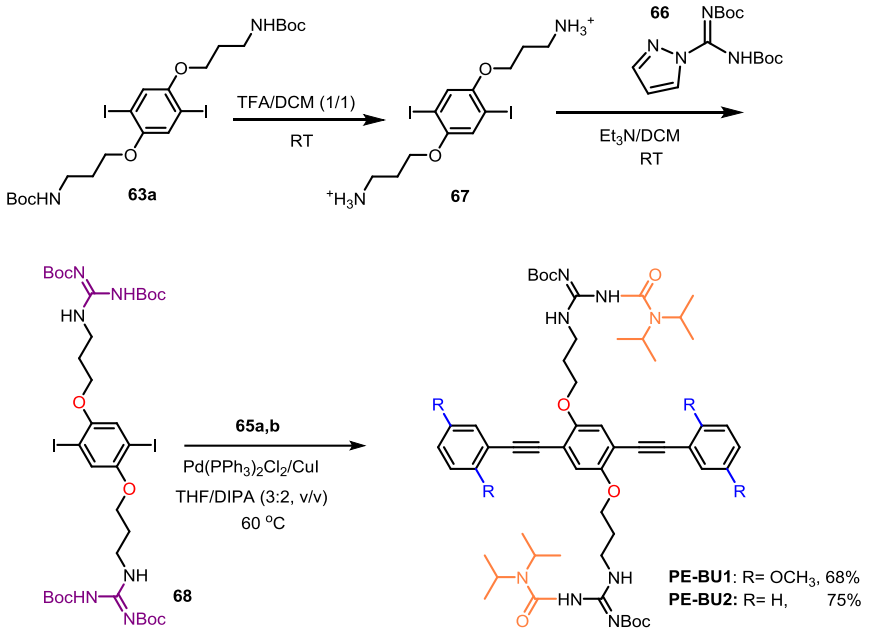

Scheme 17. Synthesis of **PE-BU1-2**.

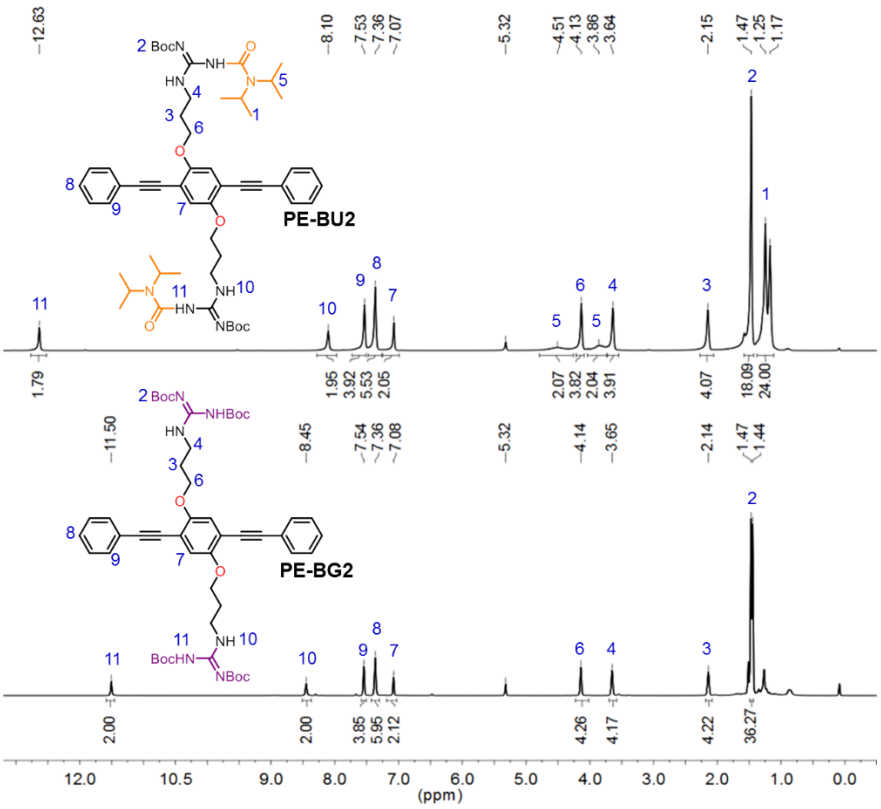

Figure 64. ^{1}H NMR spectra of **PE-BU2** and **PE-BG2** (in CD_2Cl_2). Peak assignment according to those of the molecular structures inside.

The obtained ^{1}H NMR provides more detailed structural information (Figure 64). From comparison of ^{1}H NMR features of **BU2** with **BG2**, we can conclude that a pronounced difference between **BU2** and **BG2** results from the protons in the Boc group. In **BG2**, the protons with close chemical shift values (1.47/1.44 ppm) can be properly assigned to the CH_3 of Boc, whereas, in **BU2**, only the peak at 1.47

ppm can be clearly assigned to the CH_3 of Boc and the split peaks at 1.25/1.17 ppm result from CH_3 of $N(CH(CH_3)_2)_2$ residues. Meanwhile, the NH in guanidine has an obvious chemical shift, from 12.63 ppm (**BU2**) to 11.50 ppm (**BG2**). The formation of **BU2** (m/z = 962.57) and **BG2** (m/z = 908.47) is supported by ESI mass spectra. This phenomenon is in accordance with the previous founding by Rault et al.[152, 154]

A literature search reveals that PPEs were prepared with bis-Boc-protected guanidines as monomers in a Sonogashira reaction using secondary amines at elevated temperature.[153a, c, 155] We suspect that aminolysis occurred. Sonogashira coupling of **68** with **65** in Hünig base or Et_3N unfortunately was unsuccessful in our hands and we could not isolate any defined products. Therefore, the easy but valuable amine-PEs were generated for further post-functionalization. In DCM, mono-Boc-protected **PE-BU1** presents a pronounced red shift of absorption and emission compared to **PE-BU2** (Figure 65).

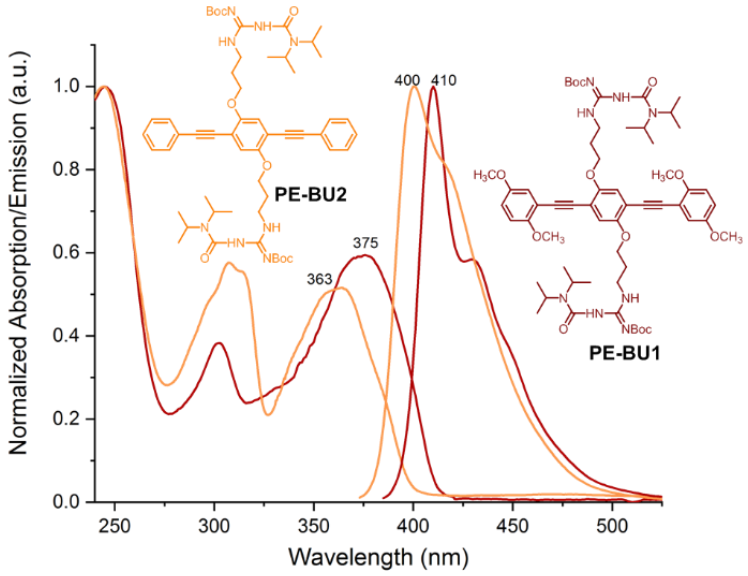

Figure 65. UV-Vis absorption and emission spectra of **PE-BU1-2** measured in DCM.

3.2.6 Deprotection of *N*-Boc-protected Amine/Guanidine PEs

The deprotection of **PE-BA1-4** and of **63a** using TFA worked very fast at room temperature and was finished after 3 min under formation of corresponding ammonium salts **PE-A1-4** and **67**. However when the deprotection was run for 3 h (Figure 66) decomposition of the products were observed for **PE-A1-3**, but not for **67** – suggesting that the PE-module is not indefinitely stable towards TFA.

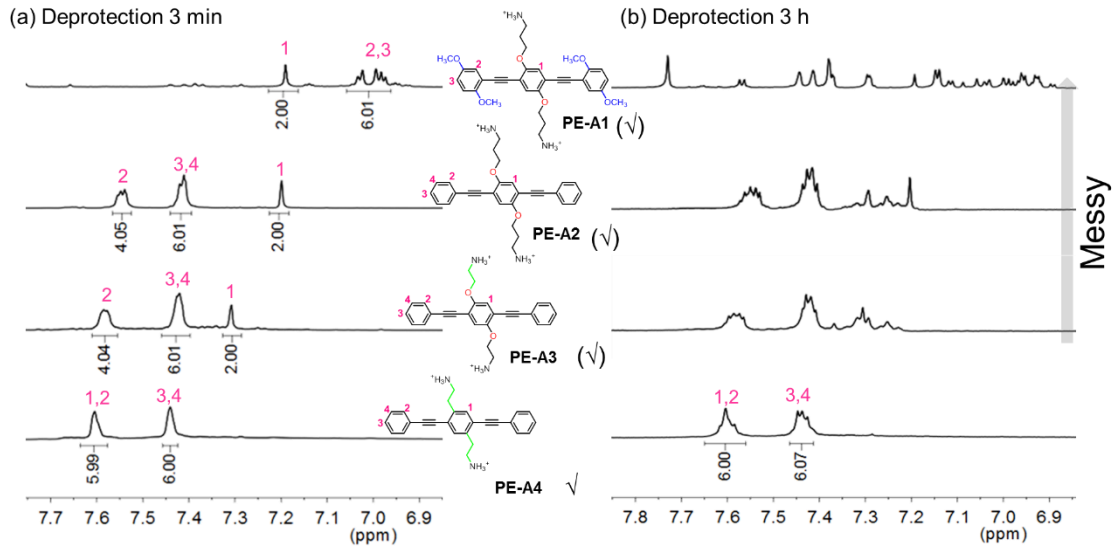

Figure 66. ^{1}H NMR spectra (in CD_3OD) of ammonium salts when the corresponding *N*-Boc-protected PEs were deprotected in DCM/TFA (1/1) at different time (a: 3 min, b: 3 h; Depicted are only the aromatic regions). Peak assignment according to those of the molecular structures inside. No assignment for messy spectra.

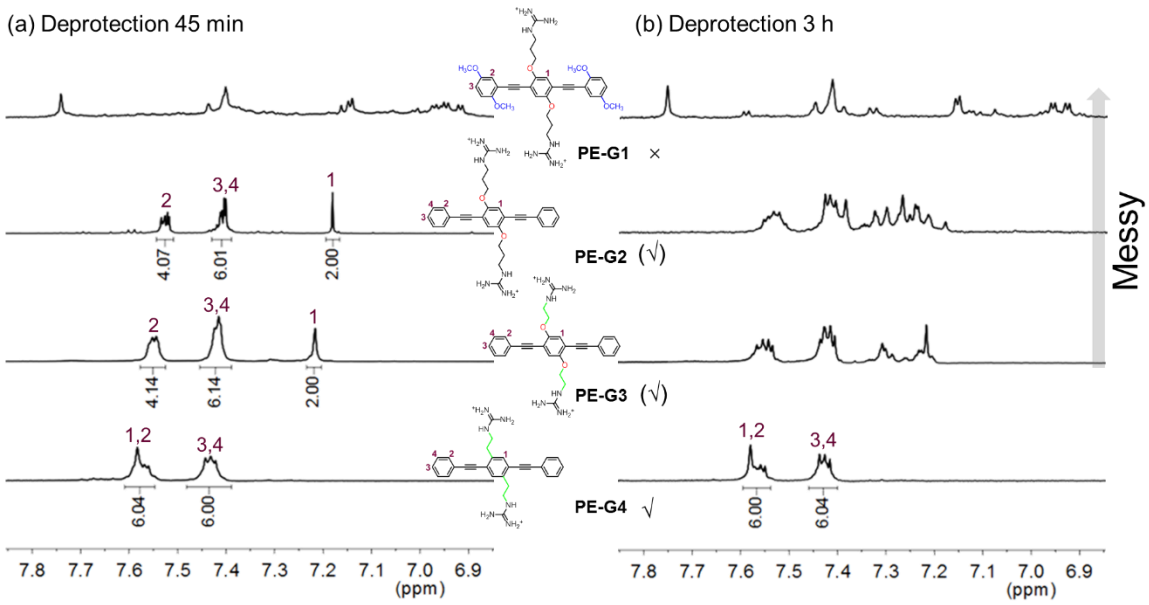

Figure 67. ^{1}H NMR spectra (in CD_3OD) of guanidinium salts when the corresponding *N*-Boc-protected PEs were deprotected in DCM/TFA (1/1) at different time (a: 45 min, b: 3 h; Depicted are only the aromatic regions). Peak assignment according to those of the molecular structures inside. No assignment for messy spectra.

As shown in Figure 67, the deprotection of **PE-BG1-4** into our targets **PE-G1-4** was tricky as **PE-BG1-4** took considerably longer (45 min) to deprotect than **PE-BA1-4** into **PE-A1-4** (3 min). Only after 45 min all of the starting material is consumed in the **PE-BG** series. Unfortunately, we could not deprotect **PE-BG1** under these conditions and unidentifiable product mixtures form. We attempted the deprotection in combination with scavengers like anisole, but a significant amount of the undesired impurities can still be observed. We suspected that the free guanidinium groups catalyze an intramolecular ether cleavage through a cyclic transition state combined with an uncontrolled polymerization of the product(s). This is the main reaction for **PE-BG1** but also for **PE-BG2**. While the

in situ NMR of **PE-G2** looks reasonably clean, workup was difficult. Is the deprotection of **PE-BG3** similar to **PE-BG2**? Encouragingly, shortening the spacer by one methylene group enhances the stability (**PE-G3**). Inspired by the deprotection result from **PE-BG1** to **PE-BG2**, the O atom in the side chain was also removed and **PE-BG4** was synthesized. Surprisingly, in this case of hydrocarbon scaffold (**PE-G4**), the deprotection product is completely resistant to the reaction conditions.

3.2.7 Optical Properties of Ammonium/Guanidinium Salts

The optical properties of four ammonium and three guanidinium salts were examined in pH 7 buffer solution (Figure 68 and Table 6). Compared with **PE-A2** (353/400 nm), the absorption and emission spectra of **PE-A1** were red-shifted by 14 nm and 28 nm, respectively, due to the enhancement of the conjugation. Different from **PE-A2**, **PE-A3** showed a slight blue-shift in absorption (348 nm) and emission (391 nm). The guanidines **PE-G2-4** display absorption and emission spectra very similar to those of the amines **PE-A2-4** at pH 7. Quantum yields of **PE-A** and **PE-G** are high and very similar. In comparison to the trimers with O in the side chain, both **PE-A4** and **PE-G4** exhibited one main absorption band, located at 323 nm, and the fluorescence was found at around 353 nm, with a shoulder peak at 371 nm and a shorter lifetime (0.34 and 0.39 ns).

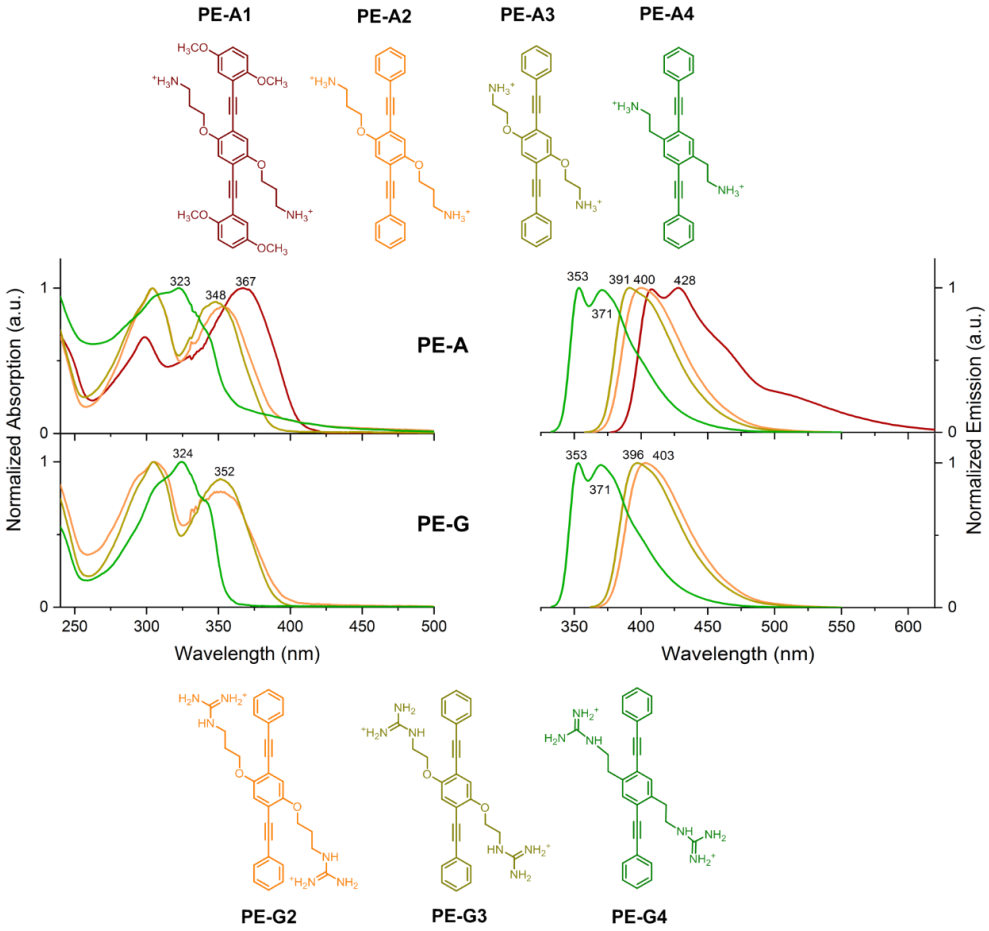

Figure 68. UV-Vis absorption (left) and emission spectra (right) of the formed ammonium/guanidinium salts measured in pH 7 buffer solution.

Table 6. Photophysical properties (in pH 7 buffer solution) of the formed salts.

Salts	λ_{max} [nm][a]	λ_{em} [nm]	$\Delta\upsilon_{st}$ [cm^{-1}][b]	QY[%][c]	τ_f [ns]
PE-A1	367	428	388	11±1	0.96
PE-A2	353	400	333	72±4	1.67
PE-A3	348	391	316	73±1	1.49
PE-A4	323	353, 371	263	54±2	0.34
PE-G1			/[d]		
PE-G2	353	403	351	71±1	1.83
PE-G3	352	396	316	70±2	1.63
PE-G4	324	353, 371	254	69±1	0.39
PE-U1			/[d]		
PE-U2	363	416	351	35±3	1.40

[a] Absorption maximum at the longest wavelength. [b] Stokes shift. [c] Fluorescence quantum yield. [d] No salts obtained.

Similarly, the cleavage of the *N*-Boc group in **PE-BU2** gave salt **PE-U2**. **PE-U2** shows absorption at 362 nm and emits a weak fluorescence (QY: 35%) in pH 7 buffer solution around 416 nm with lifetime of 1.40 ns (Figure 69).

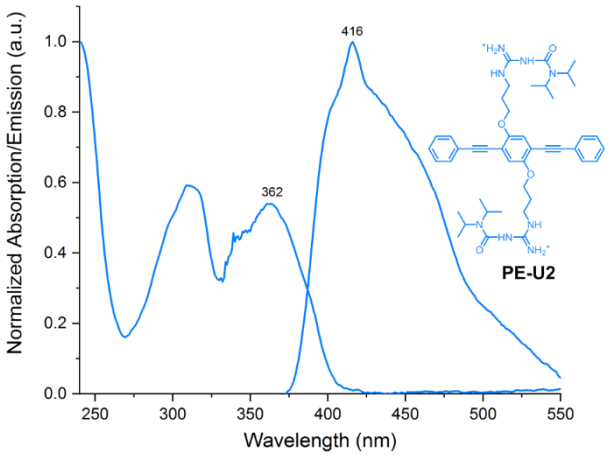

Figure 69. UV-Vis absorption and emission spectra of **PE-U2** measured in pH 7 buffer solution.

3.2.8 pH Dependence of Ammonium/Guanidinium Salts

PE-A1-4 display pH-dependent emission leading to diminished intensity upon increasing the pH value (Figure 70 and 71). At around pH 9 the midpoint intensity is reached i.e. at the pKa-value of these primary amines. As show in Figure 70, in the pH range of 1-5, the emission intensity of **PE-A1** showed a slight fluctuation and as the pH value gradually increased from 5 to 9, its intensity decreased. With further increasing pH from 9 to 13, the emission band displayed a continuous red shift with decreased intensity, indicating the occurrence of molecular aggregates. For **PE-A2** and **PE-A3**, their intensity decreased evidently when the pH was changing to 13. Different from the trimers with O in the side chain, **PE-A4** also exhibited a decrease in intensity with pH value increasing, but no red-shift of the fluorescence band was observed. Figure 71 shows the emission behaviors of all ammonium salts in

different pH buffer solutions. The apparent quench in intensity of **PE-A1** when increasing pH from 9 to 13 can be easily identified by naked eyes.

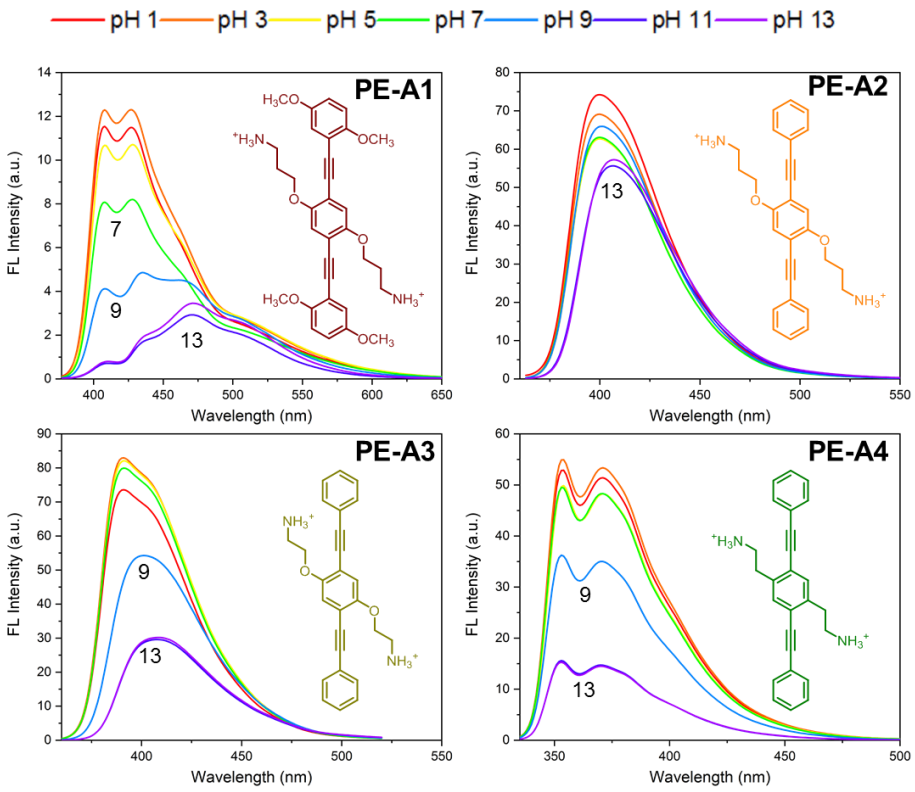

Figure 70. The emission spectra of **PE-A1-4** (6.6 μm) in different pH buffers. Spectra were measured in aqueous buffer solution excited at 367 nm, 353 nm, 348 nm and 323 nm, respectively.

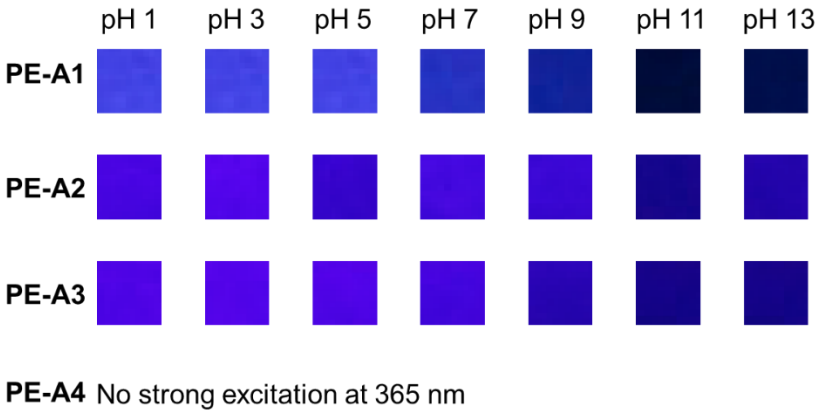

Figure 71. Photograph of **PE-A1-4** in different pH buffers under a hand-held black light with illumination at 365 nm.

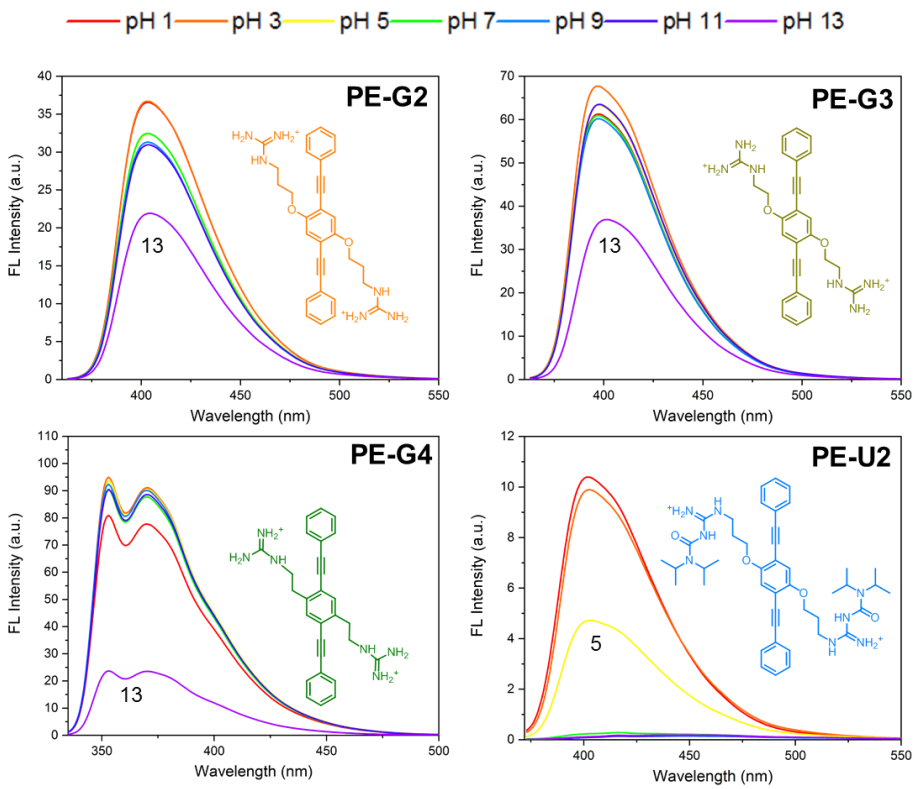

Figure 72. The emission spectra of **PE-G2-4** and **PE-U2** (6.6 µm) in different pH buffers. Spectra were measured in aqueous buffer solution excited at 353 nm, 352 nm, 324 nm and 363 nm, respectively.

As shown in Figure 72, the emission intensity of **PE-G2-4** show unnoticeable changes in the λmax as well as the fluorescence intensity with pH value range of 1-11. A significant decrease in the intensity was observed when pH was changed to 13, reflecting the higher pKa value of the guanidine group.[156] In sharp contrast, the non-basic **PE-U2** loses half of its fluorescence intensity already at pH 5, testament for decreased basicity, indicating its high sensitivity, which is further confirmed by the photographs excited at 365 nm (Figure 73).

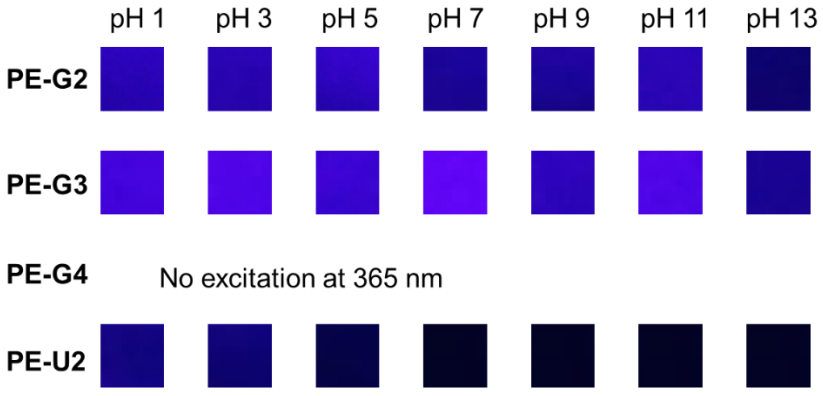

Figure 73. Photograph of **PE-G2-4** and **PE-U2** in different pH buffers under a hand-held black light with illumination at 365 nm.

3.2.9 Proposed Mechanism

The tethering of the guanidine group to the aryl skeleton by a 3-oxopropyl group leads to decomposition upon deprotection, while guanidines tethered to the arene by a shorter linker or an ethylene linker survive the deprotection conditions without any problem. We speculate that the TFA performs cleavage of the ethers as in **PE-G2** through the intramolecular assistance of the guanidinium ions under formation of a cyclic guanidine (Scheme 18). A similar mechanism will probably take place for **PE-G1**. So we assume that the guanidines form but are not stable under the deprotection conditions but lead to ether cleavage by anchimeric assistance.

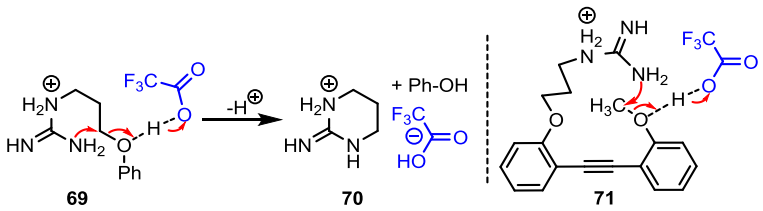

Scheme 18. Proposed mechanism of the derailed deprotection of substrates of the type **PE-BG1**.

These findings have consequences for the construction of conjugated polymers bearing guanidinium groups. Care has to be taken that the deprotected guanidine does not cannibalize itself with the help of the added trifluoracetic acid. The safe bet would therefore to use hydrocarbon linkers or a heteroatom linker that does not incur this specific type of ether cleavage. A second caveat is that some of the published matter claiming to have prepared guanidine-substituted PPEs should be repeated to exclude that cannibalized, cleaved products have been obtained.

3.2.10 Conclusion

In summary, a series of *N*-Boc-protected guanidine-based phenyleneethynylene trimers with different substituents and side chains were prepared to investigate and compare their Boc deprotection behavior. Surprisingly, the Boc deprotection of PEs was dependant upon the substitution pattern of the linker. We focused on searching for a proper substitution pattern for guanidine-based PEs that allows smooth Boc-deprotection. We observed that the PE with an alkyl side chain terminated by *N*-Boc-protected guanidine showed the best deprotection performance. The photophysical property investigation disclosed that small variation in the substituent group or side chain can greatly affect their absorption and emission. These provided new insights into the structural and deprotection of *N*-Boc-protected guanidine-based PEs.

3.3 Guanidine-Substituted Poly(*para*-phenyleneethynylene)s: Synthesis, Photophysical Properties and Nitroaromatics Sensing

In this part, on the basis of the above research about guanidine-substituted PE-trimers, we prepared two guanidine-based poly(*para*-phenyleneethynylene)s (PPEs) with hydrocarbon scaffold **PPE14-15** and their optical properties was investigated. Further, the sensing ability of guanidium-**PPE15** over nitroaromatics were tested and **PPE15** could work as a sensitive and selective chemosensor for picric acid (PA) in water, which provides a simple, convenient and low-cost method for detection of PA. Our results are helpful for further rationally designing guanidine-based PPE materials with a superior performance.

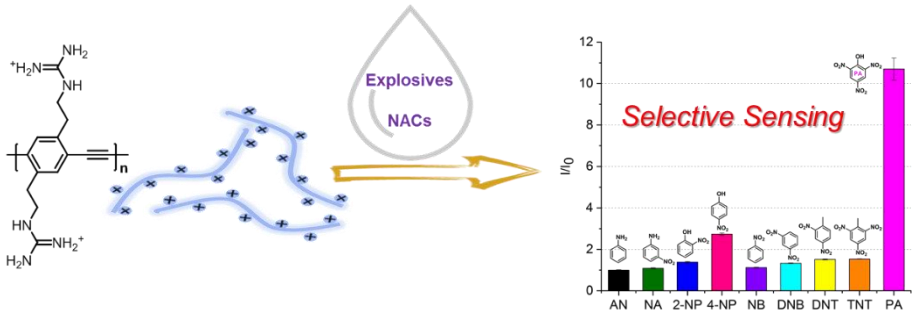

Figure 74. Schematic representation of guanidine-substituted poly(*para*-phenyleneethynylene)s: synthesis, photophysical properties and nitroaromatic compounds sensing.

3.3.1 Synthesis of Guanidine-Substituted PPEs

Scheme 19 displays the synthesis of the *N*-Boc-protected dialkyene and diiodine monomers **73** and **81**. The coupling between **64** and trimethylsilylacetylene was performed under standard Sonogashira condition, which yielded **72** in an isolated yield of 48%. Then the trimethylsilyl was removed by KF in THF/MeOH mixtures to to afford the desired dialkyne **73**.

For the synthesis of **81**, 1,4-bis(hydroxymethyl)benzene **74** was used as starting material. The hydroxy functions of **74** were protected as a diacetate, with a high yield of 87%. **75** subsequently iodinated under acidic conditions using iodine/iodic acid to get **76**. Deprotection of the acetate groups of **76** under basic conditions gave the diol **77**. Then **77** was cleanly brominated under Appel conditions (CBr_4/PPh_3) to afford **78**, which was transformed into **79** by using KCN in $EtOH/H_2O$. Initial attempts to obtain **81** by treating **79** with $NaBH_4/NiCl_2{\cdot}6H_2O/Boc_2O$ in one pot were not successful and **80** without iodine atom was generated. However, **81** could be synthesized by 2 steps. BH_3-SMe_2 was used to reduce the cyano group in the first step and the free amine obtained was protected by *tert*-butyloxycarbonyl group to afford **81** in an overall yield of 19%.

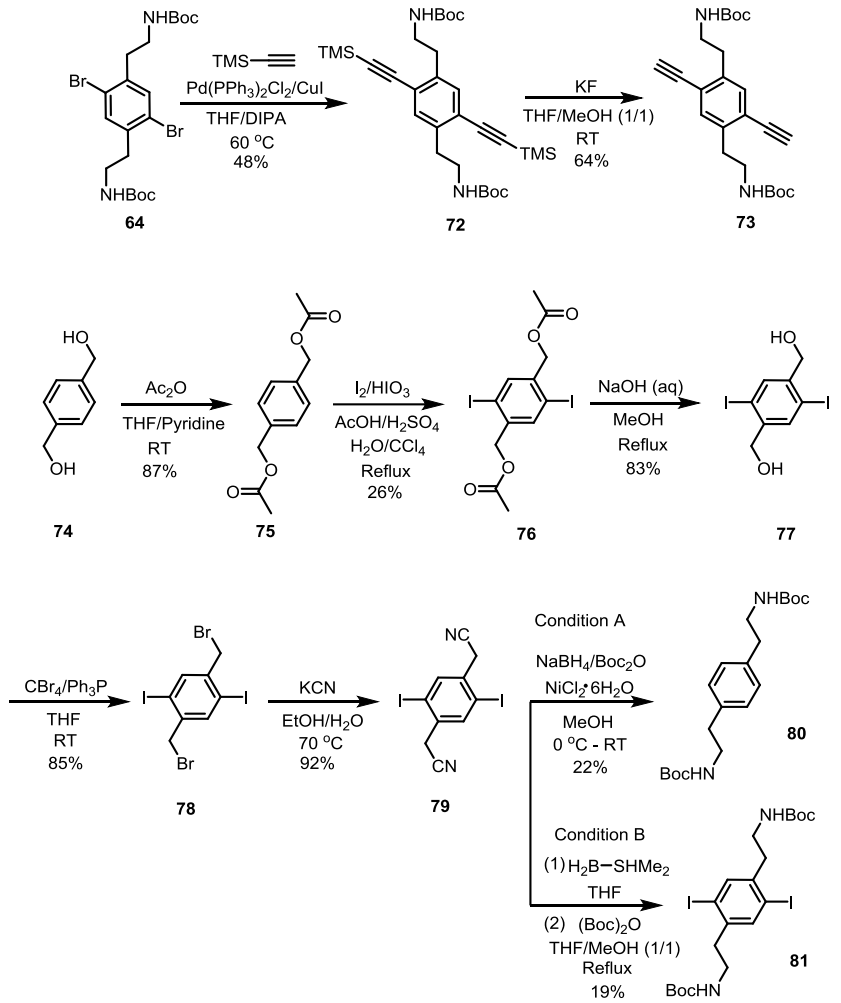

Scheme 19. Synthesis of monomers **73** and **81**.

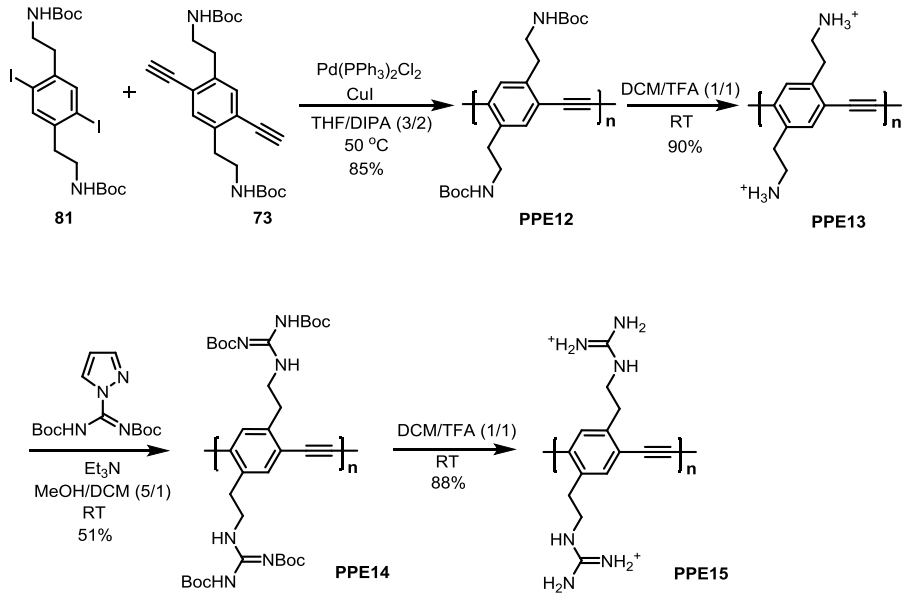

Scheme 20. Synthesis of **PPE12-15**.

The synthesis for guanidine-substituted PE-trimers and PPEs is based on the same strategy (Scheme 20). The Sonogashira coupling of **81** with **73** was performed to give **PPE12** in a yield of 85%. Deprotection

with TFA smoothly furnishes the ammonium salts **PPE13**, which were transformed into *N*-Boc-protected **PPE14** using the protected guanidine agent in MeOH/DCM mixtures. The guanidinylation was confirmed by the appearance of the peak at 1.47, 8.44, 11.47 ppm in the ^{1}H NMR spectrum and absorption at 1716 cm^{-1} in the IR spectrum, which were assigned to the protected guanidine. The subsequent hydrolysis of **PPE14** gave the desired guanidium salt **PPE15**. The number-average molecular weights (M_n) of these polymers were estimated by gel permeation chromatography in a range from 4.2×10^3 to 7.0×10^3 g/mol, with polydispersities (PDI = M_w/M_n) from 1.5 to 1.9 and degree of polymerization from 10 to 11. The structures and detailed properties of the four polymers were shown below (Figure 75, Table 7).

3.3.2 Optical Properties of Guanidine-Substituted PPEs

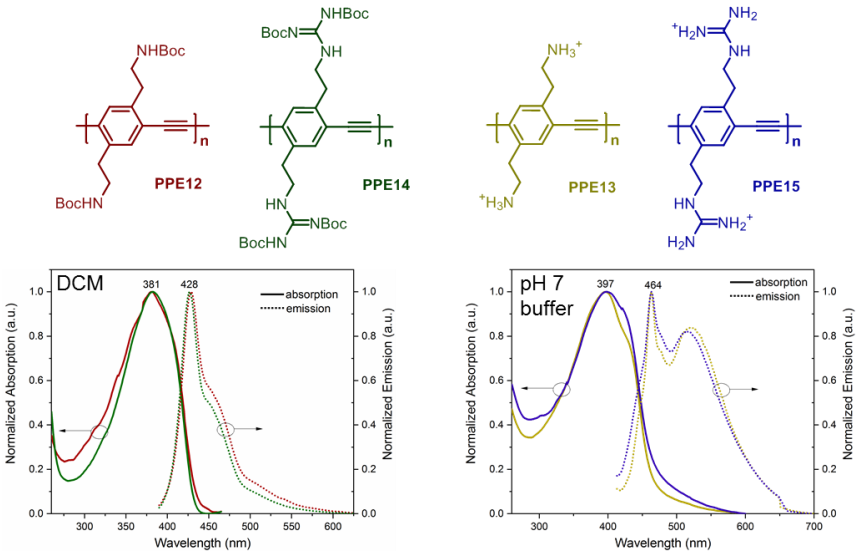

Figure 75. Normalized absorption and emission spectra of **PPE12-15**.

Table 7. Molecular weights and optical properties of **PPE12-15**.

PPEs	M_n [g/mol]	PDI	P_n	λ_{abs} [nm]	λ_{em} [nm]	QY[%][c]	τ_f [ns]
PPE12[a]	4200	1.9	11	381	428	43±1	0.39
PPE14[a]	7000	1.5	10	382	427	45±2	0.38
PPE13[b]	/[d]			397	464, 522	2±0.3	0.31
PPE15[b]	/[e]			398	464, 518	3±0.5	0.50

[a] Optical properties in DCM. [b] Optical properties in pH 7 buffer solution. [c] Fluorescence quantum yield. [d] Resulted from **PPE12**. [e] Resulted from **PPE14**.

As shown in Figure 75 and Table 7, in DCM, **PPE12** and **PPE14** showed similar absorption and emission, with a peak at 381 nm and 428 nm, respectively. Their quantum yields are high, up to 43–45% and their lifetime ranges from 0.38-0.39 ns. The absorption maxima of formed conjugated polyelectrolytes **PPE13** and **PPE15** is located at 397 nm. Their emission spectra show wide bands spanning from 420 nm to 700 nm, with a maxima peak (464 nm) and a notable shoulder peak (520 nm).

The emissive lifetime of **PPE13** and **PPE15** is 0.31-0.50 ns and their fluorescence quantum yields (QY) is 2% and 3%, respectively.

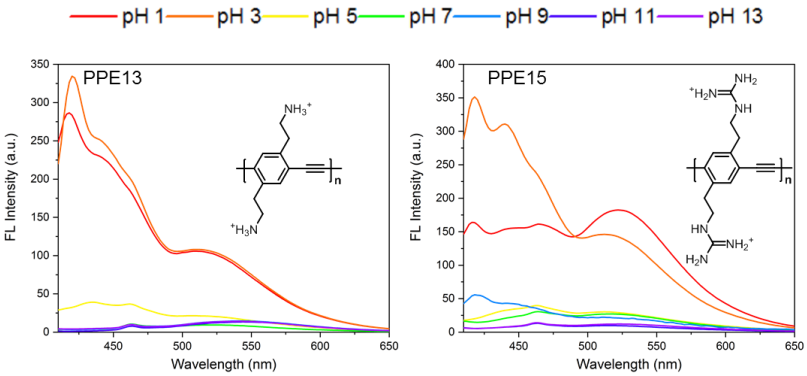

Figure 76. The emission spectra of **PPE13** and **PPE15** (5 μm) in different pH buffers. Spectra were measured in aqueous buffer solution excited at 400 nm.

Figure 76 showed the effect of pH on the emission intensity of **PPE13** and **PPE15**. Increased acidity would result in an increased intensity, while high alkalinity can decrease the intensity dramatically. The basic condition could generate neutral amine or guanidine polymer, which weaken the electronic repulsion, thus likely forming aggregates and leading to drastic quenching via hydrophobic and π–π stacking interactions.

3.3.3 Guanidine-Substituted PPEs for Sensing Nitroaromatics

Nitroaromatic explosives are toxic and hazardous pollutants. Picric acid (PA), as one of them, has high water solubility (ca. 14 g/L at 20 ºC) and thus the detection of PA in water is of great significance.[157] Although different fluorescent detecting platforms, such as organic molecules and metal-organic frameworks, have been established,[158] some sensors still rely on the use of a high portion of organic solvents to detect PA in aqueous solution due to their poor solubility. This drawback makes them limited in practical use.

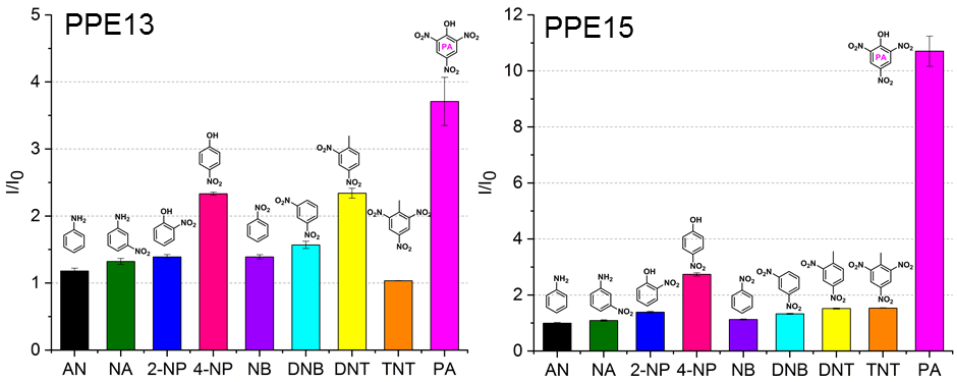

Figure 77. Fluorescence response pattern (plotted as I/I_0) obtained by **PPE13** and **PPE15** (5 μM, pH 7 buffer solution) treated with analytes (100 μM). I_0 and I denote the fluorescence intensity of PPEs before and after the addition of analytes. Each value is the average of three measurements and each error bar shows the standard error of these measurements. Inset: structures of used analytes.

Herein we evaluated **PPE13** and **PPE15** as sensors for nitroaromatics explosives. The following nitroaromatic analytes were chosen for the sensing studies: nitrobenzene (NB), dinitrobenzene (DNB), dinitrotoluene (DNT), trinitrotoluene (TNT), picric acid (PA), 2-nitrophenol (2-NP), 4-nitrophenol (4-NP) and nitroaniline (NA). Aniline (AN) served as a reference. As shown in Figure 77, all the analytes quenched the emission of **PPE13** comparably, whereas in the case of **PPE15**, PA showed the most effective quenching. The results demonstrate that **PPE15** has high selectivity for PA, especially without the interference of TNT, with highly similar chemical structures and properties.[159]

We performed fluorescence titration experiments of **PPE15** with PA to demonstrate the detection ability. The gradual addition of PA with different concentrations to a solution of **PPE15** elicited significant quenching in the fluorescence emission, as demonstrated in Figure 78, with no other significant spectral changes (such as shifts in λ_{max}) being observed. A nonlinear Stern–Volmer plot was obtained from the fluorescence quenching titration profile. The calculated binding constant log K_{SV} was determined as 4.88, higher than that of **PPE13** (4.45). The detection limit of **PPE15** was estimated to be 2.7×10^{-7} M, which is lower than the reported phosphole oxides and quinoline-based compounds for sensing of PA.[160]

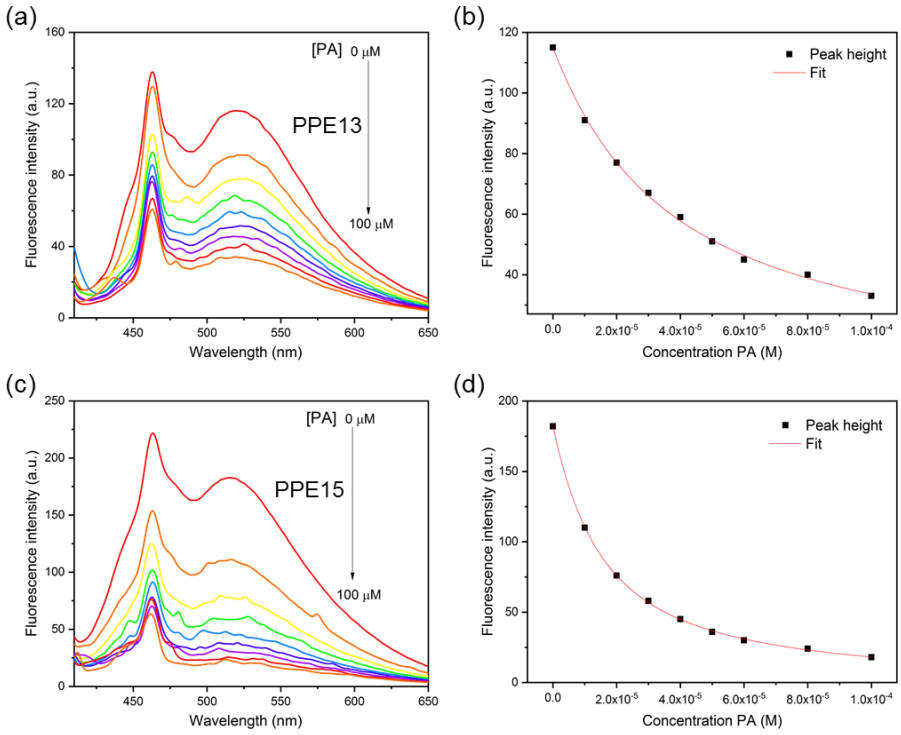

Figure 78. (a, c) Emission spectra of **PPE13** and **PPE15** (5 μM, pH 7 buffer solution) after addition of various concentrations of PA; (b, d) fluorescence intensity changes of **PPE13** and **PPE15** in the presence of increasing concentration of PA.

Table 8. Binding constants log K_{SV} and limits of detection (LOD) for **PPE13** and **PPE15** toward PA.

PPEs	log K_{SV}	LOD [M]
PPE13	4.45±0.03	1.3×10^{-6}
PPE15	4.88±0.02	2.7×10^{-7}

The fluorescence quenching mechanism via electron transfer from the electron-rich fluorophores to the electron-deficient nitro analytes has been well established.[161] When electron-deficient PA was mixed with electron-rich **PPE15** together, the electron transfer between them causes fluorescence quenching. However, the good selectivity for PA and the weaker quenching caused by other nitro compounds, especially TNT, with comparative electron accepting efficiency, suggested that other quenching mechanism associated with electron transfer, like resonance energy transfer (RET),[162] is possibly responsible for such a quenching response. As shown in Figure 79a, the absorption spectrum for PA exhibits a massive overlap with the emission of **PPE15**. In sharp contrast, negligible overlaps were observed for the other nitro-explosives, consistent with their lower quenching efficiencies. Furthermore, the hydrogen bonding between PA and **PPE15** possibly brings them well within the Förster radius, facilitating efficient energy transfer. Thus, the resonance energy transfer mechanism may also be involved in the quenching process, which can also be demonstrated by the non-linear behavior of the S–V plot of **PPE15** for PA.[163]

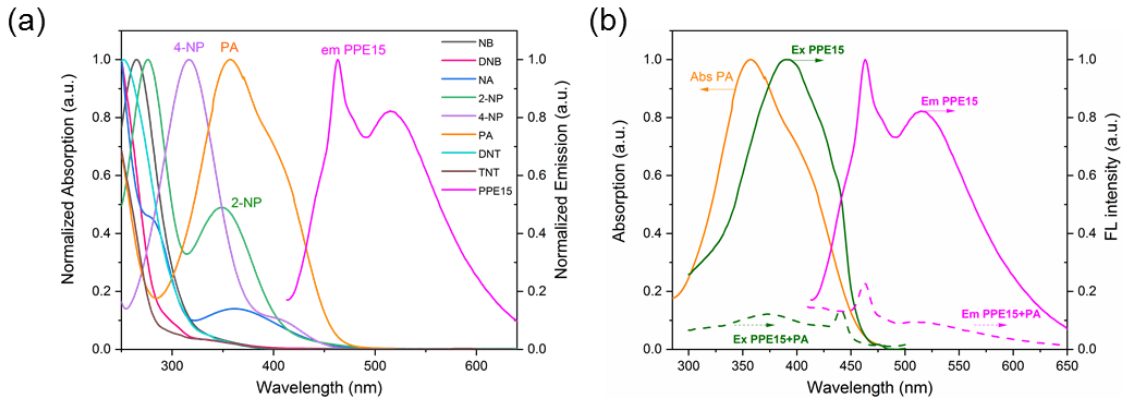

Figure 79. (a) Absorption spectra of analytes and emission spectra of **PPE15**; (b) Absorption spectra of PA, excitation spectra and emission spectra of **PPE15** (5 μM) before (solid line) and after (dash line) the addition of PA (100 μM). Solvent: pH 7 buffer solution.

Figure 79b displays the UV−vis spectra of PA, the excitation and emission spectra of **PPE15** before and after the addition of PA. Obviously, the overlap between the absorption spectrum of PA and the excitation spectrum of **PPE15** is larger than that between the absorption spectrum of PA and the emission spectrum of **PPE15**, implying that inner filter effect (IFE) is also possibly responsible for the fluorescence quenching mechanism.[164] It was observed that the excitation spectrum intensity decreased dramatically after the addition of PA, which can also result in the fluorescence intensity of **PPE15** was quenched steeply. As discussed above, the enhanced quenching efficiency of PA may be due to multiple factors, including electron transfer, energy-transfer and inner filter effect.

To get deep insight into the nature of detection mechanism, we measured fluorescence lifetime of **PPE13** and **PPE15** in the absence and presence of PA. Their fluorescence lifetime experienced a slight fluctuation at different concentration of PA (Figure 80), indicating that the static quenching appears to be predominant.[165]

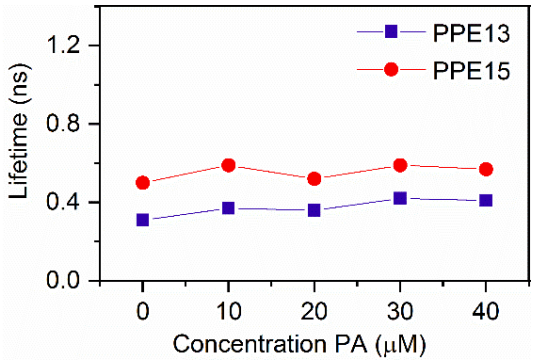

Figure 80. Lifetime of **PPE13** and **PPE15** (5 μM) with different concentration of PA in pH 7 buffer solution.

3.3.4 Conclusion

In summary, we have synthesized the true cationic poly(*para*-phenyleneethynylene)s with guanidinium side groups **PPE15**, which were facilely modified from ammonium polymer **PPE13.** The modification in the side chain from **PPE13** to **PPE15** makes it possible to modulate binding ability of the nitroaromatics and generate different fluorescence response. **PPE15** showed enhanced selectivity and senstivity over PA in water and the detection limit is as low as 0.27 μM. The selective sensing of PA is considered as a combined effect of the electron transfer, energy-transfer and inner filter effect. This work demonstrates an effective route to design and synthesize guanidinium poly(*para*-phenyleneethynylene)s with applications in fluorescent sensors.

Chapter 4. Summary and Outlook

Summary and Outlook

In summary, the synthesis, optical property and sensing applications of SBs and PEs were presented. These work mainly include: (1) construction of AIEgens by tailing simple TSB and the investigation of photophsical property, photostability and regioisomerism effect; (2) introducing lewis-base units, like pyridine or dibutylanilines, to extended DSB/TSBs for sensing/discriminating protons and metal ions; (3) construction of PPE-based sensor array for determination of Edman degradated amino acids; (4) structural tailoring the phenyleneethynylene (PE) trimers with *N*-Boc-protected guanidine side groups for yielding the desired PE guanidium salts and developing the true guanidine-substituted PPE for nitroaromatic compounds sensing.

The photophysical properties of SBs/PEs are prominent, making them a promising scaffold for molecule design. Nevertheless, many issues have not been addressed and there are extensive challenges and opportunities that ought to be noted in this research field.

(a) The method of achieving AIE activity in this work is mainly designing fluorescent SBs into propeller-shaped structures, namely twisted structure. However, improving the fluorescent efficiency in the aggregation state is highly required. Although the ACQ effect was suppressed by introducing multiple arms, the aggregation-state emission efficiency of the TSBs remained low, which restricted their further applications, like OLED. Exploring a new strategy to achieve intense aggregation-state emission of TSBs remains a challenge.

(b) For the further development of SB-based fluorescent sensors, we need to consider two aspects. First, since aggregation-induced emission (AIE) active fluorophores possessing strong fluorescence in aggregate states, it is more beneficial to design AIE-active SB-based fluorescent sensors. Second, exploring AIE-active SBs with near-infrared (NIR) emission as sensors is always preferable for the detection of chemical species in biosamples. However, successful examples are rather limited compared to number of AIE-active SBs with a short emission wavelength. If introducing the suitable building block to the π-conjugated backbone could form a fine-tuning structure, that would be helpful for achieving NIR aggregation-state emission.

(c) Benefiting from the appealing spectroscopic properties and the amphiphilic nature, guanidine-based PPEs could be further explored for distinct supramolecular assembly.

Through rational design and the incorporation of stimuli-responsive moieties to SB/PE derivatives, recently various sensing applications, especially AIE-based materials, have appeared, clearly indicating their bright future.

Chapter 5. Experimental Section

5.1 General Remarks

Chemicals were either purchased from the chemical store at the Organisch-Chemisches Institute of the University of Heidelberg or from commercial laboratory suppliersm, like Sigma-Aldrich, Abcr or Acros. Reagents were used without further purification unless otherwise noted.

Solvents were purchased from the store of the Theoretikum or chemical store at the Organisch-Chemisches Institute of the University of Heidelberg and if necessary distilled prior use. All of the other absolute solvents were dried by an MB SPS-800 using drying columns.

Buffer solutions of pH 1 (HCl/KCl), pH 2 (KHPh/HCl), pH 3 (citric acid/NaOH/NaCl), pH 4 (citric acid/NaOH/NaCl), pH 5 (citric acid/NaOH), pH 6 (citric acid/NaOH), pH 7 (KH_2PO_4/Na_2HPO_4), pH 8 (borax/HCl), pH 9 (KHPh/NaOH), pH 10 (borax/NaOH), pH 11 (boric acid/NaOH/KCl), pH 12 (Na_2HPO_4/NaOH), pH 13 (NaOH/KCl) were purchased from Sigma-Aldrich®.

Synthesis: all reactions involving moisture or air-sensitive reagents were carried out in dried glassware under an atmosphere of dry nitrogen or argon.

Photoreactions were carried out in a Rayonet UV reactor from Southern New England Ultraviolet Company.

Crystal structures were obtained from Bruker Smart CCD or Bruker APEX diffractometers at the crystallographic department under the direction of Dr. Frank. Rominger.

Analytical thin layer chromatography (TLC) was performed on Macherey & Nagel Polygram® SIL G/UV254 pre-coated plastic sheets. Components were visualized by observation under UV light (254 nm or 365 nm).

Flash column chromatography was carried out using silica gel from Sigma-Aldrich (particle size: 0.063-0.200 mm) or from Macherey-Nagel GmbH & Co. KG, Düren (Germany) (particle size: 0.040-0.063 mm).

GC/MS chromatograms were recorded using a HP 5890 Series II Plus model, coupled with a HP 5972 Mass Selective Detector. As the capillary column, a HP 1 Crosslinked Methyl Silicone (25 m x 0.2 mm x 0.33 μm) was employed, with helium as carrier gas. The acquired data were analyzed using ACD/Labs Spectrus Processor 2012.

Ultrahigh pressure liquid chromatography (UPLC-MS) was performed on a Waters Acquity system. The mass spectra were recorded with a SQD2 mass detector. The acquired data were analyzed using ACD/Labs Spectrus Processor 2012.

Dialysis was realized with cellulose ester (CE) tubular membranes (Sepctra/Por® Biotech, Spectrum) with a molecular weight cut-off of 100-500 Da for DSBs against deionized water (DI water). Unless stated otherwise the equipped tubular membranes were put into excess (~ 10 L) of deionized water and

stirred for 2 d by changing the surrounding solvent once everyday . The dialyzed solution was freeze-dried afterward. For a considerate water removal after dialysis the sample was cooled down to -196 °C with liquid nitrogen and water was removed with VirTis® Benchtop K freeze dryer.

^{1}H NMR spectra were recorded at room temperature on the following spectrometers: Bruker Avance III 300 (300 MHz), Bruker Avance III 400 (400 MHz) and Bruker Avance III 600 (600 MHz). The data were interpreted in first-order spectra. The spectra were recorded in $CDCl_3$, D_2O or MeOD as indicated in each case. Chemical shifts are reported in δ units relative to the solvent residual peak.[166] The following abbreviations are used to indicate the signal multiplicity: s (singlet), d (doublet), t (triplet), q (quartet), quin (quintet), sext (sextet), dd (doublet of doublet), dt (doublet of triplet), ddd (doublet of doublet of doublet), etc., bs (broad signal), m (multiplet). Coupling constants (*J*) are given in Hz and refer to H, H-couplings.

^{13}C NMR spectra were recorded at room temperature on the following spectrometers: Bruker Avance III 300 (75 MHz), Bruker Avance III 400 (100 MHz) and Bruker Avance III 600 (150 MHz). The spectra were recorded in $CDCl_3$ or D_2O as indicated in each case. Chemical shifts are reported in δ units relative to the solvent signal: $CDCl_3$ [δ_C = 77.16 ppm (central line of the triplet)] or TMS (δ_C = 0.00 ppm).[166] All NMR spectra were integrated and processed using Bruker's TopSpin™ Software.

High resolution mass spectra (HR-MS) were either recorded on the JEOL JMS-700 (EI^+), Bruker AutoFlex Speed (MALDI, LDI), Bruker ApexQehybrid 9.4 T FT-ICR-MS (ESI^+, $DART^+$) or a Finnigan LCQ (ESI^+) mass spectrometer at the Organisch-Chemisches Institut der Universität Heidelberg.

Elemental analyses were carried out at the Organisch-Chemisches Institut der Universität Heidelberg.

IR spectra were recorded on a JASCO FT/IR-4100. Substances were applied as a film, solid or in solution. The obtained data were processed with the software JASCO Spectra Manager™ II.

A**bsorption spectra** were recorded on a JASCO UV-VIS V-660 or JASCO UV-VIS V-670 and processed with the software JASCO Spectra Manager™ II. ASCII-files were exported and visualized by Origin.

Fluorescence spectra were recorded on a Jasco FP6500 spectrometer. Raw data were processed using JASCO Spectra Manager™ II. ASCII-files were exported and visualized with Origin.

Photographs of solutions were taken with a Canon EOS 7D camera equipped with an EF-S 60mm F/2.8 Macro lens. Solid state photographs were taken using a Samsung Galaxy S7.

Scanning electron microscopy (SEM) experiments were carried out with a Zeiss Ultra55 (Schröder Group, University of Heidelberg). Samples were imaged in a FESEM (Ultra, Carl Zeiss Microscopy) at 1.5kV using SE and InLens detectors for secondary electrons. For improved statistics large areas of the samples were screened at low resolution using the Atlas 5 platform (Carl Zeiss Microscopy), then

representative regions of interest scanned at 3 nm pixel size. All measurements were recorded with the Zeiss Smart SEM V05.04 software.

Thin-Films were prepared by spin coating employing a Spin150 spin coater (SPS, 30 sec, 1000 rpm) on glass substrate.

Polarizing optical microscopy (POM) experiments were carried out with an LV100i Pol polarizing optical microscope (POM) equipped with a digital Nikon camera and a temperature-controllable Linkam hot stage. The star-shaped compounds were observed in the heating and cooling processes.

Theory calculations were carried out using a B3LYP/6-311++G** basis set on spartan molecular modeling software or Gaussian 16.

Melting Points were determined on a Melting Point Apparatus MEL-TEMP (Electrothermal, Rochford, UK) using open glass capillaries and are uncorrected.

Fluorescence quantum yields (Φ) were obtained by the absolute method using an emission spectrometer equipped with an Ulbricht sphere. The system was calibrated with a primary light source.[167] The procedure from Würth[168] was used for substances with emission intensities ≥ 5000 counts, whereas the procedure of DeRose[167] was used < 5000 counts, applying a filter ND 2.0. Given Φ for each sample are average values of at least three independent measurements.

Fluorescence lifetimes (τ) were acquired by an exponential fit according to the least mean square with commercially available software HORIBA Scientific Decay Data Analyses 6 (DAS6) version 6.4.4. The luminescence decays were recorded with a HORIBA Scientific Fluorocube single photon counting system operated with HORIBA Scientific Data Station version 2.2.

Fluorescence response patterns were recorded using a CLARIOstar (firmware version 1.13) plate reader from BMG Labtech using the corresponding software (software version 5.20 R5). Data were analyzed with CLARIOstar MARS Data Analysis Software (software version 3.10 R5) from BMG Labtech. The resulting solutions were loaded into a 96-well plate (300 µL microplate). The analyte was then added and the solutions were adjusted with buffer to the desired concentrations. The excitation wavelength was set according to the absorption wavelength of the used complex. The specific response for each analyte was measured five times and the peak values were obtained.

5.2 Synthesis Details and Analytical Data

5.2.1 Synthesis of TSBs (Chapter 2.1)

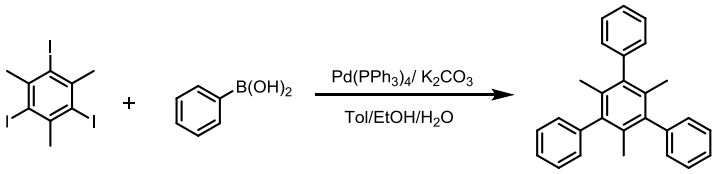

35 36

Compound **35** was synthesized according to the literature.[169]

Synthesis of 2',4',6'-trimethyl-5'-phenyl-1,1':3',1''-terphenyl (36). A solution of compound **35** (2.28 g, 5.00 mmol, 1.00 eq.) in a mixture of toluene (45 mL), EtOH (30 mL) and H_2O (15 mL) was degassed with nitrogen. Phenylboronic acid (2.74 g, 22.5 mmol, 6.50 eq.), $Pd(PPh_3)_4$ (866 mg, 750 µmol, 0.15 eq.) and K_2CO_3 (6.22 g, 45 mmol, 9.00 eq.) were added and the suspension was stirred at 100 °C for 72 h. After cooling to room temperature and addition of H_2O (200 mL) the mixture was extracted with CH_2Cl_2 (3×100 mL). Evaporation of the solvent under reduced pressure and recrystallized from EtOAc to give **36** as colorless needle crystal (1.24 g, 3.55 mmol, 71%). ^{1}H NMR (300 MHz, $CDCl_3$) δ 7.43 (m, 6H), 7.33 (m, 3H), 7.24 (m, 6H), 1.72 (s, 9H).

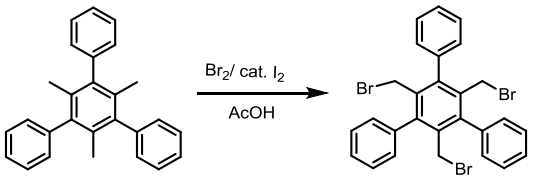

36 37

Synthesis of 2',4',6'-tris(bromomethyl)-5'-phenyl-1,1':3',1''-terphenyl (37).[95] Compound **36** (1.10 g, 3.16 mmol, 1.00 eq.) was dissolved in acetic acid (250 mL). Bromine (3.25 mL, 63.1 mmol, 20.0 eq.) and a catalytical amount of iodine were added and the reaction mixture was refluxed for 5 h. The reaction mixture was allowed to cool to room temperature slowly. After addition of 200 mL water, the precipitate was collected via filtration and washed thoroughly with water to yield **37** as a colorless solid without further purification (1.68 g, 2.84 mmol, 90%). ^{1}H NMR (300 MHz, $CDCl_3$) δ 7.52 – 7.42 (m, 15H), 3.94 (s, 6H).

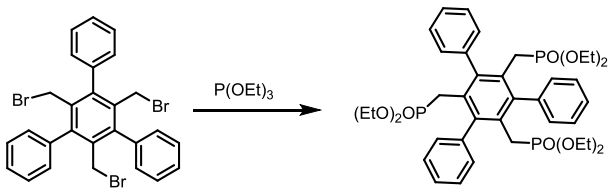

37 38

Synthesis of hexaethyl ((5'-phenyl-[1,1':3',1''-terphenyl]-2',4',6'-triyl) tris(methylene))tris(phosphonate) (38).[88b] Compound **37** (1.30 g, 2.22 mmol) and 10.0 mL triethyl

phosphite were placed in a flask with a stirring bar. The mixture was heated at 150 °C for 12 h. The excess triethyl phosphite was removed by distillation under reduced pressure. The residue was further dried in vacuo at 50 °C to give the product **38** as a colorless solid (1.56 g, 2.06 mmol, 93%). ^{1}H NMR (300 MHz, $CDCl_3$) δ 7.51 – 7.38 (m, 12H), 7.31 (m, 3H), 3.63 – 3.39 (m, 12H), 2.96 (d, *J* = 23.1 Hz, 6H), 1.02 (t, *J* = 7.1 Hz, 18H).

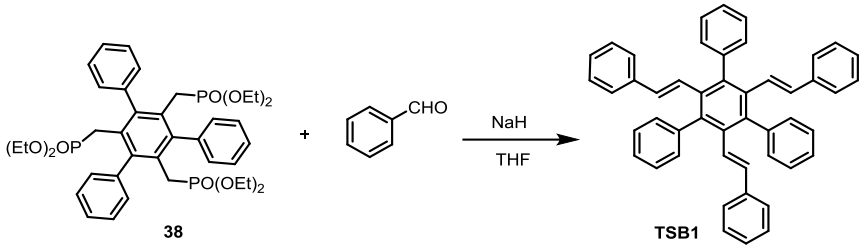

38 TSB1

Synthesis of 5'-phenyl-2',4',6'-tri((E)-styryl)-1,1':3',1''-terphenyl (TSB1). Under a nitrogen atmosphere the triphosphonate **38** (136 mg, 180 µmol, 1.00 eq.) was dissolved in dry THF and the solution was cooled to 0 °C. NaH (86.4 mg, 3.60 mmol, 20.0 eq.) was added carefully and the mixture was stirred at 0 °C for 40 min before the benzaldehyde (115 mg, 1.08 mmol, 6.00 eq.) was added slowly. The reaction mixture was then allowed to warm to RT and further stirred for 3 days. After removing THF solvent on a rotary evaporator, the residues were purified on silica gel column (silica gel, PE/DCM = 3:1, R_f = 0.35) to yield the desired product **TSB1** as a colorless powder (105 mg, 167 µmol, 93%). M.p. : 264 – 265 °C. IR (neat): υ = 3054, 3022, 2922, 1599, 1490, 1443, 1272, 1073, 965, 758, 691, 518. ^{1}H NMR (600 MHz, $CDCl_3$) δ 7.43 – 7.29 (m, 15H), 7.18 – 7.00 (m, 9H), 6.75 (d, *J* = 7.1 Hz, 6H), 6.50 (d, *J* = 16.8 Hz, 3H), 5.81 (d, *J* = 16.8 Hz, 3H). ^{13}C NMR (150 MHz, $CDCl_3$) δ 140.9, 139.5, 138.2, 135.7, 135.3, 131.5, 128.4, 128.2, 128.1, 127.1, 126.9, 126.2. HRMS (DART): m/z $[M+H]^+$ calcd for $C_{48}H_{37}$ 613.2890, found 613.2875.

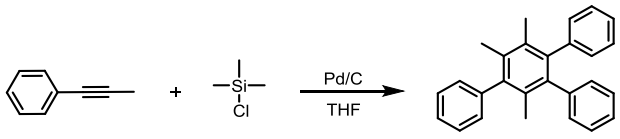

39 40

Synthesis of 3',4',6'-trimethyl-5'-phenyl-1,1':2',1''-terphenyl (40).[170] 1-Phenyl-l-propyne **39** (5.20 mL, 41.0 mmol, 1.00 eq.), trimethylsilyl chloride (5.20 mL, 41.0 mmol, 1.00 eq.), 1.00 g of Pd/C (10 %), and 15 mL of THF were refluxed for 7 days. After filtration of the reaction mixture, the brown solid obtained was recrystallized from chloroform and then subjected to column chromatography (silica gel, PE/EA = 50:1) and yielded the product **40** as colorless solid (2.57 g, 7.38 mmol, 18%). ^{1}H NMR (300 MHz, $CDCl_3$) δ 7.48 - 6.95 (m, 15H), 2.05 (s, 6H), 1.72 (s, 3H).

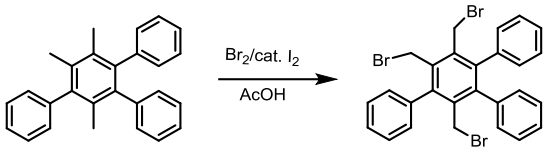

40 41

Synthesis of 3',4',6'-tris(bromomethyl)-5'-phenyl-1,1':2',1''-terphenyl (41). Compound **40** (539 mg, 1.55 mmol, 1.00 eq.) was dissolved in acetic acid (150 mL). Bromine (1.59 mL, 30.9 mmol, 20.0 eq.) and a catalytical amount of iodine were added and the reaction mixture was refluxed for 5 h. The reaction mixture was allowed to cool to room temperature slowly. After addition of 200 mL water, the precipitate was collected via filtration and washed thoroughly with water to yield **41** as a light brown solid without further purification (801 mg, 1.36 mmol, 88%). Melting point: 179-180 °C. IR (neat): υ = 3055, 3022, 1600, 1495, 1441, 1302, 1203, 1072, 995, 921, 833, 748, 691, 593, 526. ^{1}H NMR (600 MHz, $CDCl_3$) δ 7.63 – 7.44 (m, 6H), 7.23 – 7.04 (m, 9H), 4.51 (s, 4H), 3.98 (m, 2H). ^{13}C NMR (150 MHz, $CDCl_3$) δ 144.1, 144.1, 144.0, 138.3, 137.2, 135.9, 135.6, 130.2, 130.1, 129.8, 128.6, 128.6, 127.9, 127.7, 127.4, 127.3, 30.1, 29.3, 29.1. HRMS (EI): m/z $[M]^+$ calcd for $C_{27}H_{21}Br_3$ 581.91879, found 581.91778.

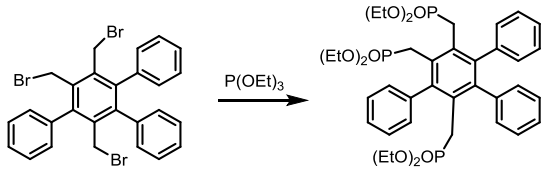

41 42

Synthesis of tetraethyl ((4'-((diethoxyphosphoryl)methyl)-5'-phenyl-[1,1':2',1''-terphenyl]-3',6'-diyl)bis(methylene))bis(phosphonate) (42). Compound **41** (750 mg, 1.28 mmol) and 6.00 mL triethyl phosphite were placed in a flask with a stirring bar. The mixture was heated at 150 °C for 12 h. The excess triethyl phosphite was removed by distillation under reduced pressure. The residue was further dried in vacuo at 50 °C to give the product **42** as a yellow oil (880 mg, 1.16 mmol, 91%). IR (neat): υ = 2980, 2905, 1441, 1391, 1248, 1163, 1022, 956, 773, 701, 517. ^{1}H NMR (300 MHz, $CDCl_3$) δ 7.82 – 7.28 (m, 6H), 7.18 – 6.90 (m, 9H), 4.28 – 3.99 (m, 4H), 3.95 – 3.73 (m, 8H), 3.64 – 3.29 (m, 4H), 3.10 – 2.84 (m, 2H), 1.34 (t, *J* = 7.1 Hz, 6H), 1.24 – 1.07 (m, 6H), 0.98 (t, *J* = 7.3 Hz, 6H). ^{13}C NMR (100 MHz, $CDCl_3$) δ 143.6, 143.2, 141.9, 140.5, 140.2, 131.3, 130.4, 130.2, 129.4, 128.8, 128.5, 128.3, 127.4, 127.0, 126.3, 63.8, 61.8, 61.6, 61.0, 60.9, 31.2, 30.4, 30.3, 29.8, 29.1, 28.9, 16.4, 16.2. HRMS (DART): m/z $[M+H]^+$calcd for $C_{39}H_{52}O_9P_3$ 757.2819, found 757.2822.

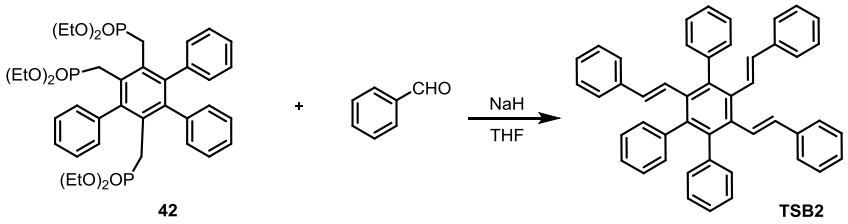

42 TSB2

Synthesis of 4'-phenyl-3',5',6'-tri((E)-styryl)-1,1':2',1''-terphenyl (TSB2). Under a nitrogen atmosphere the triphosphonate **42** (136 mg, 180 µmol, 1.00 eq.) was dissolved in dry THF and the solution was cooled to 0 °C. NaH (86.4 mg, 3.60 mmol, 20.0 eq.) was added carefully and the mixture was stirred at 0 °C for 40 min before benzaldehyde (115 mg, 1.08 mmol, 6.00 eq.) was added slowly. The reaction mixture was then allowed to warm to RT and further stirred for 3 days. After removing THF solvent on a rotary evaporator, the residues were purified on silica gel column (silica gel, PE/DCM = 2:1, R_f = 0.28) to yield the desired **TSB2** as a light yellow solid (74.4 mg, 120 µmol, 67%). M.p. : 186-187 °C. IR (neat): υ = 3055, 3022, 1598, 1492, 1442, 1263, 1072, 965, 750, 693, 516. ^{1}H NMR (300 MHz, $CDCl_3$) δ 7.83 – 7.46 (m, 6H), 7.48 – 7.19 (m, 24H), 6.90 (t, J = 9.1 Hz, 2H), 6.82 – 6.39 (m, 3H), 5.95 (m, 1H). ^{13}C NMR (150 MHz, $CDCl_3$) δ 140.9, 140.7, 140.2, 138.2, 135.8, 135.5, 135.1, 134.7, 132.9, 131.5, 129.7, 128.5, 128.2, 127.4, 127.3, 126.9, 126.3, 126.1. HRMS (DART): m/z $[M+H]^+$calcd for $C_{48}H_{37}$ 613.2890, found 613.2884.

Synthesis of TSB1a. Under argon atmosphere, **TSB1** (58.0 mg, 95.0 µmol) was dissolved in THF (20 mL) and irradiated for 1.5 h in a photoreactor (λ = 300 nm). After removing THF solvent on a rotary evaporator, the residues were purified on silica gel column (silica gel, PE/DCM = 3:1, R_f = 0.36) to yield **TSB1a** isomers as colorless solid (47.8 mg, 77.9 µmol, 82%). ^{1}H NMR (300 MHz, CD_2Cl_2) δ 7.53 (m, 3H), 7.46 – 7.24 (m, 9H), 7.26 – 6.48 (m, 15H), 4.36 – 3.82 (m, 3H), 3.77 – 3.43 (m, 2H), 3.14 – 2.53 (m, 4H). As these isomers were inseparable via preparative methods, no further data will be given. The absorption and emission spectra of **TSB1a-2** were shown in Figure 29.

Synthesis of TSB2a. Under argon atmosphere, **TSB2** (58.0 mg, 95.0 µmol) was dissolved in THF (20 ml) and irradiated for 1.5 h in a photoreactor (λ = 300 nm). After removing THF solvent on a rotary evaporator, the residues were purified on silica gel column (silica gel, PE/DCM = 6:1, R_f = 0.2) to yield **TSB2a** isomers as colorless solid (44.8 mg, 73.2 µmol, 77%). ^{1}H NMR (300 MHz, CD_2Cl_2) δ 7.43 – 7.21 (m, 12H), 7.18 – 6.70 (m, 15H), 4.26 – 3.98 (m, 3H), 3.35 – 2.74 (m, 6H). As these isomers were inseparable via preparative methods, no further data will be given. The absorption and emission spectra of **TSB2a-isomers** were shown in Figure 29.

5.2.2 Synthesis of SBs (Chapter 2.2)

General Procedure 1 (GP1): Synthesis of intermediates **50-52** by Heck reaction. The reaction was performed in a heat-gun-dried 50 mL Schlenk tube under a nitrogen atmosphere. The brominated intermediate (1.00 eq.) and the vinyl compound (1.14 eq.) were dissolved in dry DMF. $Pd(OAc)_2$ (5 mol%), tris(*o*-tolyl)phosphine (10 mol%) and dry triethylamine (800 µL) were added and the mixture was stirred at 110 °C for 48 h. After the reaction mixture was cooled to ambient temperature, it was poured into water to give a suspension which was extracted with DCM. The combined organic layers were washed with brine, dried over $MgSO_4$ and the solvents were removed under reduced pressure. The residues were purified by column chromatography.

General Procedure 2 (GP2): Synthesis of symmetric **TSB3**, **TSB6** and **TSB7** by Wittig-Horner reaction. Under nitrogen atmosphere, the triphosphonate **55** (1.00 eq) was dissolved in dry THF and the solution was cooled to 0 °C. NaH (15.0 eq) was added carefully and the mixture was stirred at 0 °C for 40 min before the monoaldehyde **50-52** (4.50 eq) was added slowly. The reaction mixture was then allowed to warm to RT and further stirred for 3 days. After removing THF on a rotary evaporator, the residues were purified on silica gel column.

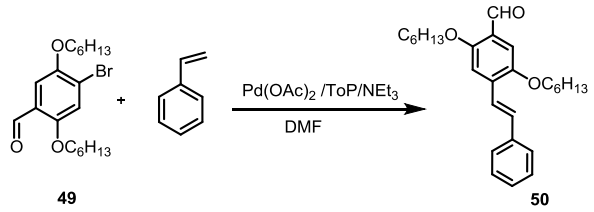

49 **50**

Compound **48** and **49** was synthesized according to the literature.[171]

Synthesis of 2,5-Bis(hexyloxy)-4-styrylbenzaldehyde (50).[113] According to **GP1** a solution of monoaldehyde **49** (694 mg, 1.80 mmol, 1.00 eq.), styrene (214 mg, 2.00 mmol, 1.12 eq.), $Pd(OAc)_2$ (20.2 mg, 90 µmol, 0.050 eq.), tris(*o*-tolyl)phosphine (54.8 mg, 180 µmol, 0.100 eq.) and triethylamine (1.40 mL) in DMF (20 mL) was stirred at 110 °C for 48 h. Column chromatography (silica gel, PE/EA = 20:1, R_f = 0.50) afforded **50** as a yellow solid (111 mg, 272 µmol, 30%). ^{1}H NMR (300 MHz, $CDCl_3$) δ 10.45 (s, 1H), 7.61 – 7.52 (m, 2H), 7.38 (m, 2H), 7.35 – 7.20 (m, 4H), 7.18 (s, 1H), 4.12 (t, *J* = 6.4 Hz, 2H), 4.03 (t, *J* = 6.5 Hz, 2H), 1.93 – 1.78 (m, 4H), 1.53 (m, 4H), 1.45 – 1.30 (m, 8H), 0.98 – 0.86 (m, 6H).

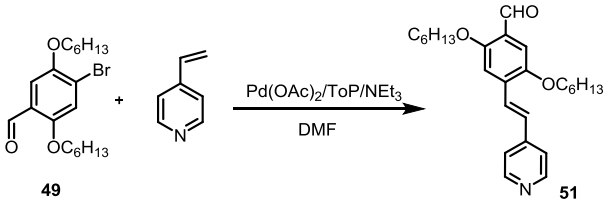

49 **51**

Synthesis of 2,5-Bis(hexyloxy)-4-(2-(pyridin-4-yl)vinyl)benzaldehyde (51). According to **GP1** a solution of monoaldehyde **49** (385 mg, 1.00 mmol, 1.00 eq.), 4-vinylpyridine (214 mg, 1.14 mmol, 1.14 eq.), $Pd(OAc)_2$ (11.2 mg, 50.0 µmol, 0.050 eq.), tris(*o*-tolyl)phosphine (30.4 mg, 100 µmol, 0.100 eq.) and triethylamine (0.7 mL) in DMF (10 mL) was stirred at 110 °C for 48 h. Column chromatography (silica gel, PE/EA = 5:1, R_f = 0.20) afforded **51** as a yellow viscous oil (343 mg, 840 µmol, 84%). ^{1}H NMR (300 MHz, $CDCl_3$) δ 10.59 (s, 1H), 8.73 (d, *J* = 5.2 Hz, 2H), 7.78 (d, *J* = 16.5 Hz, 1H), 7.52 (d, *J* = 5.6 Hz, 2H), 7.47 (s, 1H), 7.30 (t, *J* = 8.2 Hz, 2H), 4.24 (t, *J* = 6.5 Hz, 2H), 4.16 (t, *J* = 6.5 Hz, 2H), 2.11 – 1.90 (m, 4H), 1.72 – 1.27 (m, 14H), 1.05 (dd, *J* = 6.4, 4.4 Hz, 6H). ^{13}C NMR (125 MHz, $CDCl_3$) δ 189.1, 156.0, 151.1, 150.2, 144.7, 132.7, 129.4, 127.6, 125.1, 121.1, 111.3, 110.3, 69.3, 69.2, 31.6, 29.2, 25.9, 22.7, 14.1. IR (cm^{-1}): 2928, 2857, 1676, 1601, 1422, 1206, 1018, 529. HRMS (DART): m/z $[M+H]^+$ calcd for $C_{26}H_{36}NO_3$ 410.2690, found 410.2687.

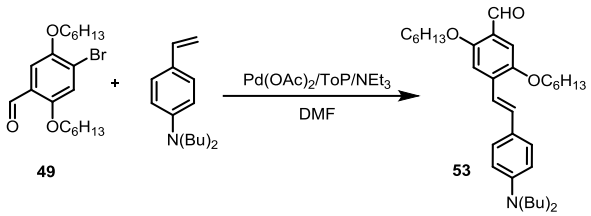

Compound *N*,*N*-Dibutyl-4-vinylaniline was synthesized according to the literature.[172]

Synthesis of 4-(4-(Dibutylamino)styryl)-2,5-bis(hexyloxy)benzaldehyde (53). According to **GP1** a solution of monoaldehyde **49** (771 mg, 2.00 mmol, 1.00 eq), 4-dibutylaminostyrene (509 mg, 2.20 mmol, 1.10 eq), $Pd(OAc)_2$ (22.4 mg, 100 µmol, 0.050 eq.), tris(*o*-tolyl)phosphine (60.9 mg, 200 µmol, 0.100 eq) and triethylamine (1.5 mL) in DMF (20 mL) was stirred at 110 °C for 48 h. Column chromatography (silica gel, PE/EA = 20:1, R_f = 0.50) afforded **53** as a yellow viscous oil (582 mg, 1.10 mmol, 54%). ^{1}H NMR (400 MHz, $CDCl_3$) δ 10.42 (s, 1H), 7.41 (d, *J* = 8.7 Hz, 1H), 7.32 – 7.27 (m, 1H), 7.25 – 7.03 (m, 3H), 6.67 – 6.40 (m, 3H), 4.17 – 3.93 (m, 4H), 3.39 – 3.20 (m, 4H), 1.91 – 1.74 (m, 4H), 1.63 – 1.47 (m, 8H), 1.42 – 1.26 (m, 12H), 0.92 (m, 12H). ^{13}C NMR (100 MHz, $CDCl_3$) δ 189.4, 189.2, 156.6, 155.8, 151.1, 150.5, 148.5, 147.7, 136.2, 135.9, 132.9, 132.8, 130.5, 128.5, 124.5, 123.9, 123.7, 123.4, 120.7, 117.6, 114.8, 111.7, 111.1, 110.2, 109.9, 109.7, 69.4, 69.3, 50.9, 31.7, 29.7, 29.4, 26.0, 22.8, 20.5, 14.2, 14.1. IR (cm^{-1}): 2955, 2928, 2870, 1682, 1612, 1519, 1466, 1366, 1214, 1186, 811. HRMS (DART): m/z $[M+H]^+$ calcd for $C_{35}H_{54}NO_3$ 536.4098, found 536.4101.

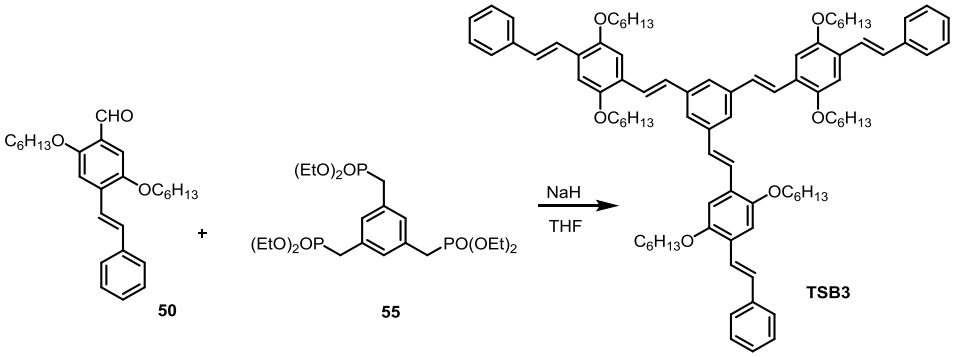

Compound **55**[173]was synthesized according to the literature.

Synthesis of 1,3,5-Tris((*E*)-2,5-bis(hexyloxy)-4-((*E*)-styryl)styryl)benzene (TSB3). According to **GP2** a solution of triphosphonate **55** (42.3 mg, 80.0 µmol, 1.00 eq.) in dry THF (8 mL) was treated with NaH (28.8 mg, 1.20 mmol, 15.0 eq.) and monoaldehyde **50** (105 mg, 256 µmol, 3.20 eq.) was added. The crude product was purified by column chromatography (silica gel, PE/EA = 20:1, R_f = 0.41) to yield the desired compound **TSB3** as a yellow green powder (79.6 mg, 61.6 µmol, 77%). M.p. : 110-111 °C. ^{1}H NMR (600 MHz, $CDCl_3$) δ 7.66 – 7.49 (m, 15H), 7.39 (t, *J* = 7.6 Hz, 6H), 7.32 – 7.22 (m, 6H), 7.22 – 7.14 (m, 9H), 4.11 (dd, *J* = 15.1, 6.6 Hz, 12H), 1.99 – 1.85 (m, 12H), 1.59 (td, *J* = 13.5, 7.0 Hz, 12H), 1.48 – 1.34 (m, 24H), 0.93 (dt, *J* = 25.7, 6.8 Hz, 18H). ^{13}C NMR (150 MHz, $CDCl_3$) δ 151.3, 151.2, 138.7, 138.1, 129.0, 128.9, 128.7, 127.5, 127.1, 126.6, 124.1, 123.6, 111.0, 110.8, 69.7, 31.7, 29.5, 26.1,

22.8, 14.2. IR (cm^{-1}): 2926, 2856, 2360, 1419, 1199, 958, 750, 690, 598, 506. HRMS (MALDI): m/z $[M]^+$ calcd for $C_{91}H_{114}O_6$ 1290.8615, found 1290.947.

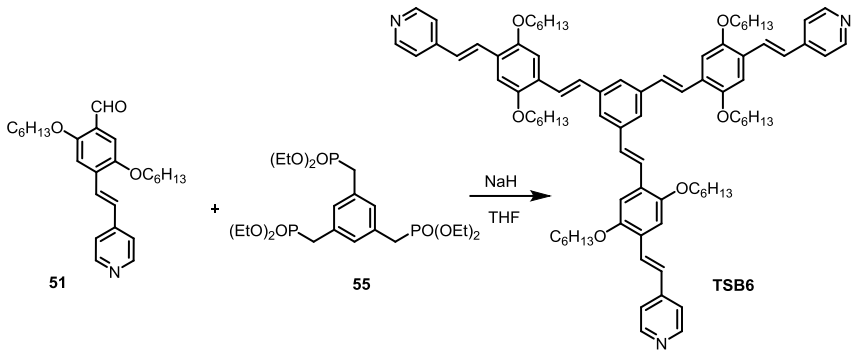

Synthesis of 1,3,5-Tris((*E*)-2,5-bis(hexyloxy)-4-((*E*)-2-(pyridin-4-yl)vinyl)styryl)benzene (TSB6). According to **GP2** a solution of triphosphonate **55** (42.3 mg, 80.0 µmol, 1.00 eq.) in dry THF (8 mL) was treated with NaH (28.8 mg, 1.20 mmol, 15.0 eq.) and monoaldehyde **51** (114.7 mg, 280 µmol, 3.50 eq.) was added. The crude product was purified by column chromatography (silica gel, DCM/MeOH = 50:1, R_f = 0.35) to yield the desired compound **TSB6** as an orange solid (34.9 mg, 26.9 µmol, 33%). M.p. : 122–123 °C. ^{1}H NMR (600 MHz, $CDCl_3$) δ 8.58 – 8.50 (d, *J* = 5.4 Hz, 6H), 7.71 – 7.39 (m, 12H), 7.23 – 6.63 (m, 15H), 4.01 – 3.93 (m, 12H), 1.91 – 1.83 (m, 12H), 1.58 (m, 12H), 1.39 – 1.27 (m, 24H), 0.96 – 0.89 (m, 18H). ^{13}C NMR (150 MHz, $CDCl_3$) δ 151.9, 151.5, 151.4, 150.8, 150.4, 149.9, 145.6, 139.0, 138.8, 130.4, 130.3, 129.9, 128.5, 128.3, 126.3, 126.2, 125.7, 125.6, 124.6 124.3, 124.2, 121.1, 115.9, 111.3, 111.0, 109.6, 69.9, 69.7, 68.8, 32.2, 31.9, 29.9, 29.7, 26.3, 26.2, 22.9, 14.4. IR (cm^{-1}): 2925, 2856, 2320, 1591, 1498, 1416, 1204, 966, 803, 517. HRMS (MALDI): m/z $[M+H]^+$ calcd for $C_{87}H_{112}N_3O_6$ 1295.8629, found 1295.8624.

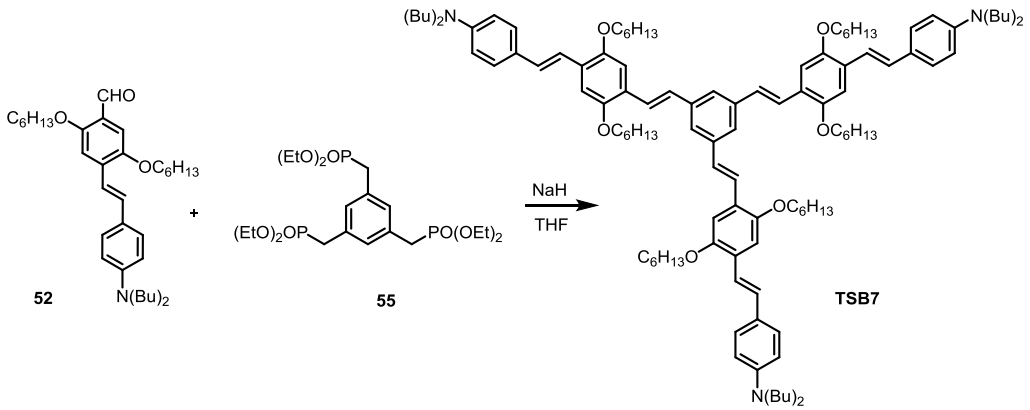

Synthesis of 4,4',4''-((1*E*,1'*E*,1''E)-(((1*E*,1'*E*,1''*E*)-benzene-1,3,5-triyltris(ethene-2,1-diyl))tris(2,5-bis(hexyloxy)benzene-4,1-diyl))tris(ethene-2,1-diyl))tris(N,N-dibutylaniline) (TSB7). According to **GP2** a solution of triphosphonate **55** (42.3 mg, 80.0 µmol, 1.00 eq.) in dry THF (8 mL) was treated with NaH (28.8 mg, 1.20 mmol, 15.0 eq.) and monoaldehyde **52** (137 mg, 256 µmol, 3.20 eq.) was added. The crude product was purified by column chromatography (silica gel, PE/DCM = 2:1 + 2% triethylamine, R_f = 0.45) to yield the desired compound **TSB7** as an orange viscous oil (90.9 mg, 54.3 µmol, 68%).^{1}H NMR (600 MHz, $CDCl_3$) δ 7.61 – 7.37 (m, 5H), 7.33 (d, *J* = 8.4 Hz, 4H), 7.26 – 7.03

(m, 11H), 7.03 – 6.89 (m, 4H), 6.82 – 6.65 (m, 1H), 6.62 – 6.15 (m, 7H), 4.16 – 3.60 (m, 12H), 3.18 (m, 12H), 1.92 – 1.63 (m, 12H), 1.48 (m, 24H), 1.41 – 1.26 (m, 24H), 1.25 – 1.07 (m, 12H), 0.95 – 0.73 (m, 36H). ^{13}C NMR (150 MHz, $CDCl_3$) δ 153.4, 151.4, 150.8, 147.8, 146.5, 138.9, 131.0, 130.3, 129.2, 128.6, 128.4, 128.3, 127.9, 127.7, 125.9, 125.8, 125.3, 124.3, 124.1, 118.4, 115.4, 114.0, 112.6, 112.0, 111.7, 111.2, 110.1, 69.8, 50.9, 31.8, 29.6, 27.8, 26.1, 22.8, 20.5, 16.0, 14.2. IR (cm^{-1}): 2953, 2926, 2857, 1607, 1519, 1366, 1185, 1030, 962, 805, 523. HRMS (MALDI): m/z $[M+H]^+$ calcd for $C_{114}H_{165}N_3O_6$ 1673.2777, found 1673.293. Elemental analysis calcd. (%) for $C_{114}H_{165}N_3O_6$: C 81.82; H 9.94; N 2.51; found: C 81.60, H 10.76, N 2.45.

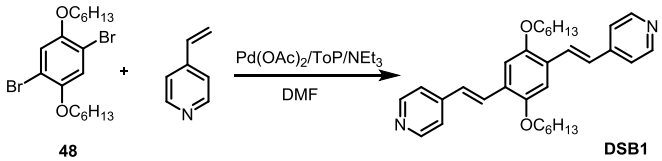

48 DSB1

Synthesis of 4,4'-((1*E*,1'*E*)-(2,5-bis(hexyloxy)-1,4-phenylene)bis(ethene-2,1-diyl))dipyridine (DSB1). Under nitrogen atmosphere, a solution of **48** (218 mg, 500 µmol, 1.00 eq.), 4-vinylpyridine (118 mg, 1.20 mmol, 2.40 eq.), $Pd(OAc)_2$ (11.2 mg, 50 µmol, 0.100 eq.), tris(*o*-tolyl)phosphine (30.4 mg, 100 µmol, 0.200 eq.) and triethylamine (1.20 mL) in dry DMF (10 mL) was stirred at 110 °C for 48 h. After the reaction mixture was cooled to ambient temperature, it was poured into water to give a suspension which was extracted with DCM. The combined organic layers were washed with brine dried over $MgSO_4$ and the solvents were removed under reduced pressure. The residues were purified by column chromatography (silica gel, DCM/EE = 5:1, R_f = 0.21) and afforded **DSB1** as a yellow solid (110 mg, 225 µmol, 45%). M.p.: 135-136 °C. ^{1}H NMR (300 MHz, $CDCl_3$) δ 8.58 (d, *J* = 6.0 Hz, 4H), 7.70 (s, 1H), 7.64 (s, 1H), 7.38 (d, *J* = 6.0 Hz, 4H), 7.18 – 7.08 (m, 3H), 7.05 (s, 1H), 4.08 (t, *J* = 6.5 Hz, 4H), 1.95 – 1.82 (m, 4H), 1.63 – 1.49 (m, 4H), 1.47 – 1.33 (m, 8H), 0.93 (t, *J* = 7.0 Hz, 6H). ^{13}C NMR (100 MHz, $CDCl_3$) δ 151.7, 150.1, 149.8, 145.4, 129.7, 128.3, 128.2, 127.6, 126.9, 126.7, 126.5, 126.0, 123.6, 121.0, 114.6, 114.1, 111.2, 110.9, 69.7, 31.8, 29.5, 26.1, 22.8, 14.2. IR (cm^{-1}): 2942, 2915, 2360, 1592, 1476, 1209, 1028, 968, 850, 803, 596, 525. HRMS (MALDI): m/z $[M+H]^+$ calcd for $C_{32}H_{41}N_2O_2$ 485.3168, found 485.372.

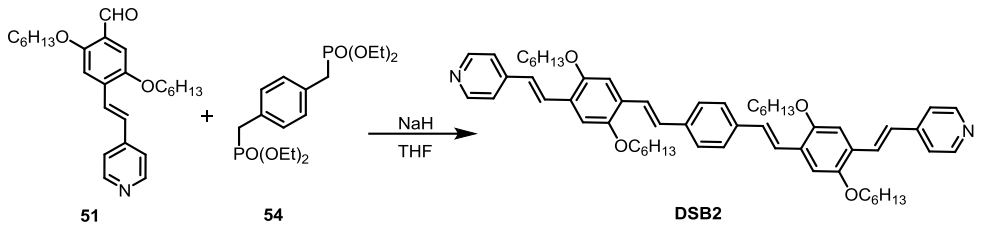

51 54 DSB2

Compound **54**[174] was synthesized according to the literature.

Synthesis of 1,4-Bis((*E*)-2,5-bis(hexyloxy)-4-((*E*)-2-(pyridin-4-yl)vinyl)styryl)benzene (DSB2). Under a nitrogen atmosphere, the bisphosphonate **54** (45.4 mg, 120 µmol, 1.00 eq.) was dissolved in dry THF (10 mL) and the solution was cooled to 0 °C. NaH (28.8 mg, 1.20 mmol, 10.0 eq.) was added

carefully and the mixture was stirred at 0 °C for 40 min before monoaldehyde **51** (103 mg, 252 µmol, 2.10 eq.) was added slowly. The reaction mixture was then allowed to warm to RT and further stirred for 2 days. After removing THF on a rotary evaporator, the residues were purified on silica gel column (silica gel, PE/EA = 20:1, R_f = 0.19) to yield the desired compound **DSB2** as an orange solid (87.9 mg, 98.9 µmol, 82%). M.p.: 147-148 °C. ^{1}H NMR (600 MHz, $CDCl_3$) δ 8.53 (m, 4H), 7.68 (d, *J* = 16.4 Hz, 2H), 7.61 – 7.42 (m, 6H), 7.38 (d, *J* = 6.0 Hz, 3H), 7.22 – 6.97 (m, 9H), 4.20 – 3.74 (m, 8H), 1.99 – 1.73 (m, 8H), 1.70 – 1.48 (m, 8H), 1.50 – 1.21 (m, 16H), 1.09 – 0.80 (m, 12H). ^{13}C NMR (150 MHz, $CDCl_3$) δ 151.7, 151.1, 150.2, 149.7, 145.4, 137.3, 129.2, 128.3, 128.2, 127.0, 126.0, 125.5, 124.1, 123.2, 120.9, 111.1, 110.5, 69.6, 31.7, 29.6, 29.5, 26.1, 22.8, 14.2. IR (cm^{-1}): 2931, 2853, 1590, 1397, 1207, 1034, 961, 847, 726, 525. HRMS (MALDI): m/z [M]$^+$ calcd for $C_{60}H_{76}N_2O_4$ 888.5805, found 888.5835.

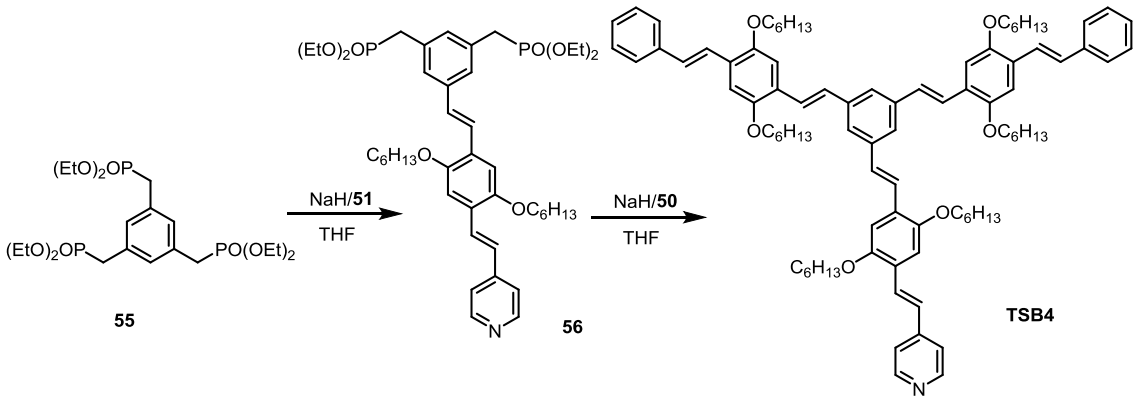

Synthesis of 4-((*E*)-4-((*E*)-3,5-bis((*E*)-2,5-bis(hexyloxy)-4-((*E*)-styryl)styryl)styryl)-2,5-bis(hexyloxy)styryl)pyridine (TSB4). Under a nitrogen atmosphere, the triphosphonate **55** (42.3 mg, 80 µmol, 1.00 eq.) was dissolved in dry THF (10 mL) and the solution was cooled to 0 °C. NaH (28.8 mg, 1.2 mmol, 15.0 eq.) was added carefully and the mixture was stirred at 0 °C for 40 min before monoaldehyde **51** (35.4 mg, 86.8 µmol, 1.09 eq.) was added slowly. The reaction mixture was stirred overnight at room temperature. After removing THF in vacuo, the residues containing **56** were dried and used in the next step without further purification. To a solution of **56** in dry THF (8 mL) was added NaH (28.8 mg, 1.20 mmol, 15.0 eq.) at 0 °C. The mixture was stirred at 0 °C for 40 min, and then another monoaldehyde **50** (71.9 mg, 176 µmol, 2.20 eq.) was added. The reaction mixture was then allowed to warm to RT and further stirred for 2 days. After removing THF on a rotary evaporator, the crude product was purified by column chromatography (silica gel, PE/EA = 1:1, R_f = 0.49) to yield the desired compound **TSB4** as an orange solid (29.8 mg, 23.1 µmol, 28% over two steps). M.p.: 71–72 °C**.** ^{1}H NMR (600 MHz, $CDCl_3$) δ 8.69 (d, *J* = 5.8 Hz, 2H), 7.82 (d, *J* = 16.4 Hz, 1H), 7.74 – 7.60 (m, 12H), 7.49 (m, 6H), 7.37 (dd, *J* = 16.3, 7.8 Hz, 4H), 7.34 – 7.23 (m, 9H), 7.19 (d, *J* = 16.4 Hz, 1H), 4.20 (dt, *J* = 10.9, 6.5 Hz, 12H), 2.07 – 1.98 (m, 12H), 1.74 – 1.66 (m, 12H), 1.57 – 1.47 (m, 24H), 1.08 – 0.99 (m, 18H). ^{13}C NMR (150 MHz, $CDCl_3$) δ 151.8, 151.2, 150.1, 145.5, 138.8, 138.5, 138.0, 129.8, 128.9, 128.7, 128.4, 128.31, 127.5, 127.0, 126.6, 125.9, 125.5, 124.3, 123.6, 120.9, 111.0, 110.7, 69.7, 31.7, 29.5, 26.1, 22.8, 14.2. IR (cm^{-1}): 2925, 2856, 2359, 1590, 1420, 1202, 1029, 960, 690, 507. HRMS (MALDI): m/z [M+H]$^+$ calcd for $C_{89}H_{114}NO_6$ 1292.8646, found 1292.963.

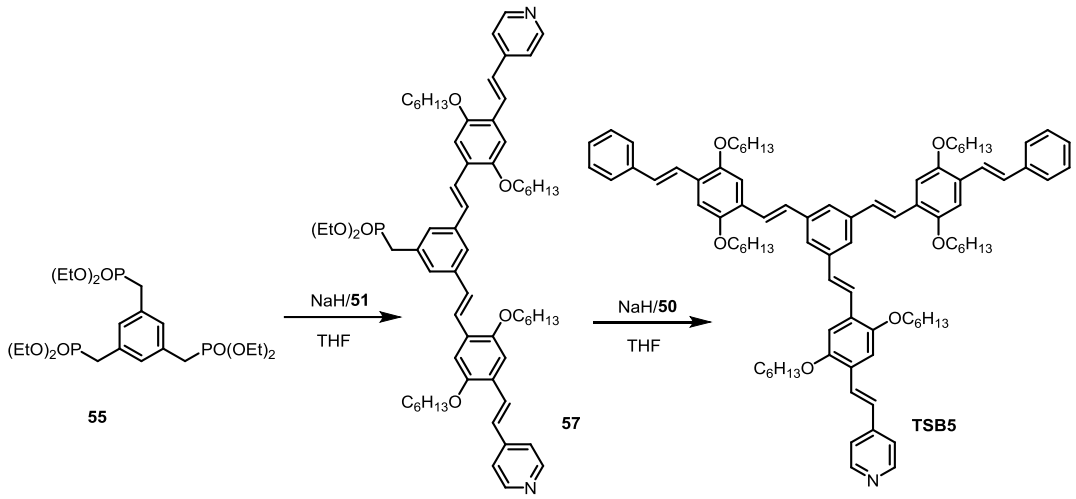

Synthesis of 4,4'-({5-[(*E*)-2-{2,5-bis(hexyloxy)-4-[(*E*)-2-phenylethenyl]phenyl}ethenyl]-1,3-phenylene}bis{[(*E*)ethene-2,1-diyl][2,5-bis(hexyloxy)-4,1-phenylene](*E*)ethene-2,1-diyl})dipyridine (TSB5). Under a nitrogen atmosphere, the triphosphonate **55** (42.3 mg, 80.0 µmol, 1.00 eq.) was dissolved in dry THF (8 mL) and the solution was cooled to 0 °C. NaH (28.8 mg, 1.20 mmol, 15.0 eq) was added carefully and the mixture was stirred at 0 °C for 40 min before monoaldehyde **51** (70.8 mg, 174 µmol, 2.18 eq.) was added slowly. The reaction mixture was stirred overnight at room temperature. After removing THF on a rotary evaporator, the residues containing **57** were dried and used in the next step without further purification. To a solution of **57** in dry THF (8 mL) was added NaH (28.8 mg, 1.20 mmol, 15.0 eq.) at 0 °C. The mixture was stirred at 0 °C for 40 min, and then another monoaldehyde **50** (36.1 mg, 88.0 µmol, 1.10 eq.) was added. The reaction mixture was then allowed to warm to RT and further stirred for 2 days. After removing THF on a rotary evaporator, the crude product was purified by column chromatography (silica gel, EE/MeOH = 50:1, R_f = 0.58) to yield the desired compound **TSB5** as an orange solid (46.4 mg, 35.8 µmol, 44% over two steps). M.p.: 121–122 °C. ^{1}H NMR (600 MHz, $CDCl_3$) δ 8.70 (d, *J* = 5.8 Hz, 4H), 7.81 (d, *J* = 16.4 Hz, 2H), 7.75 – 7.58 (m, 9H), 7.56 – 7.45 (m, 6H), 7.42 – 7.32 (m, 4H), 7.27 (m, 7H), 7.19 (d, *J* = 16.4 Hz, 2H), 4.21 (m, 12H), 2.10 – 1.90 (m, 12H), 1.82 – 1.62 (m, 12H), 1.62 – 1.42 (m, 24H), 1.04 (m, 18H). ^{13}C NMR (150 MHz, $CDCl_3$) δ 151.7, 151.3, 151.2, 150.2, 145.4, 138.8, 138.6, 138.0, 129.7, 128.9, 128.8, 128.3, 128.2, 127.6, 127.2, 126.9, 126.6, 126.1, 125.6, 124.3, 124.1, 123.6, 120.9, 111.1, 110.8, 69.7, 31.7, 29.6, 26.1, 22.8, 14.2. IR (cm^{-1}): 2926, 2856, 2360, 1589, 1419, 1203, 962, 690, 527. HRMS (MALDI): m/z $[M+H]^+$ calcd for $C_{88}H_{113}N_2O_6$ 1293.8599, found 1293.919.

5.2.3 Synthesis of PPEs and Procedure for Edman Degradation (Chapter 3.1)

(1) PPE synthesis

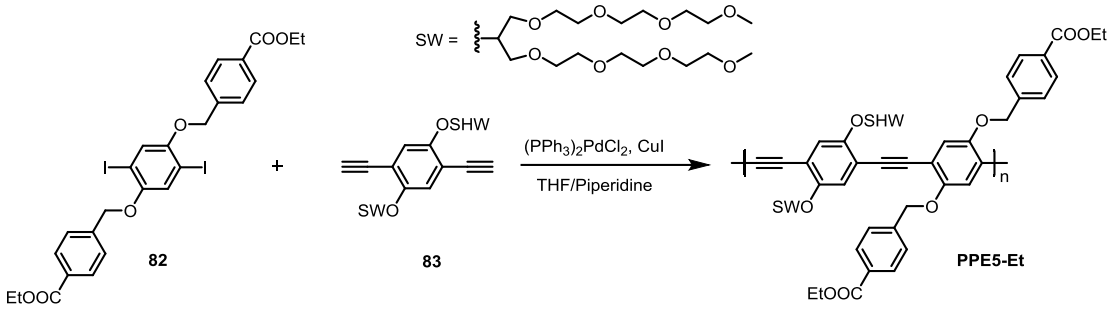

Monomer **82** and **83** were synthesized according to the literature.[140, 175] Polymer **PPE5** and **PPE6** were synthesized by Dr. Benhua Wang. Other polymers were synthesized according to the literature.[85]

Synthesis of PPE5-Et. Monomer **82** (150 mg, 218 µmol, 1.00 eq.) and monomer **83** (194.8 mg, 218.6 µmol, 1.00 eq.) were dissolved in degassed THF/piperidine (1.8 mL/1.3 mL). $Pd(PPh_3)_2Cl_2$ (470 µg, 0.67 µmol, 0.003 eq.) and CuI (260 µg, 1.36 µmol, 0.006 eq.) were then added and the mixture was stirred under nitrogen at room temperature for 2 d. $CHCl_3$ was added to the mixture, and then washed with water, NaCl saturated solution and NH_4Cl saturated solution. The combined organic layers were dried over $MgSO_4$, filtered and concentrated under vacuum. The crude product was dissolved in $CHCl_3$ and slowly added to an excess of n-hexane to give **PPE5-Et** as sticky, dark orange oil (280 mg, 210 µmol, 96%). The M_n was estimated to be 1.3 x 10^4 with a PDI of 1.9. ^{1}H NMR (600 MHz, $CDCl_3$): δ = 8.06-8.04 (m, 4 H), 7.60-7.58 (m, 4 H), 7.09-7.19(m, 4 H), 5.27-5.16 (m, 4 H), 4.49-4.48 (m, 2 H), 4.37-4.34 (m, 4 H), 3.66-3.46 (m, 56 H), 3.33-3.31 (m, 12 H), 1.39-1.36 (m, 6 H) ppm. ^{13}C NMR (150 MHz, $CDCl_3$): δ = 165.1, 152.5, 152.2, 141.0, 128.9, 128.8, 125.7, 119.8, 117.1, 114.8, 113.7, 78.7, 70.8, 70.0, 69.50, 69.4, 59.9, 57.9, 13.3 ppm. IR (cm^{-1}): ν 2916, 2869, 2361, 2342, 1715, 1508, 1489, 1460, 1413, 1364, 1274, 1200, 1100, 1019, 851, 760.

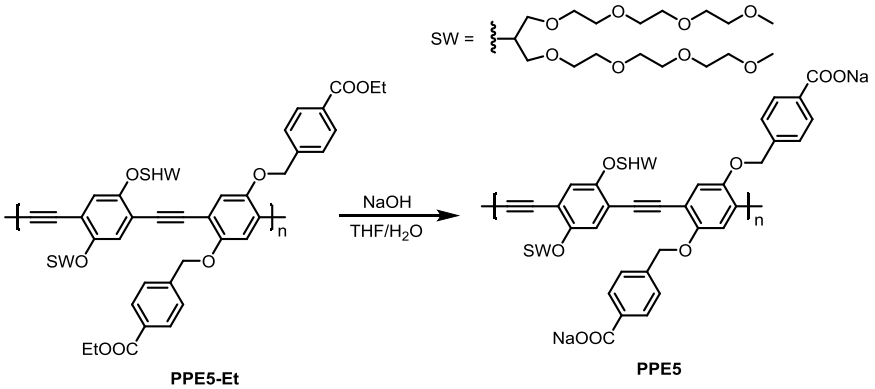

Synthesis of PPE5. NaOH (60.5 mg, 1.51 mmol, 10.0 eq.) was added to a solution of polymer **PPE5-Et** (200 mg, 150 µmol, 1.00 eq.) in THF/H_2O (10 mL/10 mL) and the mixture was stirred at 70 °C for 2 d. After reducing the solvent in vacuo, the residue was dissolved in H_2O and adjusted the pH to 7 by HCl solution and then dialyzed against DI H_2O for 3 d. After freeze-drying, a spongy, yellow solid **P2** (156 mg, 117 µmol, 78%) was obtained. The M_n and PDI result from polymer **PPE5**. ^{1}H NMR (600 MHz, D_2O): δ = 8.19-7.79 (m, 4 H), 7.73-7.33 (m, 4 H), 7.00-6.67 (m, 4 H), 5.16-4.99 (m, 4 H), 3.39-3.23 (m, 58 H), 3.14-3.06 (m, 12 H) ppm. Due to low solubility, ^{13}C NMR spectrum could not be

obtained. IR (cm^{-1}): ν 2868, 2361, 1715, 1508, 1489, 1460, 1412, 1270, 1198, 1091, 1034, 948, 847, 756, 635, 519.

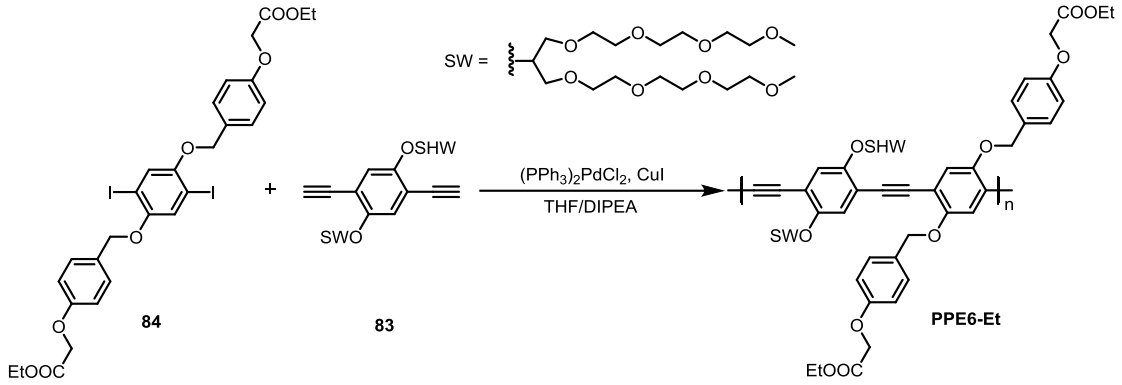

Monomer **84** was synthesized synthesized according to the literature.[140]

Synthesis of PPE6-Et. Monomer **84** (150 mg, 201 µmol, 1.00 eq.) and monomer **83** (179.09 mg, 201 µmol, 1.00 eq.) were dissolved in degassed THF/*N*,*N*-Diisopropylethylamine (1.8 mL/1.3 mL). $Pd(PPh_3)_2Cl_2$ (420 µg, 0.600 µmol, 0.003 eq.) and CuI (230 µg, 1.21 µmol, 0.006 eq.) were added and the mixture was stirred under nitrogen at room temperature for 2 d. $CHCl_3$ were added to the mixture, and then washed with water, NaCl saturated solution and NH_4Cl saturated solution. The combined organic layers were dried over $MgSO_4$, filtered and concentrated under vacuum. The crude product was dissolved in $CHCl_3$ and slowly added to an excess of n-hexane to give **PPE6-Et** as sticky, dark orange oil (230 mg, 167 µmol, 83%). The M_n was estimated to be 8.3 x 10^3 with a PDI of 3.0. ^{1}H NMR (600 MHz, $CDCl_3$): δ = 7.37-7.45 (m, 4 H), 7.13-7.18 (m, 2 H), 7.02-7.07 (m, 2 H), 6.90-6.94 (m, 4 H), 5.02-5.12 (m, 4 H), 4.60-4.62 (m, 4 H), 4.47-4.48 (m, 2 H), 4.23-4.27 (m, 4 H), 3.46-3.68 (m, 56 H), 3.31-3.34 (m, 12 H), 1.24-1.30 (m, 6 H) ppm. ^{13}C NMR (150 MHz, $CDCl_3$): δ = 169.1, 157.9, 153.7, 153.6, 130.3, 129.2, 121.3, 118.7, 117.1, 116.2, 115.0, 72.2, 72.1, 71.3, 70.8, 70.8, 70.7, 70.3, 65.6, 61.6, 59.3, 59.2, 14.5 ppm. IR (cm^{-1}): ν 2869, 2361, 1755, 1509, 1489, 1460, 1417, 1385, 1352, 1197, 1101, 1028, 950, 850, 820, 515.

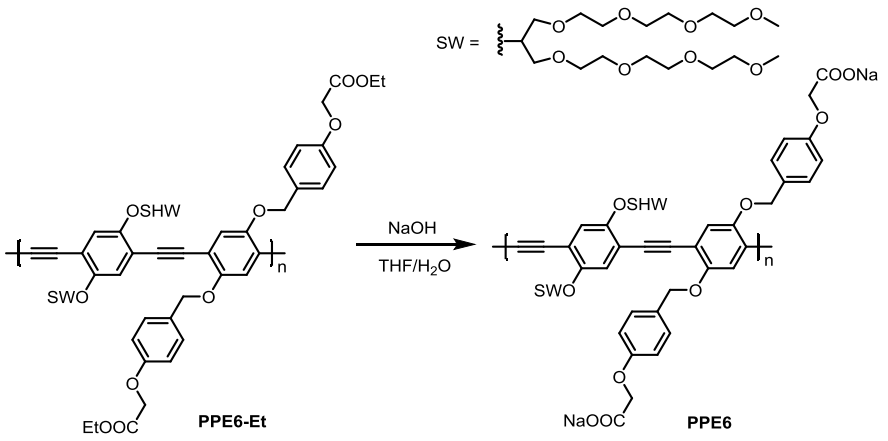

Synthesis of PPE6. NaOH (46.36 mg, 1.16 mmol, 10.0 eq.) was added to a solution of polymer **PPE6-Et** (180 mg, 116 μmol, 1.00 eq.) in THF/H_2O (10 mL/10 mL) and the mixture was stirred at 70 °C for 2 d. After reducing the solvent in vacuo, the residue was dissolved in H_2O and adjusted the pH to 7 by HCl solution and then dialyzed against DI H_2O for 3 d. After freeze-drying, a spongy, yellow solid **PPE6** (170 mg, 110 μmol, 95%) was obtained. The M_n and PDI result from polymer **PPE6-Et**. ^{1}H NMR (600 MHz, D_2O): δ = 7.42-7.28 (m, 4 H), 7.04-6.80 (m, 8 H), 5.08-4.82 (m, 4 H), 4.57-4.44 (m, 6 H), 3.71-3.20 (m, 68 H) ppm. Due to low solubility, ^{13}C NMR spectrum could not be obtained. IR (cm^{-1}): ν 3441, 3355, 2872, 1611, 1512, 1487, 1456, 1415, 1351, 1200, 1075, 1028, 951, 848, 821, 461.

(2) Detailed procedure for Edman degradation

Stepwise degradation for oligopeptide was performed by a modification of a previously described method.[127]

(a) Preparation of the PTC-peptide. To a glass centrifuge tube, 28.9 mg of Met-Ala-Ser was added and fully dissolved in 2 mL pyridine-water (1:1, v/v, pH ca. 8.8). Under nitrogen atmosphere, 200 μL phenyl isothiocyanate (PITC) was added to the solution of peptide. The reaction mixture was vigorously stirred (1000 rpm) for 30 minutes in a 50 °C water bath. After the completion of the reaction, the mixture was cooled down to 0 °C. The PTC-derivative was thoroughly washed and extracted using benzene (5-8 times) and the phases were separated by centrifuge for 3 min at 3500 rpm. The excess PITC and side products in upper phase was removed and the water phase was concentrated under a stream of nitrogen, and then dried in vacuum.

(b) Cleavage of the PTC-peptide. Under nitrogen atmosphere, the dried PTC-peptide was treated with anhydrous TFA (300 μL). The cleavage reaction was carried out in a water bath (50 °C, 10 min.). The TFA was removed using a flow of nitrogen and then dried under vacuum. The thiazoline derivative (ATZ-amino acid) was extracted from the remaining peptide with ethyl acetate/H_2O (2:1, v/v, 3 mL). The remaining peptide in water phase (1 mL) was coupled immediately for next round degradation or kept in the freezer. The ATZ-amino acid in the ethyl acetate phase was flushed with N_2 and dried under vacuum.

(c) Transformation of the ATZ-amino acid. Under nitrogen atmosphere, the dried ATZ-amino acid was dispersed in 300 μL 1N HCl and the conversion reaction was carried out in a water bath (80 °C, 10 min.). After the completion of the reaction, the mixture was cooled down to 0 °C. The mixture was extracted 3 times with ethyl acetate and the organic phase containing PTH-amino acid was collected after centrifugation. The ethyl acetate layer was washed with saturated sodium bicarbonate solution followed by washing with brine, then flushed with N_2 and dried under vacuum vacuum. The degradation residue was recrystallized from EtOH to afford final product for the sensing experiments.

In the first cycle, the residue **C1** was obtained with a yield of 80%. The second degradation was performed and the residue **C2** was obtained with a yield of 62%. The residues were dissolved in DMSO

and diluted using water to make a stock solution (2 mg/mL) for sensing experiments and the final concentration was controlled at 1 mg/mL.

5.2.4 Synthesis of PEs (Chapter 3.2 and 3.3)

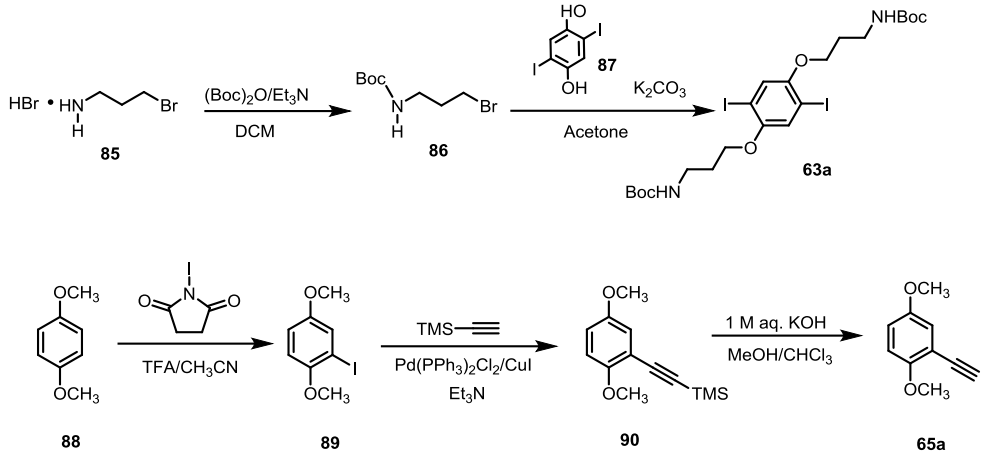

Compound **86**, **87**, **63a**,[176] **89**, **90** and **65a**[177] were synthesized according to the literature.

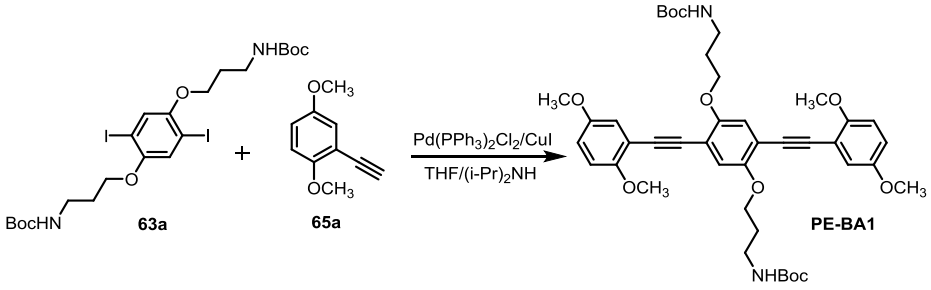

Synthesis of di-tert-butyl (((2,5-bis((2,5-dimethoxyphenyl)ethynyl)-1,4-phenylene)bis(oxy))bis(propane-3,1-diyl))dicarbamate (PE-BA1). A Schlenk flask was charged with compound **63a** (216 mg, 320 μmol, 1.00 eq.), **65a** (182 mg, 1.12 mmol, 3.50 eq.), bis(triphenylphosphine)palladium(II) dichloride $PdCl_2(PPh_3)_2$ (22.5 mg, 32 μmol, 0.100 eq.) and copper(I) iodide (CuI) (12.2 mg, 64 μmol, 0.200 eq.). The flask was evacuated and filled with N_2. A solution of tetrahydrofuran (THF) and diisopropylamine (DIPA) was mixed in a 3:2 ratio (v/v) and degassed with N_2 for 25 min, and 15 mL of the solution was transferred to the flask. The reaction was stirred at 60 °C for 1 d. $CHCl_3$ were added to the mixture, and then washed with water, NaCl saturated solution and NH_4Cl saturated solution. The combined organic layers were dried over $MgSO_4$, filtered and concentrated under vacuum. The resulting residue was purified by silica-gel column chromatography (PE/EE 10:1 to 3:1+2.5% Et_3N), which gave **PE-BA1** (209 mg, 281 μmol, 87%) as a yellow solid. M.p. : 116-118 °C. FT-IR (ATR): $\tilde{\nu}$ (cm^{-1}) = 3420, 3370, 2994, 2931, 1699, 1603, 1498, 1422, 1364, 1269, 1212, 1169, 1042, 718. ^{1}H NMR (301 MHz, $CDCl_3$) δ 7.04 (s, 4H), 6.97 – 6.68 (m, 4H), 5.09 (br, 2H), 4.11 (t, *J* = 5.7 Hz, 4H), 3.86 (s, 6H), 3.77 (s, 6H), 3.48 – 3.36 (m, 4H), 2.14 – 1.93 (m, 4H), 1.34 (s, 18H). ^{13}C NMR (126 MHz, $CDCl_3$) δ 156.2, 154.5, 153.4, 153.2, 118.1, 117.0, 116.0,

114.3, 112.9, 111.9, 91.7, 89.6, 79.0, 67.7, 56.4, 55.8, 38.2, 29.2, 28.3. HRMS (ESI): $[M+Na]^+$ calcd for $C_{42}H_{52}N_2O_{10}Na$: 767.3514; found 767.3529.

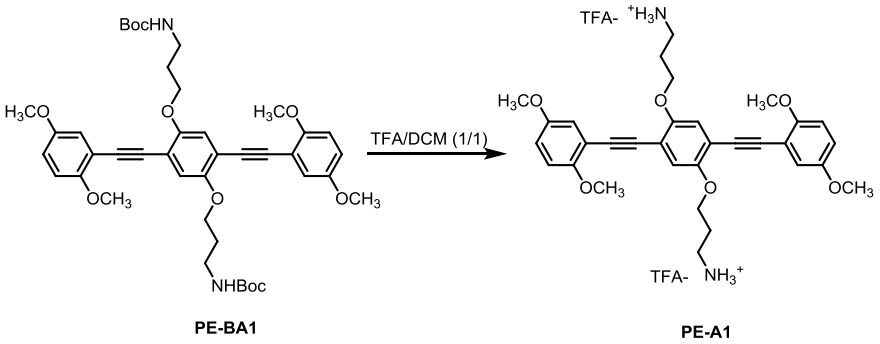

Synthesis of 3,3'-((2,5-bis((2,5-dimethoxyphenyl)ethynyl)-1,4-phenylene)bis(oxy))bis(propan-1-aminium) (PE-A1). PE-BA1 (112 mg, 150 µmol) was dissolved in 5 mL CH_2Cl_2. 5 mL of trifluoroacetic acid (TFA) was added to the solution. The reaction mixture was stirred for 3 min. The excess TFA and the solvent were removed under vacuum. Then the crude product was washed by diethyl ether and pentane to afford **PE-A1** (114 mg, 147 µmol, 98%) as yellow oily solid. FT-IR (ATR): $\tilde{\nu}$ (cm^{-1}) = 3420, 2946, 1675, 1498, 1272, 1201, 1042, 837, 800, 722. ^{1}H NMR (301 MHz, MeOD) δ 7.19 (s, 2H), 7.07 – 6.92 (m, 6H), 4.24 (t, *J* = 5.7 Hz, 4H), 3.88 (s, 6H), 3.78 (s, 6H), 3.27 (t, *J* = 6.9 Hz, 4H), 2.26 – 2.15 (m, 4H). ^{13}C NMR (126 MHz, MeOD) δ 155.7, 154.9, 154.4, 119.4, 118.1, 116.7, 115.5, 113.9, 113.7, 92.6, 90.0, 68.2, 57.0, 56.2, 39.0, 28.1. ^{19}F NMR (471 MHz, MeOD) δ -76.95. HRMS (ESI): $[M+H]^+$ calcd for $C_{32}H_{37}N_2O_6$: 545.2646; found 545.2646.

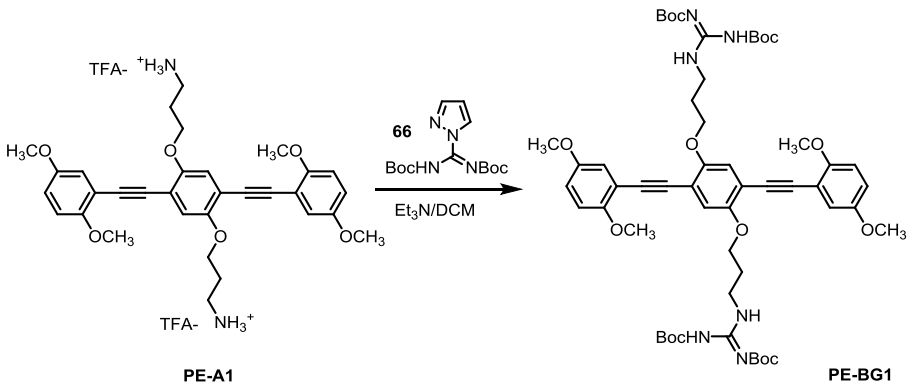

Synthesis of (((2,5-bis((2,5-dimethoxyphenyl)ethynyl)-1,4-phenylene)bis(oxy))bis(propane-3,1-diyl))-*N'*, *N''*-bis (carbamic acid tert-butyl ester) guanidine (PE-BG1). Under N_2 atmosphere, to a solution of **PE-A1** (101 mg, 130 µmol, 1.00 eq.) and Et_3N (0.5 mL) in DCM (20 mL) were added 1-H-pyrazole-1-(N,N'-bis(tert-butyloxycarbonyl))carboxamidine **66** (73 mg, 230 µmol, 1.80 eq.). The resulting solution was stirred at room temperature for 16 h. The resulting residue was purified by silica-gel column chromatography (PE/EE 10:1 to 3:1+2.5% Et_3N), which gave **PE-BG1** (110 mg, 105 µmol, 81%) as a yellow oily solid. FT-IR (ATR): $\tilde{\nu}$ (cm^{-1}) = 3327, 2971, 2929, 1721, 1637, 1618, 1499, 1418, 1368, 1332, 1218, 1135. ^{1}H NMR (500 MHz, $CDCl_3$) δ 11.47 (s, 2H), 8.50 (t, *J* = 5.0 Hz, 2H), 7.10 – 6.96 (m, 4H), 6.84 (dt, *J* = 17.7, 5.9 Hz, 4H), 4.12 (t, *J* = 6.0 Hz, 4H), 3.87 (s, 6H), 3.78 (s, 6H), 3.70

(dd, *J* = 12.5, 6.4 Hz, 4H), 2.27 – 1.90 (m, 4H), 1.47 (d, *J* = 13.6 Hz, 36H). ^{13}C NMR (126 MHz, $CDCl_3$) δ 163.7, 156.4, 154.6, 153.5, 153.2, 117.9, 117.5, 116.1, 114.4, 113.0, 112.1, 91.6, 89.7, 83.2, 79.3, 67.2, 56.5, 55.9, 37.9, 28.4, 28.1. HRMS (ESI): $[M+H]^+$ calcd for $C_{54}H_{73}N_6O_{14}$: 1029.5179; found 1029.5192.

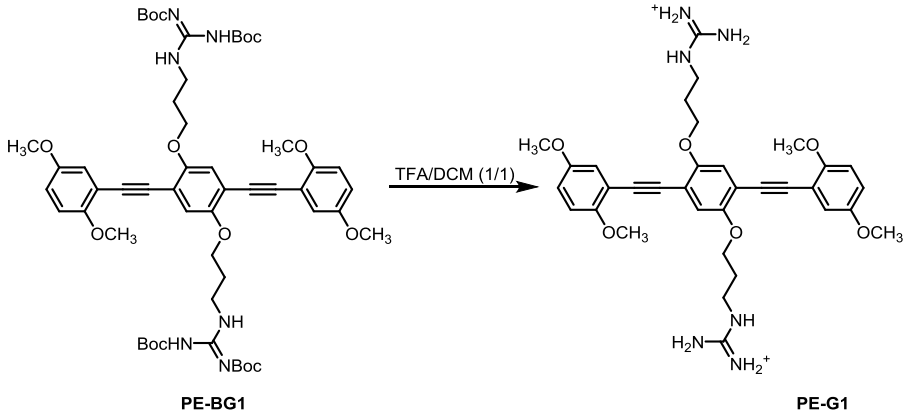

PE-BG1 **PE-G1**

Synthesis of ((((2,5-bis((2,5-dimethoxyphenyl)ethynyl)-1,4-phenylene)bis(oxy))bis(propane-3,1-diyl))bis(azanediyl))bis(aminomethaniminium) (PE-G1 ×). PE-BG1 (12.0 mg, 11.0 μmol) was dissolved in 1 mL CH_2Cl_2. 1 mL of trifluoroacetic acid (TFA) was added to the solution. The reaction mixture was stirred for 30 min/ 45 min /1 h/ 3 h. The excess TFA and the solvent were removed under vacuum. Then the crude product was washed by diethyl ether and pentane, which was proved to be messy by ^{1}H NMR.

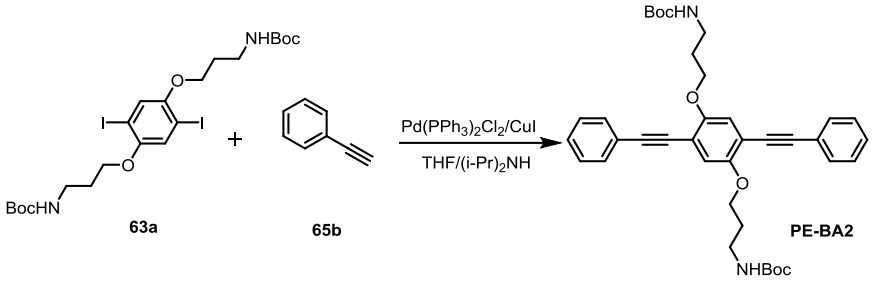

63a **65b** **PE-BA2**

Synthesis of di-tert-butyl (((2,5-bis(phenylethynyl)-1,4-phenylene)bis(oxy))bis(propane-3,1-diyl))dicarbamate (PE-BA2). A Schlenk flask was charged with compound **63a** (226 mg, 340 μmol, 1.00 eq.), bis(triphenylphosphine)palladium(II) dichloride $PdCl_2(PPh_3)_2$ (24.0 mg, 30 μmol, 0.090 eq.), and copper(I) iodide (CuI) (12.8 mg, 70 μmol, 0.210 eq.). The flask was evacuated and filled with N_2. A solution of tetrahydrofuran (THF) and diisopropylamine (DIPA) was mixed in a 3:2 ratio (v/v) and degassed with N_2 for 25 min, and 15 mL of the solution was transferred to the flask. Then **65b** (137 mg, 1.35 mmol, 3.97 eq.) was added to the mixture. The reaction was stirred at 60 °C for 2 d. $CHCl_3$ were added to the mixture, and then washed with water, NaCl saturated solution and NH_4Cl saturated solution. The combined organic layers were dried over $MgSO_4$, filtered and concentrated under vacuum. The crude product was purified by column chromatography on SiO_2 (PE/EE 10:1 to 3:1+2.5% Et_3N) to afford **PE-BA2** (199 mg, 323 μmol, 95%) as a yellow solid. M.p. : 162-164 °C. FT-IR (ATR): $\tilde{\nu}$ (cm^{-1}) = 3420, 3363, 2970, 2929, 1714, 1506, 1365, 1217, 1170, 755, 691. ^{1}H NMR (500 MHz, CD_2Cl_2) δ 7.56 (d, *J* =

4.7 Hz, 4H), 7.44 – 7.30 (m, 6H), 7.07 (s, 2H), 5.02 (br, 2H), 4.11 (t, *J* = 5.7 Hz, 4H), 3.57 – 3.24 (m, 4H), 2.14 – 1.85 (m, 4H), 1.35 (s, 18H).^{13}C NMR (126 MHz, CD_2Cl_2) δ 156.2, 153.7, 131.9, 128.8, 128.8, 123.5, 117.2, 114.3, 95.4, 85.9, 79.0, 68.1, 38.6, 29.8, 28.4. HRMS (ESI): $[M+Na]^+$ calcd for $C_{38}H_{44}N_2NaO_6$: 647.3092; found 647.3094. Elemental analysis for $C_{38}H_{44}N_2O_6$ calcd: C, 73.05, H, 7.10, N, 4.48; found: C, 72.71, H, 7.52, N, 4.28.

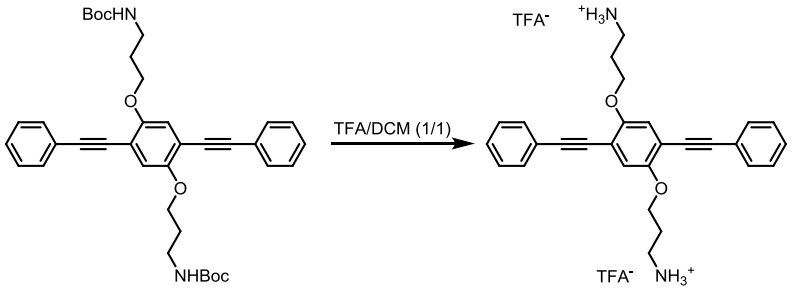

PE-BA2 **PE-A2**

Synthesis of 3,3'-((2,5-bis(phenylethynyl)-1,4-phenylene)bis(oxy))bis(propan-1-aminium) (PE-A2). **PE-BA2** (94.0 mg, 150 μmol) was dissolved in 5 mL CH_2Cl_2. 5 mL of trifluoroacetic acid (TFA) was added to the solution. The reaction mixture was stirred for 3-5 min. The excess TFA and the solvent were removed under vacuum. Then the crude product was washed by diethyl ether and pentane to afford **PE-A2** (95.6 mg, 148 μmol, 99%) as brown solid. M.p. : 196-198 °C. FT-IR (ATR): $\tilde{\nu}$ (cm^{-1}) = 3380, 3343, 2931, 2853, 1675, 1636, 1201, 1132, 834, 799, 757, 721, 694, 540. ^{1}H NMR (500 MHz, MeOD) δ 7.57 – 7.52 (m, 4H), 7.42 (d, *J* = 4.5 Hz, 6H), 7.20 (s, 2H), 4.23 (t, *J* = 5.6 Hz, 4H), 3.26 (t, *J* = 7.1 Hz, 4H), 2.29 – 2.15 (m, 4H). ^{13}C NMR (126 MHz, MeOD) δ 154.5, 132.4, 129.8, 129.7, 124.2, 118.0, 115.3, 96.0, 86.2, 67.9, 38.8, 28.3. ^{19}F NMR (471 MHz, MeOD) δ -76.87. HRMS (ESI): $[M+H]^+$ calcd for $C_{28}H_{29}N_2O_2$: 425.2224; found 425.2223. Elemental analysis for $C_{32}H_{30}F_6N_2O_6$ calcd: C, 58.90, H, 4.63, N, 4.29; found: C, 58.15, H, 4.84, N, 4.22.

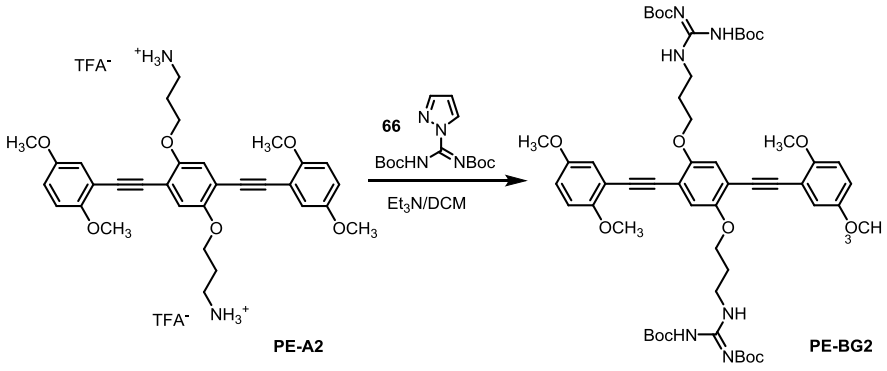

PE-A2 **PE-BG2**

Synthesis of (((2,5-bis(phenylethynyl)-1,4-phenylene)bis(oxy))bis(propane-3,1-diyl))-*N', N''*-bis (carbamic acid tert-butyl ester) guanidine (PE-BG2). Under N_2 atmosphere, to a solution of **PE-A2** (91.0 mg, 140 μmol, 1.00 eq.) and Et_3N (0.5 mL) in DCM (20 mL) were added 1-H-pyrazole-1-(N,N'-bis(tert-butyloxycarbonyl))carboxamidine **66** (78.0 mg, 250 μmol, 1.78 eq.). The resulting solution was stirred at room temperature for 16 h. The resulting residue was purified by silica-gel column chromatography (PE/EE 10:1 to 3:1+2.5% Et_3N), which gave **PE-BG2** (100 mg, 109 μmol, 78%) as a

yellow solid. M.p. : 242-244 °C. FT-IR (ATR): ṽ (cm^{-1}) = 3342, 3329, 2979, 2871, 1719, 1638, 1617,1413, 1331, 1158, 1134, 1053. ^{1}H NMR (700 MHz, CD_2Cl_2) δ 11.50 (s, 2H), 8.45 (br, 2H), 7.61 – 7.46 (m, 4H), 7.43 – 7.24 (m, 6H), 7.08 (s, 2H), 4.14 (br, 4H), 3.65 (br, 4H), 2.20 – 2.09 (m, 4H), 1.46 (d, *J* = 17.9 Hz, 36H). ^{13}C NMR (176 MHz, CD_2Cl_2) δ 163.9, 156.7, 153.9, 153.5, 131.9, 128.8, 123.6, 117.8, 114.7, 95.3, 86.0, 83.4, 79.1, 67.7, 38.2, 29.3, 28.4, 28.1. HRMS (ESI): $[M+H]^+$ calcd for $C_{50}H_{65}N_6O_{10}$: 909.4757; found 909.4761. Elemental analysis for $C_{50}H_{64}N_6O_{10}$ calcd: C, 66.06, H, 7.10, N, 9.24; found: C, 65.78, H, 7.00, N, 9.25.

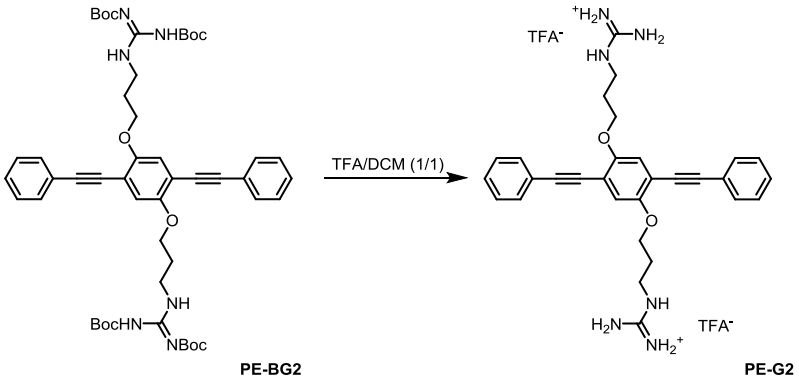

Synthesis of ((((2,5-bis(phenylethynyl)-1,4-phenylene)bis(oxy))bis(propane-3,1-diyl))bis(azanediyl))bis(aminomethaniminium) (PE-G2). PE-BG2 (9.10 mg, 10 μmol, 1.00 eq.) was dissolved in 1 mL CH_2Cl_2. 1 mL of trifluoroacetic acid (TFA) was added to the solution. The reaction mixture was stirred for 45 min. The excess TFA and the solvent were removed under vacuum. Then the crude product was washed by diethyl ether and pentane to afford **PE-G2** (7.2 mg, 9.8 μmol, 98%) as yellow oily solid. FT-IR (ATR): ṽ (cm^{-1}) = 3331, 3293, 2943, 2831, 1678, 1412, 1202, 1186, 1140, 1021. ^{1}H NMR (600 MHz, MeOD) δ 7.59 – 7.51 (m, 4H), 7.44 – 7.36 (m, 6H), 7.18 (s, 2H), 4.18 (t, *J* = 5.9 Hz, 4H), 3.53 – 3.44 (m, 4H), 2.23 – 2.05 (m, 4H). ^{13}C NMR (151 MHz, MeOD) δ 158.9, 154.9, 132.6, 129.8, 124.6, 118.5, 115.7, 96.1, 86.4, 67.7, 39.6, 29.9. ^{19}F NMR (283 MHz, MeOD) δ -76.94. HRMS (ESI): $[M+H]^+$ calcd for $C_{30}H_{33}N_6O_2$: 509.2660; found 509.2668.

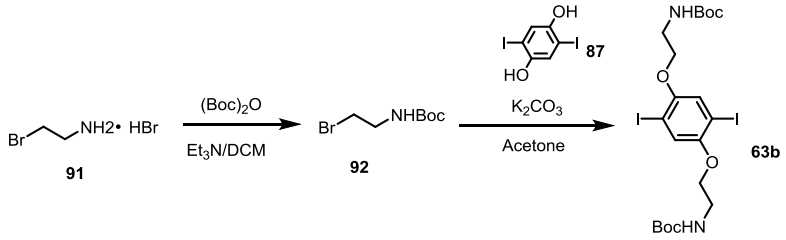

Compound **92**[178] and **63b**[176a] were synthesized according to the literature.

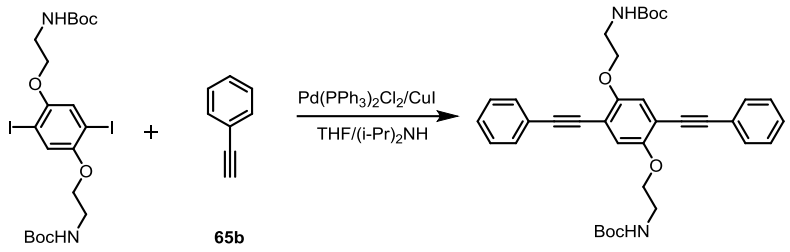

63b PE-BA3

Synthesis of di-tert-butyl (((2,5-bis(phenylethynyl)-1,4-phenylene)bis(oxy))bis(ethane-2,1-diyl))dicarbamate (PE-BA3). A Schlenk flask was charged with compound **63b** (195 mg, 300 μmol, 1.00 eq.), bis(triphenylphosphine)palladium(II) dichloride ($PdCl_2(PPh_3)_2$) 10 (22.0 mg, 30.0 μmol, 0.100 eq.), and copper(I) iodide (CuI) (12.0 mg, 60.0 μmol, 0.200 eq.). The flask was evacuated and filled with N_2. A solution of tetrahydrofuran (THF) and diisopropylamine (DIPA) was mixed in a 3:2 ratio (v/v) and degassed with N_2 for 25 min, and 15 mL of the solution was transferred to the flask. Then **65b** (123 mg, 1.20 mmol, 4.00 eq.) was added to the mixture. The reaction was stirred at 60 °C for 2 d. $CHCl_3$ were added to the mixture, which was then washed with water, NaCl saturated solution and NH_4Cl saturated solution. The combined organic layers were dried over $MgSO_4$, filtered and concentrated under vacuum. The crude product was purified by column chromatography on SiO_2 (PE/EE 3:1+2.5% Et_3N) to afford **PE-BA3** (165 mg, 276 μmol, 92%) as brown solid. M. p. : 153-155 °C. FT-IR (ATR): $\tilde{\nu}$ (cm^{-1}) = 3431, 3329, 2975, 2887, 1699, 1596, 1504, 1390, 1364, 1213, 1163, 865, 754, 735, 689. ^{1}H NMR (600 MHz, CD_2Cl_2) δ 7.63 – 7.52 (m, 4H), 7.45 – 7.31 (m, 6H), 7.08 (s, 2H), 5.18 (br, 2H), 4.12 (t, *J* = 5.0 Hz, 4H), 3.64 – 3.47 (m, 4H), 1.40 (s, 18H). ^{13}C NMR (151 MHz, CD_2Cl_2) δ 156.1, 153.7, 131.9, 128.9, 128.8, 123.3, 118.0, 114.8, 95.6, 85.6, 79.5, 69.5, 40.5, 28.4. HRMS (ESI): $[M+Na]^+$ calcd for $C_{36}H_{40}N_2O_6Na$: 619.2779; found 619.2787.

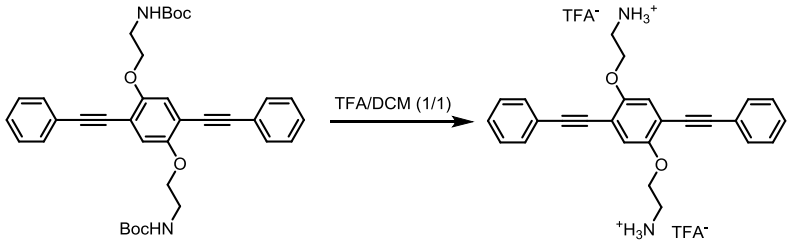

PE-BA3 PE-A3

Synthesis of 2,2'-((2,5-bis(phenylethynyl)-1,4-phenylene)bis(oxy))bis(ethan-1-aminium) (PE-A3). **PE-BA3** (96.0 mg, 160 μmol, 1.00 eq.) was dissolved in 5 mL CH_2Cl_2. 5 mL of trifluoroacetic acid (TFA) was added to the solution. The reaction mixture was stirred for 3-5 min. The excess TFA and the solvent were removed under vacuum. Then the crude product was washed by diethyl ether and pentane to afford **PE-A3** (99 mg, 158 μmol, 99%) as brown solid. M. p. : 215-217 °C. FT-IR (ATR): $\tilde{\nu}$ (cm^{-1}) = 3317, 2943, 2831, 1676, 1472, 1395, 1114, 1021. ^{1}H NMR (500 MHz, MeOD) δ 7.58 (br, 4H), 7.42 (br, 6H), 7.31 (s, 2H), 4.36 (t, *J* = 4.6 Hz, 4H), 3.45 (t, *J* = 4.6 Hz, 4H). ^{13}C NMR (126 MHz, MeOD) δ

154.7, 132.6, 129.6, 124.1, 120.1, 116.3, 96.6, 85.7, 67.8, 40.4. ^{19}F NMR (471 MHz, MeOD) δ -76.95. HRMS (ESI): $[M+H]^+$ calcd for $C_{26}H_{25}N_2O_2$: 397.1911; found 397.1909.

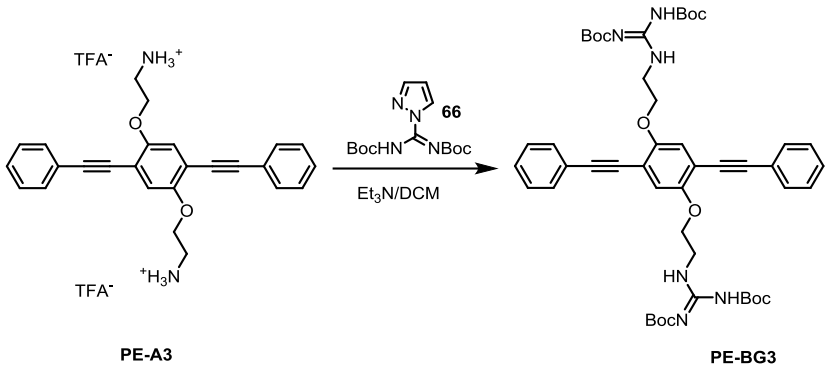

Synthesis of (((2,5-bis(phenylethynyl)-1,4-phenylene)bis(oxy))bis(ethane-2,1-diyl))-*N', N''*-bis (carbamic acid tert-butyl ester) guanidine (PE-BG3). Under N_2 atmosphere, to a solution of **PE-A3** (100 mg, 160 μmol, 1.00 eq.) and Et_3N (0.5 mL) in DCM (20 mL) were added 1-H-pyrazole-1-(N,N'-bis(tert-butyloxycarbonyl))carboxamidine **66** (90.0 mg, 288 μmol, 1.80 eq.). The resulting solution was stirred at room temperature for 16 h. The resulting residue was purified by silica-gel column chromatography (PE/EE 10:1 to 3:1+2.5% Et_3N), which gave **PE-BG3** (99 mg, 115 μmol, 72%) as a yellow solid. M. p. : 228-230 ºC. FT-IR (ATR): $\tilde{\nu}$ (cm^{-1}) = 3339, 3292, 2977, 2932, 1721, 1636, 1615, 1570, 1507, 1409, 1363, 1046, 1024, 766, 690. ^{1}H NMR (700 MHz, CD_2Cl_2) δ 11.52 (s, 2H), 8.79 (s, 2H), 7.67 – 7.50 (m, 4H), 7.36 (d, *J* = 4.6 Hz, 6H), 7.08 (s, 2H), 4.19 (t, *J* = 4.6 Hz, 4H), 3.87 (d, *J* = 4.9 Hz, 4H), 1.46 (s, 18H), 1.41 (s, 18H). ^{13}C NMR (176 MHz, CD_2Cl_2) δ 163.8, 156.7, 153.6, 153.3, 132.0, 128.8, 128.7, 123.5, 117.5, 114.4, 95.8, 85.4, 83.4, 79.2, 68.2, 40.6, 28.3, 28.0. HRMS (ESI): $[M+H]^+$ calcd for $C_{48}H_{61}N_6O_{10}$: 881.4444; found 881.4464.

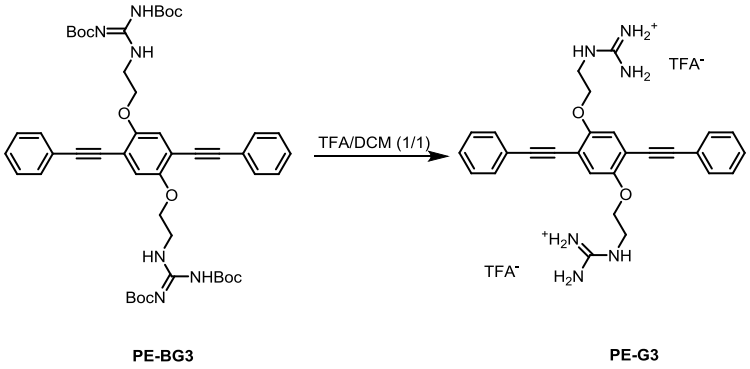

Synthesis of ((((2,5-bis(phenylethynyl)-1,4-phenylene)bis(oxy))bis(ethane-2,1-diyl))bis(azanediyl))bis(aminomethaniminium) (PE-G3). PE-BG3 (22.0 mg, 25 μmol, 1.00 eq.) was dissolved in 2 mL CH_2Cl_2. 2 mL of trifluoroacetic acid (TFA) was added to the solution. The reaction mixture was stirred for 45 min. The excess TFA and the solvent were removed under vacuum. Then the crude product was washed by diethyl ether and pentane to afford **PE-G3** (16 mg, 24.8 μmol, 99%) as light yellow oily solid. FT-IR (ATR): $\tilde{\nu}$ (cm^{-1}) = 3386, 3190, 2929, 1674, 1508, 1411, 1202, 1136, 1060,

756. ^{1}H NMR (500 MHz, MeOD) δ 7.65 – 7.50 (m, 4H), 7.48 – 7.37 (m, 6H), 7.22 (s, 2H), 4.25 (t, *J* = 4.7 Hz, 4H), 3.71 (t, *J* = 4.6 Hz, 4H). ^{13}C NMR (126 MHz, MeOD) δ 159.2, 154.6, 132.5, 129.7, 118.5, 115.5, 96.4, 86.0, 69.3, 42.5. ^{19}F NMR (471 MHz, MeOD) δ -76.92. HRMS (ESI): $[M+H]^+$ calcd for $C_{28}H_{29}N_6O_2$: 481.2347; found 481.2353.

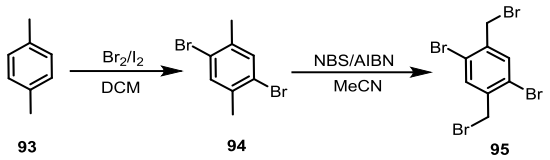

Compound **94**[179] and **95**[180] was synthesized according to the literature.

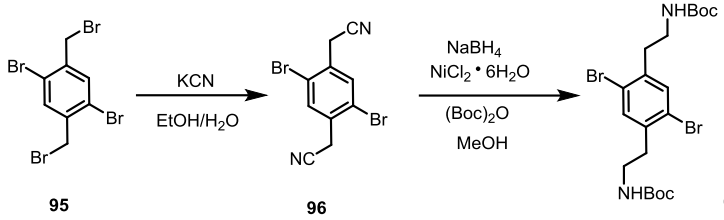

Synthesis of 2,2'-(2,5-dibromo-1,4-phenylene)diacetonitrile (96). 95 (8.50 g, 20.0 mmol, 1.00 eq.) and potassium cyanide (3.30 g, 50.0 mmol, 2.50 eq.) were suspended in a mixture of ethanol (54 ml) and water (27 ml) and stirred at 70°C for 3.5 h. More water was added and the reaction mixture was extracted with dichloromethane. The combined organic phases were washed with water and dried over $MgSO_4$. The solvent was removed in vacuo and the yellowish solid **96** (4.5 g, 14.2 mmol, 71%) dried in vacuum. ^{1}H NMR (301 MHz, $CDCl_3$) δ 7.79 (s, 2H), 3.83 (s, 4H).

Synthesis of di-tert-butyl ((2,5-dibromo-1,4-phenylene)bis(ethane-2,1-diyl))dicarbamate (64). To a stirred solution of compound **96** (3.05 g, 10.0 mmol, 1.00 eq.) in dry methanol (100 mL) at 0°C, $(Boc)_2O$ (8.47 g, 39.0 mmol, 3.90 eq.) and $NiCl_2 \cdot 6H_2O$ (238 mg, 1.00 mmol, 10 mol%) were added. $NaBH_4$ (5.70 g, 150 mmol, 15.0 eq.) was then added in small portions over 1 hour. The resulting reaction mixture was allowed to warm to room temperature and stirred for 19 hours. Then diethylentriamine (2.35 mL, 20.0 mmol) was added, and the mixture was allowed to stir for another 30 minutes. After evaporation of solvent, the residue was dissolved in ethyl acetate and washed with a $NaHCO_3$ saturated solution (2×150 mL) and brine (50 mL). The organic layer was dried over anhydrous $MgSO_4$, filtered, and evaporated to give the crude product. The colorless product **64** (1.50 g, 2.50 mmol, 25%) was recrystallized from DCM. M.p. : 171-173 °C. FT-IR (ATR): $\tilde{\nu}$ (cm^{-1}) = 3359, 2976, 2929, 1685, 1528, 1366, 1288, 1248, 1168, 1056, 869, 778. ^{1}H NMR (300 MHz, $CDCl_3$) δ 7.40 (s, 2H), 4.58 (br, 2H), 3.36 (m, 4H), 2.89 (t, *J* = 6.9 Hz, 4H), 1.44 (s, 18H). ^{13}C NMR (126 MHz, $CDCl_3$) δ 155.9, 138.6, 134.8, 123.5, 79.5, 40.1, 35.9, 28.5. HRMS (ESI): $[M+Na]^+$ calcd for $C_{20}H_{30}N_2Br_2O_4Na$: 545.0444; found 545.0450. Elemental analysis for $C_{20}H_{30}Br_2N_2O_4$ calcd: C, 45.99, H, 5.79, N, 5.36; found: C, 45.38, H, 6.20, N, 4.87.

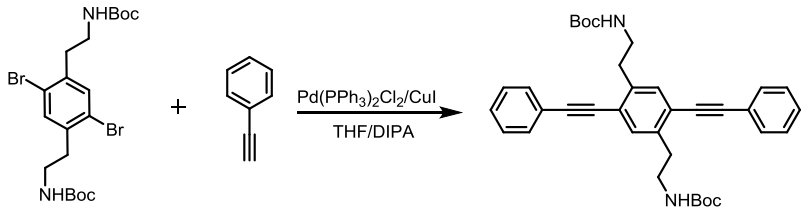

64 65b PE-BA4

Synthesis of di-tert-butyl ((2,5-bis(phenylethynyl)-1,4-phenylene)bis(ethane-2,1-diyl))dicarbamate (PE-BA4). A Schlenk flask was charged with compound **64** (157 mg, 300 μmol, 1.00 eq.), bis(triphenylphosphine)palladium(II) dichloride $PdCl_2(PPh_3)_2$ (22.0 mg, 30 μmol, 0.100 eq.), and copper(I) iodide (CuI) (12.0 mg, 60 μmol, 0.200 eq.). The flask was evacuated and filled with N_2. A solution of tetrahydrofuran (THF) and diisopropylamine (DIPA) was mixed in a 3:2 ratio (v/v) and degassed with N_2 for 25 min, and 25 mL of the solution was transferred to the flask. Then **65b** (123 mg, 1.20 mmol, 4.00 eq.) was added to the mixture. The reaction was stirred at 60 °C for 2 d. $CHCl_3$ were added to the mixture, and then washed with water, NaCl saturated solution and NH_4Cl saturated solution. The combined organic layers were dried over $MgSO_4$, filtered and concentrated under vacuum. The crude product was purified by column chromatography on SiO_2 (PE/EE 3:1+2.5% Et_3N) to afford **PE-BA4** (145 mg, 255 μmol, 85%) as brown solid. M. p. : 176-178 °C. FT-IR (ATR): $\tilde{\nu}$ (cm^{-1}) = 3394, 2975, 1704, 1686, 1520, 1506, 1365, 1248, 1169, 754, 689. ^{1}H NMR (300 MHz, $CDCl_3$) δ 7.54 (d, *J* = 3.6 Hz, 4H), 7.41 (s, 2H), 7.38 – 7.30 (m, 6H), 4.67 (br, 2H), 3.62 – 3.40 (m, 4H), 3.04 (t, *J* = 6.1 Hz, 4H), 1.42 (s, 18H). ^{13}C NMR (175 MHz, CD_2Cl_2) δ 156.0, 139.6, 133.5, 131.9, 128.8, 123.4, 123.3, 95.0, 87.9, 79.2, 41.2, 34.8, 28.4. HRMS (ESI): $[M+Na]^+$ calcd for $C_{36}H_{40}N_2O_4Na$: 587.2880; found 587.2885.

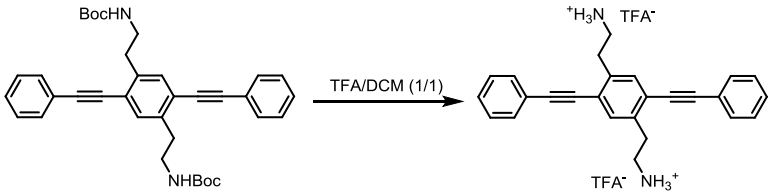

PE-BA4 PE-A4

Synthesis of 2,2'-(2,5-bis(phenylethynyl)-1,4-phenylene)bis(ethan-1-aminium) (PE-A4). PE-BA4 (102 mg, 180 μmol, 1.00 eq.) was dissolved in 4 mL CH_2Cl_2. 4 mL of trifluoroacetic acid (TFA) was added to the solution. The reaction mixture was stirred for 3-5 min. The excess TFA and the solvent were removed under vacuum. Then the crude product was washed by diethyl ether and pentane to afford **PE-A4** (105 mg, 178μmol, 99%) as brown solid. M.p. : 202-204 °C.FT-IR (ATR): $\tilde{\nu}$ (cm^{-1}) = 3337, 2830, 1675, 1446, 1114, 1019. ^{1}H NMR (700 MHz, MeOD) δ 7.60 (br, 6H), 7.44 (br, 6H), 3.62-3.49 (m, 4H), 3.24 (br, 4H). ^{13}C NMR (176 MHz, MeOD) δ 138.6, 134.5, 132.6, 130.2, 129.7, 124.8, 123.7, 96.8, 87.2, 59.7, 40.5, 32.9. ^{19}F NMR (659 MHz, MeOD) δ -76.86. HRMS (ESI): $[M+H]^+$ calcd for $C_{26}H_{25}N_2$: 365.2012; found 365.2014. Elemental analysis for $C_{30}H_{26}F_6N_2O_4$ calcd: C, 60.81, H, 4.42, N, 4.73; found: C, 60.23, H, 5.07, N, 3.94.

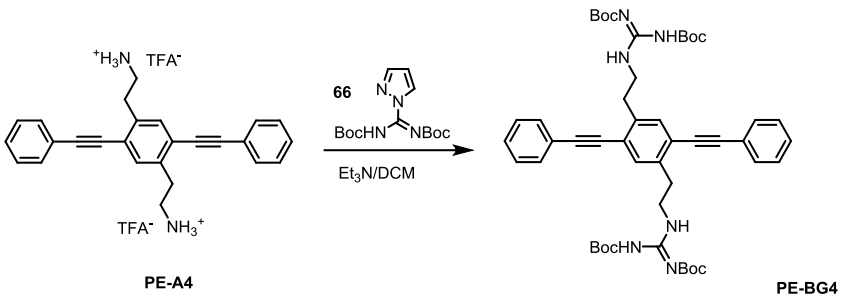

PE-A4 **PE-BG4**

Synthesis of ((2,5-bis(phenylethynyl)-1,4-phenylene)bis(ethane-2,1-diyl))-*N'*, *N''*-bis (carbamic acid tert-butyl ester) guanidine (PE-BG4). To a solution of **PE-A4** (100 mg, 160 µmol, 1.00 eq.) and Et_3N (0.5 mL) in DCM (20 mL) were added 1-H-pyrazole-1-(N,N'-bis(tert-butyloxycarbonyl))carboxamidine **66** (95.0 mg, 310 µmol, 1.94 eq.). The resulting solution was stirred at room temperature for 16 h. The crude product was purified by column chromatography on SiO_2 (PE/EE 3:1+2.5% Et_3N) to afford **PE-BG4** (110 mg, 123 µmol, 77%) as brown oily solid. FT-IR (ATR): $\tilde{\nu}$ (cm^{-1}) = 3326, 2960, 2924, 2853, 1719, 1635, 1615, 1412, 1363, 1326, 1227, 1152, 1128, 1058, 809, 754, 689. ^1H NMR (300 MHz, $CDCl_3$) δ 11.48 (s, 2H), 8.56 (br, 2H), 7.51 (m, 4H), 7.45 (s, 2H), 7.34 (m, 6H), 3.83 (m, 4H), 3.11 (t, *J* = 6.7 Hz, 4H), 1.50 (s, 18H), 1.43 (s, 18H). ^{13}C NMR (151 MHz, $CDCl_3$) δ 156.1, 153.1, 138.7, 133.4, 132.2, 131.7, 128.7, 128.6, 128.5, 123.4, 123.1, 95.0, 87.5, 33.6, 29.8, 28.4, 28.1. HRMS (ESI): $[M+H]^+$ calcd for $C_{48}H_{61}N_6O_8$: 849.4545; found 849.4553.

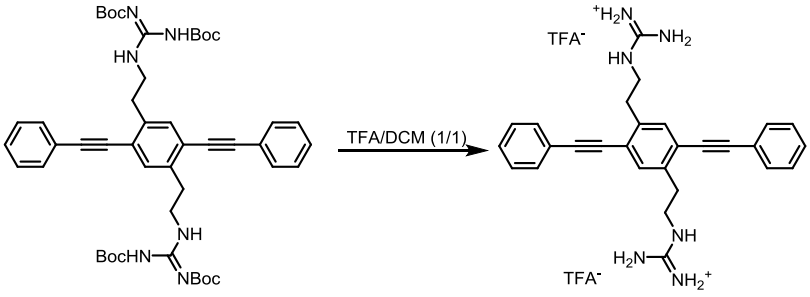

PE-BG4 **PE-G4**

Synthesis of (((2,5-bis(phenylethynyl)-1,4-phenylene)bis(ethane-2,1-diyl))bis(azanediyl))bis(aminomet-haniminium) (PE-G4). PE-BG4 (7.00 mg, 10 µmol) was dissolved in 1 mL CH_2Cl_2. 1 mL of trifluoroacetic acid (TFA) was added to the solution. The reaction mixture was stirred for 45 min. The excess TFA and the solvent were removed under vacuum. Then the crude product was washed by diethyl ether and pentane to afford **PE-G4** (5.4 mg, 9.90 µmol, 99%) as yellow oily solid. FT-IR (ATR): $\tilde{\nu}$ (cm^{-1}) = 3352, 2934, 1669, 1315, 1201, 1137, 722. ^1H NMR (300 MHz, MeOD) δ 7.58 (m, 6H), 7.42 (m, 6H), 3.59 (t, *J* = 6.2 Hz, 4H), 3.26 – 3.06 (t, *J* = 7.0 Hz, 4H). ^{13}C NMR (100 MHz, MeOD) δ 158.7, 139.7, 134.3, 132.5, 130.0, 129.7, 124.8, 124.0, 96.2, 87.8, 42.7, 34.1. ^{19}F NMR (283 MHz, MeOD) δ -76.91. HRMS (ESI): $[M+H]^+$ calcd for $C_{28}H_{29}N_6$: 449.2448; found 449.2450.

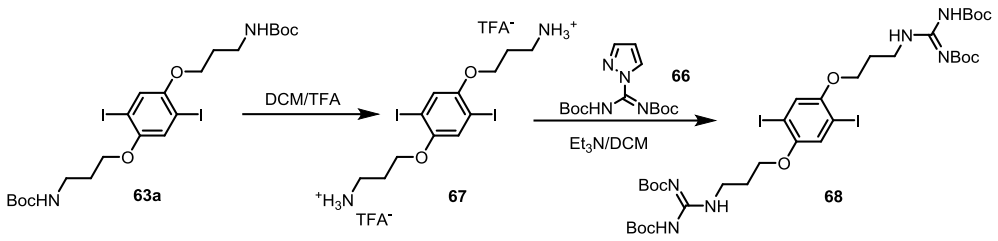

Synthesis of 3,3'-((2,5-diiodo-1,4-phenylene)bis(oxy))bis(propan-1-aminium) (67). [193a] **63a** (14.2 mg, 0.021 mmol) was dissolved in 2 mL CH_2Cl_2. 2 mL of trifluoroacetic acid (TFA) was added to the solution. The reaction mixture was stirred for 3 min. The excess TFA and the solvent were removed under vacuum. Then the crude product was washed by pentane to afford **67** (15 mg, quant.) as colorless solid. ^{1}H NMR (301 MHz, MeOD) δ 7.36 (s, 2H), 4.06 (t, *J* = 5.8 Hz, 4H), 3.48 (t, *J* = 6.8 Hz, 4H), 2.20 – 1.91 (m, 4H). Note, the reaction time was extended to 3 h or overnight, the result kept unchanged.

Synthesis of (((2,5-diiodo-1,4-phenylene)bis(oxy))bis(propane-3,1-diyl))-*N', N''*-bis (carbamic acid tert-butyl ester) guanidine (68). Under N_2 atmosphere, to a solution of **67** (453 mg, 950 μmol, 1.00 eq.) and Et_3N (0.5 mL) in DCM (40 mL) were added 1-H-pyrazole-1-(N,N'-bis(tert-butyloxycarbonyl))carboxamidine **66** (590 mg, 1.90 mmol, 2.00 eq.). The resulting solution was stirred at room temperature for 2 d. The resulting residue was purified by silica-gel column chromatography (PE/EE 3:1), which gave **68** (807 mg, 836 μmol, 88%) as a colorless solid. M.p. : 171-173 °C. FT-IR (ATR): $\tilde{\nu}$ (cm^{-1}) = 3342, 2975, 2930, 1721, 1626, 1611, 1568, 1441, 1412, 1330, 1221, 1131, 1084, 968, 808, 631. ^{1}H NMR (600 MHz, $CDCl_3$) δ 11.49 (s, 2H), 8.46 (t, *J* = 5.1 Hz, 2H), 7.18 (s, 2H), 4.00 (t, *J* = 6.0 Hz, 4H), 3.67 (m, 4H), 2.21 – 1.91 (m, 4H), 1.49 (d, *J* = 4.1 Hz, 36H). ^{13}C NMR (150 MHz, $CDCl_3$) δ 163.7, 156.4, 153.4, 152.9, 123.1, 86.5, 83.2, 79.4, 67.9, 38.0, 29.0, 28.4, 28.2, 28.1. HRMS (ESI): $[M+H]^+$ calcd for $C_{34}H_{55}I_2N_6O_{10}$: 961.2064; found 961.2067.

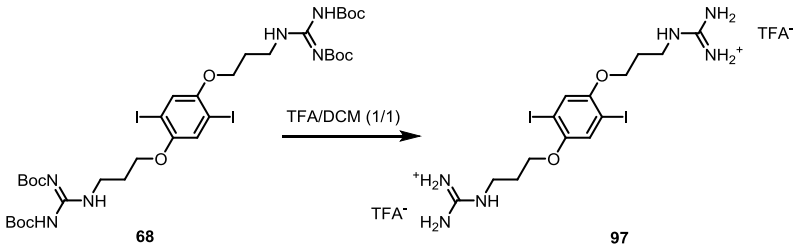

Synthesis of ((((2,5-diiodo-1,4-phenylene)bis(oxy))bis(propane-3,1-diyl))bis(azanediyl))bis(aminomethaniminium) (97). 68 (19.2 mg, 20.0 μmol, 1.00 eq.) was dissolved in 4 mL CH_2Cl_2. 4 mL of trifluoroacetic acid (TFA) was added to the solution. The reaction mixture was stirred for 45 min. The excess TFA and the solvent were removed under vacuum to afford **97** (15.0 mg, 20.0 μmol, quant.) as pale yellow oily solid. FT-IR (ATR): $\tilde{\nu}$ (cm^{-1}) = 3340, 2925, 1668, 1626, 1465, 1437, 1351, 1203, 1133, 1059, 797, 723. ^{1}H NMR (301 MHz, MeOD) δ 7.35 (s, 2H), 4.05 (t, *J* = 5.8 Hz, 4H), 3.47 (t, *J* = 6.8 Hz, 4H), 2.18 – 1.95 (m, 4H). ^{13}C NMR (126 MHz, MeOD) δ 158.4, 154.2, 124.1,

87.0, 68.2, 39.5, 29.6. ^{19}F NMR (471 MHz, MeOD) δ -76.93. HRMS (ESI): $[M+H]^+$ calcd for $C_{14}H_{23}I_2N_6O_2$: 560.9966; found 560.9964.

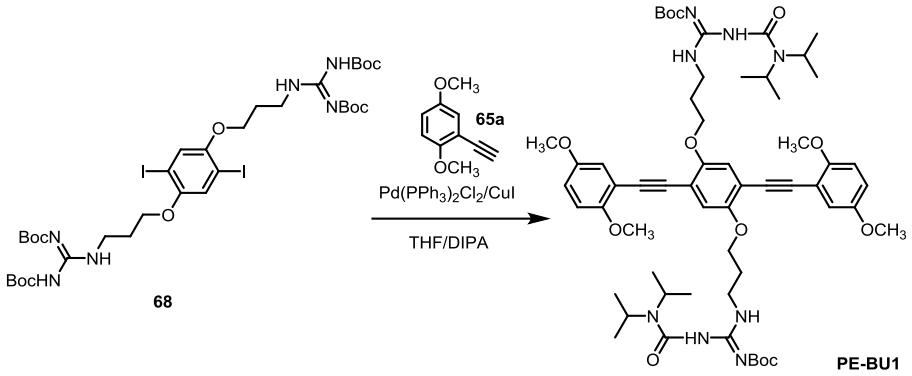

Synthesis of (((2,5-bis((2,5-dimethoxyphenyl)ethynyl)-1,4-phenylene)bis(oxy))bis(propane-3,1-diyl))N-(N′-tert-butoxycarbonylamidino)ureas (PE-BU1). A Schlenk flask was charged with compound **68** (145 mg, 150 μmol, 1.00 eq.), **65a** (73.0 mg, 450 μmol, 3.00 eq.), bis(triphenylphosphine)palladium(II) dichloride $PdCl_2(PPh_3)_2$ (11.0 mg, 15.0 μmol, 0.100 eq.), and copper(I) iodide (CuI) (5.80 mg, 30.0 μmol, 0.200 eq.). The flask was evacuated and filled with N_2. A solution of tetrahydrofuran (THF) and diisopropylamine (DIPA) was mixed in a 3:2 ratio (v/v) and degassed with N_2 for 25 min, and 10 mL of the solution was transferred to the flask. The reaction was stirred at 60 °C for 1d. $CHCl_3$ were added to the mixture, and then washed with water, NaCl saturated solution and NH_4Cl saturated solution. The combined organic layers were dried over $MgSO_4$, filtered and concentrated under vacuum. The crude product was purified by column chromatography on SiO_2 (PE/EE 3:1+2.5% Et_3N) to afford **PE-BU1** (105 mg, 102 μmol, 68%) as a yellow oily solid. FT-IR (ATR): $\tilde{\nu}$ (cm^{-1}) = 3338, 2963, 2923, 1710, 1629, 1580, 1499, 1427, 1369, 1330, 1268, 1212, 1142, 1048, 1022, 854, 810, 776, 731, 603. ^{1}H NMR (300 MHz, $CDCl_3$) δ 12.43 (s, 2H), 8.14 (t, *J* = 5.6 Hz, 2H), 7.08 – 7.01 (m, 4H), 6.89 – 6.76 (m, 4H), 4.65 – 4.21 (m, 2H), 4.11 (t, *J* = 6.0 Hz, 4H), 4.02 – 3.91 (m, 2H), 3.86 (s, 6H), 3.77 (s, 6H), 3.65 (dd, *J* = 14.1, 7.9 Hz, 4H), 2.26 – 2.00 (m, 4H), 1.44 (s, 18H), 1.26 – 1.16 (m, 24H). ^{13}C NMR (126 MHz, $CDCl_3$) δ 163.3, 154.5, 153.7, 153.6, 153.5, 153.2, 117.9, 117.3, 116.0, 114.3, 113.0, 112.0, 91.5, 89.7, 82.0, 67.0, 56.4, 55.8, 37.6, 29.3, 28.1, 20.8. HRMS (ESI): $[M+H]^+$ calcd for $C_{58}H_{83}N_8O_{12}$: 1083.6125; found 1083.6124.

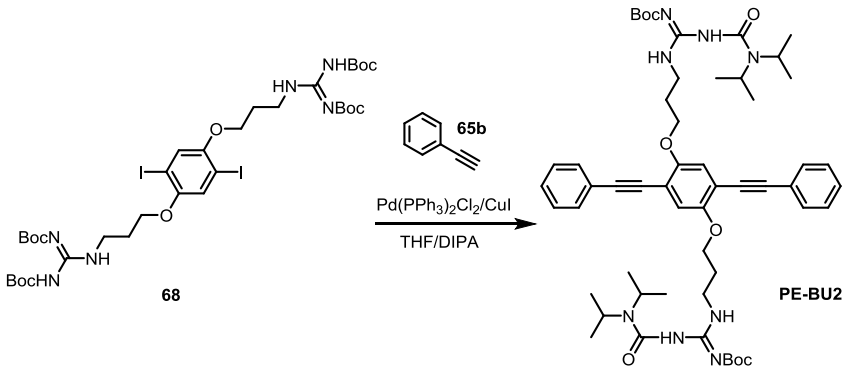

Synthesis of (((2,5-bis(phenylethynyl)-1,4-phenylene)bis(oxy))bis(propane-3,1-diyl)) *N*-(*N′*-tert-butoxycarbonylamidino)ureas (PE-BU2). A Schlenk flask was charged with compound **68** (96.0 mg, 100 μmol,), bis(triphenylphosphine)palladium(II) dichloride $PdCl_2(PPh_3)_2$ (11.0 mg, 15.0 μmol, 0.150 eq.) and copper(I) iodide (CuI) (6.00 mg, 30.0 μmol, 0.300 eq.). The flask was evacuated and filled with N_2. A solution of tetrahydrofuran (THF) and diisopropylamine (DIPA) was mixed in a 3:2 ratio (v/v) and degassed with N_2 for 25 min, and 10 mL of the solution was transferred to the flask. Then **65b** (41.0 mg, 400 μmol, 4.00 eq.) was added to the mixture. The reaction was stirred at 60 °C for 1d. $CHCl_3$ were added to the mixture, and then washed with water, NaCl saturated solution and NH_4Cl saturated solution. The combined organic layers were dried over $MgSO_4$, filtered and concentrated under vacuum. The crude product was purified by column chromatography on SiO_2 (PE/EE 3:1+2.5% Et_3N) to afford **PE-BU2** (68 mg, 75.0 μmol, 75%) as a yellow oliy solid. M.p. : 202-204 °C. FT-IR (ATR): $\tilde{\nu}$ (cm^{-1}) = 3339, 2966, 1710, 1628, 1587, 1432, 1367, 1336, 1213, 1144, 1048, 755. ^{1}H NMR (700 MHz, CD_2Cl_2) δ 12.63 (s, 2H), 8.10 (br, 2H), 7.53 (s, 4H), 7.36 (s, 6H), 7.07 (s, 2H), 4.67 – 4.36 (m, 2H), 4.13 (br, 4H), 4.02 – 3.72 (m, 2H), 3.77 – 3.45 (m, 4H), 2.43 – 1.97 (m, 4H), 1.47 (s, 18H), 1.21 (d, *J* = 50.9 Hz, 24H). ^{13}C NMR (176 MHz, CD_2Cl_2) δ 163.6, 154.2, 153.9, 131.9, 128.8, 128.8, 123.6, 117.6, 114.6, 95.3, 86.0, 82.3, 67.6, 44.9, 38.0, 29.6, 28.2, 21.3, 21.0. HRMS (ESI): $[M+H]^+$ calcd for $C_{54}H_{75}N_8O_8$: 963.5702; found 963.5731. Elemental analysis for $C_{54}H_{74}N_8O_8$ calcd: C, 67.34, H, 7.74, N, 11.63; found: C, 67.41, H, 7.73, N, 11.65.

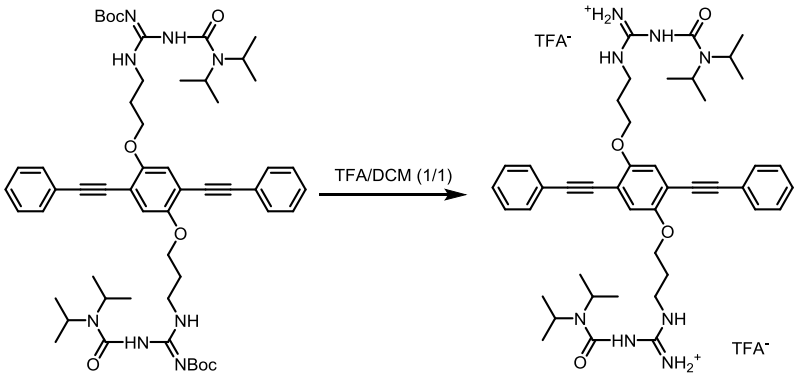

PE-BU2 PE-U2

Synthesis of PE-U2. PE-BU2 (7.80 mg, 8.00 μmol) was dissolved in 1 mL CH_2Cl_2. 1 mL of trifluoroacetic acid (TFA) was added to the solution. The reaction mixture was stirred for 45 min. The excess TFA and the solvent were removed under vacuum. Then the crude product was washed by diethyl ether and pentane to afford **PE-U2** (7.6 mg, 7.68 μmol, 96%) as yellow oily solid. FT-IR (ATR): $\tilde{\nu}$ (cm^{-1}) = 3299, 2969, 2936, 1667, 1597, 1442, 1327, 1201, 1133, 1027, 977. ^{1}H NMR (500 MHz, MeOD) δ 7.55 – 7.50 (m, 4H), 7.43 – 7.38 (m, 6H), 7.21 (s, 2H), 4.23 (t, *J* = 5.6 Hz, 4H), 3.78 (br, 4H), 3.62 (t, *J* = 6.7 Hz, 4H), 2.29 – 2.11 (m, 4H), 1.30 (d, *J* = 6.6 Hz, 24H). ^{13}C NMR (126 MHz, MeOD) δ 156.6, 154.9, 153.3, 132.4, 129.7, 124.4, 118.9, 115.8, 96.0, 86.3, 68.0, 57.3, 39.8, 29.1, 20.8. ^{19}F NMR (471 MHz, MeOD) δ -76.85. HRMS (ESI): $[M+H]^+$ calcd for $C_{44}H_{59}N_8O_4$: 763.4654; found 763.4665.

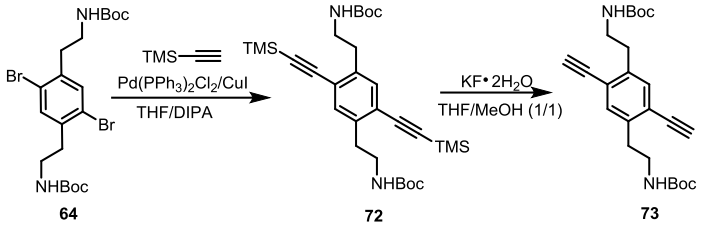

Synthesis of di-tert-butyl ((2,5-bis((trimethylsilyl)ethynyl)-1,4-phenylene)bis(ethane-2,1-diyl))dicarbamate (72). A Schlenk flask was charged with compound **64** (1.04 g, 2.00 mmol, 1.00 eq.), bis(triphenylphosphine)palladium(II) dichloride $PdCl_2(PPh_3)_2$ (141 mg, 200 μmol, 0.100 eq.), and copper(I) iodide (CuI) (76.2 mg, 400 μmol, 0.200 eq.). The flask was evacuated and filled with N_2. A solution of tetrahydrofuran (THF) and diisopropylamine (DIPA) was mixed in a 3:2 ratio (v/v) and degassed with N_2 for 25 min, and 25 mL of the solution was transferred to the flask. Then trimethylsilylacetylene (786 mg, 8.00 mmol, 4.00 eq.) was added to the mixture. The reaction was stirred at 80 °C for 2 d. $CHCl_3$ were added to the mixture, and then washed with water, NaCl saturated solution and NH_4Cl saturated solution. The combined organic layers were dried over $MgSO_4$, filtered and concentrated under vacuum. The crude product was purified by column chromatography on SiO_2 (PE/EE 6:1+2.5% Et_3N) to afford **72** (532 mg, 960 μmol, 48%) as brown solid. M. P.: 167-169 °C. ^{1}H NMR (500 MHz, CD_2Cl_2) δ 7.27 (s, 2H), 4.60 (s, 2H), 3.36 (q, *J* = 6.5 Hz, 4H), 2.89 (t, *J* = 6.6 Hz, 4H), 1.40 (s, 18H), 0.25 (s, 18H). ^{13}C NMR (101 MHz, CD_2Cl_2) δ 156.0, 140.0, 133.7, 132.4, 132.3, 128.9, 123.5, 103.4, 100.6, 79.2, 41.1, 34.5, 28.5, -0.05. FT-IR (ATR): $\tilde{\nu}$ (cm^{-1}) = 3397, 2960, 2931, 2154, 1691, 1515, 1364, 1247, 1167, 838, 758, 625. HRMS (ESI) m/z: $[M+Na]^+$: calcd. for $C_{30}H_{48}N_2O_4Si_2Na$: 579.3045; found 579.3048.

Synthesis of di-tert-butyl ((2,5-diethynyl-1,4-phenylene)bis(ethane-2,1-diyl))dicarbamate (73). Compound **72** (724 mg, 1.30 mmol) was dissolved in a degassed mixture of THF/MeOH (1:1, 15 mL/15 mL). $KF{\cdot}2H_2O$ (490 mg, 5.20 mmol) was added and the resulting mixture was stirred for 12 h at ambient temperature until TLC showed a complete conversion. H_2O and CH_2Cl_2 were added, the aqueous layer was extracted. The combined organic layers were washed with H_2O and brine, dried over $MgSO_4$, filtered and concentrated in vacuo. The crude product was purified by column chromatography on SiO_2 (PE/EE 4:1+2% Et_3N) to afford **73** (343 mg, 832 μmol, 64%) as brown solid. M. P.: 152-154 °C. ^{1}H NMR (300 MHz, CD_2Cl_2) δ 7.34 (s, 2H), 4.60 (s, 2H), 3.40 (s, 2H), 3.38 – 3.32 (m, 4H), 2.92 (t, *J* = 6.9 Hz, 4H), 1.40 (s, 18H). ^{13}C NMR (100 MHz, CD_2Cl_2) δ 156.0, 140.2, 134.1, 123.0, 82.8, 81.8, 79.2, 41.0, 34.5, 28.5. FT-IR (ATR): $\tilde{\nu}$ (cm^{-1}) = 3361, 3297, 2975, 2929, 1684, 1364, 1246, 1162, 976, 842, 599. HRMS (ESI) m/z: $[M+Na]^+$: calcd. for $C_{24}H_{32}N_2O_4Na$: 435.2254; found 435.2254.

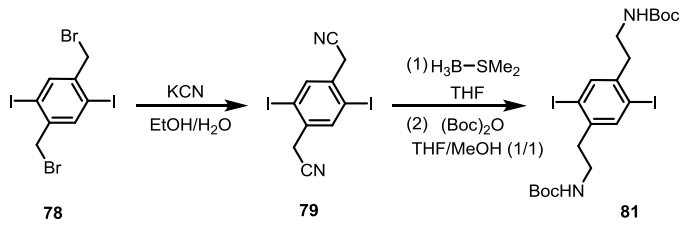

Compound **78** was synthesized according to the literature.[181]

Synthesis of 2,2'-(2,5-diiodo-1,4-phenylene)diacetonitrile (79). 78 (19.1 g, 37.0 mmol, 1.00 eq.) and potassium cyanide (6.10 g, 92.5 mmol, 2.50 eq.) were suspended in a mixture of ethanol (98 ml) and water (49 ml) and stirred at 70°C for 5 h. More water was added and the reaction mixture was extracted with dichloromethane. The combined organic phases were washed with water, dried over $MgSO_4$ and filtered. The solvent was removed in vacuo and the yellowish solid **79** (13.9 g, 34.0 mmol, 92%) dried in vacuum. ^{1}H NMR (300 MHz, $CDCl_3$) δ 7.98 (s, 2H), 3.78 (s, 4H).

Synthesis of di-tert-butyl ((2,5-diiodo-1,4-phenylene)bis(ethane-2,1-diyl))dicarbamate (81). 79 (2.65 g, 6.50 mmol, 1.00 eq.) was dissolved in dry THF (100 mL) and $BH_3{\cdot}SMe_2$ (2.47 mL, 26 mmol, 1.00 eq.) was added slowly to the mixture over of a time period of 10 minutes at 0 °C.The single neck flask was fitted with a reflux condenser. The reaction mixture was then refluxed overnight at 72 °C. After cooling to room temperature, the reaction mixture was quenched by a slow addition of conc. HCl in MeOH and stirred for an hour. The solution was basified with 10% NaOH and extracted three times with DCM. The combined organics were dried over $MgSO_4$, filtered and the solvent was removed by distillation under reduced pressure to yield the desired amine intermediate. To a stirred solution of amine intermediate in 1:1 MeOH/THF (20/20 mL) was treated with Boc_2O (3.56 g, 16.3 mmol, 2.50 eq.) and Et_3N (1.00 mL). The reaction mixture was refluxed for 4 h and then concentrated under reduced pressure. The residue was dissolved in EtOAc, washed with water and saturated aq NaCl, dried over Na_2SO_4, filtered and concentrated under reduced pressure. The crude product was purified by column chromatography on SiO_2 (PE/EE 4:1+2.5% Et_3N) to afford **81** (760 mg, 1.24 mmol, 19%, 2 steps) as colorless solid. M. P.: 182-184 °C. ^{1}H NMR (400 MHz, $CDCl_3$) δ 7.63 (s, 2H), 4.57 (s, 2H), 3.33 (dd, *J* = 13.5, 6.7 Hz, 4H), 2.85 (t, *J* = 7.0 Hz, 4H), 1.45 (s, 18H). ^{13}C NMR (101 MHz, $CDCl_3$) δ 155.9, 142.1, 140.4, 100.5, 79.6, 40.4, 39.9, 28.5. FT-IR (ATR): $\tilde{\nu}$ (cm^{-1}) = 3337, 2976, 2928, 1683, 1523, 1363, 1284, 1249, 1162, 1040, 967. HRMS (ESI) m/z: $[M+Na]^+$: calcd. for $C_{20}H_{30}I_2N_2O_4Na$: 639.0187; found 639.0188.

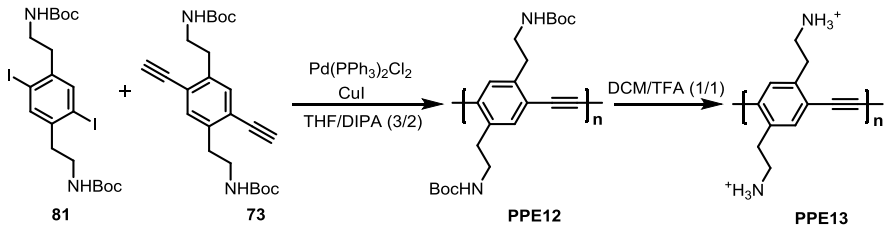

Synthesis of PPE12. 81 (185 mg, 300 µmol, 1.00 eq.) and **73** (124 mg, 300 µmol, 1.00 eq.) were dissolved in degassed THF/diisopropylamine (24 mL/16 mL). $Pd(PPh_3)_2Cl_2$ (1.26 mg, 1.80 µmol, 0.006 eq.) and CuI (686 µg, 3.60 µmol, 0.012 eq.) were added and the mixture was stirred under nitrogen at 50 °C for 48 h. $CHCl_3$ were added to the mixture and the organic phase was then washed with NH_4Cl saturated solution (×3) and water (×2), respectively. The organic layers were dried over $MgSO_4$, filtered

and concentrated under vacuum. The crude product was dissolved in $CHCl_3$ and slowly added to an excess of *n*-hexane, repeated the precipitate process for two times to give **PPE12** as sticky orange solid (204 mg, 485 µmol, 85 %). The M_n was estimated to be 4.2 x 10^3, with a PDI of 1.9. ^{1}H NMR (700 MHz, $CDCl_3$) δ 7.44 (s, 4H), 5.03 (br, 2H), 3.48 – 3.35 (m, 4H), 3.14 – 2.66 (m, 4H), 1.50 (s, 9H), 1.49 (s, 9H). Due to low solubility, ^{13}C NMR spectrum could not be obtained. FT-IR (ATR): ṽ (cm^{-1}) = 3362, 2980, 2835, 2918, 2714, 1701, 1683, 1519, 1390, 1367, 1253, 1167, 967, 741.

Synthesis of PPE13. PPE12 (175 mg, 420 µmol) in 20 mL of CH_2Cl_2 was cooled down to 0 °C. TFA (20 mL) was added dropwise to the polymer solution. Upon the completion of the addition, the reaction mixture was allowed to warm to room temperature and stirred for 2 h. The excess TFA and the solvent were removed under vacuum. Then the crude product was washed by diethyl ether and pentane to afford **PPE13** (167 mg, 378 µmol, 90%) as oily orange solid. The M_n and PDI result from **PPE12.** ^{1}H NMR (300 MHz, MeOD) δ 7.78 – 7.60 (m, 2H), 3.58 – 3.44 (m, 4H), 3.28 – 3.12 (m, 4H). Due to low solubility, ^{13}C NMR spectrum could not be obtained. FT-IR (ATR): ṽ (cm^{-1}) = 3462, 3028, 2932, 2854, 1675, 1638, 1430, 1197, 1126, 837, 800, 722.

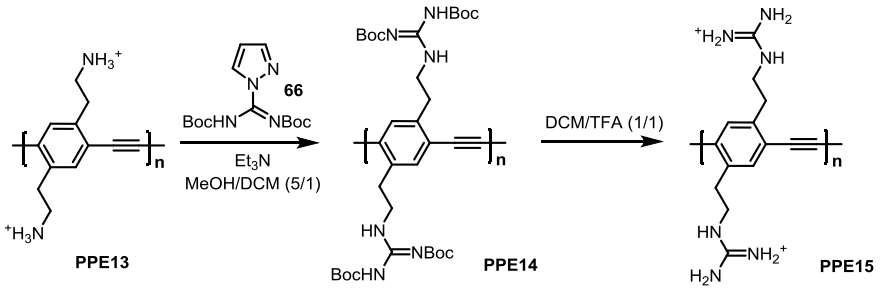

Synthesis of PPE14. Under argon atmosphere, **PPE13** (151mg, 340 µmol) was dissolved in MeOH/DCM (5/1, 96 mL). Then Et_3N (478 µL, 3.40 mmol) was added and the mixture was stirred for 30 minutes. 1-H-pyrazole-1-(N,N'-bis(tert-butyloxycarbonyl))carboxamidine **66** (422 mg, 1.36 mmol) were added to the solution. The resulting solution was stirred at room temperature for 5 days before the solvents were removed under vacuum. $CHCl_3$ were added to the mixture and the organic phase was then washed with water for three times. The organic layers were dried over $MgSO_4$, filtered and concentrated under vacuum. The crude product was dissolved in $CHCl_3$ and slowly added to an excess of n-hexane, repeated the precipitate process for two times to give **PPE14** (122 mg, 173 µmol, 51%) as oily orange solid. The M_n was estimated to be 7.0 x 10^3 with a PDI of 1.5. ^{1}H NMR (300 MHz, $CDCl_3$) δ 11.47 (s, 2H), 8.44 (s, 2H), 7.48 (s, 2H), 3.76 (s, 4H), 3.12 (s, 4H), 1.47 (s, 36H). Due to low solubility, ^{13}C NMR spectrum could not be obtained. FT-IR (ATR): ṽ (cm^{-1}) = 3325, 3288, 2967, 2921, 2851, 1716, 1642, 1612, 1422, 1364, 1327, 1223, 1153, 1123, 1060, 807.

Synthesis of PPE15. PPE14 (35.0 mg, 50.0 µmol) in 5 mL of CH_2Cl_2 was cooled down to 0 °C. TFA (5 mL) was added dropwise to the polymer solution. Upon the completion of the addition, the reaction mixture was allowed to warm to room temperature and stirred for 2 h. The excess TFA and the solvent were removed under vacuum. Then the crude product was washed by diethyl ether and pentane to afford

PPE15 (22.8 mg, 44.0 μmol, 88%) as oily orange solid. The M_n and PDI result from **PPE14**. ^{1}H NMR (300 MHz, MeOD) δ 7.61 (s, 2H), 3.76 – 3.42 (m, 4H), 3.24 – 3.00 (m, 4H). Due to low solubility, ^{13}C NMR spectrum could not be obtained. FT-IR (ATR): $\tilde{\nu}$ (cm^{-1}) = 3354, 3195, 2928, 2857, 1667, 1686, 1438, 1205, 1138, 848, 800, 726.

5.3 Appendix

5.3.1 Photophsical Data

Table 9. Photophsical data of SBs in selected solvents.

	Hexane			Toluene			DCM			Acetonitrile			DMSO		
	λ_{ab} (nm)	λ_{em} (nm)	$\Delta\upsilon_{st}$ (cm^{-1})	λ_{ab} (nm)	λ_{em} (nm)	$\Delta\upsilon_{st}$ (cm^{-1})	λ_{ab} (nm)	λ_{em} (nm)	$\Delta\upsilon_{st}$ (cm^{-1})	λ_{ab} (nm)	λ_{em} (nm)	$\Delta\upsilon_{st}$ (cm^{-1})	λ_{ab} (nm)	λ_{em} (nm)	$\Delta\upsilon_{st}$ (cm^{-1})
DSB1	393	442	2821	398	459	3339	402	466	3416	398	471	3894	411	476	3322
DSB2	424	475	2532	432	489	2698	434	499	3001	428	516	3985	444	532	3726
TSB3	396	440	2525	402	449	2604	403	454	2787	401	452	2814	407	459	2784
TSB4	397	443	2616	403	454	2787	405	463	3093	402	465	3370	409	465	2945
TSB5	400	445	2528	405	457	2810	407	466	3111	405	467	3278	412	473	3130
TSB6	398	444	2603	404	455	2774	406	461	2939	405	458	2857	408	463	2912
TSB7	415	465	2591	424	483	2881	428	536	4708	426	560	5617	436	566	5268

Table 10. Slopes of Lippert-Mataga plot for SBs.

	DSB1	**DSB2**	**TSB3**	**TSB4**	**TSB5**	**TSB6**	**TSB7**
Slope (cm^{-1})	2022	4104	878	1774	1987	892	9673

5.3.2 Calculated orbital energies

Table 11. Calculated orbital energies (in eV) for **TSB1** and **TSB2** based on the geometries of the B3LYP/6-311++G**.

Compounds	E_{H-2}	E_{H-1}	E_H	E_L	E_{L+1}
TSB1	-6.00	-5.80	-5.70	-1.56	-1.48
TSB2	-6.30	-5.90	-5.46	-1.81	-1.40

Table 12. Calculated orbital energies (in eV) for **DSB1-2** and **TSB3-7** based on the geometries of the B3LYP/6-311++G**.

Compounds	E_{H-2}	E_{H-1}	E_H	E_L	E_{L+1}
DSB1	-6.99	-6.62	-5.70	-2.64	-1.59
DSB2	-6.32	-5.70	-5.23	-2.67	-2.23
TSB3	-5.29	-5.17	-5.15	-2.18	-2.08
TSB4	-5.47	-5.28	-5.21	-2.35	-2.22

TSB5	-5.56	-5.48	-5.28	-2.41	-2.38
TSB6	-5.64	-5.50	-5.48	-2.52	-2.44
TSB7	-4.76	-4.69	-4.68	-1.86	-1.74

5.3.3 Optical Spectra

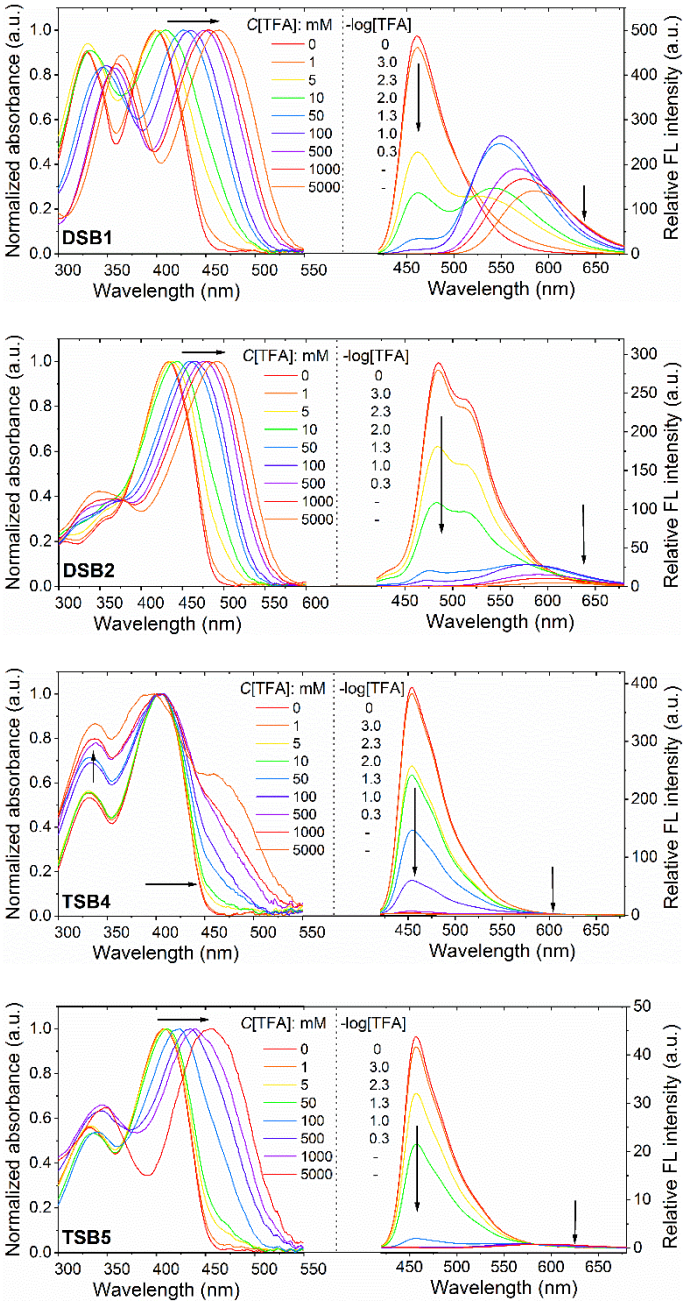

Figure 81. Normalized UV/vis absorption (left) and emission (right) spectra for the titrations of **DSB1-2** and **TSB4-5** in THF with different concentration of TFA.

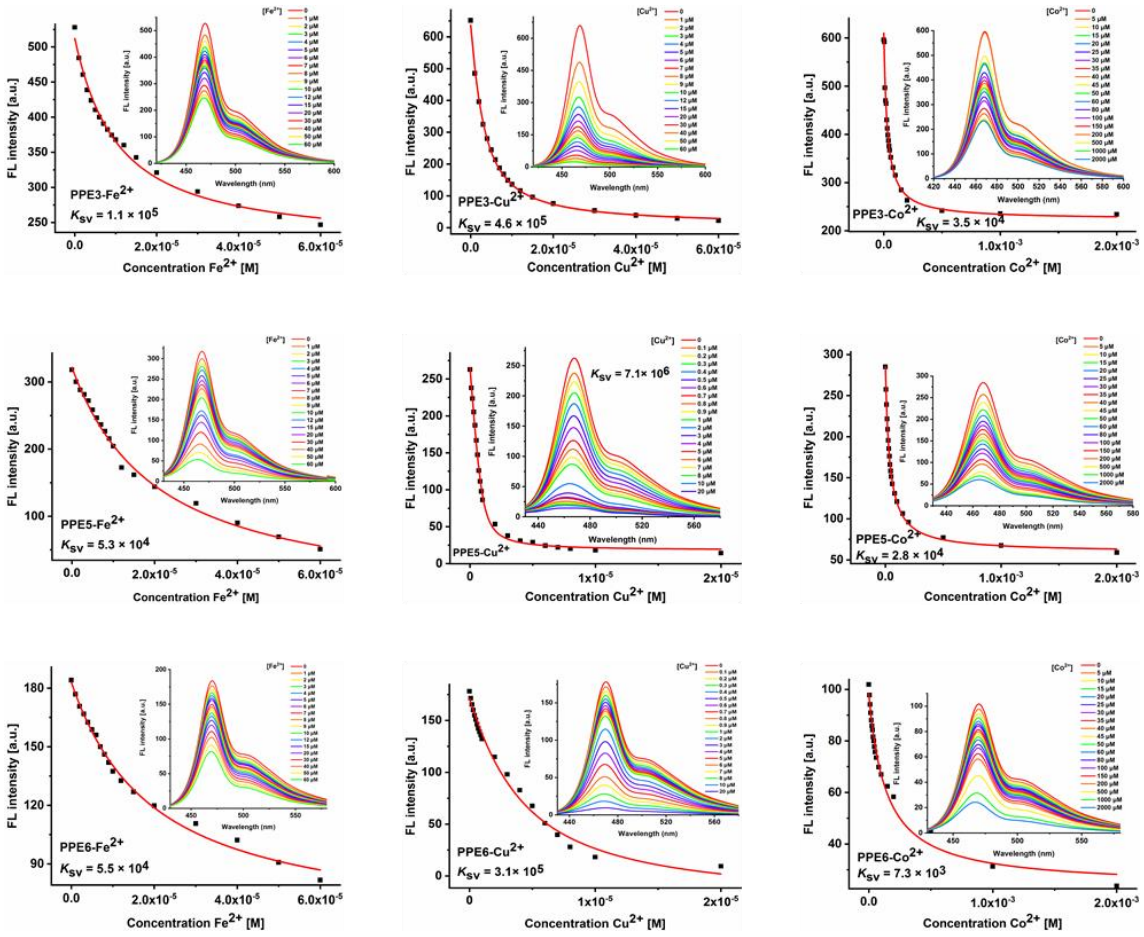

Figure 82. Stern–Volmer plots for fluorescence quenching of **PPE3,5,6** (2 μM) titrated with metal cations (Fe^{2+}, Cu^{2+} and Co^{2+}) in DMSO/H_2O (1:1). The inset show the emission of quenching data and K_{SV} values.

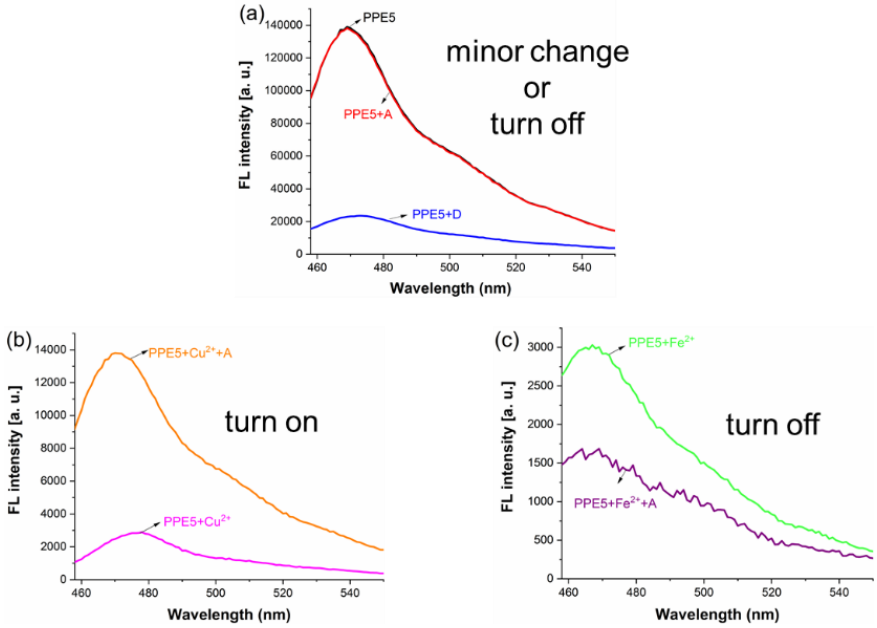

Figure 83. (a) Emission spectra of **PPE5** (2 μM) upon interaction with PTH-amino acids; (b, c) emission spectra of **PPE5** upon interaction with metal ions/ PTH-amino acids. The spectra were measured in DMSO/H_2O (1:1). **PPE5**, PTH-amino acids (A, D) and metal ions (Fe^{2+}, Cu^{2+}) were selected as examples to illustrate the overall changes in fluorescence intensity. 'PTH' was omitted for clarity.

5.3.4 Mass and NMR Spectra

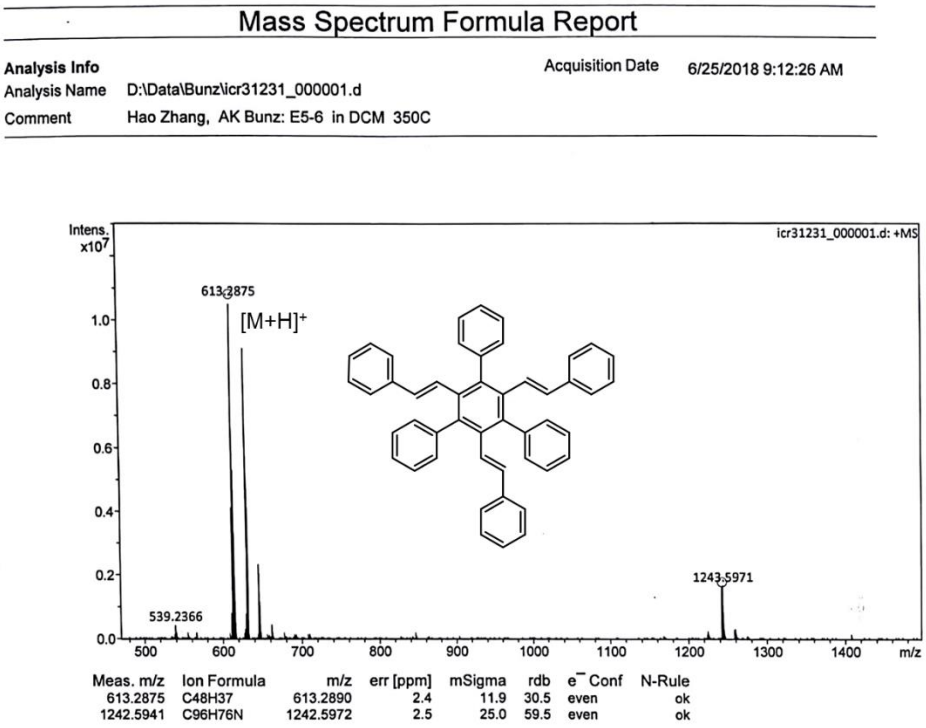

Figure 84. HRMS spectra of **TSB1**.

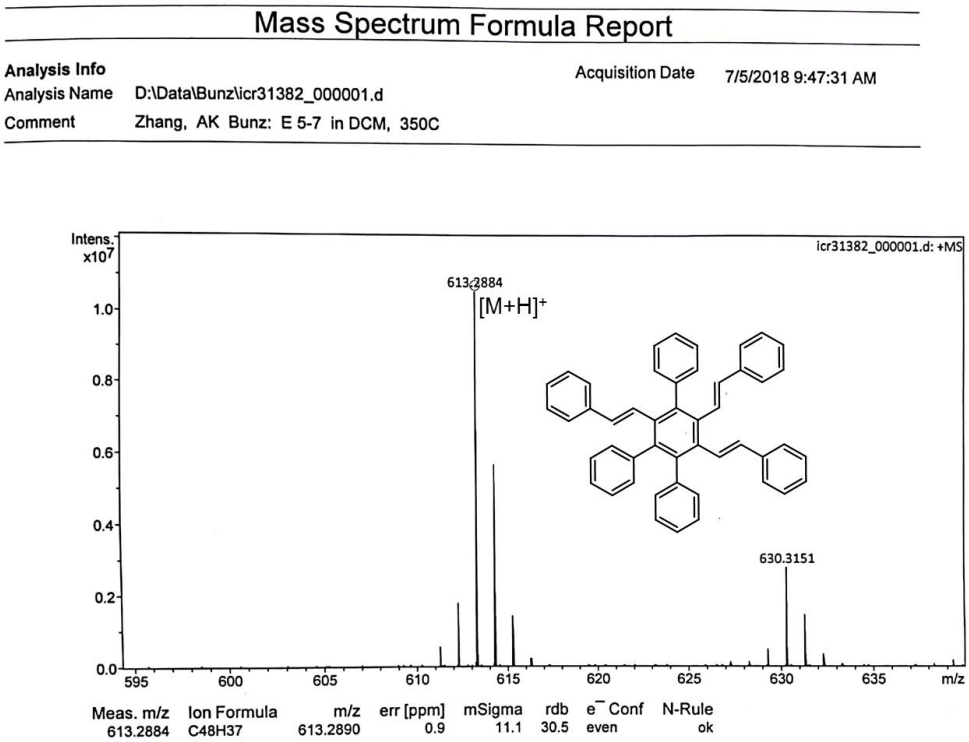

Figure 85. HRMS spectra of **TSB2**.

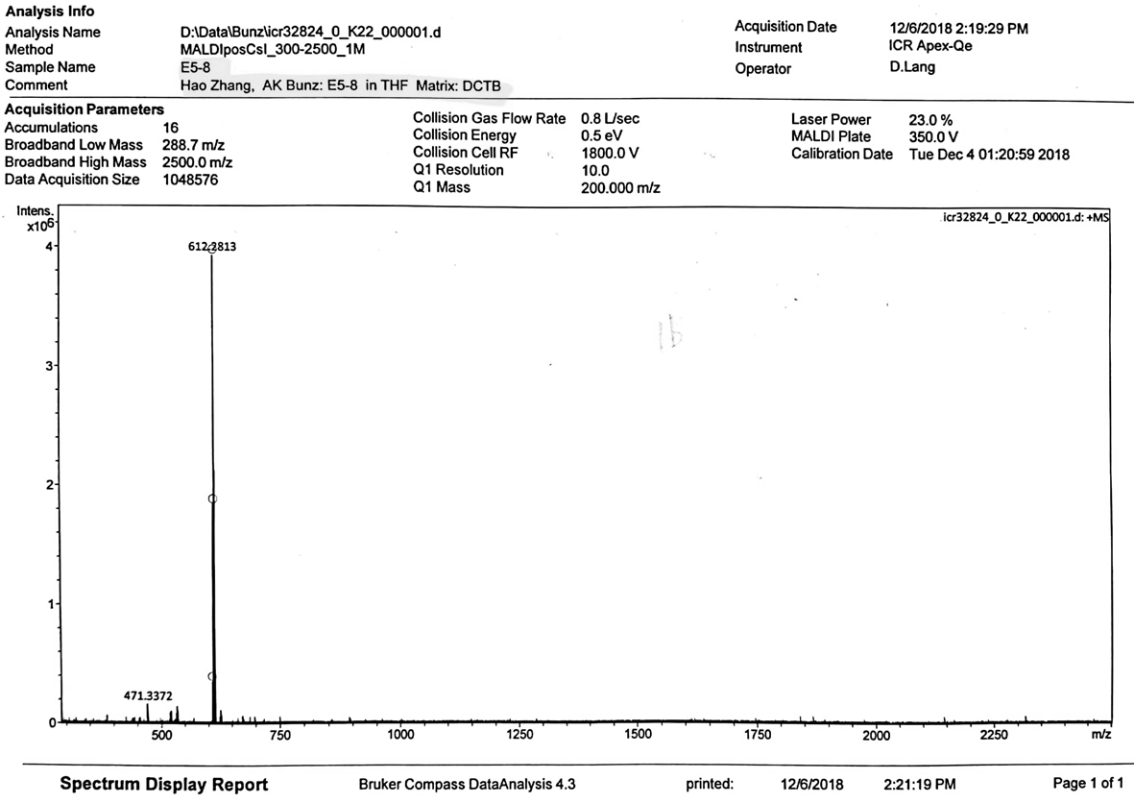

Figure 86. HRMS spectra of **TSB1a**.

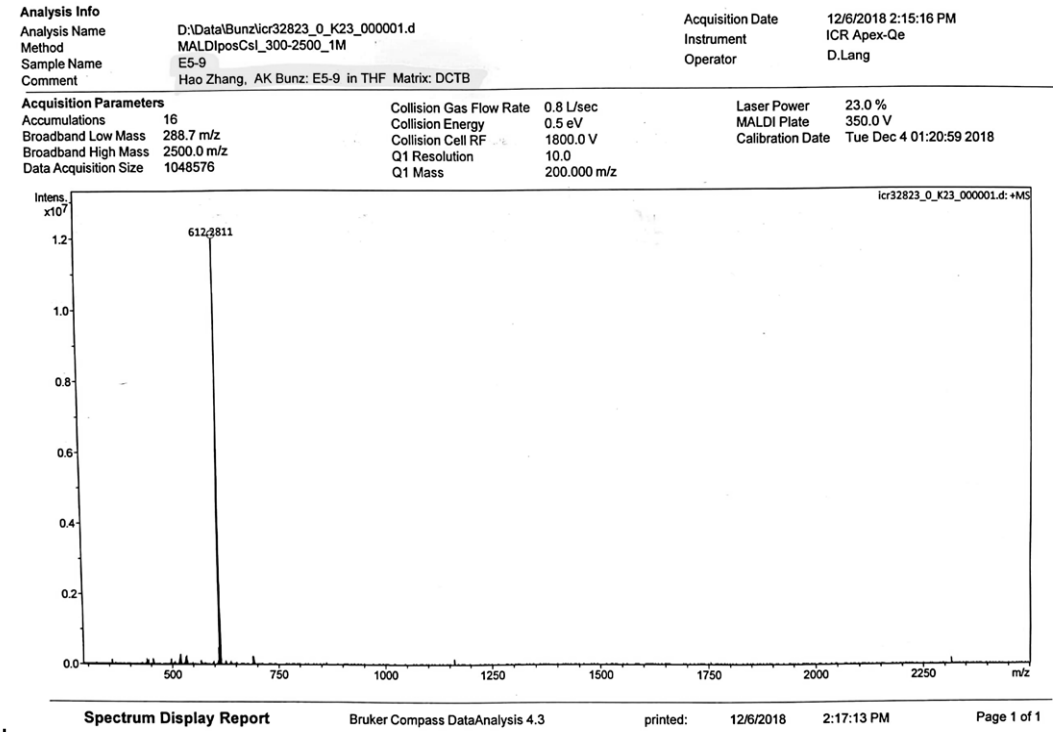

Figure 87. HRMS spectra of **TSB2a**.

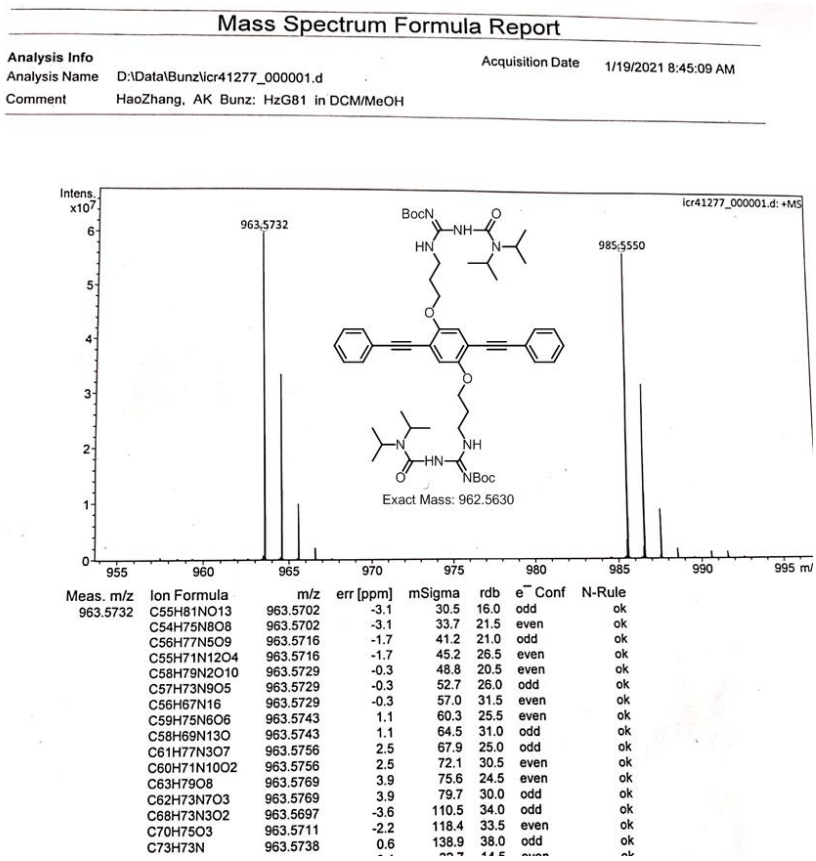

Figure 88. HRMS spectra of **PE-BU2**.

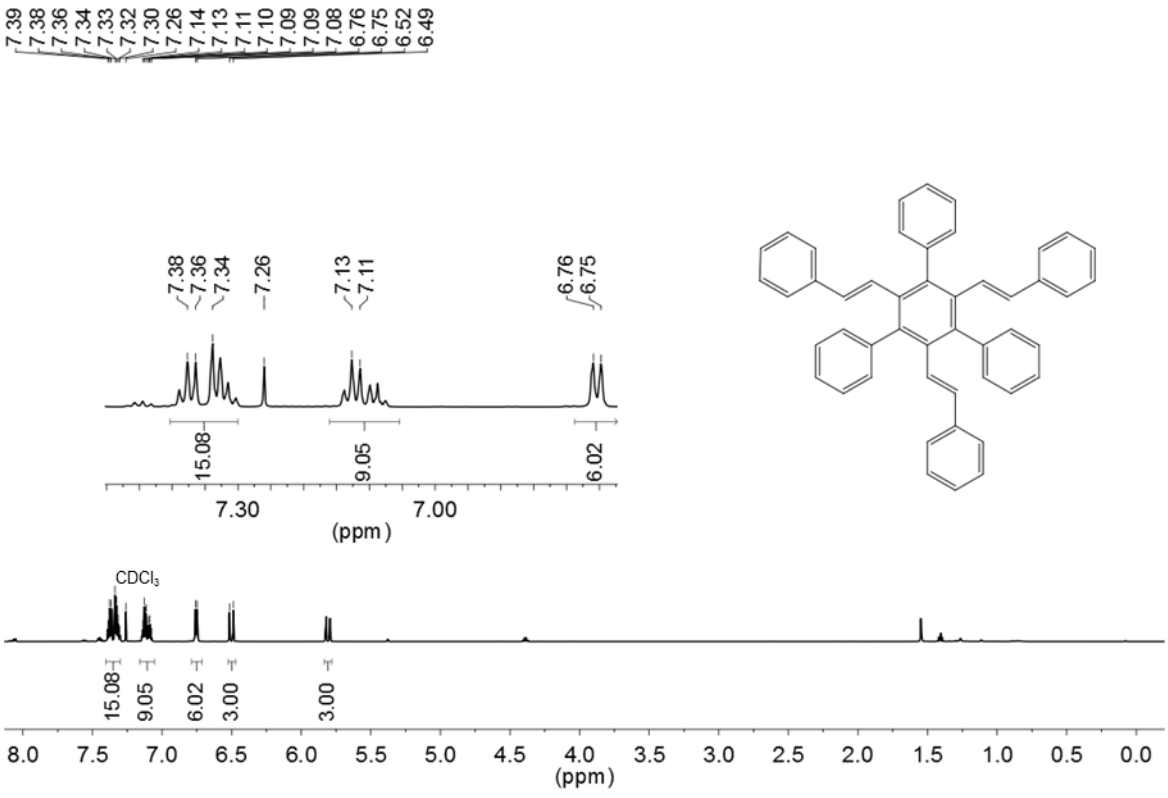

Figure 89. ^{1}H NMR spectra of **TSB1** in $CDCl_3$.

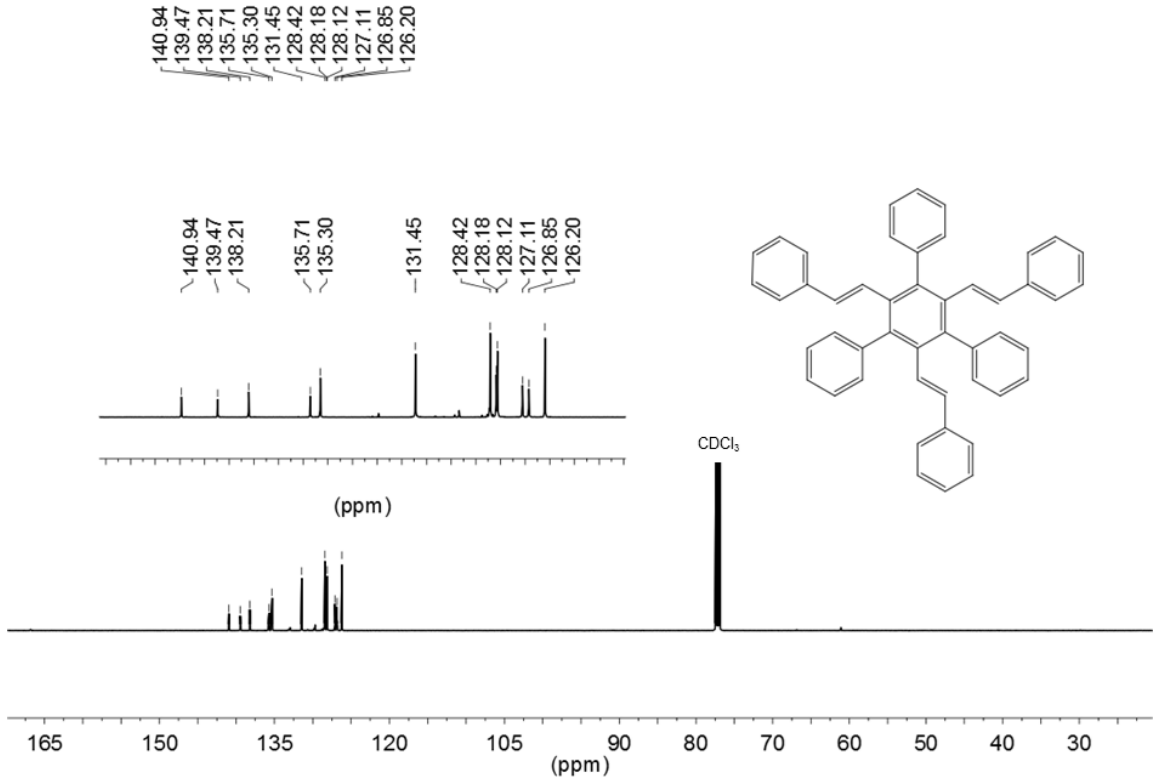

Figure 90. ^{13}C NMR (bottom) spectra of **TSB1** in $CDCl_3$.

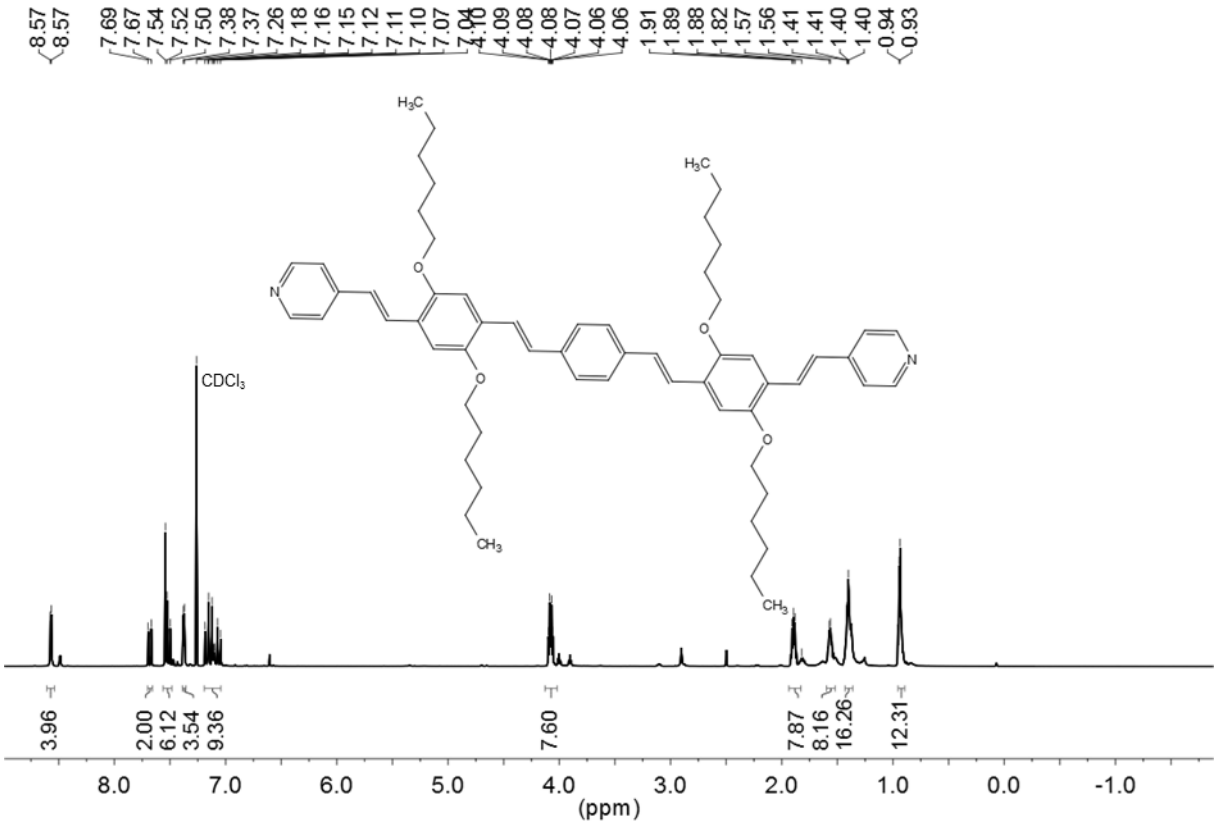

Figure 91. ^{1}H NMR spectra of **DSB2** in $CDCl_3$.

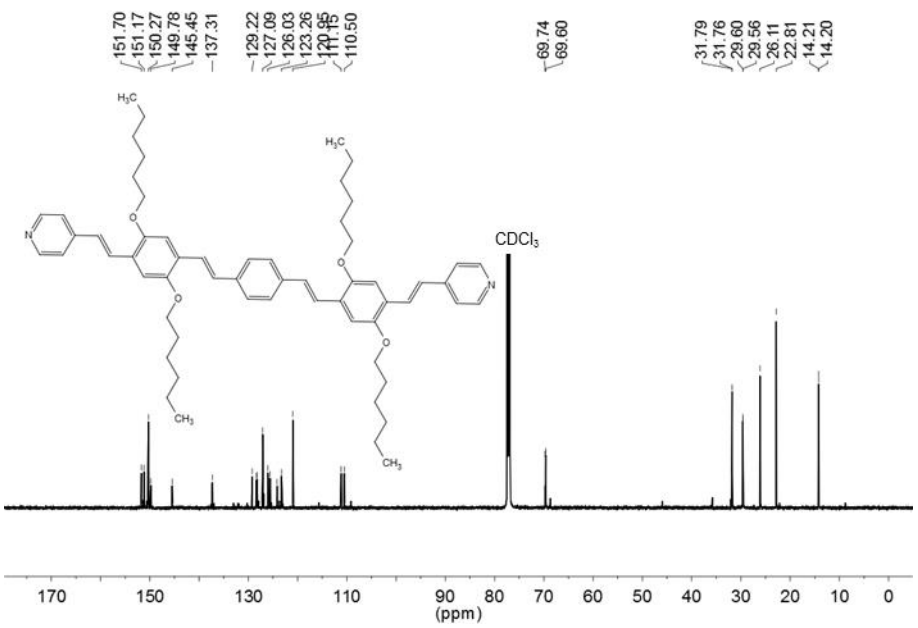

Figure 92. ^{13}C NMR spectra of **DSB2** in $CDCl_3$.

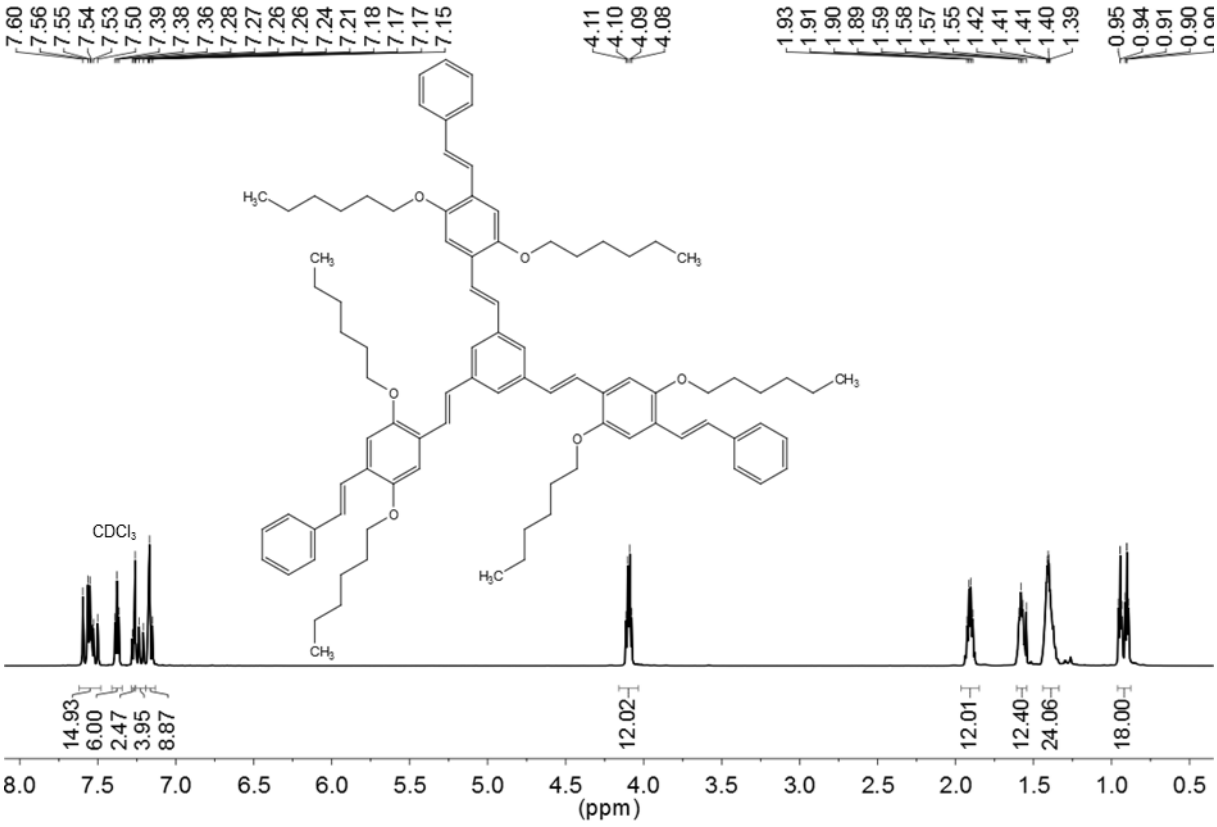

Figure 93. ^{1}H NMR spectra of **TSB3** in $CDCl_3$.

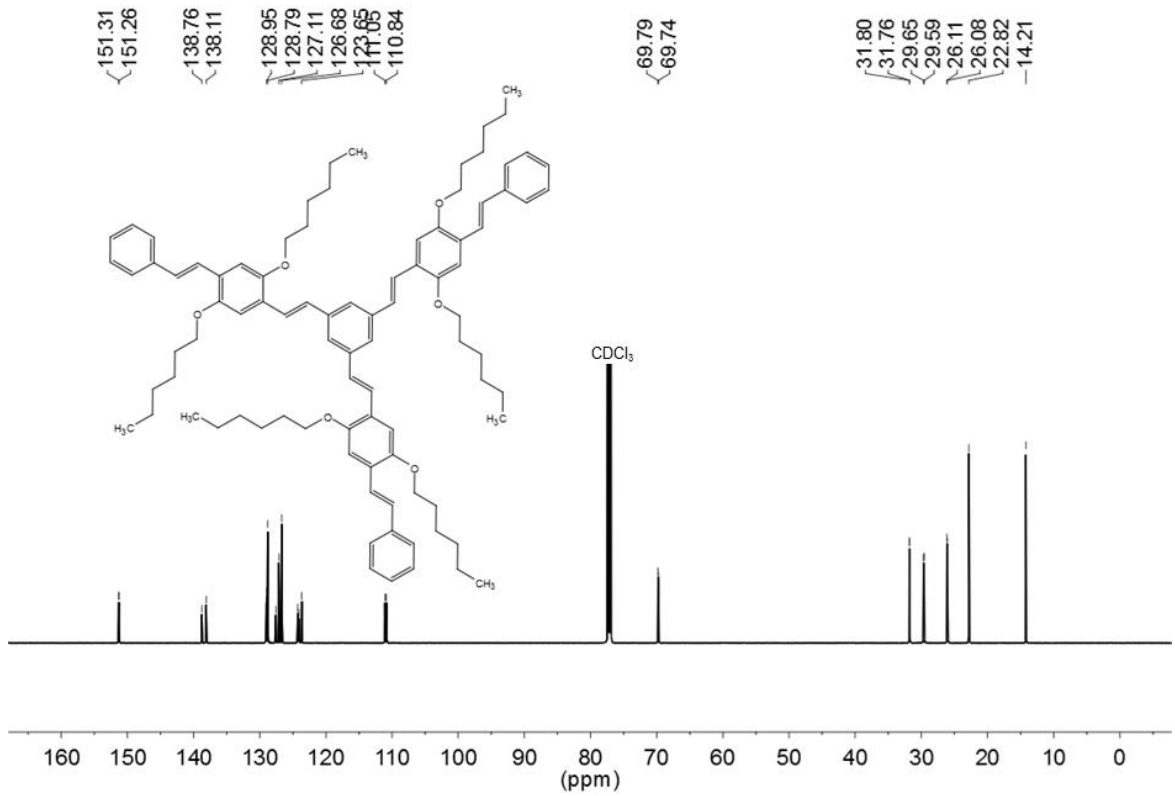

Figure 94. ^{13}C NMR spectra of **TSB3** in $CDCl_3$.

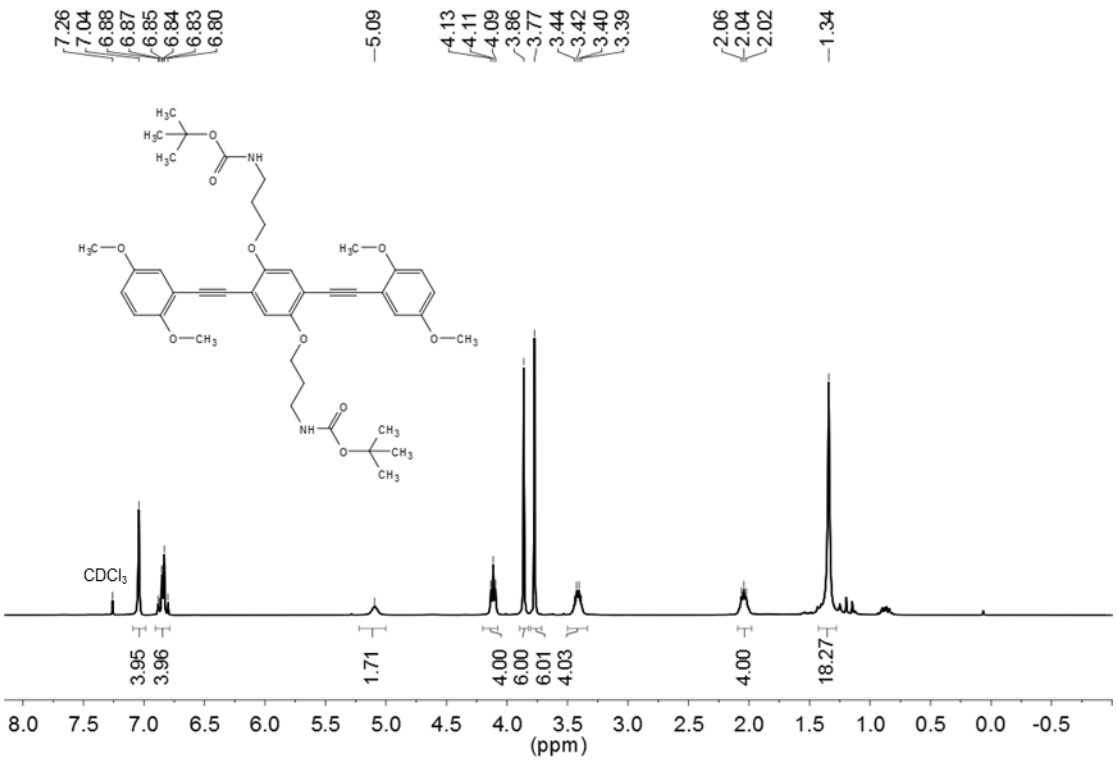

Figure 95. ^{1}H NMR spectra of **PE-BA1** in $CDCl_3$.

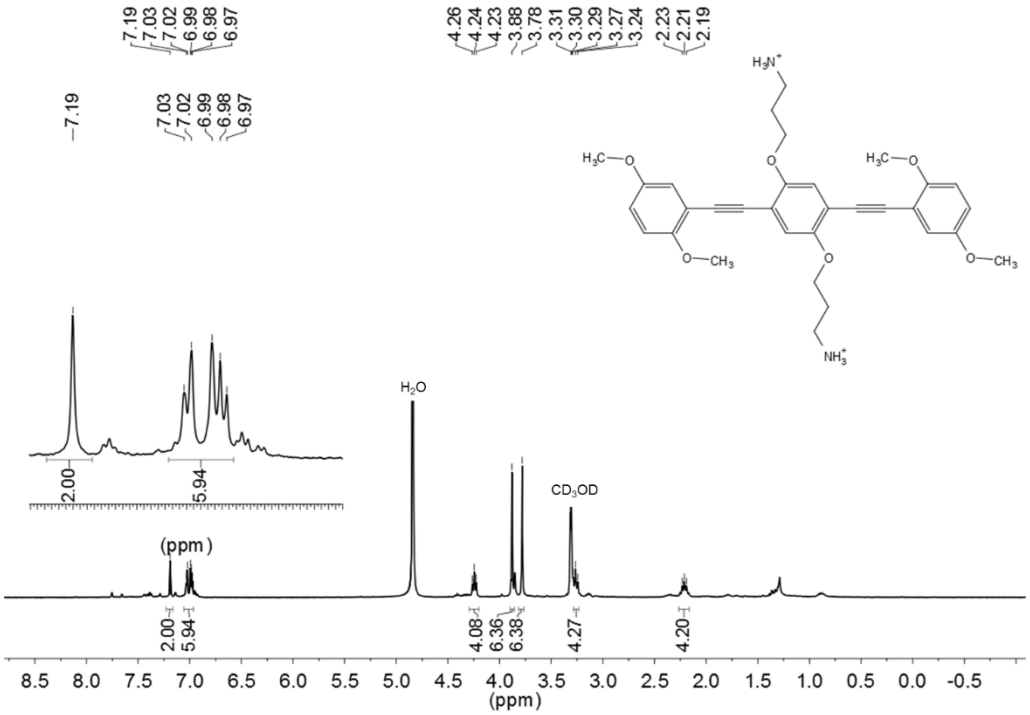

Figure 96. ^{1}H NMR spectra of **PE-A1** in CD_3OD.

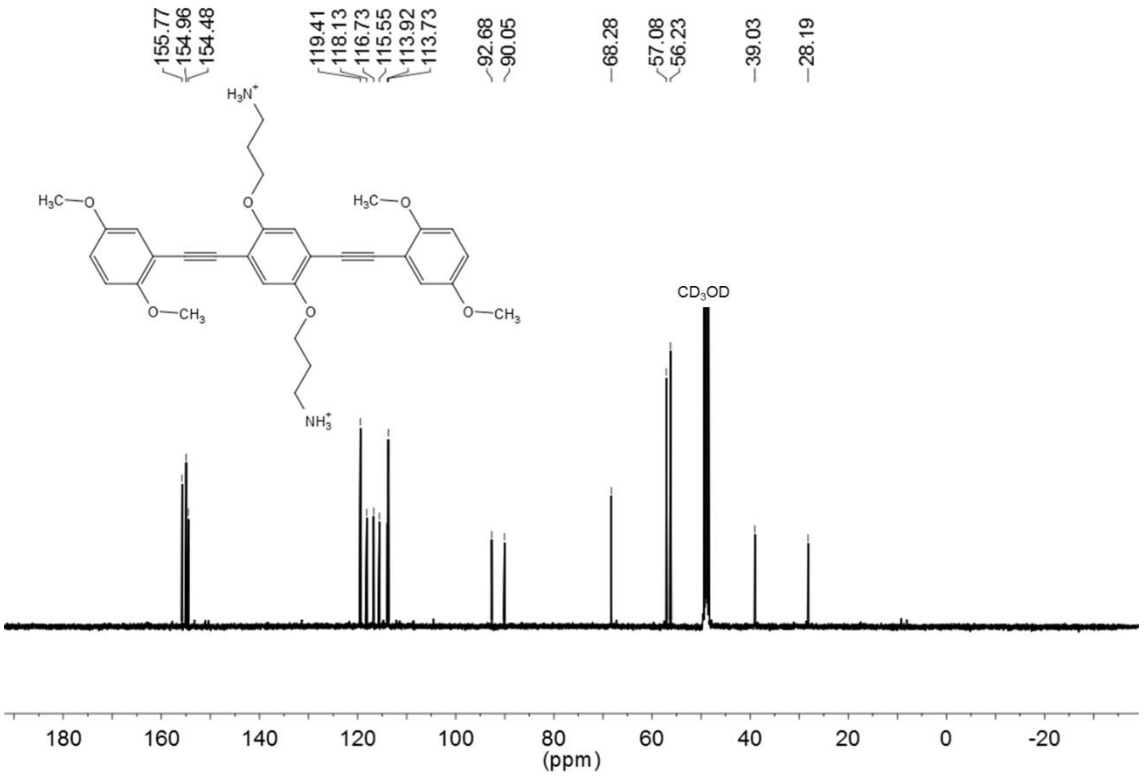

Figure 97. ^{13}C NMR spectra of **PE-A1** in CD_3OD.

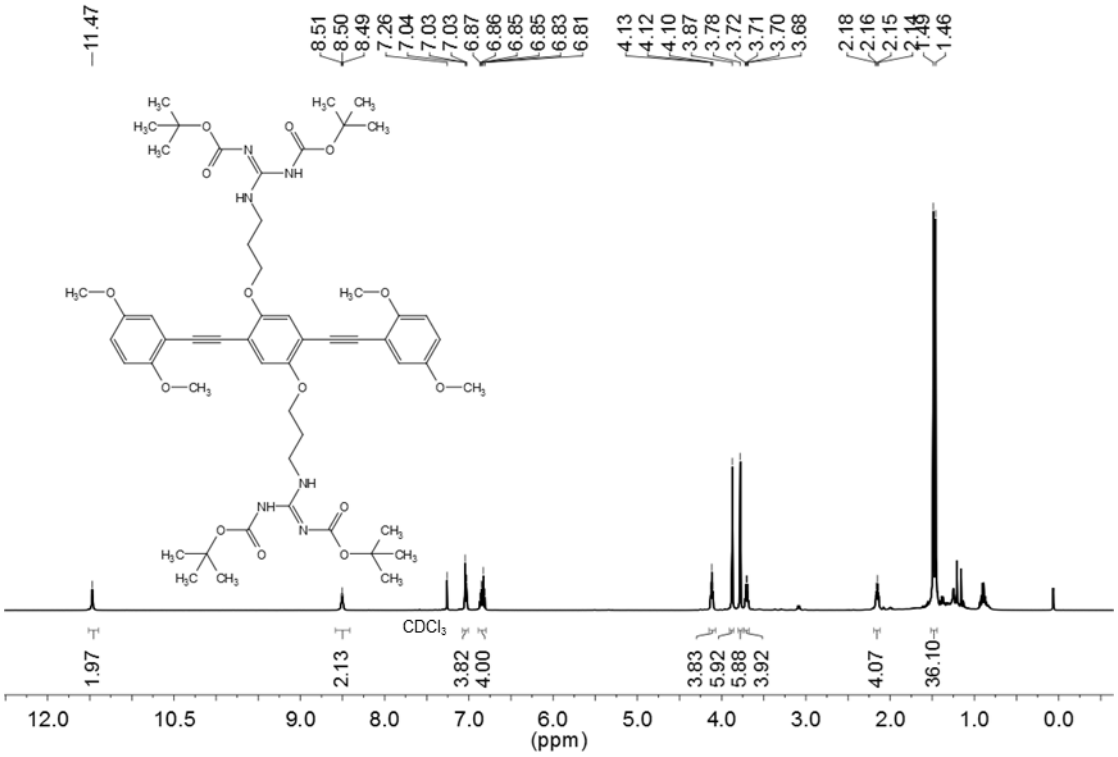

Figure 98. ^{1}H NMR spectra of **PE-BG1** in $CDCl_3$.

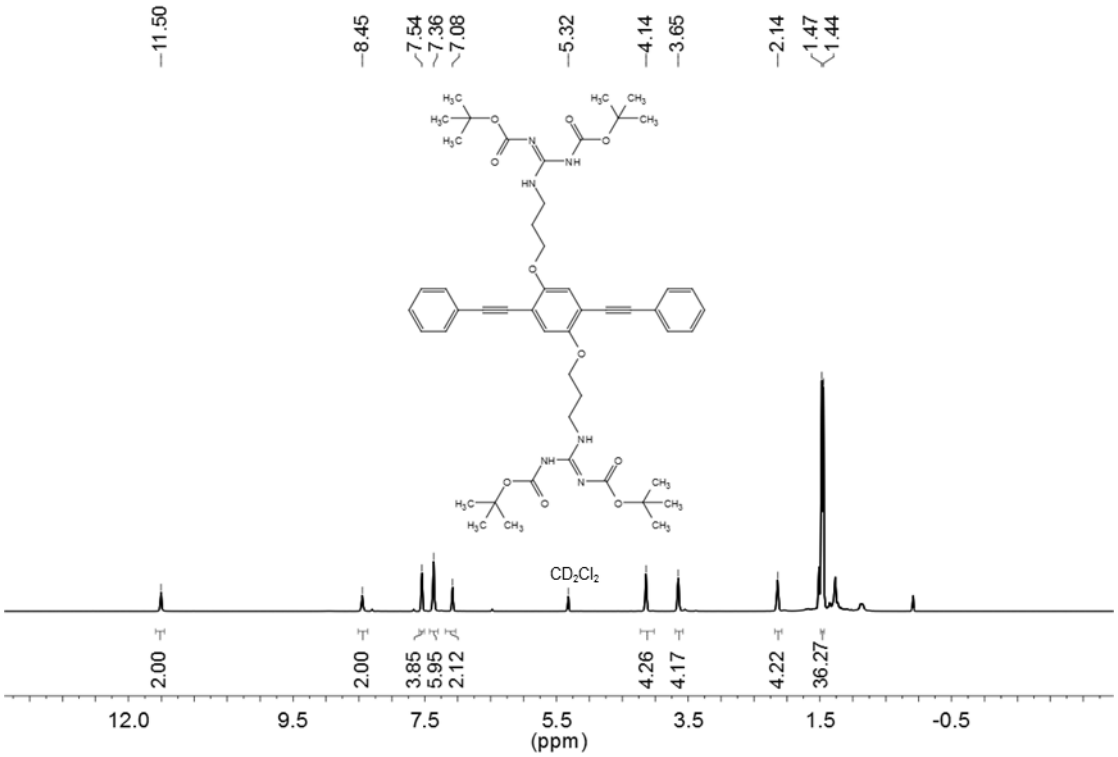

Figure 99. ^{1}H NMR spectra of **PE-BG2** in CD_2Cl_2.

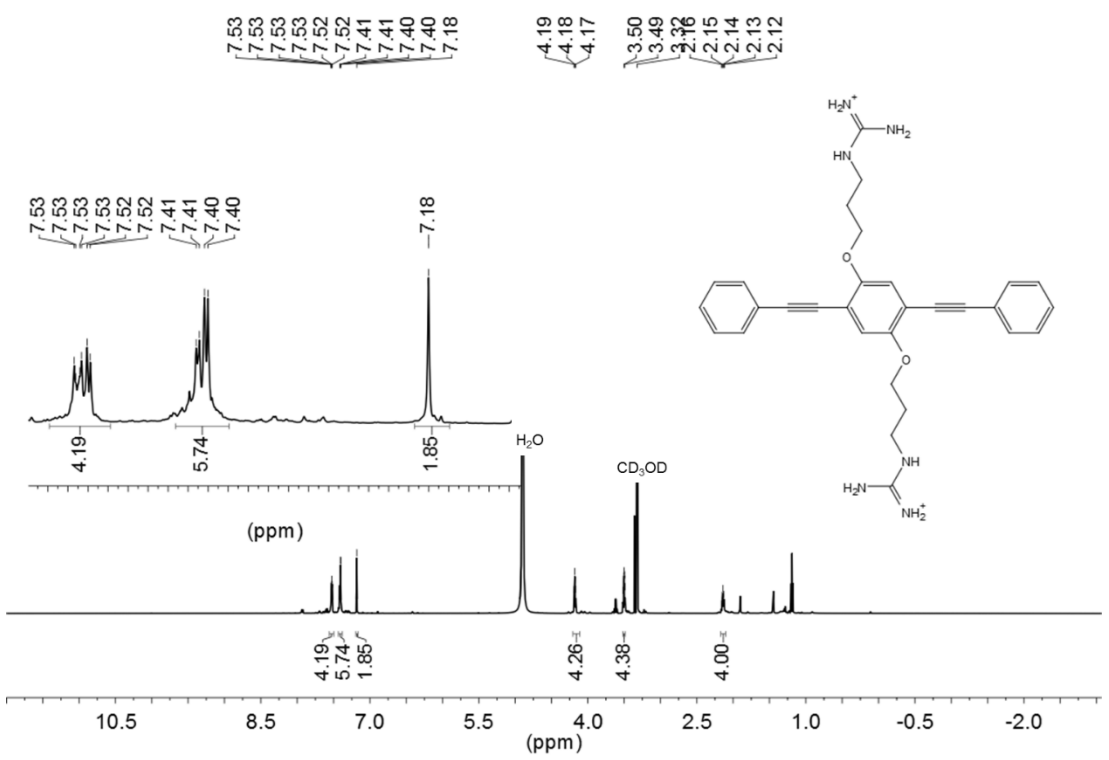

Figure 100. ^{1}H NMR spectra of **PE-G2** in CD_3OD.

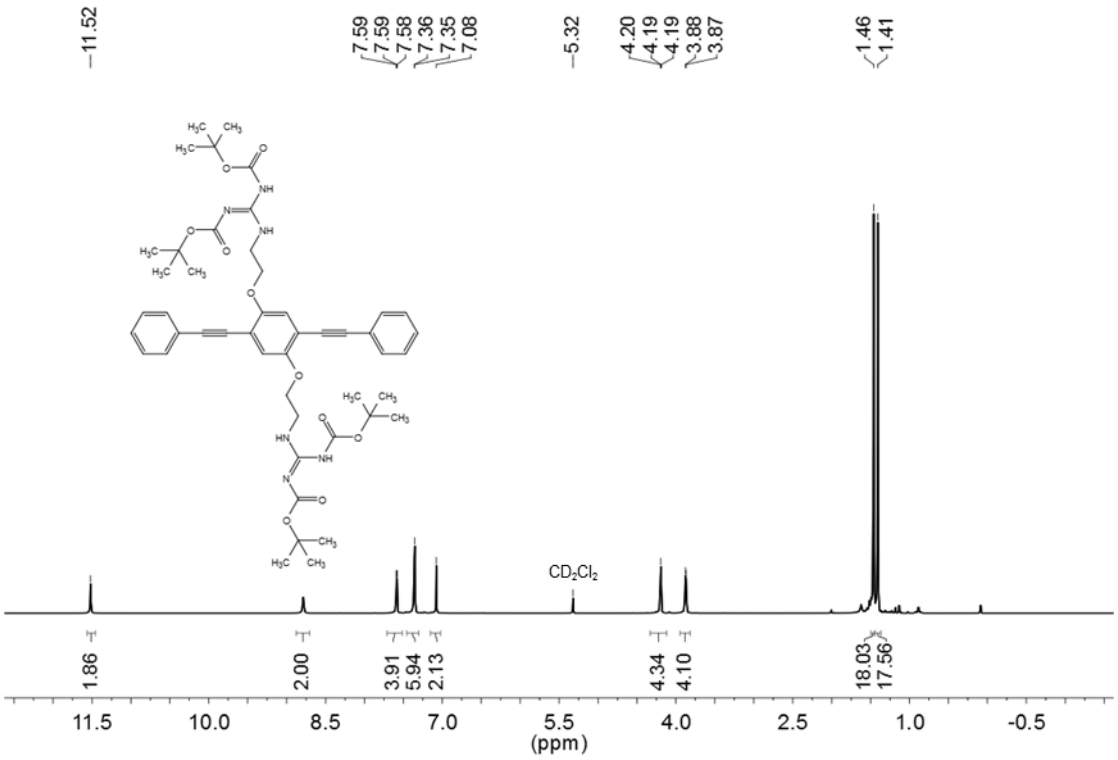

Figure 101. ^{1}H NMR spectra of **PE-BG3** in CD_2Cl_2.

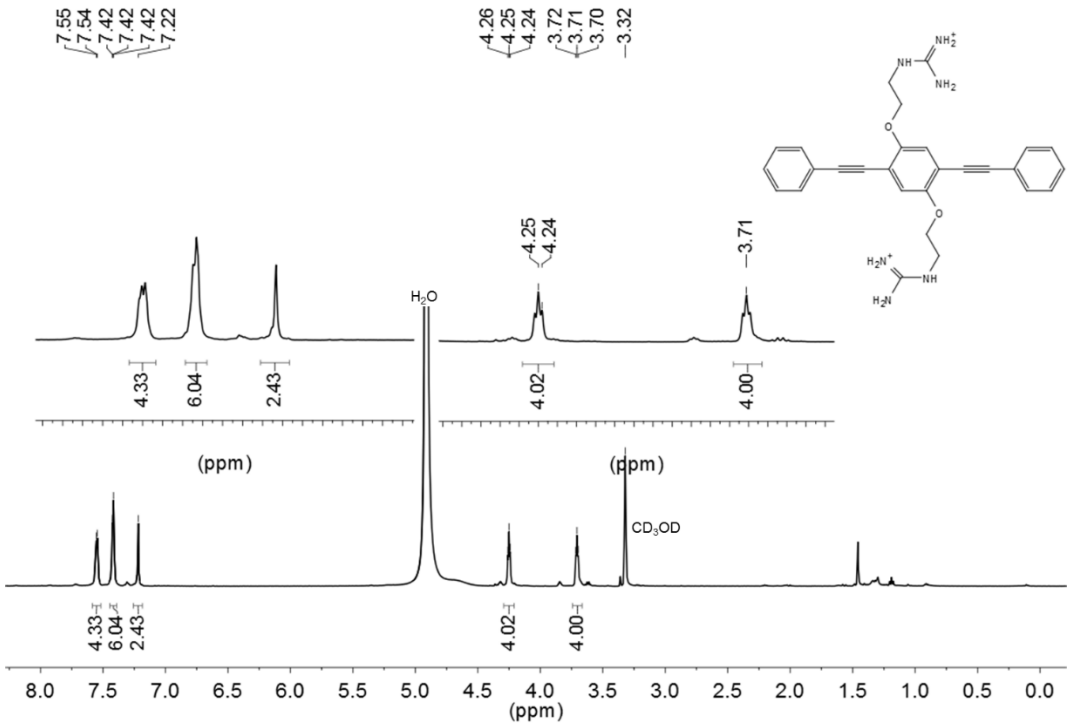

Figure 102. ^{1}H NMR spectra of **PE-G3** in CD_3OD.

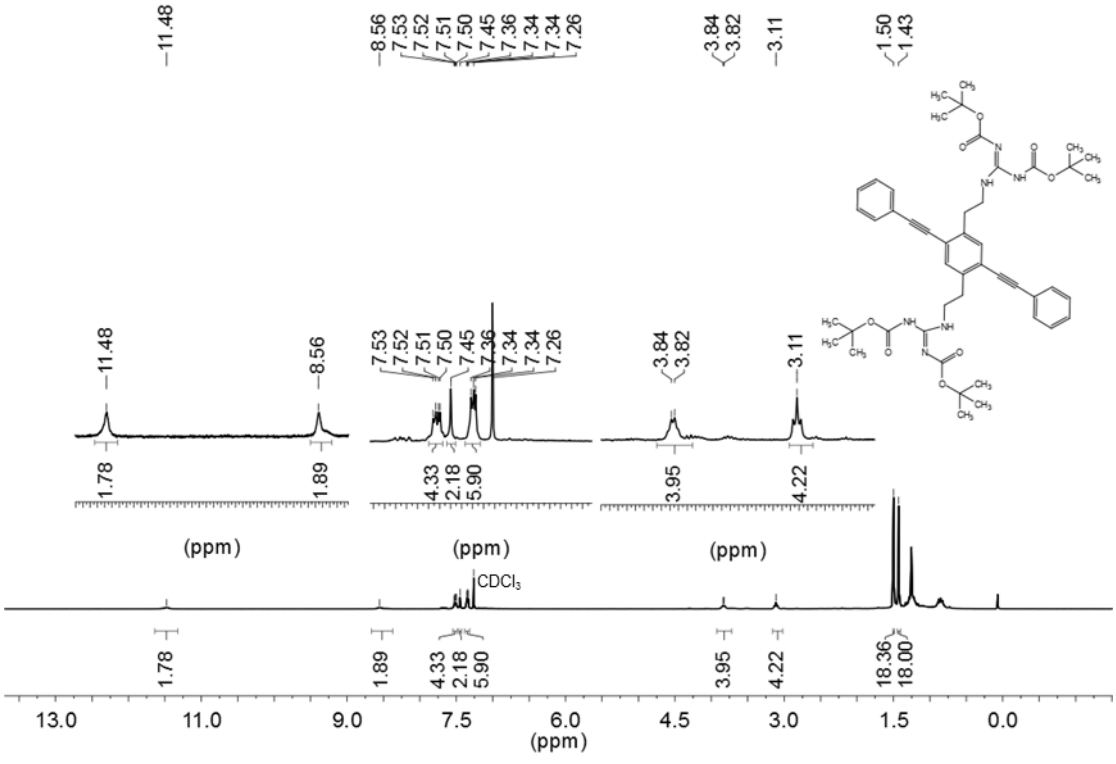

Figure 103. ^{1}H NMR spectra of **PE-BG4** in $CDCl_3$.

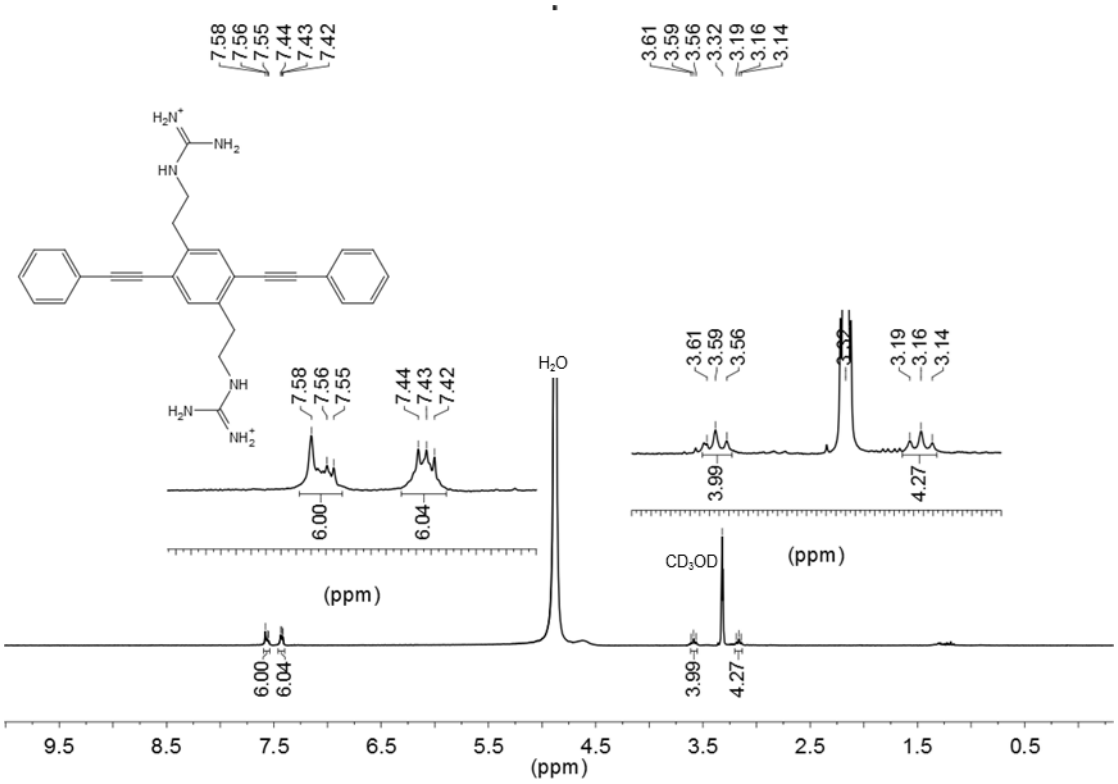

Figure 104. ^{1}H NMR spectra of **PE-G4** in CD_3OD.

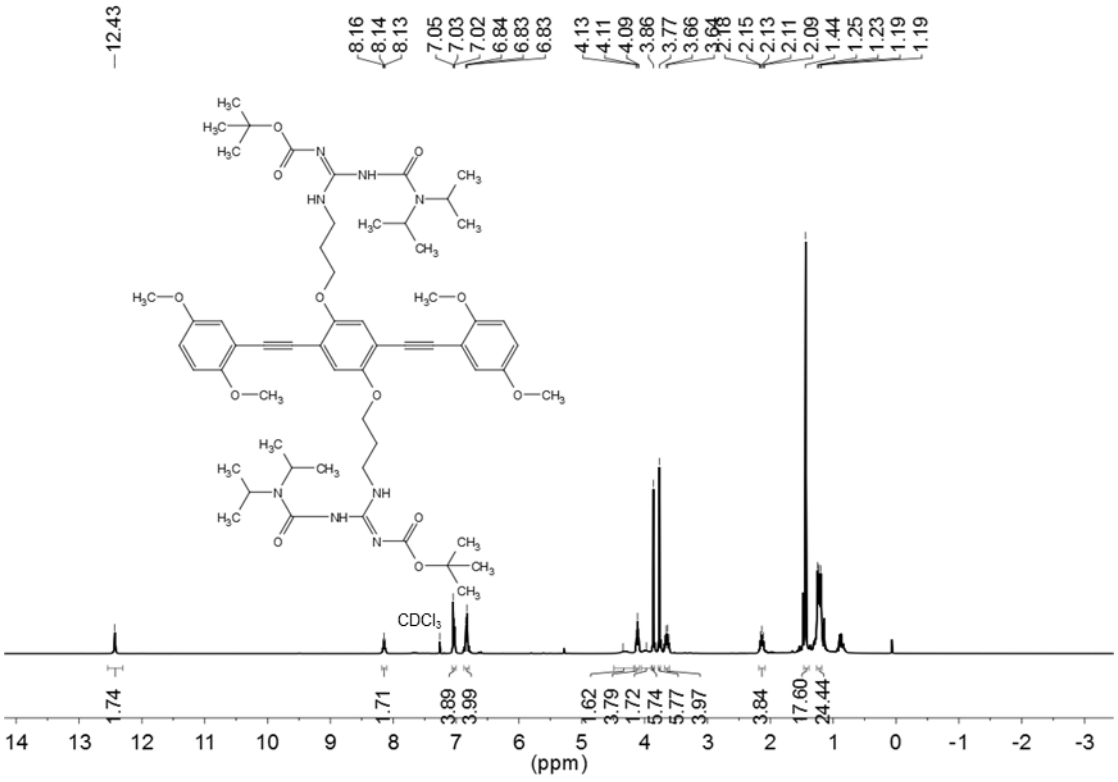

Figure 105. ^{1}H NMR spectra of **PE-BU1** in $CDCl_3$.

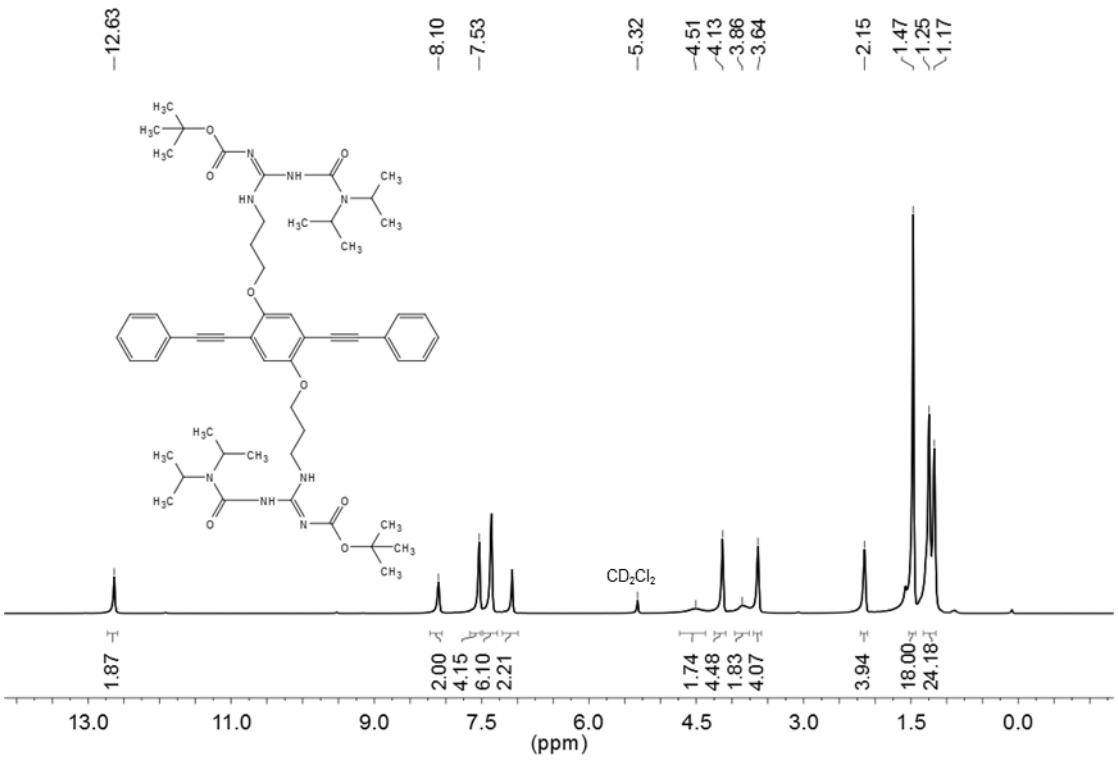

Figure 106. ^{1}H NMR spectra of **PE-BU2** in CD_2Cl_2.

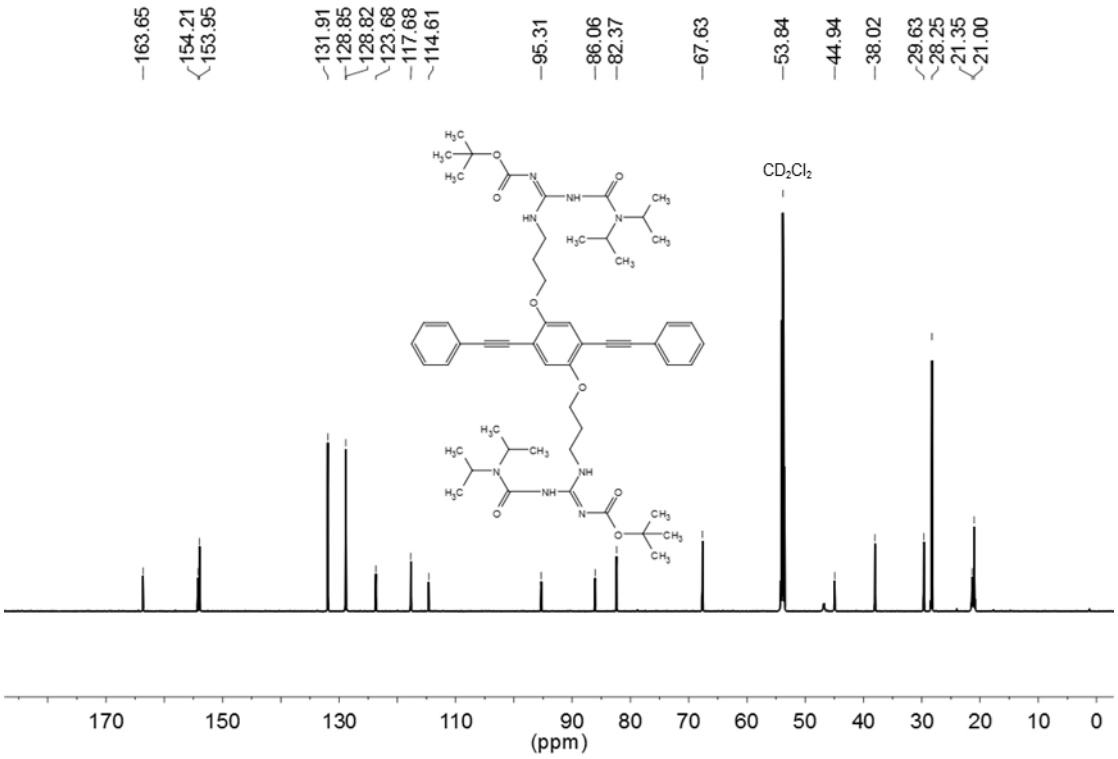

Figure 107. ^{13}C NMR spectra of **PE-BU2** in CD_2Cl_2.

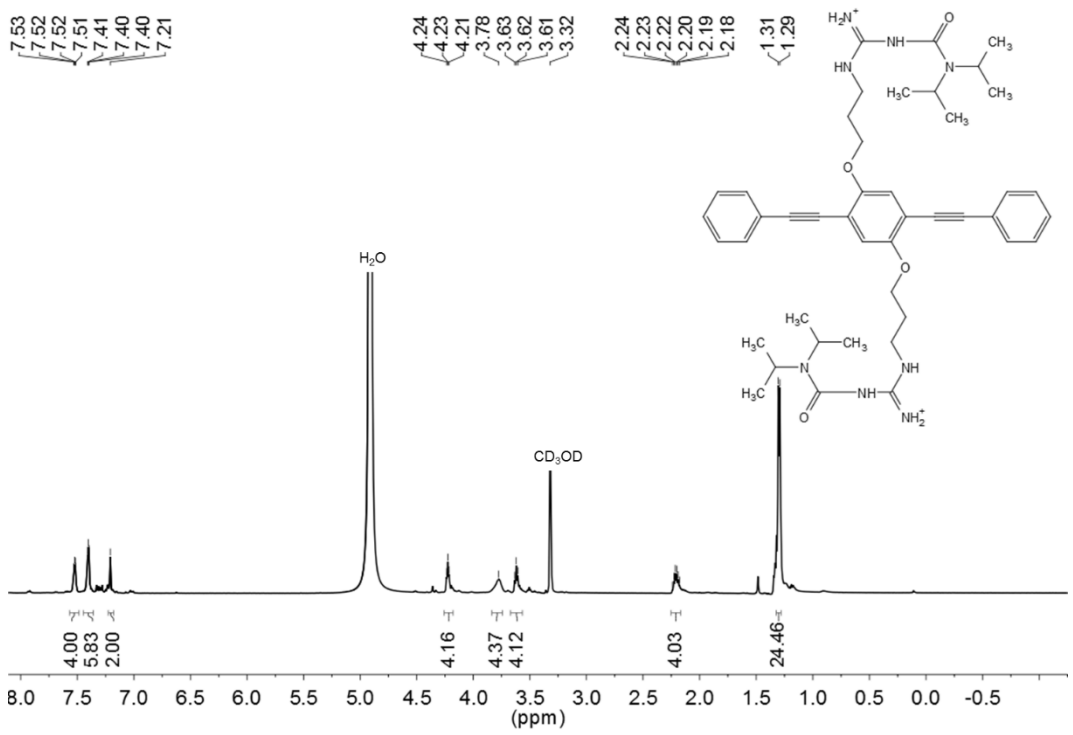

Figure 108. ^{1}H NMR spectra of **PE-U2** in CD_3OD.

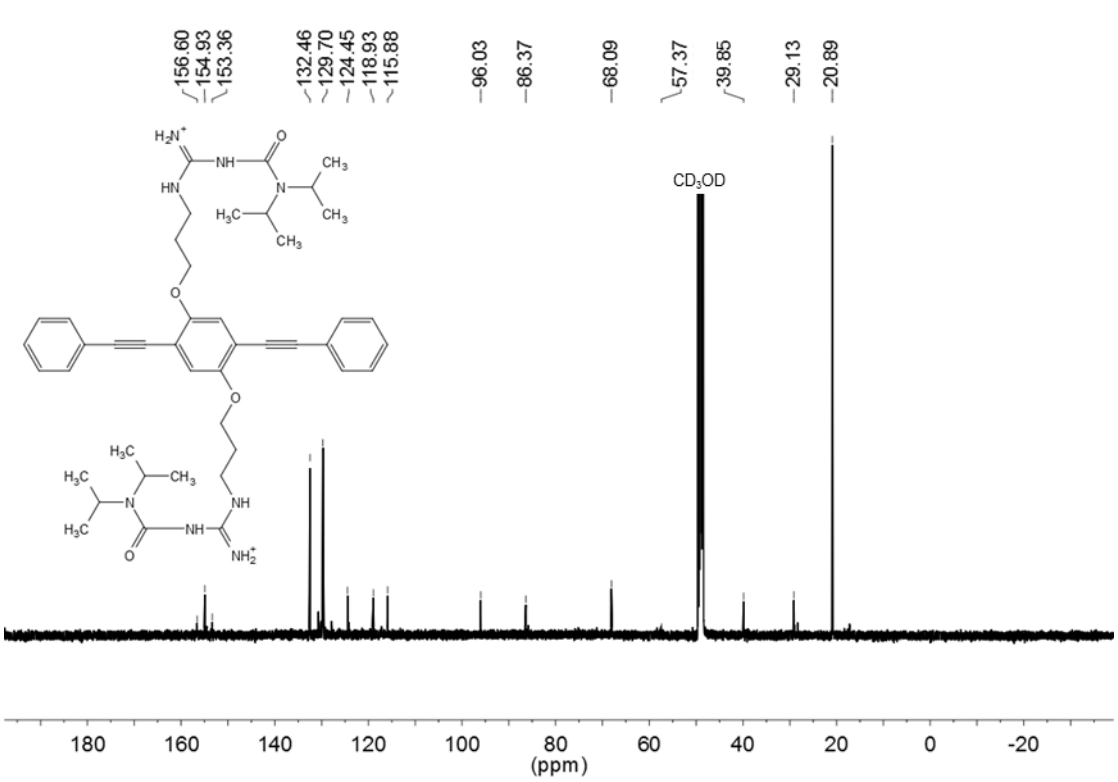

Figure 109. ^{13}C NMR spectra of **PE-U2** in CD_3OD.

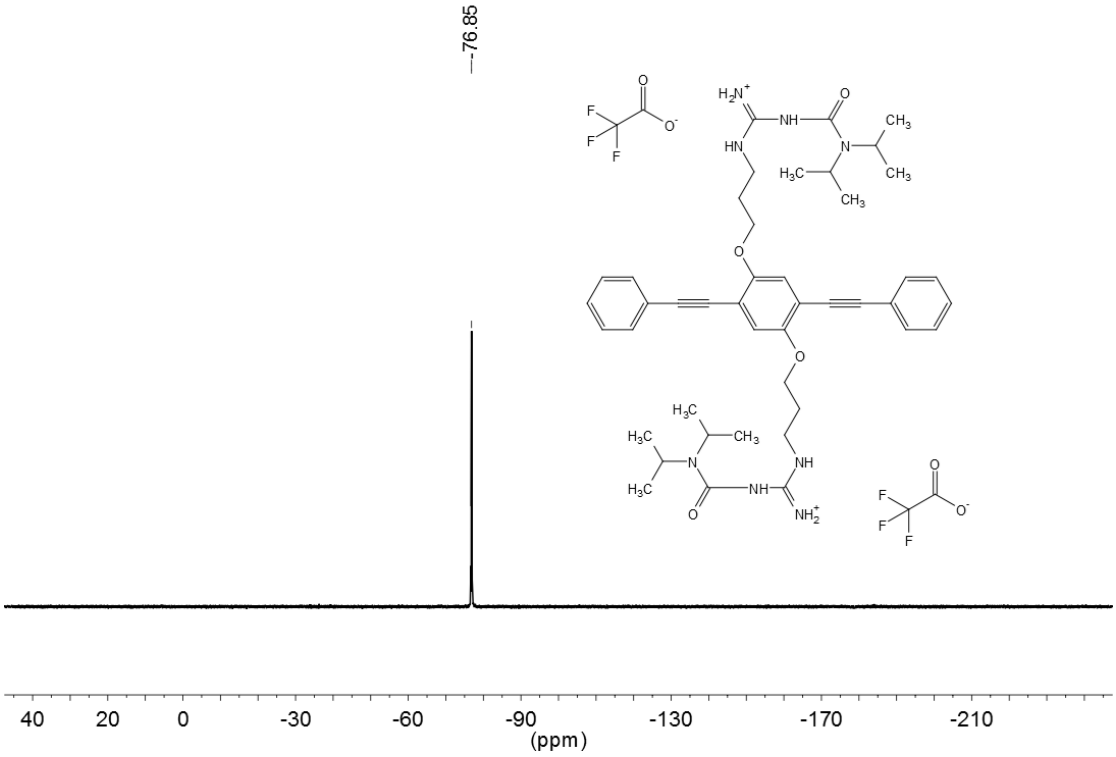

Figure 110. ^{19}F NMR spectra of **PE-U2** in CD_3OD.

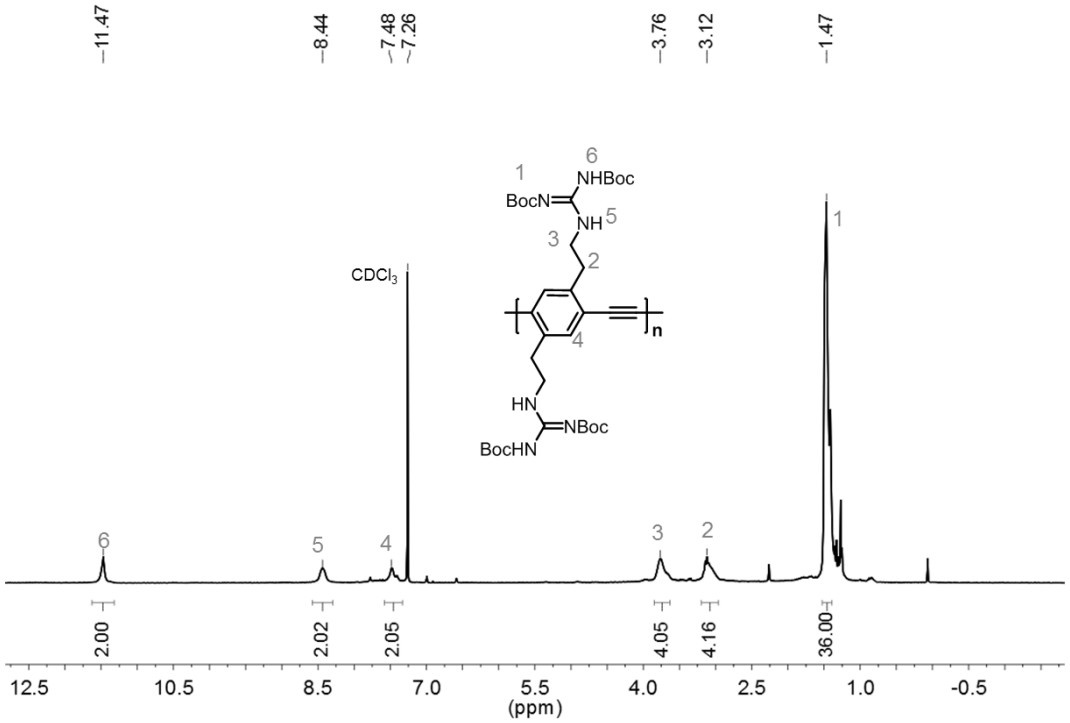

Figure 111. ^{1}H NMR spectra of **PPE14** in $CDCl_3$.

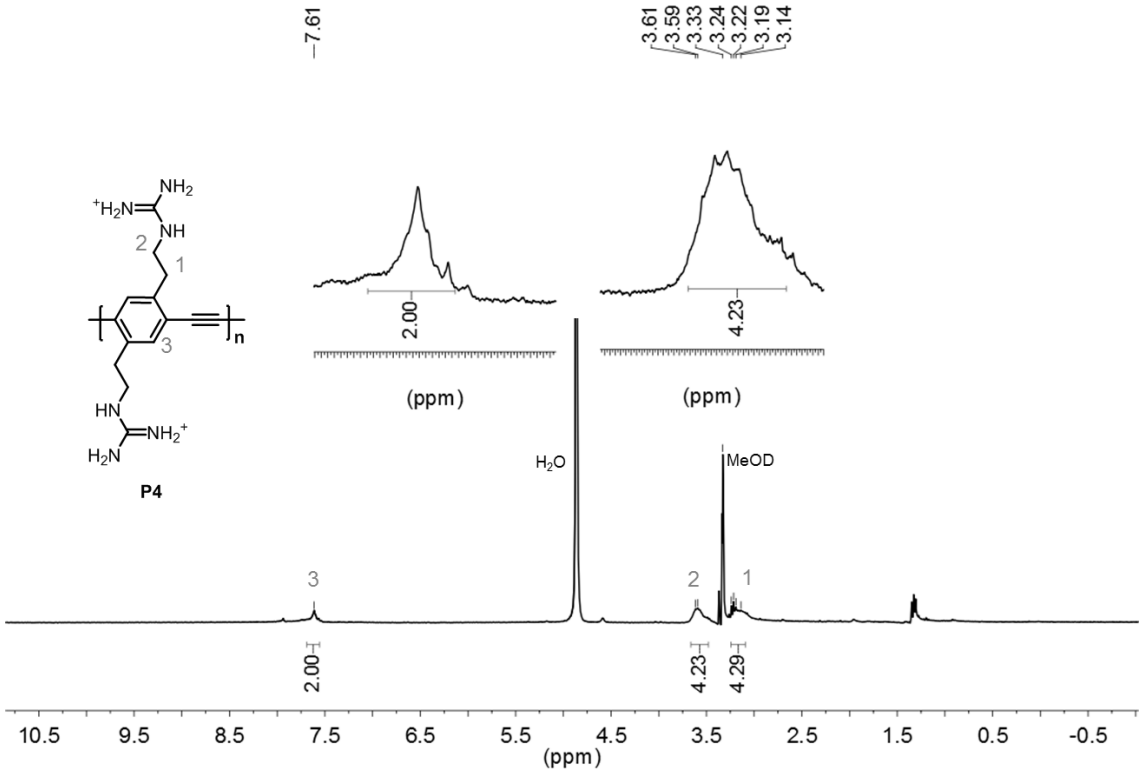

Figure 112. ^{1}H NMR spectra of **PPE15** in CD_3OD.

5.3.5 Multivariate Analysis of Variance (MANOVA)

Table 13. Matrix generated from MANOVA statistics using a SB array (**DSB1-2** and **TSB3-7**) against 13 metal cations.

	blank	Al^{3+}	Zn^{2+}	Cu^{2+}	Cu^{+}	Mn^{2+}	Fe^{2+}	Fe^{3+}	Co^{2+}	Ni^{2+}	Cd^{2+}	Ag^{+}	Pb^{2+}	Hg^{2+}
blank	0.000	0.131	0.011	0.015	0.019	0.283	0.256	0.217	0.197	0.011	0.267	0.148	0.151	0.262
Al^{3+}	0.131	0.000	0.127	0.120	0.141	0.230	0.197	0.147	0.142	0.126	0.212	0.106	0.160	0.197
Zn^{2+}	0.011	0.127	0.000	0.009	0.024	0.279	0.251	0.212	0.193	0.009	0.263	0.141	0.146	0.258
Cu^{2+}	0.015	0.120	0.009	0.000	0.027	0.276	0.248	0.207	0.187	0.012	0.259	0.138	0.144	0.254
Cu^{+}	0.019	0.141	0.024	0.027	0.000	0.295	0.268	0.229	0.208	0.020	0.279	0.157	0.160	0.274
Mn^{2+}	0.283	0.230	0.279	0.276	0.295	0.000	0.062	0.129	0.167	0.281	0.026	0.222	0.180	0.084
Fe^{2+}	0.256	0.197	0.251	0.248	0.268	0.062	0.000	0.114	0.169	0.253	0.037	0.185	0.173	0.055
Fe^{3+}	0.217	0.147	0.212	0.207	0.229	0.129	0.114	0.000	0.102	0.214	0.118	0.165	0.117	0.121
Co^{2+}	0.197	0.142	0.193	0.187	0.208	0.167	0.169	0.102	0.000	0.195	0.162	0.172	0.127	0.166
Ni^{2+}	0.011	0.126	0.009	0.012	0.020	0.281	0.253	0.214	0.195	0.000	0.264	0.144	0.150	0.260
Cd^{2+}	0.267	0.212	0.263	0.259	0.279	0.026	0.037	0.118	0.162	0.264	0.000	0.203	0.172	0.068
Ag^{+}	0.148	0.106	0.141	0.138	0.157	0.222	0.185	0.165	0.172	0.144	0.203	0.000	0.168	0.191
Pb^{2+}	0.151	0.160	0.146	0.144	0.160	0.180	0.173	0.117	0.127	0.150	0.172	0.168	0.000	0.187
Hg^{2+}	0.262	0.197	0.258	0.254	0.274	0.084	0.055	0.121	0.166	0.260	0.068	0.191	0.187	0.000

5.3.6 Linear Discriminant Analysis (LDA)

Table 14. Training matrix of fluorescence response pattern from an array of twelve elements against twenty PTH-amino acids.

Analyte	Fluorescence response pattern											
PTH-amino acids	PPE3	PPE5	PPE6	PPE3-Fe^{2+}	PPE5-Fe^{2+}	PPE6-Fe^{2+}	PPE3-Cu^{2+}	PPE5-Cu^{2+}	PPE6-Cu^{2+}	PPE3-Co^{2+}	PPE5-Co^{2+}	PPE6-Co^{2+}
PTH-A	-0.022	0.066	0.050	-0.497	-0.485	-0.975	15.553	4.455	20.110	0.215	0.736	1.369
PTH-A	0.001	0.060	0.054	-0.586	-0.451	-0.979	16.029	4.235	19.869	0.209	0.719	1.415
PTH-A	0.021	0.049	0.035	-0.494	-0.452	-0.969	15.584	4.539	20.745	0.217	0.672	1.444
PTH-A	0.009	0.038	0.027	-0.586	-0.475	-0.973	16.460	4.495	20.576	0.254	0.690	1.408
PTH-A	0.000	0.019	0.027	-0.495	-0.478	-0.974	15.857	4.390	19.958	0.258	0.709	1.409
PTH-C	-0.817	-0.742	-0.746	-0.698	-0.798	-0.916	3.454	0.380	1.610	0.032	-0.522	-0.351
PTH-C	-0.870	-0.775	-0.751	-0.699	-0.782	-0.915	3.559	0.400	1.570	0.046	-0.540	-0.340
PTH-C	-0.860	-0.773	-0.782	-0.648	-0.754	-0.936	3.632	0.430	1.720	0.027	-0.595	-0.354
PTH-C	-0.860	-0.785	-0.793	-0.691	-0.794	-0.947	3.862	0.470	1.660	0.066	-0.513	-0.429
PTH-C	-0.850	-0.782	-0.805	-0.617	-0.767	-0.930	3.648	0.420	1.660	0.074	-0.569	-0.334
PTH-D	-0.472	-0.819	-0.915	-0.417	4.867	-0.898	8.767	3.471	1.299	1.473	1.116	0.468
PTH-D	-0.482	-0.827	-0.917	-0.458	5.269	-0.887	8.862	3.503	1.148	1.348	1.091	0.447
PTH-D	-0.596	-0.831	-0.920	-0.458	4.925	-0.805	9.012	3.638	1.121	1.361	1.417	0.463
PTH-D	-0.588	-0.827	-0.924	-0.439	4.957	-0.826	8.388	3.271	1.001	1.395	1.463	0.504
PTH-D	-0.588	-0.829	-0.918	-0.439	4.596	-0.826	9.092	2.858	1.069	1.383	1.212	0.447
PTH-E	-0.388	-0.812	-0.902	-0.500	2.723	-0.941	10.212	3.931	1.617	1.748	1.549	0.497
PTH-E	-0.416	-0.821	-0.904	-0.500	3.141	-0.944	9.768	3.817	1.435	1.726	1.578	0.434
PTH-E	-0.432	-0.821	-0.906	-0.535	3.356	-0.911	9.535	3.864	1.151	1.646	1.586	0.376
PTH-E	-0.505	-0.818	-0.905	-0.533	2.375	-0.917	8.555	2.820	1.697	1.834	1.593	0.584
PTH-E	-0.505	-0.817	-0.908	-0.551	2.487	-0.917	8.696	3.660	1.571	1.719	1.432	0.471
PTH-F	-0.007	0.075	0.058	-0.590	-0.752	-0.980	15.220	3.345	22.585	0.077	-0.014	0.336
PTH-F	0.017	0.068	0.062	-0.599	-0.663	-0.983	14.995	3.304	22.853	0.069	-0.011	0.361
PTH-F	-0.065	0.037	0.030	-0.588	-0.711	-0.978	16.326	3.528	24.475	0.086	-0.014	0.330
PTH-F	-0.011	0.027	0.020	-0.562	-0.706	-0.979	15.549	3.006	23.011	0.108	0.064	0.345
PTH-F	0.000	-0.012	0.092	-0.561	-0.777	-0.978	16.260	2.826	20.793	0.124	0.009	0.376
PTH-G	-0.122	-0.546	-0.081	-0.740	-0.857	-0.975	10.242	0.277	2.540	0.145	0.648	1.071
PTH-G	-0.128	-0.575	-0.067	-0.738	-0.871	-0.981	10.247	0.169	2.188	0.137	0.756	1.058
PTH-G	-0.101	-0.561	-0.076	-0.775	-0.812	-0.978	9.581	0.284	2.027	0.129	0.685	1.150

PTH-G	-0.174	-0.565	-0.094	-0.763	-0.809	-0.977	9.328	0.287	1.970	0.183	0.671	1.147
PTH-G	-0.100	-0.589	-0.072	-0.781	-0.818	-0.975	9.651	0.336	1.441	0.165	0.755	1.140
PTH-H	-0.509	-0.819	-0.916	-0.604	3.145	-0.896	5.914	2.607	0.793	1.364	1.363	0.386
PTH-H	-0.514	-0.821	-0.920	-0.608	3.367	-0.896	4.586	2.708	0.578	1.330	1.359	0.396
PTH-H	-0.626	-0.829	-0.915	-0.615	3.188	-0.906	4.811	2.816	0.778	1.409	1.199	0.330
PTH-H	-0.633	-0.825	-0.923	-0.591	2.384	-0.906	5.507	3.142	0.802	1.398	1.449	0.368
PTH-H	-0.550	-0.833	-0.923	-0.617	3.028	-0.910	4.573	2.841	0.730	1.402	1.445	0.371
PTH-I	-0.157	-0.015	-0.048	-0.110	-0.654	-0.971	15.606	16.746	25.603	-0.034	0.184	0.566
PTH-I	-0.141	-0.007	-0.084	-0.213	-0.623	-0.978	15.420	17.029	24.629	-0.017	0.184	0.617
PTH-I	-0.153	-0.047	-0.030	-0.157	-0.629	-0.976	15.838	17.193	27.284	0.006	0.163	0.547
PTH-I	-0.174	-0.028	-0.050	-0.203	-0.711	-0.977	15.277	18.194	27.093	0.058	0.168	0.579
PTH-I	-0.140	-0.061	-0.050	-0.188	-0.652	-0.974	15.577	17.973	25.849	0.084	0.151	0.560
PTH-K	-0.022	0.049	0.012	-0.444	-0.729	-0.972	1.194	0.041	1.216	0.147	0.329	0.842
PTH-K	-0.033	0.018	0.024	-0.462	-0.686	-0.977	1.126	0.015	1.390	0.136	0.459	0.904
PTH-K	0.081	0.012	-0.002	-0.451	-0.710	-0.972	1.177	0.101	1.446	0.103	0.427	0.841
PTH-K	-0.051	-0.013	-0.007	-0.495	-0.737	-0.972	1.131	-0.063	1.435	0.185	0.362	0.860
PTH-K	0.000	-0.028	0.001	-0.452	-0.729	-0.972	1.351	0.151	1.501	0.194	0.384	0.798
PTH-L	0.001	0.008	0.041	-0.911	-0.766	-0.982	18.637	8.237	24.231	0.069	0.253	0.476
PTH-L	0.005	0.023	0.045	-0.911	-0.748	-0.984	18.765	8.561	25.180	0.075	0.255	0.468
PTH-L	0.011	-0.004	0.011	-0.913	-0.758	-0.979	18.540	8.618	25.192	0.082	0.203	0.527
PTH-L	0.049	-0.016	0.024	-0.914	-0.734	-0.983	18.003	8.770	25.908	0.114	0.301	0.547
PTH-L	0.000	0.005	0.024	-0.913	-0.790	-0.983	18.238	7.481	23.822	0.171	0.292	0.501
PTH-M	0.048	0.049	0.049	-0.532	-0.525	-0.979	15.866	3.639	17.389	0.155	0.539	1.270
PTH-M	0.028	0.017	0.048	-0.551	-0.513	-0.981	15.009	3.602	16.317	0.140	0.522	1.269
PTH-M	0.031	0.018	0.060	-0.556	-0.523	-0.975	16.881	3.672	15.608	0.141	0.551	1.280
PTH-M	0.012	0.019	0.080	-0.536	-0.532	-0.978	15.380	3.708	17.299	0.206	0.518	1.177
PTH-M	0.000	0.007	0.057	-0.554	-0.578	-0.978	15.083	3.469	15.682	0.217	0.529	1.314
PTH-N	0.028	0.057	0.041	-0.602	-0.741	-0.972	15.171	3.804	18.812	0.138	1.055	1.416
PTH-N	0.003	0.043	0.056	-0.591	-0.709	-0.977	15.157	3.801	18.007	0.145	1.051	1.325
PTH-N	0.023	0.059	0.038	-0.592	-0.719	-0.972	15.602	4.040	18.131	0.148	0.985	1.419
PTH-N	-0.012	0.011	0.030	-0.587	-0.709	-0.971	15.325	4.099	15.860	0.132	1.105	1.535
PTH-N	0.000	-0.004	0.094	-0.618	-0.704	-0.971	15.627	3.986	17.178	0.152	1.081	1.541

PTH-P	0.018	0.012	0.032	-0.855	-0.478	-0.969	4.318	1.391	1.350	0.069	0.611	0.803
PTH-P	0.013	-0.018	0.011	-0.867	-0.504	-0.972	3.357	1.564	1.316	0.060	0.504	0.766
PTH-P	-0.027	-0.054	-0.035	-0.849	-0.481	-0.961	4.417	1.765	1.456	0.089	0.636	0.765
PTH-P	-0.056	-0.093	-0.060	-0.866	-0.482	-0.961	3.282	1.937	1.473	0.126	0.609	0.825
PTH-P	0.000	-0.091	-0.074	-0.851	-0.489	-0.961	4.319	1.908	1.539	0.123	0.776	0.835
PTH-Q	0.013	0.052	-0.015	-0.810	-0.633	-0.975	16.467	5.214	20.329	0.260	1.026	1.522
PTH-Q	-0.099	0.013	0.001	-0.829	-0.669	-0.977	17.497	5.176	21.086	0.235	1.054	1.795
PTH-Q	0.001	0.029	-0.026	-0.818	-0.645	-0.971	14.640	5.401	20.169	0.275	1.018	1.642
PTH-Q	-0.004	0.002	-0.080	-0.809	-0.674	-0.972	17.356	5.659	19.442	0.318	1.008	1.586
PTH-Q	0.000	0.000	-0.063	-0.825	-0.703	-0.972	16.448	5.134	17.946	0.303	1.110	1.668
PTH-R	-0.239	-0.333	-0.589	-0.860	-0.739	-0.975	5.023	3.227	0.725	0.532	1.142	1.490
PTH-R	-0.274	-0.294	-0.619	-0.861	-0.709	-0.977	4.866	3.321	0.684	0.491	1.087	1.691
PTH-R	-0.337	-0.302	-0.599	-0.866	-0.707	-0.972	4.837	3.514	0.722	0.558	0.964	1.869
PTH-R	-0.331	-0.383	-0.617	-0.861	-0.724	-0.975	4.978	3.587	0.442	0.577	1.152	1.771
PTH-R	-0.300	-0.406	-0.550	-0.863	-0.733	-0.975	4.803	3.355	0.724	0.596	1.205	1.872
PTH-S	-0.723	-0.702	-0.730	-0.887	-0.908	-0.990	3.738	1.291	5.892	-0.669	-0.651	-0.352
PTH-S	-0.740	-0.702	-0.758	-0.866	-0.839	-0.991	2.624	1.336	5.396	-0.662	-0.625	-0.350
PTH-S	-0.813	-0.735	-0.767	-0.909	-0.874	-0.990	4.373	1.293	5.382	-0.659	-0.709	-0.434
PTH-S	-0.856	-0.713	-0.795	-0.891	-0.838	-0.990	3.215	1.481	5.204	-0.646	-0.684	-0.350
PTH-S	-0.810	-0.742	-0.796	-0.917	-0.881	-0.990	3.850	1.122	4.796	-0.635	-0.655	-0.407
PTH-T	0.026	0.046	-0.026	-0.187	-0.369	-0.620	12.237	5.122	20.647	0.071	0.474	0.839
PTH-T	-0.056	0.047	-0.041	-0.094	-0.358	-0.696	11.962	5.215	19.704	0.061	0.521	0.900
PTH-T	-0.038	0.007	-0.035	-0.105	-0.271	-0.624	12.192	5.275	18.772	0.084	0.373	0.630
PTH-T	-0.033	-0.001	-0.040	-0.079	-0.362	-0.726	12.115	5.625	18.342	0.123	0.419	0.823
PTH-T	0.000	0.006	-0.044	-0.062	-0.278	-0.726	11.905	5.336	18.893	0.116	0.512	0.867
PTH-V	-0.119	-0.386	-0.170	-0.151	5.992	-0.513	13.718	3.508	12.559	0.889	0.778	0.798
PTH-V	-0.164	-0.351	-0.158	-0.143	5.358	-0.503	13.963	3.505	12.304	0.869	0.757	0.719
PTH-V	-0.033	-0.386	-0.143	-0.208	5.721	-0.473	13.731	3.738	13.361	0.857	0.708	0.744
PTH-V	-0.070	-0.422	-0.158	-0.198	5.064	-0.506	13.004	3.730	13.184	0.855	0.708	0.666
PTH-V	-0.100	-0.399	-0.193	-0.103	5.336	-0.568	12.569	3.670	12.961	0.915	0.757	0.704
PTH-W	-0.452	-0.483	-0.534	-0.649	-0.660	-0.960	5.125	-0.147	8.582	-0.392	-0.427	-0.185
PTH-W	-0.433	-0.439	-0.539	-0.678	-0.643	-0.968	5.735	-0.092	7.347	-0.436	-0.441	-0.186
PTH-W	-0.507	-0.491	-0.532	-0.678	-0.634	-0.963	5.808	0.010	7.742	-0.438	-0.415	-0.213

PTH-W	-0.540	-0.470	-0.520	-0.659	-0.632	-0.963	5.750	0.041	8.103	-0.400	-0.430	-0.233
PTH-W	-0.500	-0.524	-0.594	-0.669	-0.628	-0.963	5.601	0.081	7.921	-0.409	-0.384	-0.269
PTH-Y	-0.004	0.036	-0.023	-0.475	-0.694	-0.977	13.637	3.076	18.551	0.061	0.198	0.720
PTH-Y	0.014	0.041	-0.006	-0.431	-0.669	-0.980	13.719	3.348	18.694	0.059	0.240	0.769
PTH-Y	-0.023	0.012	-0.047	-0.476	-0.631	-0.977	13.719	3.287	19.149	0.065	0.267	0.668
PTH-Y	-0.052	0.004	-0.063	-0.518	-0.728	-0.977	13.769	3.512	18.475	0.054	0.154	0.706
PTH-Y	0.000	0.025	-0.035	-0.470	-0.664	-0.977	13.461	3.376	18.288	0.109	0.233	0.600

Table 15. LDA was carried out as described above resulting in the final nine factors of the canonical scores and group generation.

Analyte	Resuls LDA (nine scores)									
PTH-amino acids	Group	(1)	(2)	(3)	(4)	(5)	6)	(7)	(8)	(9)
PTH-A	1	5.62	21.84	-4.48	6.87	-1.02	-1.36	-0.05	2.92	-1.11
PTH-A	1	5.47	21.16	-6.57	7.48	1.59	-0.16	-0.02	1.87	-1.10
PTH-A	1	5.15	21.97	-3.67	7.71	-0.73	-1.61	0.14	1.93	0.27
PTH-A	1	6.52	21.84	-5.71	7.92	2.67	-0.87	0.62	1.23	-0.50
PTH-A	1	5.93	20.83	-3.97	7.71	-0.15	-2.56	0.00	1.61	-0.37
PTH-C	2	-35.98	-30.59	9.84	-0.31	2.14	-2.99	5.66	-0.70	-2.19
PTH-C	2	-36.25	-31.66	11.05	-0.07	2.92	-3.32	5.91	-0.31	-2.64
PTH-C	2	-37.00	-31.30	12.57	0.54	1.51	-3.93	5.81	-0.76	-2.70
PTH-C	2	-35.51	-31.30	11.14	0.08	3.18	-3.95	5.67	-0.56	-2.54
PTH-C	2	-35.63	-31.30	12.74	0.67	0.89	-4.98	6.00	-0.95	-2.45
PTH-D	3	44.27	-31.59	10.49	0.70	0.31	1.94	0.56	-2.56	-0.94
PTH-D	3	41.78	-32.91	11.75	1.13	1.12	4.72	-1.59	-2.29	-1.33
PTH-D	3	42.99	-31.69	10.31	-1.00	2.03	3.14	-3.41	2.12	-2.87
PTH-D	3	44.01	-32.77	9.51	-0.46	0.86	2.87	-3.13	2.84	-2.16
PTH-D	3	40.62	-32.61	9.85	1.77	1.36	1.35	-0.80	0.36	-2.95
PTH-E	4	48.31	-22.81	-0.34	-4.66	5.57	-7.85	2.70	-2.87	0.52
PTH-E	4	48.99	-24.87	0.72	-4.20	5.09	-6.01	1.84	-1.78	0.45
PTH-E	4	47.35	-25.81	1.05	-4.70	5.55	-4.01	0.51	-1.16	0.18

PTH-E	4	48.21	-26.41	-2.91	-3.42	5.66	-8.46	5.75	0.71	1.02
PTH-E	4	44.66	-25.29	-0.16	-5.56	6.12	-6.61	5.10	-0.80	0.38
PTH-F	5	-5.09	19.57	-2.31	14.01	1.00	0.83	6.30	-0.97	0.87
PTH-F	5	-5.22	19.14	-2.31	14.40	1.13	1.25	6.00	-0.98	1.85
PTH-F	5	-4.71	20.38	0.14	16.47	3.24	0.13	6.29	0.18	0.88
PTH-F	5	-4.46	18.40	-1.63	16.17	1.37	-0.81	5.37	-0.34	1.70
PTH-F	5	-5.29	16.85	-2.02	15.62	1.73	-2.25	4.89	-3.21	0.01
PTH-G	6	-17.21	-13.61	-9.30	2.17	4.45	-7.75	-7.33	-5.68	0.70
PTH-G	6	-17.47	-14.38	-9.56	2.06	4.77	-8.50	-8.84	-4.95	0.94
PTH-G	6	-17.91	-14.78	-10.15	1.02	4.88	-6.99	-8.02	-5.64	1.72
PTH-G	6	-16.59	-15.59	-9.41	0.76	4.71	-7.05	-6.57	-4.65	0.82
PTH-G	6	-16.91	-15.42	-10.57	0.30	5.48	-7.68	-8.59	-5.83	1.79
PTH-H	7	33.87	-31.78	1.15	-4.17	3.74	-0.57	0.58	2.15	2.41
PTH-H	7	33.02	-33.43	1.91	-5.47	2.66	1.19	0.26	3.11	3.52
PTH-H	7	33.64	-33.82	3.33	-5.38	3.74	0.79	3.82	3.08	1.70
PTH-H	7	32.40	-29.75	1.13	-7.90	4.25	-3.30	1.87	4.69	1.17
PTH-H	7	34.28	-32.65	0.85	-6.63	3.66	-0.45	1.14	4.06	3.54
PTH-I	8	-0.63	47.03	30.68	-23.91	-4.35	-1.92	-2.04	-0.75	-0.99
PTH-I	8	0.25	46.68	28.24	-26.48	-2.07	0.17	-1.53	-1.85	-1.20
PTH-I	8	0.38	47.77	31.59	-23.44	-1.62	-1.57	-1.22	-0.63	0.80
PTH-I	8	2.38	49.42	31.27	-27.97	-0.60	-0.24	0.21	-0.66	0.65
PTH-I	8	2.58	47.97	31.13	-27.63	-0.82	-1.30	-0.35	-2.57	0.44
PTH-K	9	-11.30	-7.64	-15.04	-7.86	-21.04	1.79	4.12	-0.99	-0.50
PTH-K	9	-11.28	-8.34	-15.27	-7.88	-20.01	1.66	2.52	0.37	0.25
PTH-K	9	-12.59	-7.47	-15.52	-7.71	-20.51	1.02	1.41	-1.73	2.11
PTH-K	9	-11.30	-9.58	-15.08	-7.31	-18.49	1.49	4.17	-0.54	0.58
PTH-K	9	-10.91	-8.77	-14.24	-7.38	-19.27	0.24	3.26	-1.46	1.37

PTH-L	10	-0.18	30.35	-1.40	0.48	15.76	5.36	2.45	-3.21	0.33
PTH-L	10	0.71	31.84	-0.90	0.36	16.03	5.75	2.78	-2.80	0.72
PTH-L	10	-0.09	31.08	-0.13	0.36	16.36	5.45	3.08	-3.39	1.49
PTH-L	10	1.26	31.32	-0.53	-0.04	16.46	5.24	2.60	-2.57	3.58
PTH-L	10	2.38	28.30	-3.60	2.06	15.40	4.58	3.95	-2.93	0.71
PTH-M	11	1.54	18.88	-6.29	7.82	-1.13	-1.47	-0.25	-1.53	-2.24
PTH-M	11	-0.15	16.61	-6.12	6.37	-1.11	-1.09	-0.47	-1.58	-1.92
PTH-M	11	1.00	18.09	-6.64	6.92	0.23	-1.95	-1.56	-3.22	-4.43
PTH-M	11	2.09	17.55	-5.60	7.30	-0.72	-1.71	0.79	-1.24	-1.82
PTH-M	11	1.70	15.80	-6.86	6.14	-0.79	-1.80	0.70	-1.87	-2.67
PTH-N	12	3.60	20.74	-10.35	5.55	1.04	-1.26	-3.95	4.66	-0.05
PTH-N	12	3.56	19.84	-9.90	4.97	0.75	-1.49	-4.08	4.42	-0.88
PTH-N	12	3.89	21.09	-9.67	4.79	0.90	-1.33	-3.51	3.24	-1.30
PTH-N	12	3.00	18.92	-9.74	2.16	0.72	-2.05	-5.74	3.32	-2.47
PTH-N	12	3.33	19.04	-9.77	4.11	2.42	-2.01	-5.11	3.44	-1.19
PTH-P	13	-9.02	-4.82	-21.59	-11.80	-6.67	8.12	-0.21	-2.36	-1.35
PTH-P	13	-11.11	-6.23	-20.31	-12.75	-6.57	8.49	0.67	-2.78	-0.01
PTH-P	13	-9.37	-5.67	-19.43	-12.43	-5.35	7.08	-0.78	-1.99	-0.98
PTH-P	13	-9.69	-7.53	-18.57	-13.69	-4.90	7.33	0.22	-1.40	0.49
PTH-P	13	-8.14	-5.84	-19.86	-13.04	-4.62	6.09	-2.13	-1.50	0.45
PTH-Q	14	9.11	23.58	-12.04	2.68	8.96	2.30	-1.22	3.27	0.05
PTH-Q	14	8.07	23.24	-10.36	4.29	11.41	1.87	-1.71	5.06	-1.53
PTH-Q	14	8.18	21.71	-11.54	0.47	8.25	2.94	-0.48	4.29	2.10
PTH-Q	14	10.22	23.54	-10.94	1.50	10.46	0.89	-1.23	1.44	-1.04
PTH-Q	14	9.45	21.31	-13.23	0.55	9.58	1.06	-2.27	2.17	-0.95
PTH-R	15	1.79	-9.09	-16.83	-17.65	2.05	0.01	-0.83	0.93	0.03
PTH-R	15	1.06	-8.53	-16.50	-18.27	1.32	1.33	-0.26	1.45	-1.20

PTH-R	15	2.20	-9.11	-15.24	-18.56	1.89	1.56	2.27	1.04	-2.11
PTH-R	15	2.39	-10.33	-14.90	-18.90	3.23	-0.40	-0.37	1.76	-0.78
PTH-R	15	2.62	-11.03	-15.46	-17.98	3.52	-1.10	-0.85	1.93	0.65
PTH-S	16	-56.84	-25.19	12.62	0.16	6.90	3.79	-2.89	1.76	1.44
PTH-S	16	-56.76	-26.39	12.99	-1.30	5.37	4.23	-2.79	2.71	1.91
PTH-S	16	-57.21	-26.52	13.87	0.45	8.56	3.87	-2.30	1.72	-0.56
PTH-S	16	-56.56	-26.92	14.22	-1.49	6.99	4.77	-1.54	3.35	-0.59
PTH-S	16	-56.68	-27.62	12.82	-0.17	8.31	3.81	-2.39	2.04	-0.17
PTH-T	17	-1.82	21.20	5.61	5.32	-11.84	-3.84	-0.91	3.19	2.65
PTH-T	17	-1.96	20.78	7.79	4.11	-14.65	-4.93	-1.54	4.65	0.60
PTH-T	17	-2.60	19.22	8.83	4.13	-13.94	-5.09	-0.79	1.93	0.46
PTH-T	17	-1.49	19.90	9.05	2.41	-14.45	-6.12	-0.89	1.65	0.41
PTH-T	17	-0.85	19.85	8.41	3.64	-15.21	-6.24	-1.89	2.68	1.56
PTH-V	18	40.71	-11.98	16.94	17.20	-9.37	8.71	-4.17	-1.91	-0.95
PTH-V	18	38.25	-9.69	15.65	15.86	-9.62	6.80	-3.06	-1.53	-2.64
PTH-V	18	38.44	-10.32	15.69	16.83	-7.65	8.62	-3.92	-3.52	1.19
PTH-V	18	34.64	-10.29	15.48	15.24	-7.48	5.71	-3.28	-2.81	2.01
PTH-V	18	38.03	-10.76	16.92	15.43	-10.79	5.49	-2.89	-1.64	1.19
PTH-W	19	-41.37	-18.34	6.82	8.27	-1.88	0.38	-0.40	1.11	2.68
PTH-W	19	-41.54	-17.32	5.17	7.02	-1.89	1.53	-0.95	-0.24	0.59
PTH-W	19	-42.38	-18.48	7.11	7.36	-0.62	0.99	-1.37	1.12	0.53
PTH-W	19	-40.90	-18.02	7.43	7.49	-1.23	1.06	-0.12	1.79	-0.06
PTH-W	19	-42.00	-19.09	7.68	7.36	-0.35	0.24	-1.60	1.23	1.61
PTH-Y	20	-5.96	15.90	-2.39	10.01	-4.09	-1.33	2.66	-0.63	-0.01
PTH-Y	20	-5.34	17.03	-1.52	9.46	-5.21	-1.95	1.90	-0.55	0.10
PTH-Y	20	-5.44	15.97	-1.51	10.01	-3.29	-1.44	1.91	0.40	0.52
PTH-Y	20	-6.95	15.60	-1.32	8.66	-2.06	-0.82	2.94	-0.78	-0.43

PTH-Y	20	-4.30	15.96	-2.27	8.68	-4.08	-1.55	2.83	-0.84	0.24

5.3.7 Single Crystal Data

Table 16. Crystal data and structure refinement for **TSB1**.

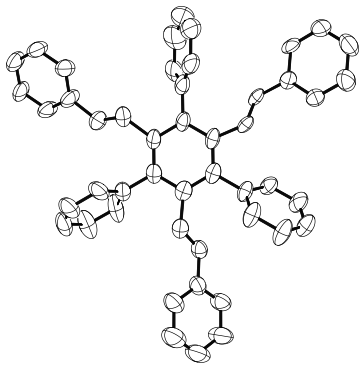

Identification code	1916511		
Empirical formula	$C_{48}H_{36}$		
Formula weight	612.77		
Temperature	100(2) K		
Wavelength	1.54178 Å		
Crystal system	triclinic		
Space group	$P\bar{1}$		
Z	4		
Unit cell dimensions	a = 10.5157(4) Å	=	85.275(3) deg.
	b = 16.0773(7) Å	=	78.563(3) deg.
	c = 22.8909(9) Å	=	84.816(3) deg.
Volume	3769.4(3) $Å^3$		
Density (calculated)	1.08 g/cm^3		
Absorption coefficient	0.46 mm^{-1}		
Crystal shape	brick		
Crystal size	0.940 x 0.088 x 0.073 mm^3		
Crystal colour	colourless		
Theta range for data collection	2.8 to 55.1 deg.		
Index ranges	-10≤h≤11, -17≤k≤12, -23≤l≤24		
Reflections collected	39056		
Independent reflections	9447 (R(int) = 0.1265)		
Observed reflections	5576 (I > 2 (I))		
Absorption correction	Semi-empirical from equivalents		
Max. and min. transmission	1.62 and 0.54		
Refinement method	Full-matrix least-squares on F^2		
Data/restraints/parameters	9447 / 5583 / 1065		
Goodness-of-fit on F^2	1.04		
Final R indices (I>2sigma(I))	R1 = 0.089, wR2 = 0.188		
Largest diff. peak and hole	0.38 and -0.27 $eÅ^{-3}$		

Table 17. Crystal data and structure refinement for **TSB2**.

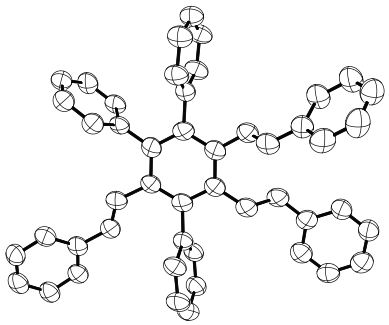

Identification code	1916512		
Empirical formula	$C_{48}H_{36}$		
Formula weight	612.77		
Temperature	100(2) K		
Wavelength	1.54178 Å		
Crystal system	monoclinic		
Space group	$P2_1/c$		
Z	4		
Unit cell dimensions	a = 9.9090(9) Å	=	90 deg.
	b = 13.7850(10) Å	=	99.607(7) deg.
	c = 24.970(2) Å	=	90 deg.
Volume	3362.9(5) $Å^3$		
Density (calculated)	1.21 g/cm^3		
Absorption coefficient	0.52 mm^{-1}		
Crystal shape	needle		
Crystal size	0.257 x 0.034 x 0.029 mm^3		
Crystal colour	yellow		
Theta range for data collection	3.6 to 55.1 deg.		
Index ranges	$-7\leq h\leq 10$, $-14\leq k\leq 14$, $-26\leq l\leq 26$		
Reflections collected	19134		
Independent reflections	4220 (R(int) = 0.1443)		
Observed reflections	2734 (I > 2 (I))		
Absorption correction	Semi-empirical from equivalents		
Max. and min. transmission	2.15 and 0.46		
Refinement method	Full-matrix least-squares on F^2		
Data/restraints/parameters	4220 / 378 / 433		
Goodness-of-fit on F^2	1.07		
Final R indices (I>2sigma(I))	R1 = 0.102, wR2 = 0.259		
Largest diff. peak and hole	0.69 and -0.28 $eÅ^{-3}$		

Table 18. Crystal data and structure refinement for **DSB2**.

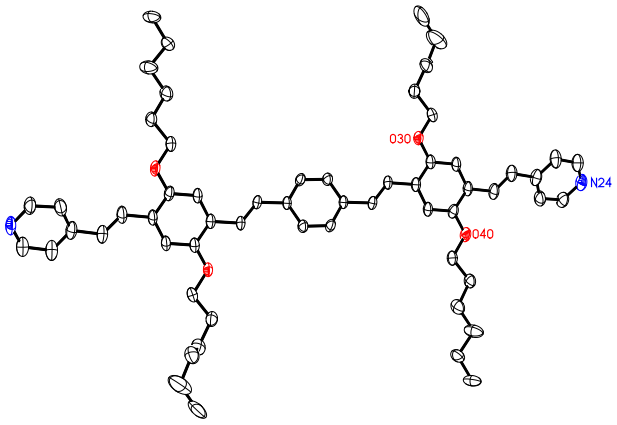

CCDC	1959608		
Empirical formula	$C_{60}H_{76}N_2O_4$		
Formula weight	889.22		
Temperature	110(2) K		
Wavelength	1.54178 Å		
Crystal system	triclinic		
Space group	$P\bar{1}$		
Z	2		
Unit cell dimensions	a =	12.1325(9) Å	= 99.905(6) deg.
	b =	15.0247(11) Å	= 107.287(6) deg.
	c =	15.1022(11) Å	= 95.066(6) deg.
Volume	2560.8(3) $Å^3$		
Density (calculated)	1.15 g/cm^3		
Absorption coefficient	0.55 mm^{-1}		
Crystal shape	brick		
Crystal size	0.155 x 0.137 x 0.066 mm^3		
Crystal colour	orange		
Theta range for data collection	3.1 to 66.9 deg.		
Index ranges	-11≤h≤14, -17≤k≤15, -16≤l≤17		
Reflections collected	19962		
Independent reflections	8562 (R(int) = 0.0300)		
Observed reflections	4917 (I > 2 (I))		
Absorption correction	Semi-empirical from equivalents		
Max. and min. transmission	1.72 and 0.56		
Refinement method	Full-matrix least-squares on F^2		
Data/restraints/parameters	8562 / 1478 / 715		
Goodness-of-fit on F^2	1.05		
Final R indices (I>2sigma(I))	R1 = 0.077, wR2 = 0.213		
Largest diff. peak and hole	0.58 and -0.36 $eÅ^{-3}$		

Table 19. Crystal data and structure refinement for **TSB3**.

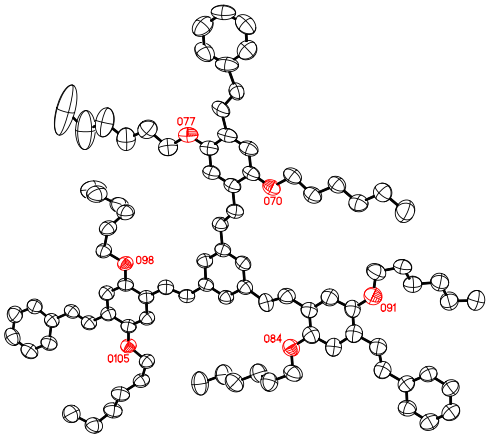

CCDC	1959609		
Empirical formula	$C_{90}H_{114}O_6$		
Formula weight	1291.81		
Temperature	100(2) K		
Wavelength	1.54178 Å		
Crystal system	monoclinic		
Space group	$P2_1/c$		
Z	4		
Unit cell dimensions	a = 15.8983(5) Å	=	90 deg.
	b = 9.8893(3) Å	=	92.562(3) deg.
	c = 49.2710(16) Å	=	90 deg.
Volume	7738.8(4) $Å^3$		
Density (calculated)	1.11 g/cm^3		
Absorption coefficient	0.52 mm^{-1}		
Crystal shape	plate		
Crystal size	0.220 x 0.088 x 0.050 mm^3		
Crystal colour	neonyellow		
Theta range for data collection	4.6 to 51.1 deg.		
Index ranges	-16≤h≤12, -9≤k≤9, -49≤l≤46		
Reflections collected	25405		
Independent reflections	8039 (R(int) = 0.0497)		
Observed reflections	5304 (I > 2 (I))		
Absorption correction	Semi-empirical from equivalents		
Max. and min. transmission	1.58 and 0.51		
Refinement method	Full-matrix least-squares on F^2		
Data/restraints/parameters	8039 / 1099 / 940		
Goodness-of-fit on F^2	1.03		
Final R indices (I>2sigma(I))	R1 = 0.101, wR2 = 0.271		
Largest diff. peak and hole	0.48 and -0.26 $eÅ^{-3}$		

Table 20. Crystal data and structure refinement for **TSB6**.

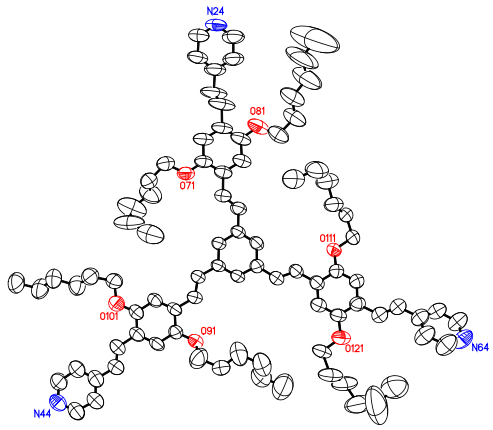

CCDC	1959610		
Empirical formula	$C_{87}H_{111}N_3O_6$		
Formula weight	1294.78		
Temperature	110(2) K		
Wavelength	1.54178 Å		
Crystal system	triclinic		
Space group	$P\bar{1}$		
Z	2		
Unit cell dimensions	a = 14.1922(17) Å	=	94.03(1) deg.
	b = 14.7488(17) Å	=	93.06(1) deg.
	c = 19.855(3) Å	=	113.568(9) deg.
Volume	3784.9(8) $Å^3$		
Density (calculated)	1.14 g/cm^3		
Absorption coefficient	0.54 mm^{-1}		
Crystal shape	brick		
Crystal size	0.260 x 0.157 x 0.075 mm^3		
Crystal colour	yellow		
Theta range for data collection	3.4 to 49.1 deg.		
Index ranges	-13≤h≤10, -12≤k≤14, -19≤l≤19		
Reflections collected	21659		
Independent reflections	7396 (R(int) = 0.0325)		
Observed reflections	4270 (I > 2 (I))		
Absorption correction	Semi-empirical from equivalents		
Max. and min. transmission	1.65 and 0.57		
Refinement method	Full-matrix least-squares on F^2		
Data/restraints/parameters	7396 / 1065 / 865		
Goodness-of-fit on F^2	2.38		
Final R indices (I>2sigma(I))	R1 = 0.154, wR2 = 0.371		
Largest diff. peak and hole	0.63 and -0.31 $eÅ^{-3}$		

References

[1] J.-S. Wu, S.-W. Cheng, Y.-J. Cheng and C.-S. Hsu, *Chem. Soc. Rev.* **2015**, *44*, 1113-1154.

[2] S.-C. Lo and P. L. Burn, *Chem. Rev.* **2007**, *107*, 1097-1116.

[3] M. Elbing and G. C. Bazan, *Angew. Chem. Int. Ed.* **2008**, *47*, 834-838.

[4] Y. Yi, L. Zhu and Z. Shuai, *Macromol. Theory Simul.* **2008**, *17*, 12-22.

[5] a) Z. Hu, H. Zhang, Y. Chen, Q. Wang, M. R. Elsegood, S. J. Teat, X. Feng, M. M. Islam, F. Wu and B. Z. Tang, *Dyes Pigm.* **2020**, *175*, 108175; b) Y. Zhang, S. Xie, Z. Zeng and B. Z. Tang, *Matter* **2020**, *3*, 1862-1892; c) D. D. La, S. V. Bhosale, L. A. Jones and S. V. Bhosale, *ACS Appl. Mater. Interfaces* **2017**, *10*, 12189-12216; d) M. H. Chua, H. Zhou, Q. Zhu, B. Z. Tang and J. W. Xu, *Mater. Chem. Front.* **2021**, *5*, 659-708.

[6] F. J. Hoeben, P. Jonkheijm, E. Meijer and A. P. Schenning, *Chem. Rev.* **2005**, *105*, 1491-1546.

[7] a) R. Corriu and J. Masse, *J. Chem. Soc., Chem. Commun.* **1972**, 144a-144a; b) J. Zhou, Z. Chang, Y. Jiang, B. He, M. Du, P. Lu, Y. Hong, H. S. Kwok, A. Qin and H. Qiu, *Chem. Commun.* **2013**, *49*, 2491-2493; c) Z. Zhao, S. Chen, J. W. Lam, Z. Wang, P. Lu, F. Mahtab, H. H. Sung, I. D. Williams, Y. Ma and H. S. Kwok, *J. Mater. Chem.* **2011**, *21*, 7210-7216; d) T. Itoh, K. Kude, S. Hayase and M. Kawatsura, *Tetrahedron Lett.* **2007**, *48*, 7774-7777; e) J. G. De Vries, *Can. J. Chem.* **2001**, *79*, 1086-1092; f) B. Tian and J. Liu, *J. Sci. Food Agric.* **2020**, *100*, 1392-1404; g) W. Perkin, *J. Chem. Soc.* **1868**, *21*, 181-186; h) F. von Nussbaum, M. Rüth, P. Spiteller, T. Hübscher‐Weissert, F. Löbermann, K. Polborn and W. Steglich, *Eur. J. Org. Chem.* **2012**, *2012*, 380-390; i) N.-Y. Chen, L.-P. Ren, M.-M. Zou, Z.-P. Xu, X.-S. Shao, X.-Y. Xu and Z. Li, *Chin. Chem. Lett.* **2014**, *25*, 197-200; j) P. J. Kocienski, B. Lythgoe and I. Waterhouse, *J. Chem. Soc., Perkin Trans. 1* **1980**, 1045-1050; k) Y. Takaya, K. Terashima, J. Ito, Y.-H. He, M. Tateoka, N. Yamaguchi and M. Niwa, *Tetrahedron* **2005**, *61*, 10285-10290.

[8] N. Zhang, Z.-J. Quan, Z. Zhang, Y.-X. Da and X.-C. Wang, *Chem. Commun.* **2016**, *52*, 14234-14237.

[9] F. B. Mallory, C. S. Wood and J. T. Gordon, *J. Am. Chem. Soc.* **1964**, *86*, 3094-3102.

[10] K. Muszkat, N. Castel, A. Jakob, E. Fischer, W. Luettke and K. Rauch, *J. Photochem. Photobiol. A* **1991**, *56*, *219-226.*

[11] J. Freudenberg, F. Rominger and U. H. Bunz, *Chem. Eur. J.* **2016**, *22*, 8740-8744.

[12] Z. Zhao, H. Zhang, J. W. Lam and B. Z. Tang, *Angew. Chem. Int. Ed.* **2020**, *59*, 9888-9907.

[13] J. Mei, N. L. Leung, R. T. Kwok, J. W. Lam and B. Z. Tang, *Chem. Rev.* **2015**, *115*, 11718-11940.

[14] S. Suzuki, S. Sasaki, A. S. Sairi, R. Iwai, B. Z. Tang and G. i. Konishi, *Angew. Chem. Int. Ed.* **2020**, *132*, 9940-9951.

[15] J. Wang, Y. Zhao, C. Dou, H. Sun, P. Xu, K. Ye, J. Zhang, S. Jiang, F. Li and Y. Wang, *J. Phys. Chem. B* **2007**, *111*, 5082-5089.

[16] J. Luo, Z. Xie, J. W. Lam, L. Cheng, H. Chen, C. Qiu, H. S. Kwok, X. Zhan, Y. Liu and D. Zhu, *Chem. Commun.* **2001**, 1740-1741.

[17] a) A. Qin, J. W. Lam, F. Mahtab, C. K. Jim, L. Tang, J. Sun, H. H. Sung, I. D. Williams and B. Z. Tang, *Appl. Phys. Lett.* **2009**, *94*, 173; b) Z. Shuai and Q. Peng, *Phys. Rep.* **2014**, *537*, 123-156.

[18] Z. Zhao, X. Zheng, L. Du, Y. Xiong, W. He, X. Gao, C. Li, Y. Liu, B. Xu and J. Zhang, *Nat. Commun.* **2019**, *10*, 1-10.

[19] a) C. J. Bhongale, C.-W. Chang, C.-S. Lee, E. W.-G. Diau and C.-S. Hsu, *J. Phys. Chem. B* **2005**, *109*, 13472-13482; b) K. Itami, Y. Ohashi and J.-i. Yoshida, *J. Org. Chem.* **2005**, *70*, 2778-2792.

[20] Y. Li, F. Li, H. Zhang, Z. Xie, W. Xie, H. Xu, B. Li, F. Shen, L. Ye and M. Hanif, *Chem. Commun.* **2007**, 231-233.

[21] Y. Jiang, Y. Wang, J. Hua, J. Tang, B. Li, S. Qian and H. Tian, *Chem. Commun.* **2010**, *46*, 4689-4691.

[22] a) P. W. Bohn, *Annu. Rev. Phys. Chem.* **1993**, *44*, 37-60; b) M. Kasha, H. Rawls and M. A. El-Bayoumi, *Pure Appl. Chem.* **1965**, *11*, 371-392.

[23] Z. Xie, B. Yang, W. Xie, L. Liu, F. Shen, H. Wang, X. Yang, Z. Wang, Y. Li and M. Hanif, *J. Phys. Chem. B* **2006**, *110*, 20993-21000.

[24] Y. Cai, L. Du, K. Samedov, X. Gu, F. Qi, H. H. Sung, B. O. Patrick, Z. Yan, X. Jiang and H. Zhang, *Chem. Sci.* **2018**, *9*, 4662-4670.

[25] T.-C. Lin, Y.-H. Lee, B.-R. Huang, C.-L. Hu and Y.-K. Li, *Tetrahedron* **2012**, *68*, 4935-4949.

[26] a) J. Lott, C. Ryan, B. Valle, J. R. Johnson III, D. A. Schiraldi, J. Shan, K. D. Singer and C. Weder, *Adv. Mater.* **2011**, *23*, 2425-2429; b) S. B. Brown, E. A. Brown and I. Walker, *Lancet Oncol.* **2004**, *5*, 497-508.

[27] Y. Chen, R. Guan, C. Zhang, J. Huang, L. Ji and H. Chao, *Coord. Chem. Rev.* **2016**, *310*, 16-40.

[28] C.-L. Sun, J. Li, X.-Z. Wang, R. Shen, S. Liu, J.-Q. Jiang, T. Li, Q.-W. Song, Q. Liao and H.-B. Fu, *Chem* **2019**, *5*, 600-616.

[29] Z. Chi, X. Zhang, B. Xu, X. Zhou, C. Ma, Y. Zhang, S. Liu and J. Xu, *Chem. Soc. Rev.* **2012**, *41*, 3878-3896.

[30] N. B. Shustova, T.-C. Ong, A. F. Cozzolino, V. K. Michaelis, R. G. Griffin and M. Dincă, *J. Am. Chem. Soc.* **2012**, *134*, 15061-15070.

[31] N. S. Kumar, S. Varghese, C. Suresh, N. P. Rath and S. Das, *J. Phys. Chem. C* **2009**, *113*, 11927-11935.

[32] C. Dou, L. Han, S. Zhao, H. Zhang and Y. Wang, *J. Phys. Chem. Lett.* **2011**, *2*, 666-670.

[33] L. Kloppenburg, D. Song and U. H. Bunz, *J. Am. Chem. Soc.* **1998**, *120*, 7973-7974.

[34] T. Dutta, K. B. Woody and M. D. Watson, *J. Am. Chem. Soc.* **2008**, *130*, 452-453.

[35] a) R. Chinchilla and C. Nájera, *Chem. Rev.* **2007**, *107*, 874-922; b) U. H. Bunz, K. Seehafer, M. Bender and M. Porz, *Chem. Soc. Rev.* **2015**, *44*, 4322-4336.

[36] Y.-J. Cheng, S.-H. Yang and C.-S. Hsu, *Chem. Rev.* **2009**, *109*, 5868-5923.

[37] J. Wang, F. Lv, L. Liu, Y. Ma and S. Wang, *Coord. Chem. Rev.* **2018**, *354*, 135-154.

[38] Q. Zhou and T. M. Swager, *J. Am. Chem. Soc.* **1995**, *117*, 7017-7018.

[39] L.-J. Fan, Y. Zhang, C. B. Murphy, S. E. Angell, M. F. Parker, B. R. Flynn and W. E. Jones Jr, *Coord. Chem. Rev.* **2009**, *253*, 410-422.

[40] K. P. Carter, A. M. Young and A. E. Palmer, *Chem. Rev.* **2014**, *114*, 4564-4601.

[41] P. Zheng and N. Wu, *Chem. Asian J.* **2017**, *12*, 2343-2353.

[42] L. Basabe-Desmonts, D. N. Reinhoudt and M. Crego-Calama, *Chem. Soc. Rev.* **2007**, *36*, 993-1017.

[43] a) P. Xie, F. Guo, S. Yang, D. Yao, G. Yang and L. Xie, *J. Fluoresc.* **2014**, *24*, 473-480; b) S. Chowdhury, B. Rooj, A. Dutta and U. Mandal, *J. Fluoresc.* **2018**, *28*, 999-1021.

[44] A. Gupta and N. Kumar, *RSC Adv.* **2016**, *6*, 106413-106434.

[45] Z. Kowser, U. Rayhan, T. Akther, C. Redshaw and T. Yamato, *Mater. Chem. Front.* **2021**, *5*, 2173-2200.

[46] Z. S. Pehlivan, M. Torabfam, H. Kurt, C. Ow-Yang, N. Hildebrandt and M. Yüce, *Microchim. Acta* **2019**, *186*, 1-22.

[47] H. K. Cho, D. H. Lee and J.-I. Hong, *Chem. Commun.* **2005**, 1690-1692.

[48] L. You, D. Zha and E. V. Anslyn, *Chem. Rev.* **2015**, *115*, 7840-7892.

[49] K. T. Mahmudov, M. N. Kopylovich, M. F. C. G. da Silva and A. J. Pombeiro, *Coord. Chem. Rev.* **2017**, *345*, 54-72.

[50] G. R. Desiraju, *Angew. Chem. Int. Ed.* **2011**, *50*, 52-59.

[51] Y. Zhou, J. F. Zhang and J. Yoon, *Chem. Rev.* **2014**, *114*, 5511-5571.

[52] V. Goral, M. I. Nelen, A. V. Eliseev and J.-M. Lehn, *Proc. Natl. Acad. Sci. U.S.A.* **2001**, *98*, 1347-1352.

[53] S. Otto, R. L. Furlan and J. K. Sanders, *J. Am. Chem. Soc.* **2000**, *122*, 12063-12064.

[54] G. C. Vougioukalakis and R. H. Grubbs, *Chem. Rev.* **2010**, *110*, 1746-1787.

[55] D. Wu, A. C. Sedgwick, T. Gunnlaugsson, E. U. Akkaya, J. Yoon and T. D. James, *Chem. Soc. Rev.* **2017**, *46*, 7105-7123.

[56] a) M. Gao and B. Z. Tang, *ACS Sens.* **2017**, *2*, 1382-1399; b) L. Mao, Y. Liu, S. Yang, Y. Li, X. Zhang and Y. Wei, *Dyes Pigm.* **2019**, *162*, 611-623.

[57] S. Gozem, H. L. Luk, I. Schapiro and M. Olivucci, *Chem. Rev.* **2017**, *117*, 13502-13565.

[58] S. Chen, Y.-L. Yu and J.-H. Wang, *Anal. Chim. Acta* **2018**, *999*, 13-26.

[59] A. C. Sedgwick, L. Wu, H.-H. Han, S. D. Bull, X.-P. He, T. D. James, J. L. Sessler, B. Z. Tang, H. Tian and J. Yoon, *Chem. Soc. Rev.* **2018**, *47*, 8842-8880.

[60] J. Li, B. Fu, D. Huo, C. Hou, M. Yang, C. Shen, H. Luo and P. Yang, *Sens. Actuators B Chem.* **2017**, *240*, 770-778.

[61] T. D. James, K. S. Sandanayake and S. Shinkai, *Nature* **1995**, *374*, 345-347.

[62] A. C. Sedgwick, J. T. Brewster, T. Wu, X. Feng, S. D. Bull, X. Qian, J. L. Sessler, T. D. James, E. V. Anslyn and X. Sun, *Chem. Soc. Rev.* **2021**, *50*, 3-8.

[63] D. G. Smith, I. L. Topolnicki, V. E. Zwicker, K. A. Jolliffe and E. J. New, *Analyst* **2017**, *142*, 3549-3563.

[64] N. A. Rakow and K. S. Suslick, *Nature* **2000**, *406*, 710-713.

[65] H. Lin, M. Jang and K. S. Suslick, *J. Am. Chem. Soc.* **2011**, *133*, 16786-16789.

[66] J. Freudenberg, F. Hinkel, D. Jänsch and U. H. Bunz, *Polymer Synthesis Based on Triple-bond Building Blocks* **2017**, 191-239.

[67] R. Kumar, S. Sandhu, P. Singh and S. Kumar, *Chem. Rec.* **2017**, *17*, 441-471.

[68] a) J. Motoyoshiya, J.-y. Wada, K. Itoh, K. Wakabayashi, T. Maruyama, K. Ono, K. Fukasawa, T. Fujimoto, Y. Akaiwa and E. Nonaka, *Spectrochim. Acta A Mol. Biomol. Spectrosc.* **2018**, *195*, 223-229; b) X. Chen, X. Y. Shen, E. Guan, Y. Liu, A. Qin, J. Z. Sun and B. Z. Tang, *Chem. Commun.* **2013**, *49*, 1503-1505.

[69] N. Kumar, I. Leray and A. Depauw, *Coord. Chem. Rev.* **2016**, *310*, 1-15.

[70] a) A. J. Zucchero, P. L. McGrier and U. H. Bunz, *Acc. Chem. Res.* **2010**, *43*, 397-408; b) J. Tolosa, A. J. Zucchero and U. H. Bunz, *J. Am. Chem. Soc.* **2008**, *130*, 6498-6506.

[71] M. Bender, K. Seehafer, M. Findt and U. H. Bunz, *RSC Adv.* **2015**, *5*, 96189-96193.

[72] Y. Zhang, D. Li, Y. Li and J. Yu, *Chem. Sci.* **2014**, *5*, 2710-2716.

[73] K. Ji, H. Wu, J. Chen, J. Shen, X. Wang, H. Wu and C. Liu, *Luminescence* **2016**, *31*, 924-928.

[74] W. Huang, M. Bender, K. Seehafer, I. Wacker, R. R. Schröder and U. H. Bunz, *Macromolecules* **2018**, *51*, 1345-1350.

[75] J. Freudenberg, J. Kumpf, V. Schäfer, E. Sauter, S. J. Wörner, K. Brödner, A. Dreuw and U. H. Bunz, *J. Org. Chem.* **2013**, *78*, 4949-4959.

[76] Y. Cai, L. Li, Z. Wang, J. Z. Sun, A. Qin and B. Z. Tang, *Chem. Commun.* **2014**, *50*, 8892-8895.

[77] K. Ma, H. Wang, H. Li, B. Xu and W. Tian, *Sens. Actuators B Chem.* **2017**, *253*, 92-96.

[78] J. Kumpf, J. Freudenberg and U. H. Bunz, *Analyst* **2015**, *140*, 3136-3142.

[79] J. Han, M. Bender, K. Seehafer and U. H. Bunz, *Angew. Chem. Int. Ed.* **2016**, *55*, 7689-7692.

[80] J. R. Askim, M. Mahmoudi and K. S. Suslick, *Chem. Soc. Rev.* **2013**, *42*, 8649-8682.

[81] J. Wu, B. Kwon, W. Liu, E. V. Anslyn, P. Wang and J. S. Kim, *Chem. Rev.* **2015**, *115*, 7893-7943.

[82] Y. Wu, B. Wang, K. Wang and P. Yan, *Anal. Methods* **2018**, *10*, 3939-3944.

[83] S. Rana, S. G. Elci, R. Mout, A. K. Singla, M. Yazdani, M. Bender, A. Bajaj, K. Saha, U. H. Bunz and F. R. Jirik, *J. Am. Chem. Soc.* **2016**, *138*, 4522-4529.

[84] B. Wang, J. Han, M. Bender, S. Hahn, K. Seehafer and U. H. Bunz, *ACS Sens.* **2018**, *3*, 504-511.

[85] J. Han, C. Ma, B. Wang, M. Bender, M. Bojanowski, M. Hergert, K. Seehafer, A. Herrmann and U. H. Bunz, *Chem* **2017**, *2*, 817-824.

[86] H. Zhang, F. Rominger, U. H. Bunz and J. Freudenberg, *Chem. Eur. J.* **2019**, *25*, 11218-11222.

[87] a) H. Meier, *Angew. Chem. Int. Ed.* **1992**, *31*, 1399-1420; b) d. A. Bosman, H. Janssen and E. Meijer, *Chem. Rev.* **1999**, *99*, 1665-1688.

[88] a) M. Lehmann, P. Maier, M. Grüne and M. Hügel, *Chem. Eur. J.* **2017**, *23*, 1060-1068; b) M. Lehmann and P. Maier, *Angew. Chem. Int. Ed.* **2015**, *54*, 9710-9714.

[89] H. Meier and M. Lehmann, *Angew. Chem.* **1998**, *110*, 666-669.

[90] a) C. Coya, A. de Andrés, C. Zaldo, A. Álvarez, B. Arredondo, R. Gómez, J. Segura and C. Seoane, *J. Appl. Phys.* **2009**, *105*, 044510; b) C. Coya, A. de Andrés, R. Gómez, C. Seoane and J. Segura, *J. Lumin.* **2008**, *128*, 761-764.

[91] B. R. Cho, K. H. Son, S. H. Lee, Y.-S. Song, Y.-K. Lee, S.-J. Jeon, J. H. Choi, H. Lee and M. Cho, *J. Am. Chem. Soc.* **2001**, *123*, 10039-10045.

[92] a) M. Uda, A. Momotake and T. Arai, *Org. Biomol. Chem.* **2003**, *1*, 1635-1637; b) P. J. Pacheco-Liñán, A. s. Garzón, J. Tolosa, I. n. Bravo, J. s. Canales-Vázquez, J. n. Rodríguez-López, J. Albaladejo and J. C. García-Martínez, *J. Phys. Chem. C* **2016**, *120*, 18771-18779.

[93] R. T. Kwok, C. W. Leung, J. W. Lam and B. Z. Tang, *Chem. Soc. Rev.* **2015**, *44*, 4228-4238.

[94] P. Jagadesan, T. Whittemore, T. Beirl, C. Turro and P. L. McGrier, *Chem. Eur. J.* **2017**, *23*, 917-925.

[95] J. Freudenberg, F. Rominger and U. H. Bunz, *Chem. Eur. J.* **2015**, *21*, 16749-16753.

[96] Y. Tang and B. Z. Tang, *Principles and Applications of Aggregation-Induced Emission*, Springer, **2018**, 1-514.

[97] T. H. Regan and J. B. Miller, *J. Org. Chem.* **1967**, *32*, 592-596.

[98] M. Oelgemöller, B. Brem, R. Frank, S. Schneider, D. Lenoir, N. Hertkorn, Y. Origane, P. Lemmen, J. Lex and Y. Inoue, *Journal of the Chemical Society, Perkin Transactions 2* **2002**, 1760-1771.

[99] J. Gierschner, L. Lüer, B. a. Milián-Medina, D. Oelkrug and H.-J. Egelhaaf, *J. Phys. Chem. Lett.* **2013**, *4*, 2686-2697.

[100] D. Dang, Z. Qiu, T. Han, Y. Liu, M. Chen, R. T. Kwok, J. W. Lam and B. Z. Tang, *Adv. Funct. Mater.* **2018**, *28*, 1707210.

[101] Y. Dong, J. W. Lam, A. Qin, Z. Li, J. Sun, Y. Dong and B. Z. Tang, *J. Inorg. Organomet. P.* **2007**, *17*, 673-678.

[102] J. J. Bryant, B. D. Lindner and U. H. Bunz, *J. Org. Chem.* **2013**, *78*, 1038-1044.

[103] J. Freudenberg, A. C. Uptmoor, F. Rominger and U. H. Bunz, *J. Org. Chem.* **2014**, *79*, 11787-11791.

[104] H. Zhang, E. A. Kotlear, S. Kushida, S. Maier, F. Rominger, J. Freudenberg and U. H. Bunz, *Chem. Eur. J.* **2020**, *26*, 8137-8143.

[105] J. Wang, S. Wang, X. Li, L. Zhu, Q. Meng, Y. Xiao and D. Li, *Chem. Commun.* **2014**, *50*, 5829-5832.

[106] T. Schwaebel, V. Schäfer, J. Wenz, B. A. Coombs, J. Tolosa and U. H. Bunz, *J. Org. Chem.* **2013**, *78*, 960-965.

[107] J.-J. Huang, L.-K. Yun, T.-J. Kung, C.-L. Chen, J.-H. Lee, Y.-R. Wu, T.-L. Chiu, P.-T. Chou and M.-k. Leung, *J. Mater. Chem. C* **2017**, *5*, 3600-3608.

[108] L. Feng, C. Zhu, H. Yuan, L. Liu, F. Lv and S. Wang, *Chem. Soc. Rev.* **2013**, *42*, 6620-6633.

[109] a) P. L. McGrier, K. M. Solntsev, A. J. Zucchero, O. R. Miranda, V. M. Rotello, L. M. Tolbert and U. H. Bunz, *Chem. Eur. J.* **2011**, *17*, 3112-3119; b) E. A. Davey, A. J. Zucchero, O. Trapp and U. H. Bunz, *J. Am. Chem. Soc.* **2011**, *133*, 7716-7718.

[110] B. Sadowski, K. Hassanein, B. Ventura and D. T. Gryko, *Org. Lett.* **2018**, *20*, 3183-3186.

[111] A. Sánchez-Ruiz, S. González-Alfaro, J. C. García-Martínez and J. Rodríguez-López, *Dyes Pigm.* **2020**, *182*, 108610.

[112] J. Kumpf, J. Freudenberg, K. Fletcher, A. Dreuw and U. H. Bunz, *J. Org. Chem.* **2014**, *79*, 6634-6645.

[113] H. Meier, M. Lehmann, H. C. Holst and D. Schwöppe, *Tetrahedron* **2004**, *60*, 6881-6888.

[114] M. Lehmann, B. Schartel, M. Hennecke and H. Meier, *Tetrahedron* **1999**, *55*, 13377-13394.

[115] B. Jędrzejewska, J. Kabatc, B. Ośmiałowski and J. Pączkowski, *Spectrochim. Acta A Mol. Biomol. Spectrosc.* **2007**, *67*, 306-315.

[116] M. Zheng, M. Sun, D. Zhang, T. Liu, S. Xue and W. Yang, *Dyes Pigm.* **2014**, *101*, 109-115.

[117] M. Frisch, G. Trucks, H. Schlegel, G. Scuseria, M. Robb, J. Cheeseman, G. Scalmani, V. Barone, G. Petersson and H. Nakatsuji, *Gaussian Inc. Wallingford CT* **2016**, *1*.

[118] T. Lu and F. Chen, *J. Comput. Chem.* **2012**, *33*, 580-592.

[119] X. Y. Shen, Y. J. Wang, E. Zhao, W. Z. Yuan, Y. Liu, P. Lu, A. Qin, Y. Ma, J. Z. Sun and B. Z. Tang, *J. Phys. Chem. C* **2013**, *117*, 7334-7347.

[120] J. Tolosa, K. M. Solntsev, L. M. Tolbert and U. H. Bunz, *J. Org. Chem.* **2009**, *75*, 523-534.

[121] D. Li, B. Li, S. Wang, C. Zhang, H. Cao, X. Tian and Y. Tian, *Spectrochim. Acta A Mol. Biomol. Spectrosc.* **2020**, *224*, 117448.

[122] L. Xue, C. Liu and H. Jiang, *Org. Lett.* **2009**, *11*, 1655-1658.

[123] T. Schwaebel, S. Menning and U. H. Bunz, *Chem. Sci.* **2014**, *5*, 1422-1428.

[124] H. Zhang, B. Wang and K. Seehafer and U. H. F. Bunz, *Chem. Eur. J.* **2020**, *26*, 7779-7782.

[125] A. D. Jangale, Y. B. Wagh, Y. A. Tayade and D. S. Dalal, *Synth. Commun.* **2015**, *45*, 1876-1886.

[126] H. Mutlu and J. F. Lutz, *Angew. Chem. Int. Ed.* **2014**, *53*, 13010-13019.

[127] P. Edman, *Acta chem. scand* **1950**, *4*, 283-293.

[128] a) M. Qi, X.-F. Li, C. Stathakis and N. J. Dovichi, *J. Chromatogr. A* **1999**, *853*, 131-140; b) T. Hanai, *J. Chromatogr. Sci.* **2016**, *54*, 604-608; c) C. L. Zimmerman, E. Appella and J. J. Pisano, *Anal. Biochem.* **1977**, *77*, 569-573; d) B. C. Pramanik, S. M. Hinton, D. S. Millington, T. A. Dourdeville and C. A. Slaughter, *Anal. Biochem.* **1988**, *175*, 305-318.

[129] G. A. Grant and M. W. Crankshaw in *Identification of PTH-amino acids by high-performance liquid chromatography*, Springer, **1997**, pp. 197-215.

[130] V. Valderrey, A. Bonasera, S. Fredrich and S. Hecht, *Angew. Chem. Int. Ed.* **2017**, *56*, 1914-1918.

[131] a) Z. Li, J. R. Askim and K. S. Suslick, *Chem. Rev.* **2018**, *119*, 231-292; b) E. G. Shcherbakova, T. Minami, V. Brega, T. D. James and P. Anzenbacher Jr, *Angew. Chem. Int. Ed.* **2015**, *54*, 7130-7133.

[132] Z. Jiao, P. Zhang, H. Chen, C. Li, L. Chen, H. Fan and F. Cheng, *Sens. Actuators B Chem.* **2019**, *295*, 110-116.

[133] A. Bigdeli, F. Ghasemi, H. Golmohammadi, S. Abbasi-Moayed, M. A. F. Nejad, N. Fahimi-Kashani, S. Jafarinejad, M. Shahrajabian and M. R. Hormozi-Nezhad, *Nanoscale* **2017**, *9*, 16546-16563.

[134] K. L. Diehl and E. V. Anslyn, *Chem. Soc. Rev.* **2013**, *42*, 8596-8611.

[135] B. Wang, J. Han, H. Zhang, M. Bender, A. Biella, K. Seehafer and U. H. Bunz, *Chem. Eur. J.* **2018**, *24*, 17361-17366.

[136] W. Huang, E. Smarsly, J. Han, M. Bender, K. Seehafer, I. Wacker, R. R. Schröder and U. H. Bunz, *ACS Appl. Mater. Interfaces* **2017**, *9*, 3068-3074.

[137] J. Han, H. Cheng, B. Wang, M. S. Braun, X. Fan, M. Bender, W. Huang, C. Domhan, W. Mier and T. Lindner, *Angew. Chem. Int. Ed.* **2017**, *56*, 15246-15251.

[138] W. Huang, K. Seehafer and U. H. Bunz, *ACS Appl. Polym. Mater.* **2019**, *1*, 1301-1307.

[139] H. L. Mark and D. Tunnell, *Anal. Chem.* **1985**, *57*, 1449-1456.

[140] B. Wang, J. Han, M. Bender, K. Seehafer and U. H. Bunz, *Macromolecules* **2017**, *50*, 4126-4131.

[141] H. Khajehsharifi and A. Sheini, *Sens. Actuators B Chem.* **2014**, *199*, 457-462.

[142] B. Wang, J. Han, C. Ma, M. Bender, K. Seehafer, A. Herrmann and U. H. Bunz, *Chem. Eur. J.* **2017**, *23*, 12471-12474.

[143] S. L. Wicks and A. E. Hargrove, *Methods* **2019**, *167*, 3-14.

[144] T. Ishikawa, *Superbases for organic synthesis: guanidines, amidines, phosphazenes and related organocatalysts*, John Wiley & Sons, **2009**, 1-336.

[145] M. Eckert‐Maksić, Z. Glasovac, P. Trošelj, A. Kütt, T. Rodima, I. Koppel and I. A. Koppel, *Eur. J. Org. Chem.* **2008**, 5176-5184.

[146] J. E. Taylor, S. D. Bull and J. M. Williams, *Chem. Soc. Rev.* **2012**, *41*, 2109-2121.

[147] G. Sartori, R. Ballini, F. Bigi, G. Bosica, R. Maggi and P. Righi, *Chem. Rev.* **2004**, *104*, 199-250.

[148] D. Castagnolo, S. Schenone and M. Botta, *Chem. Rev.* **2011**, *111*, 5247-5300.

[149] R. Wolfenden, L. Andersson, P. Cullis and C. Southgate, *Biochemistry* **1981**, *20*, 849-855.

[150] T. Noguchi, T. Shiraki, A. Dawn, Y. Tsuchiya, T. Yamamoto and S. Shinkai, *Chem. Commun.* **2012**, *48*, 8090-8092.

[151] I. A. Levitsky, J. Kim and T. M. Swager, *J. Am. Chem. Soc.* **1999**, *121*, 1466-1472.

[152] H. Miel and S. Rault, *Tetrahedron Lett.* **1998**, *39*, 1565-1568.

[153] a) X. Zhu, J. Yang and K. S. Schanze, *Photochem. Photobiol. Sci.* **2014**, *13*, 293-300; b) F. Chen, P. Manandhar, M. S. Ahmed, S. Chang, N. Panday, H. Zhang, J. H. Moon and J. He, *Macromol. Biosci.* **2019**, *19*, 1800271; c) M. Twomey, T. Vokatá, M. R. Kumar and J. H. Moon, *Chem. Commun.* **2015**, *51*, 4065-4068.

[154] R. G. Berlinck, A. C. B. Burtoloso and M. H. Kossuga, *Nat. Prod. Rep.* **2008**, *25*, 919-954.

[155] H.-Y. Mi, J.-L. Liu, M.-M. Guan, Q.-W. Liu, Z.-Q. Zhang and G.-D. Feng, *Talanta* **2018**, *187*, 314-320.

[156] a) F. Guodong, G. Mingming, L. Qi, M. Hongyu, L. Guanghua, M. Qiang, F. Qiang, H. Yanfu and S. Zhiguang, *New J. Chem.* **2016**, *40*, 8444-8450; b) A. Gobbi and G. Frenking, *J. Am. Chem. Soc.* **1993**, *115*, 2362-2372.

[157] L. Zhang, Z. Kang, X. Xin and D. Sun, *CrystEngComm* **2016**, *18*, 193-206.

[158] a) S. S. Nagarkar, B. Joarder, A. K. Chaudhari, S. Mukherjee and S. K. Ghosh, *Angew. Chem. Int. Ed.* **2013**, *125*, 2953-2957; b) A. S. Tanwar, S. Hussain, A. H. Malik, M. A. Afroz and P. K. Iyer, *ACS Sens.* **2016**, *1*, 1070-1077.

[159] Y. Ma, S. Huang, M. Deng and L. Wang, *ACS Appl. Mater. Interfaces* **2014**, *6*, 7790-7796.

[160] a) S. Halder, P. Ghosh, A. Hazra, P. Banerjee and P. Roy, *New J. Chem.* **2018**, *42*, 8408-8414; b) K. Shiraishi, T. Sanji and M. Tanaka, *ACS Appl. Mater. Interfaces* **2009**, *1*, 1379-1382.

[161] S. Pramanik, C. Zheng, X. Zhang, T. J. Emge and J. Li, *J. Am. Chem. Soc.* **2011**, *133*, 4153-4155.

[162] S. Kumari, S. Joshi, T. C. Cordova-Sintjago, D. D. Pant and R. Sakhuja, *Sens. Actuators B* **2016**, *229*, 599-608.

[163] Y. Salinas, R. Martínez-Máñez, M. D. Marcos, F. Sancenón, A. M. Costero, M. Parra and S. Gil, *Chem. Soc. Rev.* **2012**, *41*, 1261-1296.

[164] M. Van de Weert and L. Stella, *J. Mol. Struct.* **2011**, *998*, 144-150.

[165] D. Zhao and T. M. Swager, *Macromolecules* **2005**, *38*, 9377-9384.

[166] G. R. Fulmer, A. J. M. Miller, N. H. Sherden, H. E. Gottlieb, A. Nudelman, B. M. Stoltz, J. E. Bercaw and K. I. Goldberg, *Organometallics* **2010**, *29*, 2176-2179.

[167] P. C. DeRose, E. A. Early and G. W. Kramer, *Rev. Sci. Instrum.* **2007**, *78*, 033107.

[168] C. Würth, M. Grabolle, J. Pauli, M. Spieles and U. Resch-Genger, *Nat. Protoc.* **2013**, *8*, 1535-1550.

[169] B. Wang, X.-L. Lv, D. Feng, L.-H. Xie, J. Zhang, M. Li, Y. Xie, J.-R. Li and H.-C. Zhou, *J. Am. Chem. Soc.* **2016**, *138*, 6204-6216.

[170] A. K. Jhingan and W. F. Maier, *J. Org. Chem.* **1987**, *52*, 1161-1165.

[171] a) M. Nojima, K. Kosaka, M. Kato, Y. Ohta and T. Yokozawa, *Macromol. Rapid Commun.* **2016**, *37*, 79-85; b) C. H. Huang and Y. J. Chang, *Tetrahedron Lett.* **2014**, *55*, 4938-4942.

[172] E. W. Miller, J. Y. Lin, E. P. Frady, P. A. Steinbach, W. B. Kristan and R. Y. Tsien, *Proc. Natl. Acad. Sci. U.S.A.* **2012**, *109*, 2114-2119.

[173] N. Mizoshita, M. Ikai, T. Tani and S. Inagaki, *J. Am. Chem. Soc.* **2009**, *131*, 14225-14227.

[174] Z. Shi, J. Davies, S.-H. Jang, W. Kaminsky and A. K.-Y. Jen, *Chem. Commun.* **2012**, *48*, 7880-7882.

[175] I.-B. Kim, R. Phillips and U. H. Bunz, *Macromolecules* **2007**, *40*, 5290-5293.

[176] a) L. X. Chen, S. Xiao and L. Yu, *J. Phys. Chem. B* **2006**, *110*, 11730-11738; b) A. Y.-T. Huang, C.-H. Tsai, H.-Y. Chen, H.-T. Chen, C.-Y. Lu, Y.-T. Lin and C.-L. Kao, *Chem. Commun.* **2013**, *49*, 5784-5786; c) H. Gan, Y. Li, H. Liu, S. Wang, C. Li, M. Yuan, X. Liu, C. Wang, L. Jiang and D. Zhu, *Biomacromolecules* **2007**, *8*, 1723-1729.

[177] a) Y. Yamaguchi, Y. Matsubara, T. Ochi, T. Wakamiya and Z.-i. Yoshida, *J. Am. Chem. Soc.* **2008**, *130*, 13867-13869; b) M. Bergström, G. Suresh, V. R. Naidu and C. R. Unelius, *Eur. J. Org. Chem.* **2017**, *2017*, 3234-3239.

[178] M. U. Luescher, C.-V. T. Vo and J. W. Bode, *Org. Lett.* **2014**, *16*, 1236-1239.

[179] X. Yang, D. Liu and Q. Miao, *Angew. Chem. Int. Ed.* **2014**, *126*, 6904-6908.

[180] M. Auffray, F. Charra, L. S. Vargas, F. Mathevet, A.-J. Attias and D. Kreher, *New J. Chem.* **2020**, *44*, 7665-7674.

[181] G. Gaefke, V. Enkelmann and S. Höger, *Synthesis* **2006**, *2006*, 2971-2973.

Eidesstattliche Versicherung gemäß § 8 der Promotionsordnung der Naturwissenschaftlich-Mathematischen Gesamtfakultät der Universität Heidelberg

Bei der eingereichten Dissertation zu dem Thema

„Styrylbenzene and Phenyleneethynylene Derivatives: Synthesis, Properties and Their Application in Fluorescent Sensor Field “

handelt es sich um meine eigenständig erbrachte Leistung.

Ich habe nur die angegebenen Quellen und Hilfsmittel benutzt und mich keiner unzulässigen Hilfe Dritter bedient. Insbesondere habe ich wörtlich oder sinngemäß aus anderen Werken übernommene Inhalte als solche kenntlich gemacht.

Die Arbeit oder Teile davon habe ich bislang nicht an einer Hochschule des In- oder Auslands als Bestandteil einer Prüfungs- oder Qualifikationsleistung vorgelegt.

Die Richtigkeit der vorstehenden Erklärung bestätige ich.

Die Bedeutung der eidesstaatlichen Versicherung und die strafrechtlichen Folgen einer unrichtigen oder unvollständigen eidesstattlichen Versicherung sind mir bekannt.

Ich versichere an Eides statt, dass ich nach bestem Wissen die reine Wahrheit erklärt und nichts verschwiegen habe.

_____ _____

Ort und Datum Unterschrift